DYNAMICS AND IMPACTS OF OIL SPILLS FROM SEABED RELEASES IN THE FAROE-SHETLAND CHANNEL

A thesis submitted to the School of Environmental Sciences
of the University of East Anglia in partial fulfilment
of the requirements for the degree of Doctor of Philosophy

RYAN GILCHRIST

JULY 2020

© This copy of the thesis has been supplied on condition that anyone who consults it is understood to recognise that its copyright rests with the author and that use of any information derived there from must be in accordance with current UK Copyright Law. In addition, any quotation or extract must include full attribution.

© Copyright 2020

Ryan Gilchrist

ABSTRACT

Oil and gas exploration are well-established in the Faroe-Shetland Channel (FSC) and gradually moving into deeper waters. The FSC is a complex physical system, host to strong currents, mesoscale variability, internal waves and tides, and a unique stratification structure. This thesis explores how these hydrodynamic features influence oil plume dynamics and the subsequent far-field transport, by using the Oil Spill Contingency and Response (OSCAR) modelling system.

The operational hydrodynamic model commonly used as part of UK spill response (AMM7) is compared against CTD observations. AMM7 is poor at representing ocean stratification, because mid-water-column property gradients are too weak and there are large same-depth differences in temperature (order 5 °C) and salinity (order 0.2 g kg^{-1}).

Model-observation differences are then quantified and used to guide idealised plume modelling using the DeepBlow component of OSCAR. Plume trapping almost always occurs below the thermocline, irrespective of non-hydrodynamic parameters or the stratification and current structures. When oil is released from 1000 m, AMM7 will estimate the trapping depth to be too deep by order 100 m. Most oil (85–90%) will eventually surface and be advected north-eastward towards the Norwegian Sea. Four-fifths of the remaining submerged oil will instead be advected westward into the open North Atlantic.

Regional spill modelling shows that the coasts of Shetland and Norway are at risk of contamination by a spill originating from the FSC, depending on the time of year and the release location. Compared to a deep (> 1000 m) release, a shelf (< 200 m) release increases the risk of coastline contamination but prevents the south-westward advection of oil. Simulating a spill using a finer resolution hydrodynamic model (AMM15) suggests that mesoscale processes act to recirculate and contain oil within the central FSC, but also act to increase the difficulty of a clean-up operation.

Access Condition and Agreement

Each deposit in UEA Digital Repository is protected by copyright and other intellectual property rights, and duplication or sale of all or part of any of the Data Collections is not permitted, except that material may be duplicated by you for your research use or for educational purposes in electronic or print form. You must obtain permission from the copyright holder, usually the author, for any other use. Exceptions only apply where a deposit may be explicitly provided under a stated licence, such as a Creative Commons licence or Open Government licence.

Electronic or print copies may not be offered, whether for sale or otherwise to anyone, unless explicitly stated under a Creative Commons or Open Government license. Unauthorised reproduction, editing or reformatting for resale purposes is explicitly prohibited (except where approved by the copyright holder themselves) and UEA reserves the right to take immediate ‘take down’ action on behalf of the copyright and/or rights holder if this Access condition of the UEA Digital Repository is breached. Any material in this database has been supplied on the understanding that it is copyright material and that no quotation from the material may be published without proper acknowledgement.

CONTENTS

LIST OF FIGURES

LIST OF TABLES

LISTS OF SYMBOLS AND ACRONYMS

Table 1: Common mathematical symbols used in this thesis (alphabetical; lower case, upper case, Greek). Dashes in the units column indicate either changeable units or a dimensionless variable.

Symbol	Name	units
d	Release orifice diameter	m
f	Inertial frequency	s^{-1}
g	Gravity	$m\,s^{-2}$
g'	Reduced gravity	$m\,s^{-2}$
k	Coefficient (various)	-
p	Pressure	-
r	Plume radius	m
s	Solubility	$g\,l^{-1}$
s_{topog}	Topography slope	-
s_{wave}	Wave characteristic slope	-
u_E	Horizontal plume entrainment velocity	$m\,s^{-1}$
w	Vertical plume velocity	$m\,s^{-1}$
C	Concentration	-
D	Oil/gas bubble diameter	mm
G	Mass	kg
H	Depth of the water-column	m
N^2	Buoyancy frequency squared	s^{-2}
R	Process rate	-
S_a	Absolute salinity	$g\,kg^{-1}$
S_p	Practical salinity	-
T	In-situ temperature	°C
V_H	Hydrate volume	m^3
V_p	Plume volume	m^3
Z	Compressibility factor	-
α	Ratio (various)	-
dT/dz	Vertical in-situ temperature gradient	$°C\,m^{-1}$
ω	Angular frequency	s^{-1}
ρ_0	Water column density at the seabed	$kg\,m^{-3}$
ρ_w	Water column density	$kg\,m^{-3}$
ρ_b	Gas bubble density	$kg\,m^{-3}$
ρ_H	Hydrate density	$kg\,m^{-3}$

Symbol	Name	units
ρ_p	Plume density	$\mathrm{kg\,m^{-3}}$
ρ_{ref}	Reference density	$\mathrm{kg\,m^{-3}}$
σ_p	Pressure scale level	-
θ	Potential temperature	°C
Θ	Conservative temperature	°C

Table 2: Acronyms used in this thesis (alphabetical order).

AI/NIW	Arctic Intermediate/North Icelandic Water
CTD	Conductivity-Temperature-Depth
DWH	Deepwater Horizon
EKE	Eddy Kinetic Energy
FBC	Faroe Bank Channel
FCW	Faroe-Cape Wrath
FIM	Fair-Isle Munken
FSC	Faroe-Shetland Channel
FSCBW	Faroe-Shetland Channel Bottom Water
GoM	Gulf of Mexico
MNAW	Modified North Atlantic Water
NAW	North Atlantic Water
NOL	Nolso Flugga
NSAIW	Norwegian Sea Arctic Intermediate Water
OSCAR	Oil Spill Contingency and Response
SSH	Sea Surface Height
SST	Sea Surface Temperature
TLPD	Terminal Layer of Plume Thickness
WTR	Wyville Thomson Ridge

ACKNOWLEDGEMENTS

This PhD was funded by a National Environment Research Council studentship (1642888), which is an industrial CASE studentship in association with the EnvEast DTP. Cefas have supported this studentship financially through additional stipend and research grant funding.

Many thanks to my supervisors Rob Hall, John Bacon, Jon Rees, and Karen Heywood. Rob has consistently reminded me to focus on what is important during the many times I've wandered off-track, and has also given me the opportunity to visit Oban several times (despite my inability to drive the van!). John and Jon have made sure I'm thinking about the bigger picture and have given the project a respectable amount of industrial motivation and drive. Karen has overseen the project from day one, and has ensured I'm getting the most out of everything (and initially convinced me to work towards publishing a paper!). Jennifer Graham has also been second-to-none in patiently answering my questions about AMM7 and AMM15.

I have a lengthy list of other people to thank. Adam Nicholls and Mark Barham hosted me during a three-month internship at Gardline, which was the deciding factor in securing my first job. Chris Rhodes referred me for that job, and has unknowingly made the final six months all but stress-free. Bill Sturges and the EnvEast team have been fundamental to my professional development and provided many opportunities to gain experience teaching and networking. Adrian Matthews and Alejandro Gallego have allowed me to take part in oceanographic cruises in the Bay of Bengal and the (less exotic) Faroe-Shetland Channel. Sonja van Leeuwen and John Aldridge from Cefas have taken my technical knowledge of using oil spill modelling software to the next level (Sonja even dedicated an entire morning to teaching me how to use OSCAR). Rob Holland has invited me down to OSRL several times to get an appreciation of the spill industry, and to ITAC where I met the entire spill response industry in one go. And without Bee Berx generously sending over some CTD data from Marine Scotland Science, I wouldn't have a Chapter 2!

Chapter 6 is a paper currently in the process of resubmission for publication.

I would like to acknowledge the co-authors for this submission (Rob Hall, John Bacon, Jon Rees, Jennifer Graham), and the two anonymous reviewers who were more constructive than I ever thought possible.

A massive thank you is due to my girlfriend Katy for putting up with her overly long commute over the past four years, and for making me realise that there is a world beyond academia. I'm now very much looking forward to the next chapter! Thank you also to all the PhD students who have made the effort to visit what feels like every pub in Norwich, explore the Norfolk coast by bike, or simply those who leave their office each day to enjoy a lunch break. And finally, thanks to everyone from office 3.16 (it's not just the working air-con, promise!), but please don't tell anyone about the pandas.

1

INTRODUCTION

1.1 MOTIVATION

Oil spills from seabed releases are a considerable environmental and economic threat to the marine environment. Between 1970-1999, the 3.1% of spills originating from subsurface well heads accounted for 15.4% of the volume of oil that was released into the marine environment (Burgherr, 2007). Deep-water drilling is gradually moving into deeper waters as a result of technological innovation and the discovery of new resources, and recent accidental releases have prompted the need to further understand what happens to oil when it interacts with the ocean. This thesis investigates how those interactions may influence the behaviour of an oil spill from a seabed release in an energetic hydrodynamic environment.

1.1.1 DEEPWATER HORIZON

The 2010 Macondo oil spill in the Gulf of Mexico (GoM) is the highest profile case study of a recent subsurface spill, and the second largest release of oil into the marine environment from any source. On 10th April, at 88.4°W, 28.7°N, approximately 80 km off the Louisiana coast, the Deepwater Horizon (DWH) platform suffered an explosion at 1552 m depth. This resulted in a continuous release of oil and gas into the marine environment in the range 0.093–0.127 $m^3 s^{-1}$ (Crone & Tolstoy, 2010; McNutt *et al.*,

2012) over 86 days. The well head was sealed on July 24th, 2010, and officially declared safe by BP on September 19th, 2010. DWH was financially the worst US marine environmental disaster in history, costing BP $145 billion including market loss (Lee *et al.*, 2018).

A total of 7–8 $\times 10^5$ m^3 of light crude oil and natural gas escaped into the GoM (Crone & Tolstoy, 2010; Camilli *et al.*, 2010; McNutt *et al.*, 2012; Joye *et al.*, 2016), making DWH the largest acute (lasting less than one year) accidental seabed release of oil into the marine environment by volume[1]. This is 50% more than IXTOC I (Mexico, 1980), which is the next largest acute seabed release. For a summary of the largest oil spills by volume, see Table 2 in Hoffman & Jennings (2011).

Approximately two-thirds of the oil released from DWH reached the sea surface (Diercks *et al.*, 2010). From Natural Resource Disaster Assessment (NRDA), it is estimated that oil slicks with a thickness of 0.1–1 mm covered over 10^5 km^2 of water (Lee *et al.*, 2013; Beyer *et al.*, 2016). Michel *et al.* (2013) inferred from Shoreline Clean-up Assessment Technique (SCAT) that 1773 km of shoreline had been contaminated, but more recently Nixon *et al.* (2016) have demonstrated that if NRDA rapid assessment data are included, the estimation is 20% higher (2113 km). Roughly 2.5 $\times 10^4$ m^3 of oil, or 4% of the total released volume, is estimated to have reached the coasts of Florida, Alabama, Mississippi, Louisiana and Texas (Boufadel *et al.*, 2014).

From fear of contamination, many fisheries immediately local to the area closed. The influence of oil on fish could not be detected in less affected areas of the GoM, with toxic levels of polycyclic aromatic hydrocarbons present in less than 5% of analysed samples (Fitzgerald & Gohlke, 2014). Over a million individual birds were affected, with species situated close to the shore showing increased mortality rates in the year immediately following the spill (Antonio *et al.*, 2011; Henkel *et al.*, 2012; Tran *et al.*, 2014).

A considerable proportion (at least 30%) of the oil did not surface, instead residing at 1100–1300 m depth and forming a trapped plume (Diercks *et al.*, 2010; Camilli *et al.*, 2010; Spier *et al.*, 2013). The plume was 2 km wide and extended downstream by up to 100 km (Camilli *et al.*, 2010; Kessler *et al.*, 2011; Du & Kessler, 2012). The trapping was partly a consequence of much of the oil entrained as very small (< 70 µm) droplets. At

[1]The Taylor Energy oil spill, also in the GoM, is likely to be considerably larger, and has been ongoing since September 16th, 2004 following Hurricane Ivan. However, this is not an 'acute' release due to the 15 years of continuous activity.

this diameter, the droplets are neutrally-buoyant and will remain below the surface indefinitely. Small droplet sizes were caused by a combination of the hot (100 °C) oil coming into sudden contact with cold water, high pressure at the well head, and the application of chemical dispersant.

A large amount (7×10^6 kg) of dispersant was used as part of the clean-up effort, with 40% of this applied at the well head, and 60% at the surface. Dispersant effectiveness is determined by a complex interaction between initial oil droplet sizes, ocean circulation and mixing, native species of micro-organisms, and nutrient availability. Dispersant usage remains controversial, and there is ongoing debate as to whether it had a net positive or net negative influence on overall degradation rates during DWH (Beyer *et al.*, 2016). Dispersants reduce the average droplet diameter, resulting in a greater droplet surface area to volume ratio. However, they also chemically alter hydrocarbon composition, which can reduce the rates of biodegradation, since local species are likely to have adapted to consume the original pollutant from natural leaks at the seabed. Biodegradation helped to reduce surface oil concentration, from 100 mgl^{-1} in the hours after surfacing to 1 mgl^{-1} after several weeks (Lee *et al.*, 2013). Surface in-situ burning was used as a major part of the clean-up effort; a total of 411 separate burning events took place, consuming 4×10^4 m^3, or 8% of the surfaced oil (Beyer *et al.*, 2016).

A considerable research effort specific to DWH and the GoM has been made since this disaster, for example the Gulf of Mexico Research Initiative[2]. The aim of this thesis is to improve our understanding of the physical dynamics of a similar sized seabed release in UK waters.

1.1.2 EXPLORATION IN THE FAROE-SHETLAND CHANNEL

The Faroe-Shetland Channel (FSC) has been an active area of UK offshore drilling since the early 1990s (Smallwood & Kirk, 2005). Whilst subsurface releases are far less likely to occur than those at the surface in a global context (Burgherr, 2007), the significance is more pronounced here because the FSC sees almost no tanker transport (MMO, 2014). As of August 2018, there are a total of 162 active well heads

[2]See http://gulfresearchinitiative.org/.

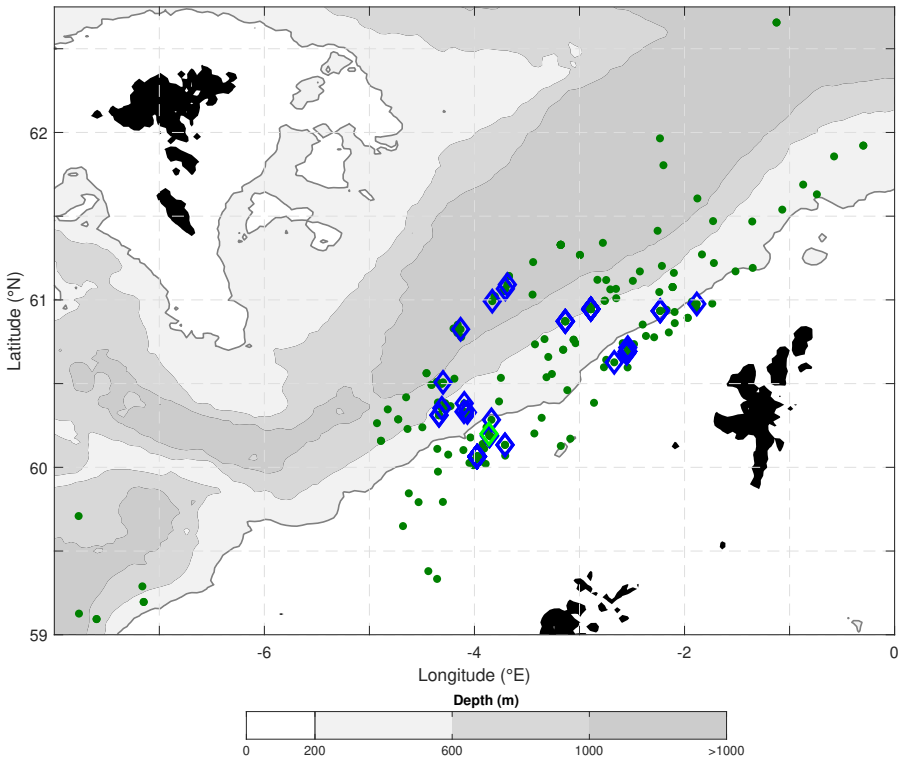

Figure 1.1: Oil and gas activity in the FSC. Well head locations as of August 2018 (source: UK Oil and Gas Authority) are indicated by green dots, where present-day activity and planned future activity are surrounded by blue diamonds and green diamonds, respectively. Bathymetry is from Smith & Sandwell (1997).

situated between the Faroe and Shetland Isles[3] (Fig. 1.1). Of these, more than three-quarters (124) are off shelf (> 200 m depth), with nine deeper than 600 m and five deeper than 1000 m. If a blow-out were to occur, and assuming each well is equally likely to fail, there is a 3% chance oil will be released in waters below 1000 m depth, and a 6% chance of a 'deep' (> 600 m) release.

Gallego *et al.* (2018) estimated the potential size of a seabed release in the FSC, considering variables such as likely well head capping time, the potential for severe weather conditions to inhibit work, and likely flow rates from a large installation. Gallego *et al.* (2018) estimated that a release of up to 3.4×10^5 m^3 could occur within a 30-day period[4], and that if it were to last the same duration as DWH then potentially up to 9.6×10^5 m^3 could be released, which would be larger than DWH. It is possible that a spill of this magnitude in a hydrodynamically energetic system such as the FSC

[3] Data from the UK Oil and Gas Authority was downloaded from arcgis.com. Where duplicates occurred in the dataset, the most recent installation was retained and the rest discarded.

[4] Gallego *et al.* (2018) reference a mass in tonnes; conversion to m^3 was made assuming an oil density of 890 kg m^{-3}

could have severe consequences for the United Kingdom's economy and environment (Baxter *et al.*, 2011; Joint Nature Conservation Committee, 2014), and pose a threat to nearby coastlines such as the Faroe, Shetland and Orkney islands, west Norway, and north Scotland.

1.1.3 OIL SPILLS ORIGINATING FROM THE FSC

Compared to the extensive scientific coverage for DWH, there is limited literature covering how oil released in the FSC will behave. The next three short sections describe a recent accidental release, field experiments undertaken in the area, and regionally applicable numerical modelling.

ACCIDENTAL RELEASES

On 2 October 2016, approximately 75 km west of Shetland, the CLAIR platform suffered a fault, releasing an estimated 106 m^3 of crude oil into the marine environment from approximately 200 m depth. Production was taken off-line immediately after the leak was identified, and the well-head was fully sealed within an hour. The oil propagated northward[5] away from the coastline, and much of it evaporated due to the high volatility of some components, which is typical of the oil type found in this region[6]. The decision was made to let the oil biodegrade or evaporate naturally. Because the oil was released in shallow water (< 200 m), almost all reached the sea surface. There are no known environmental or ecological impacts, likely due to the high evaporation rates and minimal oil trapped below the sea surface. At the time of writing, there have been no known considerable seabed releases of oil in the FSC off-shelf (> 200 m).

FIELD EXPERIMENTS

Rye & Brandvik (1997) describe two controlled releases undertaken near the Frigg field (60.1°N, 2.33°E, between Shetland and the south Norwegian coastline). The experiment consisted of an oil-only release of 25 m^3 in 1995 to simulate a pipeline rupture, and 40 m^3 of oil released alongside compressed air in 1996 to simulate a

[5] A Guardian news article states the oil moved 'in a northerly direction'. This is assumed to mean northward, taking into account the interchange of terminology used by the public, and the likely presence of a northward shelf slope current west of Shetland.

[6] See Appendix A for the chemical composition of the oil type most commonly found in the FSC

blow out event. Plume development observed from sonar recordings agreed well with model predictions. However, modelling typically overestimated the size of the surface slick, most likely due to a higher than expected suspension rate of oil droplets within the water-column. This may have been a result of a high exit velocity at the well head, which likely reduced the droplet size distribution and therefore the buoyancy of the liquid oil droplets.

The DeepSpill field experiment (Johansen *et al.*, 2001, 2003) involved four controlled discharges of oil (125 m^3 in total) and natural gas (10^4 m^3 in total) in June 2000, with the primary aim of calibrating numerical models. DeepSpill was a joint industry project involving 22 oil companies and the US government. The Hellend Hansen site was chosen for the experiment (125 km off the Norwegian coast, 65°N, 4.5°E), at a depth of 844 m. The structure of the water-column here is similar to the central FSC, with the maximum vertical density gradient (pycnocline) occurring at several hundred metres depth. Oil was observed to reach the surface an hour after the discharge began. The horizontal displacement of the surface slick was order 10^2 m relative to the release site upon surfacing. Although no direct measurements of plume entrainment were possible, it was concluded that trajectory paths agreed well with model predictions through photography.

NUMERICAL MODELLING

Most regionally applicable numerical modelling focusses on near-field plume development. Plume modelling using stratification and currents similar to what is found within the channel shows that a trapped plume is likely to form below the pycnocline at several hundred metres depth (Johansen, 2000b; Reed *et al.*, 2000; Yapa & Chen, 2004). However, these studies do not show how oil is subsequently transported in the far-field, or if a change in plume behaviour leads to a change in the eventual fate of pollutants.

Only a single research paper models far-field oil transport from a spill originating from the FSC. Main *et al.* (2017) used a general circulation model with a particle tracking algorithm to investigate the fate of neutrally-buoyant oil droplets. Oil in shallow water (< 200 m) tended to travel from the central FSC northward into the Arctic, up to 700 km away from the source. Oil in deeper water (> 600 m) travelled across the North Atlantic as far west as Greenland, controlled primarily by basin

bathymetry. Biodegradation reduced the distance oil could travel from the release site; in reality this would be difficult to measure because smaller droplet sizes are more difficult to detect. Main *et al.* (2017) showed a depth-dependant transport but did not consider the expected vertical distribution of oil droplets, or weathering processes such as evaporation and emulsification. This thesis aims to improve our understanding of how oil spills develop in the FSC by considering plume dynamics and far-field transport in the same simulation, as well as weathering processes that are not investigated by Main *et al.* (2017).

1.2 A PHYSICAL DESCRIPTION OF THE FAROE-SHETLAND CHANNEL

The FSC is of interest not only because it is an area of active oil and gas development, but also because it is a highly energetic physical system. The next section describes this system in more detail.

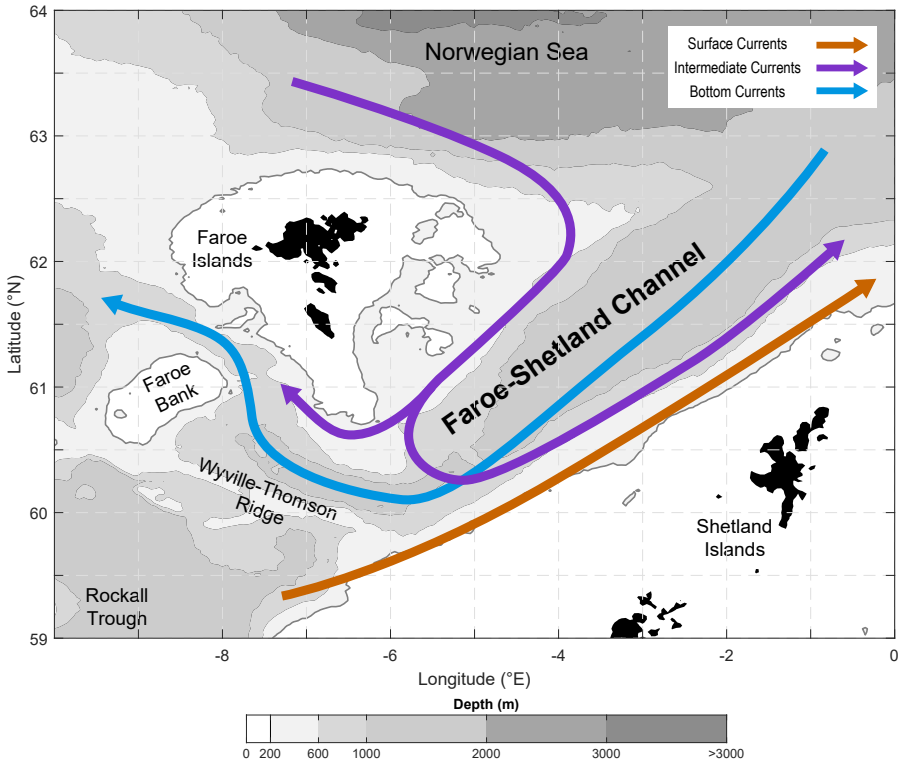

Figure 1.2: Water mass transport in the FSC. Arrows indicate dominant transport pathways for different water masses (NAW - orange; MNAW and AI/NIW - purple; NSAIW and FSCBW - blue). Bathymetry is from Smith & Sandwell (1997).

1.2.1 WATER MASS CIRCULATION

The Faroe-Shetland Channel hosts a complex circulation system. Water masses can be defined and divided into two circulating through the channel near the surface, a further two at intermediate depths, and a fifth, bottom water (Fig. 1.2; current schematics are adapted from Turrell *et al.*, 1999). Circulation, and by extension the distribution of temperature and salinity, also shows considerable seasonal, inter-annual and decadal variability (Knudsen, 1911; Blindheim & Borovkov, 1996; Turrell *et al.*, 1999; Berx *et al.*, 2013).

North Atlantic Water (NAW) originates from south-west of the Wyville-Thomson Ridge (WTR; approximately 60°N, 7°W), on the continental slope west of Scotland where North-East Atlantic Central Water is dominant (Hill & Mitchelson-Jacob, 1993). NAW flows poleward in an along-slope surface current that extends to 400 m depth along the west Shetland Slope (Fig. 1.3) and eventually into Nordic seas and the Arctic. The slope current is order $0.1\,\mathrm{m\,s^{-1}}$ but can vary considerably in the presence of mesoscale eddies (Sherwin *et al.*, 1999), and has been reported to reach velocities greater than $1\,\mathrm{m\,s^{-1}}$ (Hopkins, 1991).

A second surface water mass exists; Modified North Atlantic Water (MNAW). Residing at a similar depth to NAW, MNAW is dominant in terms of surface area covered (Dooley & Meincke, 1981). It approaches the FSC from north-west of the Faroe Islands, before branching into two paths on approach to the WTR (Becker & Hansen, 1988). Most of the water recirculates in the FSC, exiting to the north-east after mixing with NAW. The remaining flow escapes westward through the Faroe Bank Channel (FBC; approximately 61°N, 9°W; van Aken & Eisma, 1987; van Aken, 1988).

Arctic Intermediate/North Icelandic Water (AI/NIW) originates from north of the Iceland-Faroe Ridge (> 62.5°N), likely formed from a mixture of Atlantic and Arctic waters during winter convection (Meincke, 1978). Much like MNAW, the majority recirculates in the FSC after travelling anti-cyclonically around the Faroe Islands, with a relatively small amount exiting westward through the FBC (Meincke, 1978). Within the FSC, AI/NIW typically resides at 400–600 m depth, beneath both NAW and MNAW (Becker & Hansen, 1988), with a reduced and slightly shallower depth range on the Shetland side of the channel.

Norwegian Sea Arctic Intermediate Water (NSAIW) typically occupies the channel

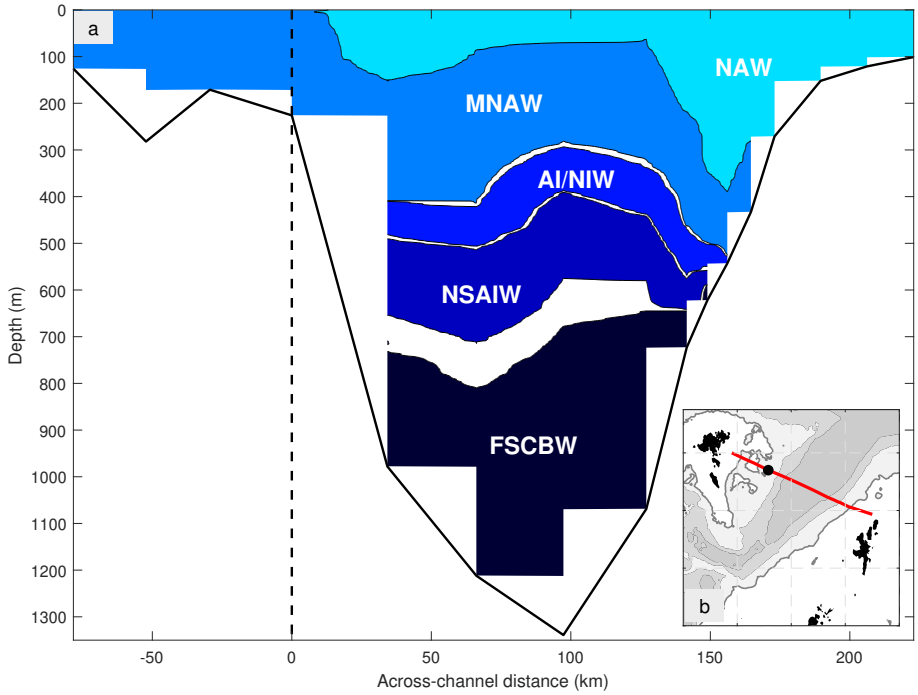

Figure 1.3: Typical observed across-channel water mass distribution. Note that water masses do not reach extend to the bathymetry because measurements have not been taken in all locations. (**a**) Cross-section of in-situ temperature in the FSC from CTD observations taken in May 2014. Contours illustrate FSC Bottom Water ($\leq -0.25\,^{\circ}$C), Norwegian Sea Arctic Intermediate Water (0–2.75 °C), Arctic Intermediate/North Icelandic Water (3–6.25 °C), Modified North Atlantic Water (6.5–9 °C), and North Atlantic Water ($\geq 9\,^{\circ}$C). Note that these water mass definitions are a guide only, and vary between authors. In this case, temperature has been used to distinguish between water masses, but salinity may also be used in some cases. Also shown is the position of the Faroe shelf edge (black dashed line). (**b**) Position of the cross-section (red line) and position of the Faroe shelf edge (black dot). Bathymetry has a scale identical to Fig. 1.1.

at 600–800 m depth. NSAIW originates from the Norwegian sea and exits primarily through the FBC, the majority flowing westward through the FBC and eventually into the open North Atlantic. Its presence is indicated on a θ-S_p (potential temperature-practical salinity) diagram as a salinity minimum (Turrell *et al.*, 1999). It is most likely formed at the surface, north of the Arctic front (Blindheim, 1990; Mauritzen, 1996), and separates AI/NIW from deeper, bottom water (Blindheim, 1990; Martin, 1993; Blindheim & Borovkov, 1996). However, seasonal variability occasionally results in NSAIW failing to reach the Shetland slope (Turrell *et al.*, 1999).

FSC Bottom Water (FSCBW) typically fills the channel below 800 m depth. It is sourced from Norwegian Deep-Sea Water (NDSW), flowing south-westward into the northern entrance of the FSC and eventually exiting through the FBC (Saunders, 1990;

Turrell *et al.*, 1999). This entrance has a maximum depth of around 2000 m, which prevents deeper layers of NDSW from entering the FSC. Intermittently, FSCBW flows over the WTR into the Rockall Trough (Sherwin *et al.*, 2008), where stratification is relatively weak. This overflow has a seasonal signal and is strongest during summer months.

1.2.2 MESOSCALE VARIABILITY

Mesoscale variability is likely to be important in determining the location and extent of horizontal oil dispersion in the FSC, because oil advection is controlled mainly by the current velocity (Reed *et al.*, 1994). Meanders have been observed to occur along the Shetland slope current, and often extend across the entire width of the channel (Sherwin *et al.*, 1999, 2006). Meanders can deflect the flow by up to 80 km across the channel (Chafik, 2012).

Eddies have been observed in the FSC and FBC for almost 40 years (Hansen & Meincke, 1979). Over the sill of the FBC, eddies are likely to be important in determining overflow dynamics (Tanaka & Akitomo, 2001; Tanaka, 2006; Seim *et al.*, 2010). By perturbing the mean residual current flow, eddies can also enhance mixing through vertical dissipation and horizontal stirring (Seim *et al.*, 2010), the latter of which may lead to greater entrainment of water and oil (Quadfasel & Käse, 2007; Voet *et al.*, 2010).

GENERATION MECHANISMS

Eddies in the central FSC can be generated as a result of the jet-like structure of the slope current and consequently a large lateral shear (Hopkins, 1991), or from the interface between NAW and MNAW (Oey, 1998). Eddy growth rates correlate with the magnitude of lateral shear, and so a strengthening of opposing surface flows will likely enhance their occurrence. Eddy generation can also be encouraged by the presence of current meanders that occur in specific areas along the FSC (Sherwin *et al.*, 2006).

In an overflow, eddies can be generated by vortex stretching (Lane-Serff & Baines, 1998; Spall & Price, 1998), or from baroclinic instability (Swaters, 1991; Smith, 1976). Darelius *et al.* (2011) discuss these generation mechanisms for the FBC overflow and conclude that the eddies were instead produced from a source of Rossby Waves south of the FBC. The authors also infer that eddies within the central FSC could

be generated in the same way. However, Sherwin *et al.* (1999) show that the Rossby radius is much smaller than the diameter of a typical eddy along the Shetland Slope, implying that Rossby wave forcing may not be an explanation for the eddies generated there.

OCCURRENCE AND BEHAVIOUR WITHIN THE CHANNEL

Eddies have been observed in the FSC since 1979. Prior to this, most hydrographic studies within the channel used gridded stations that were too coarse to resolve eddies of a small enough scale. Hansen & Meincke (1979) observed a cold core eddy with AI/NIW at its centre, likely generated at the Iceland-Faroe front.

Dooley & Meincke (1981) describe an eddy-like structure on the Faroe side of the FSC with a diameter of approximately 30 km, observed from an AVHRR image. The surface temperature structure correlated well with data from a mooring on the 890 m isobath. Unfortunately, the current meter on the mooring failed, so it is difficult to make further comparisons between surface and deeper waters to provide a full conclusion on the vertical structure.

Otto & van Aken (1996) show that a cyclonic eddy with a diameter of approximately 30 km occurred near the northern entrance of the FSC, trapping a drifter for approximately 2 months. Oil residing on the sea surface could potentially behave in a similar manner, depending on the strength of surface winds. The authors conclude that eddies are likely generated off the channel banks, which have a similar length scale to the eddy diameter. Enhanced eddy-kinetic-energy (EKE) was observed in the FBC and Rockall Trough during winter months compared to during summer months.

Sherwin *et al.* (1999) observed a 42 km cyclonic eddy at the surface (increasing to 57 km in diameter at the 300 m isobath) from an AVHRR image. Eddy activity could be further examined from drifter data, which showed considerable temperature and velocity variability and cool MNAW at its core. During the eddy's passage, the surface slope current was deflected approximately 40 km to the west.

Sherwin *et al.* (2006) show three distinct areas of enhanced surface eddy kinetic energy dissipation rates ($> 250\,\mathrm{cm^2\,s^{-1}}$) and high current velocities along the Shetland slope of 0.7–0.9 $\mathrm{m\,s^{-1}}$, inferred from drifters that correlated with altimeter data. Drifter propagation patterns varied considerably depending on location, inferring

that the currents are highly variable and could cause substantial dispersion of oil at the surface. Near the FBC, drifters tended to become stuck in eddy rotation for long periods of time. In contrast, drifters that encountered cyclonic eddies in the FSC only completed one or two rotations before continuing to propagate north-east in the slope current.

Darelius *et al.* (2011) observed an alternating band of warm cyclonic and cool anti-cyclonic eddies propagating past a series of moorings south of the FBC, similar to what was observed by Geyer *et al.* (2006). The cold core centres were slightly offset from the centre of rotation of the anti-cyclonic eddies.

1.2.3 INTERNAL WAVES

Internal waves can enhance turbulent EKE dissipation rates (Hosegood & van Haren, 2004), and could therefore be an important subsurface mixing and dispersion process for oil. Conditions in the FSC, particularly on the Shetland slope and near the WTR, provide ideal conditions for internal waves to propagate, with a mid-water-column pycnocline at approximately 500–600 m depth on the west Shetland slope (Mauritzen *et al.*, 2005; Hosegood *et al.*, 2005; Hall *et al.*, 2011). The pycnocline tends to shoal[7] by approximately 100 m towards the Faroe slope, and separates north-eastward surface transport from south-westward bottom transport (Berx *et al.*, 2013).

OBSERVATIONS IN THE FSC

Sherwin (1991) observed a linear semidiurnal internal wave on the southern Shetland slope near the WTR, with an amplitude of 37 m at a depth of 580 m. The wave was associated with a large energy flux of between $2.2 \times 10^{-3}\,\mathrm{W\,m^{-1}}$ and $4.7 \times 10^{-3}\,\mathrm{W\,m^{-1}}$, and was likely generated at the WTR.

Hosegood & van Haren (2004) observed a train of high frequency non-linear waves at the seabed, propagating onto the Shetland Slope. These waves had short, irregular periods of 5–20 min, implying that they were not tidally forced. The waves had amplitudes of order 100 m and were associated with order $10^{-7}\,\mathrm{W\,kg^{-1}}$ turbulent EKE dissipation rates, which is enough to re-suspend sediment. They were likely generated on the continental slope during the passage of a Kelvin wave.

[7] Pycnocline shoaling is defined here as where the maximum density gradient decreases in depth when moving across the channel.

Hall *et al.* (2011) analyse data from a ship survey and an array of ADCP and thermistor moorings from September 2005 and observe a semidiurnal internal tide on the west Shetland slope. Along-slope and across-slope depth integrated fluxes were order $10^2\,\mathrm{W\,m^{-1}}$, with most energy concentrated near the pycnocline at 600 m depth. The pycnocline was displaced by order 10 m during the passage of the internal tide. This displacement is generally smaller than the previous observations detailed above. Bottom-trapped, non-linear waves of a higher frequency were also observed.

GENERATION AND PROPAGATION

Internal waves can travel thousands of kilometres from their source (Alford, 2003; Simmons & Alford, 2012). Globally, many waves that have been observed are likely to have been remotely generated (Duda *et al.*, 2004; Rainville, 2010; Hall *et al.*, 2011; Nash *et al.*, 2012; Kerry *et al.*, 2013). Submarine canyons and areas of complex bathymetry such as the FSC and surrounding region can confine the direction of propagation (Gordon & Marshall, 1976; Wunsch & Webb, 1979; Hotchkiss & Wunsch, 1982; Aslam *et al.*, 2018). Internal waves that have been funnelled and amplified can produce stratified turbulence and mixing within the water-column (Kunze *et al.*, 2012; Zhao *et al.*, 2012). Mesoscale current fields can influence the direction of wave propagation (Rainville, 2010; Alford *et al.*, 2012; Nash *et al.*, 2012; Kelly *et al.*, 2013). An interference pattern of different dynamic modes may occur if internal waves from multiple sources converse on one another, producing areas of constructive and destructive interference. Model output shows that this is likely to occur within the FSC (Hall *et al.*, 2011). Other possible controls on internal wave propagation in the FSC include bottom-trapping by stratification (Hall *et al.*, 2011) and rotational effects (Helfrich & Melville, 2006).

REFLECTION

Upon encountering a continental shelf slope, an internal wave may either continue to shoal into shallower water, reflect back int deeper water, or dissipate on the slope (Fig. 1.4). The behaviour of a wave in this respect is governed by the ratio α_{iw} between the topographic slope s_{topog} and the wave characteristic slope s_{wave},

$$\alpha_{iw} = \frac{s_{topog}}{s_{wave}} = \frac{\partial H/\partial x}{\sqrt{[(\omega^2 - f^2)/N^2 - \omega^2)]}}. \tag{1.1}$$

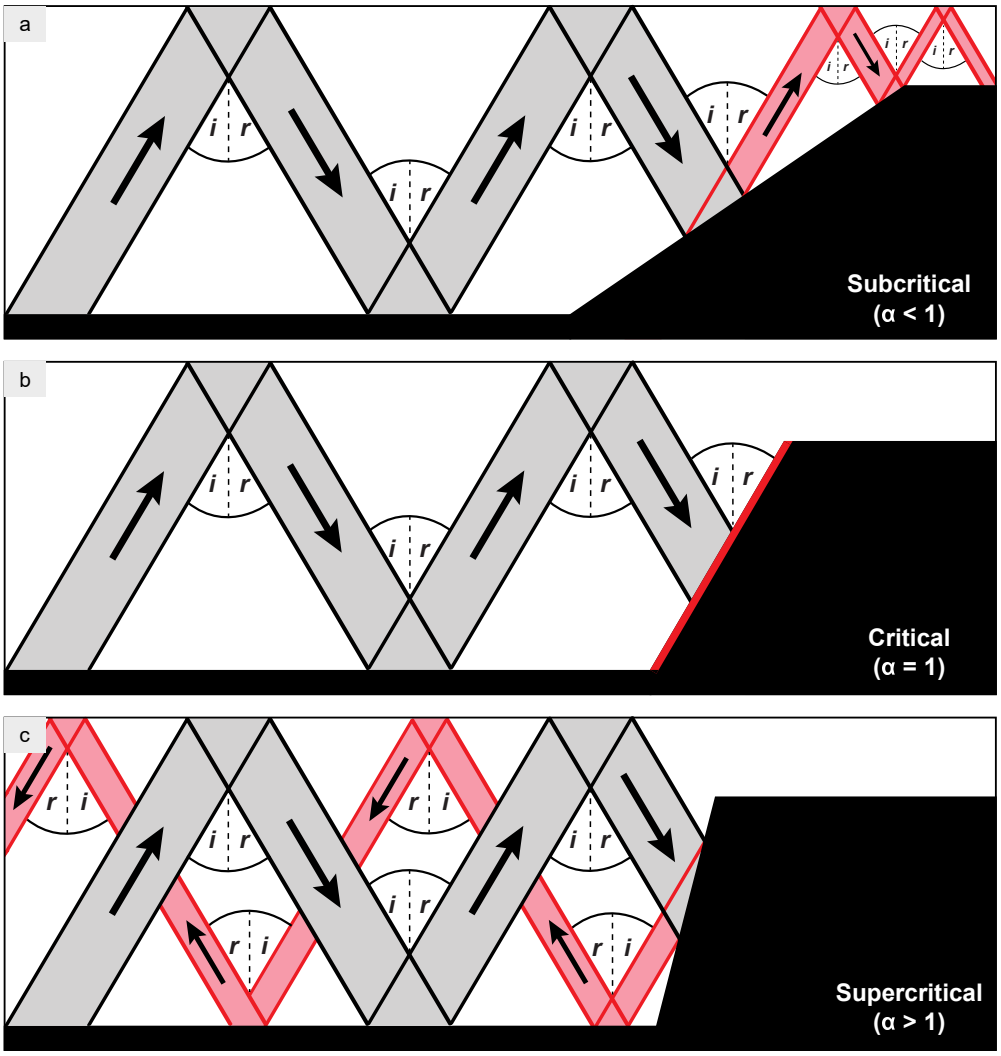

Figure 1.4: Interaction of an internal wave with a shelf slope. (**a**) Schematic reflection of a sub-critical wave. Narrower beams represent a higher energy flux density. Beams show propagation before (grey) and after (red) slope interaction. i is the incident internal wave characteristic angle, and r is the reflected internal wave characteristic angle. Arrows indicate the direction of propagation. (**b**) as (a) but for critical reflection. (**c**) as (a) but for super-critical reflection.

H is the water-column depth, x is distance across the slope, ω is the angular frequency of the wave, f is inertial frequency and N^2 is buoyancy frequency squared. If the slope is sub-critical ($\alpha_{iw} < 1$), a wave will continue to propagate up the continental slope and onto the shelf (Fig. 1.4). If the slope is super-critical ($\alpha_{iw} > 1$), a wave will be reflected back into deeper water. The Shetland slope transitions from a sub-critical state to a super-critical state, which can confine energy dissipation in non-uniform stratification (Hall *et al.*, 2011). The dependence on $\partial H/\partial x$ may be important in determining where in the FSC wave reflection can occur, with relatively

gentle (0.016) slopes on the Shetland side, and steeper (0.04) slopes towards the Faroe Islands (Sherwin *et al.*, 2006).

DISSIPATION

The dissipation of internal wave energy depends on the vertical density structure (Hall *et al.*, 2011, 2013). Model output from Hall *et al.* (2013) suggests that in the presence of a mid-water-column pycnocline, most energy is dissipated at or below maximum N^2. A deep density gradient may therefore play an important role in subsurface energy dissipation and mixing, because it is likely to prevent the shoaling of internal wave energy flux onto the continental shelf, instead confining this energy by trapping waves near the seabed and thus near to the source of a seabed oil release. Although internal wave breaking in the FSC is associated with high vertical diffusivity peaks (order $10^{-1}\,\mathrm{m^2\,s^{-1}}$), these peaks are usually brief (Hosegood & van Haren, 2004), and so it is unlikely that they can sustain deep-sea mixing for long periods of time.

1.3 BEHAVIOUR OF OIL IN WATER

Considering the physical processes described in Section 1.2, the state of the ocean will almost certainly have a large influence on oil fate and trajectory from a theoretical seabed release in the FSC. This section describes the various oil transport and weathering mechanisms that may be sensitive to these processes.

1.3.1 NEAR-FIELD PLUME DYNAMICS

Oil below the surface is initially driven by plume dynamics (Fig. 1.5), associated with high pressure at the well head and a large density difference between oil ($\approx 890\,\mathrm{kg\,m^{-3}}$) and water ($\approx 1025\,\mathrm{kg\,m^{-3}}$). Liquid oil droplets are typically 1–10 mm in diameter but can be as small as 10 µm (Johansen *et al.*, 2003; Yapa *et al.*, 2012; Johansen *et al.*, 2013; Brandvik *et al.*, 2013; Beyer *et al.*, 2016). The droplet size distribution depends on variables such as oil viscosity, temperature, diameter of the release orifice and the release rate (Yapa & Chen, 2004; Yapa *et al.*, 2012). A higher release rate, higher oil temperature and smaller release orifice will all act to reduce the droplet size distribution. Surrounding seawater is entrained and advected with the oil, which increases the mass of the plume. The mass of the plume consists of

oil, entrained water, gas hydrates, and gas bubbles. As more water is entrained, the aggregate density of the oil-water mixture increases. In a stratified environment, it is possible for the density of the plume to eventually match the density of the ambient conditions. After this stage, the plume is no longer buoyant, and the vertical velocity eventually reaches zero. This is known as the terminal layer of plume dynamics (TLPD), which depends on the vertical structure of the water-column and the rate of water entrainment (Dasanayaka & Yapa, 2009). In the FSC, the TLPD is likely to occur below the mid-water-column pycnocline (Reed *et al.*, 2000; Johansen, 2000b; Yapa & Chen, 2004). Plume dynamics are further detailed in Yapa *et al.* (2012).

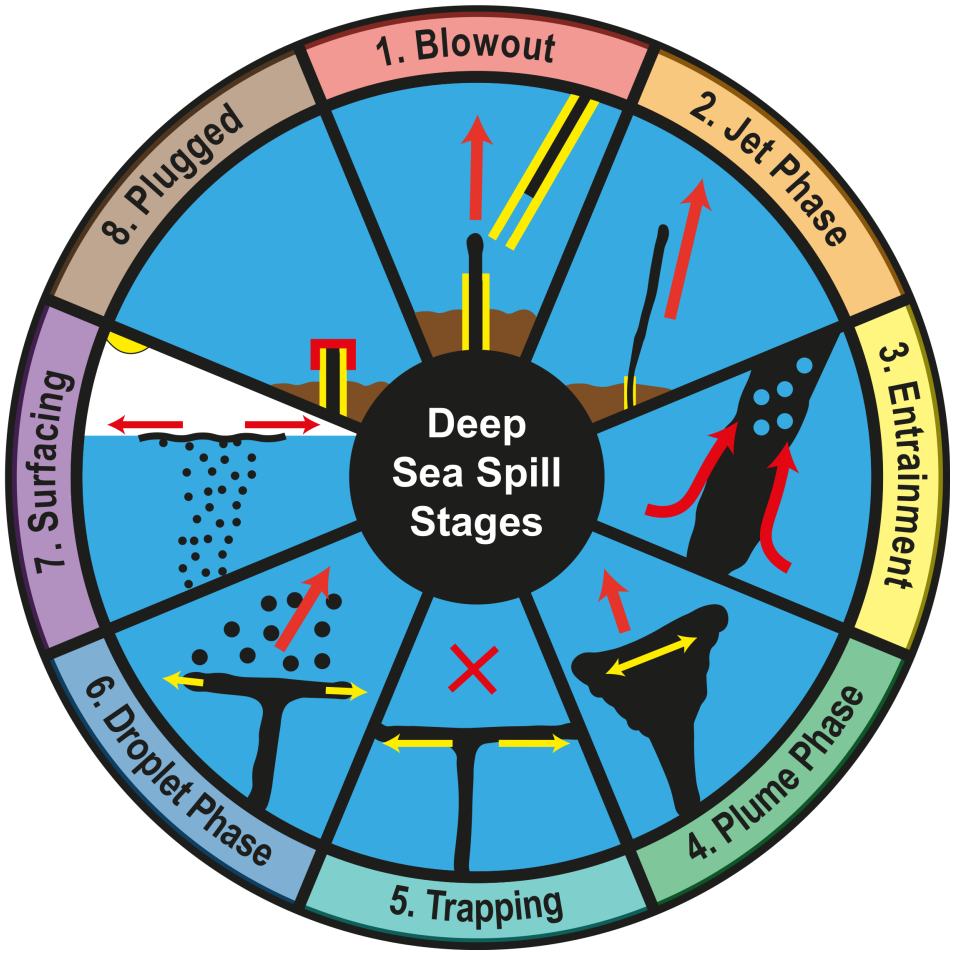

Figure 1.5: Schematic of near-field plume dynamics. Various turbulent breakup mechanisms determine the relationship between the jet phase, entrainment phase and plume phase. These stages of plume development can occur at different times for different releases.

Beyond the TLPD, oil transport is driven by advection and diffusion. The plume stops behaving as a single entity, and individual droplets instead move independently of one another. The exact way in which the plume breaks up depends primarily on the

Table 1.1: Hydrate formation and shedding depths (above: gas bubbles; below: gas hydrates), to the nearest 25 m. Adapted from Sloan & Koh (2007).

Temperature (°C)	**Methane** (m)	**Natural gas** (m)
0	300	75
2	375	100
4	450	125
6	550	150
8	675	200
10	825	250

chemical composition of the oil (Bandara & Yapa, 2011). Oil will typically not reform into a homogeneous solution above the TLPD (Rye *et al.*, 1996; Rye & Brandvik, 1997; Johansen *et al.*, 2003). However, it is possible for the plume to reform in cases of weak ocean stratification or high plume buoyancy, where heavier plume components 'peel' off and the average plume density decreases (Asaeda & Imberger, 1993). Multiple horizontal intrusions of hydrocarbons below the TLPD were observed during DWH (Socolofsky *et al.*, 2011; Spier *et al.*, 2013). Because of the order 100 kg m^{-3} density difference between oil and water, liquid oil droplets are typically buoyant and so will rise to the surface. Droplets can also be dispersed horizontally by ocean currents, which determine the initial surfacing location and direction of transport. The vertical rise velocity of each droplet depends on the droplet diameter; larger droplets have a higher buoyancy and so will reach the sea surface sooner. From 800 m depth, a 10 mm droplet will take 1 h to surface, but a 2 mm droplet will take 4 h and a 1 mm droplet will take 9.5 h (Johansen, 2000b). Small ($< 70\,\mu$m) droplets are neutrally-buoyant and so will remain within the water-column indefinitely (Yapa *et al.*, 2012; Beyer *et al.*, 2016).

Gas is typically released alongside oil from a seabed release (e.g. DWH). Gas bubble diameter has an influence on the initial stages of a plume, because the rate of both gas dissolution and gas hydrate formation is dependent on the surface area to volume ratio (Yapa *et al.*, 2012). Gas bubbles and large oil droplets can separate from the plume if ocean currents are strong enough, which will reduce the buoyancy of the plume (Johansen *et al.*, 2001; Yapa *et al.*, 2012). Gas hydrates form in high pressure and low temperature environments (Table 1.1), and typically have constant densities of 900 kg m^{-3} (methane) and 930 kg m^{-3} (natural gas), which add to the buoyancy of

the plume (Johansen, 2000a). Gas that is dissolved into any entrained seawater will contribute to the mass of the plume, but not the volume (Johansen, 2000a).

1.3.2 FAR-FIELD TRANSPORT AND WEATHERING PROCESSES

Near-field plume dynamics determine the initial conditions of oil in the ocean, including the position and size distribution of liquid oil droplets. The fate and trajectory of oil after this stage is determined by a series of physical, chemical and biological weathering processes (Fig. 1.6), in addition to ambient currents and stratification.

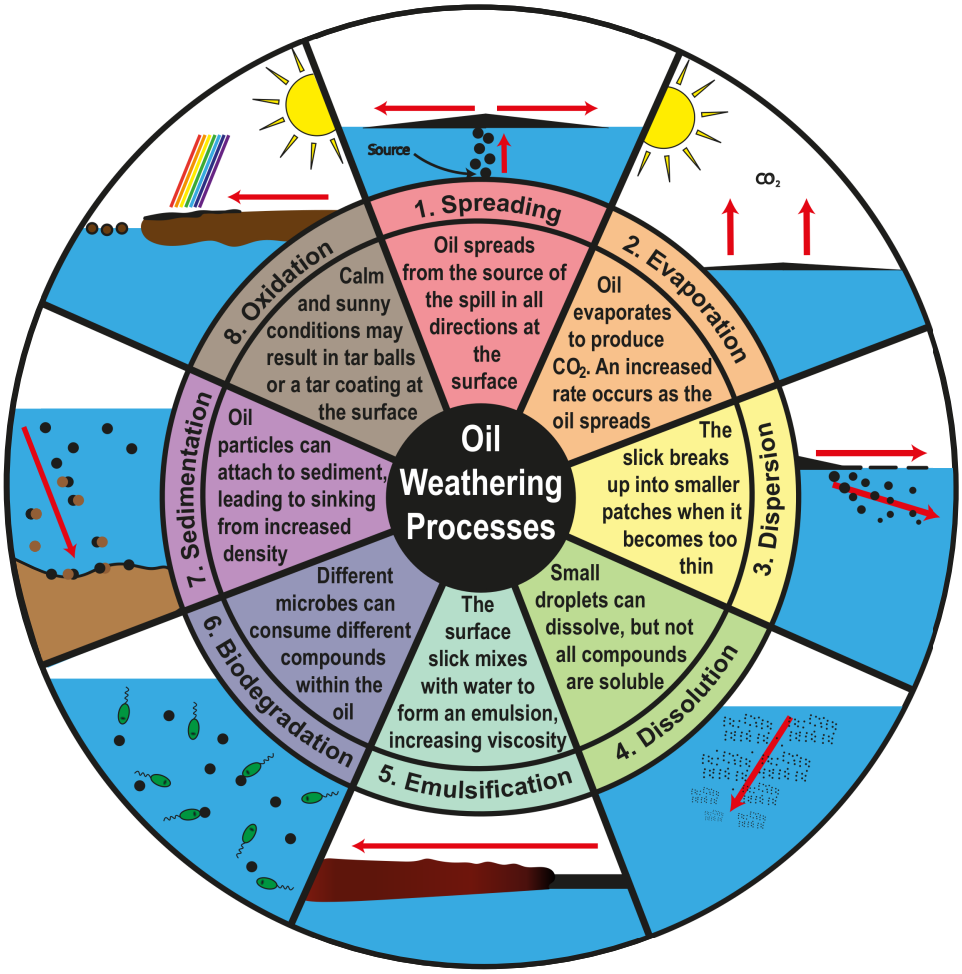

Figure 1.6: Schematic of far-field transport and weathering processes.

Oil will continue to be advected by ocean currents, with a contribution from surface winds if at the sea surface. Trajectory at the sea surface is typically calculated as the current velocity plus several percent of the wind velocity (Reed *et al.*, 1994).

The percentage influence of wind can vary with the wind speed (Youssef & Spaulding, 1993), which is typically 5–15 $m\,s^{-1}$ in the FSC (Gallego *et al.*, 2018). The direction of advection in the FSC will primarily be determined by the depth oil resides at, due to the vertical shear-flow caused by opposing currents (Fig. 1.2; Main *et al.* 2017). The dispersion of oil in the ocean is due to turbulent processes such as mesoscale eddies, surface waves and wind gusts (National Research Council, 2003). Energetic mesoscale activity in the FSC at the surface (Section 1.2.2; Sherwin *et al.*, 2006) and at up to 800 m depth (Dooley & Meincke, 1981; Sherwin *et al.*, 1999) suggests that high rates of dispersion will occur through the water-column.

Oil can be degraded by bacteria, and the presence of oil in the ocean may in fact promote the growth of bacterial colonies specifically designed to consume it (MacNaughton *et al.*, 1999). Smaller droplets, increased nutrient and light availability, and higher ambient temperatures will increase the rate of biodegradation. The unique stratification structure of the FSC (Fig. 1.3) may divide the water-column into a region of low degradation in cold, deep-water (> 500 m), and a region of high degradation in warm, shallow water (< 500 m). Much of the biota within the FSC also originates from Atlantic Water transported by surface currents (Edwards *et al.*, 2002).

Within the water-column, the adhesion of sediment and organic particles to oil (sedimentation) can cause liquid oil droplets to become negatively buoyant and sink. At the surface, the burning of oil, such as during the DWH clean-up effort (Beyer *et al.*, 2016) can create a dense residue, which will also promote sinking. Sedimentation occurs more readily in shelf seas such as those surrounding the Faroe and Shetland Islands, where there are increased rates of primary productivity and particle suspension. Deeper within the water-column on the Shetland slope (500–600 m), bottom-trapped internal wave trains can enhance sediment re-suspension (Hosegood & van Haren, 2004; Hall *et al.*, 2011).

Oil that reaches the sea surface may not stay there and can evaporate into the atmosphere or re-enter the water-column. The rate of evaporation depends largely on the volatility of the individual oil components. Within several days of surfacing, light crude oils can lose up to 75% of their mass, whereas heavy crude oils may only lose 10% (National Research Council, 2003). The oil type typically found within the FSC (Clair, see Table A.1 for a full chemical composition) is volatile relative to other medium crude oils. The rate of evaporation is also determined by the temperature

of the oil, as well as the atmospheric wind speed and humidity. A more dispersed and spread out oil slick will evaporate more readily due to a higher surface area to volume ratio. Dissolution from the surface into the water-column can occur for droplets with a diameter of approximately 100 µm or less (National Research Council, 2003). Dissolution takes place if there is enough mechanical mixing to re-suspend oil below the surface. In the FSC, wave heights are typically 1–4 m between April and September, and 3–7 m between October and March (Gallego *et al.*, 2018), and so the rate of dissolution will likely vary seasonally.

Less volatile components of the oil that remain at the surface for longer periods of time can emulsify with seawater. Stable emulsions typically consist of 60–85% water (National Research Council, 2003), which will increase the volume of pollutant at the surface by a factor of 3–5. Viscosity will also increase by several orders of magnitude, which increases the difficulty of recovering the oil because it is more difficult to pump. On the other hand, increased viscosity acts to slow down horizontal spreading, so oil may be easier to manage if contained quickly enough. Oxidation occurs at the surface, from either light-catalysed reactions (photo-oxidation) or from microbes in the ocean (microbial oxidation), both of which provide energy to form new chemical compounds such as alcohols and organic acids. This eventually results in tars and the formation of tar balls within the surface emulsion. A coating of tar-like residue can increase the lifetime of a slick by reducing the rate in which other weathering processes occur.

1.4 CHOICE OF OIL SPILL MODEL

To model oil from a seabed release, a combination of a near-field plume model and a far-field transport model should ideally be used to best represent the processes described in Section 1.3. There are several options for modelling such a spill in the FSC. The Advanced Deepwater Modelling Suite (ADMS) includes the Clarkson Deepwater Oil and Gas model (CDOG; Zheng *et al.*, 2003; Bandara & Yapa, 2011; Yapa *et al.*, 2012), which is the only plume model still in continuous development according to literature that is available publicly. This may not be the case when considering literature that is not publicly accessible. However, using the ADMS modelling system is unsuitable for a PhD thesis because it is not available in the public domain; model

set-up, spill simulations and results analysis must be done in-house at Clarkson University.

OILMAP (Jayko & Howlett, 1992; Spaulding *et al.*, 1992) is a second oil spill modelling system that incorporates a plume model (a choice between OILMAP's native model or CDOG v2.02). The far-field transport component of OILMAP has been validated using observations of contaminated Shetland coastline from the 1993 Braer oil spill (Spaulding *et al.*, 1994). However, the native plume model has not been validated in publicly accessible scientific literature.

A third option for modelling seabed releases is to use Oil Spill Contingency and Response (OSCAR). OSCAR comprises of a far-field particle tracking model (3-D Fates; Reed *et al.*, 1995, 2000), a near-field plume model (DeepBlow; Johansen, 2000a) and a droplet breakup model (Johansen *et al.*, 2013). The 3-D Fates model has been validated against historical emulsion observations in the Bay of Biscay (Abascal *et al.*, 2010). The DeepBlow model has been validated against the DeepSpill field experiment (Section 1.1.3; Johansen *et al.*, 2003).

OSCAR has been chosen for the purposes of this thesis primarily because the model is available in the public domain[8], and both the near-field and far-field components have been validated in published scientific literature. A second reason for using OSCAR is that it is commonly-used by companies such as the Centre for Environment, Fisheries and Aquaculture Science (Cefas) and Oil Spill Response (OSRL). This improves the immediate applicability of the research presented in this thesis, since the model can be critically analysed and improvements can be suggested for future development.

1.4.1 THE OSCAR MODELLING SYSTEM

Fig. 1.7 shows a schematic of how the OSCAR modelling system functions. An operational hydrodynamic model is used to force both the 3-D Fates and DeepBlow models. For the 3-D Fates model, 3-D current fields are used as a forcing input. For the DeepBlow model, 1-D profiles of temperature, salinity and currents are used as initial conditions. An operational atmospheric model is used to force the 3-D Fates model at the sea surface with 2-D surface wind fields. Atmospheric and hydrodynamic models

[8]OSCAR is available to use under licensing from SINTEF, Norway.

may or may not be coupled to one another prior to their inclusion in OSCAR, and the upper ocean may include some indirect wind forcing. Cefas and OSRL typically use operational hydrodynamic and atmospheric models available from the Met Office. Release characteristics, which are parameters separate from ambient conditions (e.g. release rate, release period, the chemical composition of oil, well-head depth and location) are site-specific and usually obtained in advance from the oil and gas industry.

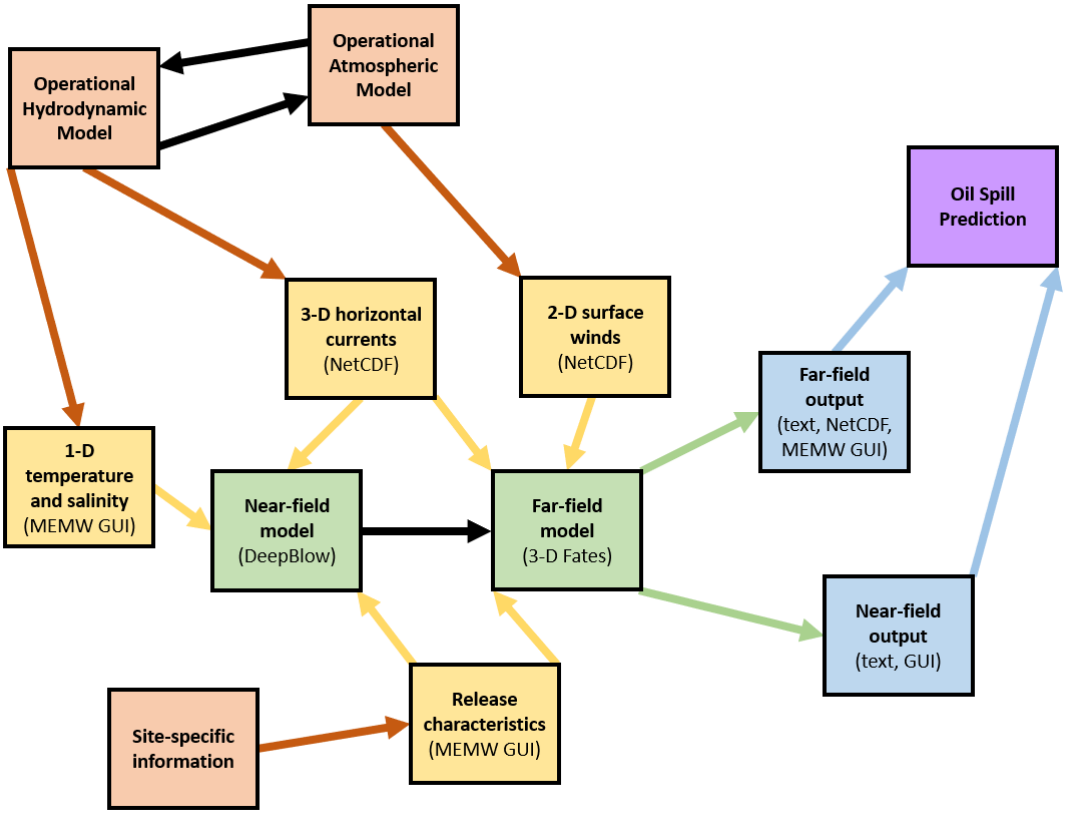

Figure 1.7: Schematic of how an oil spill prediction is made using the OSCAR modelling system. Red boxes indicate sources of information. Yellow boxes indicate inputs into OSCAR. Green boxes indicate numerical modelling components of OSCAR. Blue boxes indicate model output. The purple box indicates the final oil spill prediction.

The initial hydrodynamic, atmospheric and release characteristic inputs determine how oil behaves in the DeepBlow and 3-D Fates models. Both models must be run together when using the OSCAR modelling system. The DeepBlow model outputs an individual plume profile per time-step of the operational hydrodynamic model, providing initial conditions of the droplet size distribution and depth distribution of oil. These initial conditions feed into the 3-D Fates mode, where oil

is advected and dispersed as individual droplets (or spillets). Currents and droplet buoyancy determine the behaviour of submerged oil, whereas surface current and wind fields determine the behaviour of surfaced oil. Model output takes the form of formatted text files, NetCDF files (as of OSCAR v8.0) and visualisation in the Marine Environmental Monitoring Workbench (MEMW) GUI. These outputs form an overall picture of how an oil spill develops. The research chapters in this thesis test the behaviour of a spill by changing the initial inputs of currents and stratification.

1.5 THIS THESIS

This thesis has three primary aims. The first aim is to assess the suitability of the hydrodynamic model commonly-used as part of UK spill forecasting, and determine whether an updated version of this model is a better choice. The second aim is to model idealised ocean conditions to determine schematically how physical characteristics of the FSC alter the behaviour of oil below the sea surface. The third aim is to show the development of a large spill in a regional context, and to outline the key environmental consequences should such a spill occur in real life. The following six questions are posed in order to achieve these three aims:

1. How well does a commonly-used operational hydrodynamic model represent the structure of the water-column in the FSC?

2. Do differences in stratification between model and observations substantially influence the behaviour of an oil plume?

3. How sensitive is the advection and dispersion of oil to the magnitude and structure of barotropic and baroclinic ocean currents?

4. Can we use the results from idealised spill simulations to make informed and accurate predictions on how pollutants behave in a regional simulation?

5. How does the advection of oil by ocean currents change with the location and depth of a release?

6. Does a change in hydrodynamic model resolution influence oil transport and dispersion?

This thesis contains five research chapters. Chapter 2 is an analysis of temperature and salinity observations during 2013 and 2014 along three different CTD sections, and comparison with an operational hydrodynamic model. The next two chapters are results from a series of idealised modelling studies with the DeepBlow and 3-D fates components of OSCAR. Chapter 3 focusses on stratification, with parameter space guided by the differences found in Chapter 2. Chapter 4 focusses on the response of a plume to barotropic and baroclinic currents, and subsequent far-field transport. The next two chapters are concerned with regional oil spill simulations forced by operational hydrodynamic models. Chapter 5 investigates how the release location and time of year influence the behaviour of a large seabed release. Chapter 6 is a comparison between two hydrodynamic models with different resolutions, and is in the process of being resubmitted for publication. The work presented in this thesis is summarised and synthesised in Chapter 7.

2

REPRESENTATION OF STRATIFICATION IN AN OPERATIONAL OCEAN MODEL

2.1 INTRODUCTION

The fate and trajectory of oil in the ocean is primarily determined by ocean hydrodynamics. In the near-field, the buoyancy and vertical momentum of an oil plume are controlled by the temperature and salinity of entrained seawater. In the far-field, the vertical advection of oil is controlled by the buoyancy of individual oil droplets, and the horizontal advection of oil is controlled by ocean currents.

Because of the key role ocean hydrodynamics play in determining the fate and trajectory of oil, it is important that the ocean models utilised in spill prediction are skilful at representing reality. In this chapter, the operational hydrodynamic model currently used by emergency spill responders such as Cefas and OSRL is validated against observations of the FSC taken during 2013 and 2014. These observations take the form of conductivity-temperature-depth (CTD) profiles along frequently sampled channel cross-sections.

The aim of this chapter is to outline any differences between the model output and CTD observations, before testing the sensitivity of an oil plume to those differences in Chapter 3. Section 2.2 describes the operational hydrodynamic model, and Section 2.3 describes the CTD observations. Section 2.4 outlines the method of comparison

between both representations of reality. Section 2.5 is a physical description of the channel from the CTD observations, and Section 2.6 shows a comparison between the CTD observations and the hydrodynamic model. The potential implications of any differences found are discussed in Section 2.7 in the context of a potential oil spill in the FSC.

2.2 DETAILS OF THE HYDRODYNAMIC MODEL

The Met Office Forecasting Ocean Assimilation Model 7 km Atlantic Margin Model of the North-West European Shelf (FOAM AMM7 NWS, hereafter referred to as AMM7; Edwards *et al.*, 2012; O'Dea *et al.*, 2012) is currently used by spill responders to force both the DeepBlow and 3-D Fates components of the OSCAR modelling system. Vertical point-profiles of horizontal current velocities, in-situ temperature T and practical salinity S_p are used as initial conditions for the DeepBlow model. The 3-D Fates model is forced by 3-D time-varying fields of horizontal current velocities, and a single time-constant value of T for the sea surface temperature (SST).

AMM7 is one-way nested to the global Met Office model, and hydrodynamics are a regional configuration of the Nucleus for European Modelling of the Oceans v3.4 (NEMO; Madec, 2016). AMM7 extends across the north-west European shelf from 19.9°W-13°E, 40.1°N-65°N. Horizontal resolution is approximately 7 km ($\frac{1}{15}^\circ$ latitude and $\frac{1}{9}^\circ$ longitude). The vertical grid uses a hybrid s-σ-z^* co-ordinate system. z^* co-ordinates provide depth-constant vertical levels (isobaths) near the surface, σ co-ordinates are terrain following and scale the vertical resolution to the depth, and s co-ordinates allow for vertical perturbations of the free surface. A total of 51 vertical levels are used to run AMM7, which are interpolated onto 24 isobaths for the operational output (0 m, 3 m, 10 m, 15 m, 20 m, 30 m, 50 m, 75 m, 100 m, 125 m, 150 m, 200 m, 250 m, 300 m, 400 m, 500 m, 600 m, 750 m, 1000 m, 1500 m, 2000 m, 3000 m, 4000 m and 5000 m).

Operational AMM7 forecasts of horizontal currents, potential temperature θ and S_p are available in NetCDF format through the Copernicus Marine Environmental Monitoring Service (CMEMS; EU Copernicus Marine Services Information, 2018a). The forecast is run with the most up-to-date atmospheric forcing available from the Met Office Global Unified Model (MetUM) atmospheric model (Walters *et al.*, 2011),

in addition to a 'best guess' AMM7 analysis of ocean conditions over the previous 48 h. Forecasts are available for up to one week in advance (+144 h from the release date at 0000 UTC). Operational AMM7 forecasts are available either as hourly instantaneous values, or 25 h mean values. For this analysis, only hourly instantaneous values are used.

Bathymetry is taken from the General Bathymetric Chart of the Oceans (GEBCO) 1 arc-minute dataset, which is interpolated to match the horizontal grid resolution of AMM7. 15 tidal constituents are forced at the model boundaries using the Flather condition (Flather, 1976), which estimates the barotropic velocities and phases of each constituent from the Met Office $\frac{1}{12}^{\circ}$deep ocean model (Storkey *et al.*, 2010). AMM7 is forced at the surface by 3-hourly mean heat and moisture fluxes, hourly instantaneous surface pressure and wind fields, and assimilated using a mixture of remote and in-situ observations of SST (Mogensen *et al.*, 2012). AMM7 has been validated against tide gauge data from the British Oceanographic Data Centre (BODC) and performed better than other operational hydrodynamic models at the time (O'Dea *et al.*, 2012). AMM7 has also been validated against archived operational SST data (O'Dea *et al.*, 2012), and the authors found that assimilating AMM7 with SST by the method described above substantially reduces model bias. At the time of writing AMM7 is not currently assimilated using CTD observations, but this is likely to change for future versions of the model. The aim of this chapter is to test the skill of the current (at the time of writing) version of AMM7 at reproducing CTD observations taken in the FSC.

In this analysis, operational AMM7 model output of θ and S_a is compared with CTD observations of T and S_p. The comparison is made between May 1st, 2013 (the first available operational AMM7 forecast) and December 31st, 2014 (the most recent available CTD observations). All AMM7 forecasts are produced from the same version of NEMO (v3.4); previous and future versions of AMM7 may perform differently to the version tested here.

2.3 DETAILS OF THE CTD OBSERVATIONS

In this chapter, the following definitions are used to provide consistency:

- **CTD Cast** - A single point-profile of T and S_p taken at a specific point in time.
- **CTD Station** - A specific location at a which CTD cast is taken regularly (e.g. those shown in Fig. 2.1).
- **CTD Section** - A line of CTD stations that are visited one after another during a transit across the channel.
- **Section Occupation** - A series of CTD casts taken along a CTD section during an oceanographic cruise.

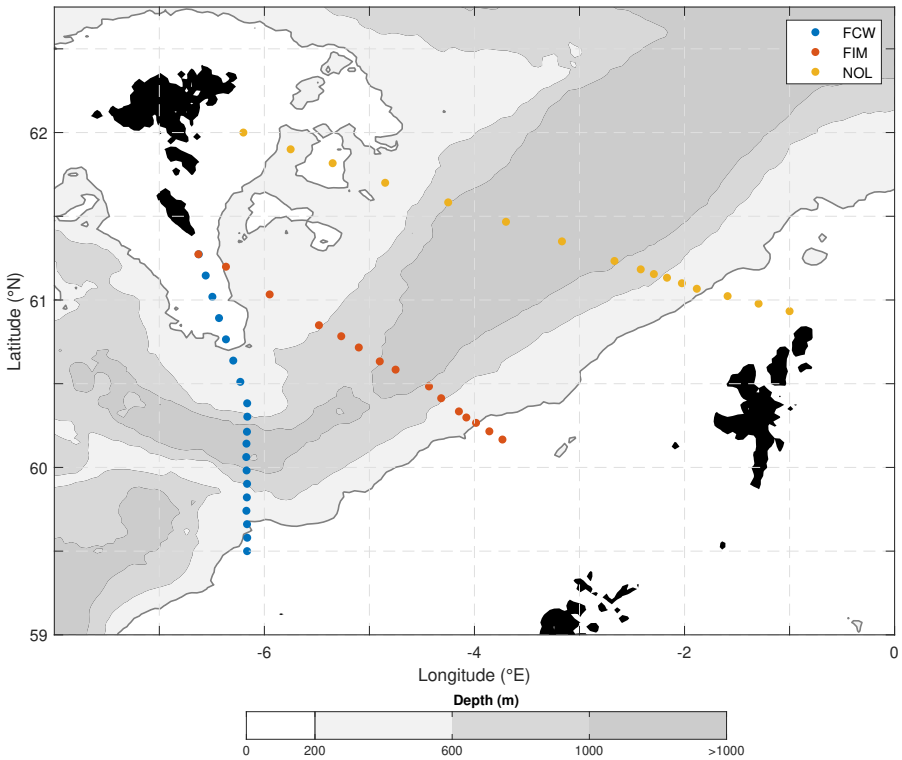

Figure 2.1: CTD section and CTD station locations. Shown are the Faroe-Cape Wrath (FCW; blue dots), Fair-Isle Munken (FIM; red dots) and Nolso Flugga (NOL; yellow dots) CTD sections. Bathymetry is from Smith & Sandwell (1997).

Table 2.1: Functions used from the Gibbs Seawater Matlab toolbox for CTD observations and AMM7 model output.

Initial Variable	Function Called	New Variable
(CTD) depth	*gsw_p_from_z.m*	(CTD) pressure
(CTD) S_p	*gsw_SA_from_SP.m*	(CTD) S_a
(CTD) T	*gsw_CT_from_t.m*	(CTD) Θ
–	*gsw_rho.m*	(CTD) ρ_w
(AMM7) depth	*gsw_p_from_z.m*	(AMM7) pressure
(AMM7) S_p	*gsw_SA_from_SP.m*	(AMM7) S_a
(AMM7) θ	*gsw_CT_from_pt.m*	(AMM7) Θ
–	*gsw_rho.m*	(AMM7) ρ_w

CTD casts taken between May 1st, 2013 and December 31st, 2014 were obtained from Marine Scotland Science (personal communications), which included all section occupations carried out along either the Faroe-Cape Wrath (FCW), Fair-Isle Munken (FIM), or Nolso Flugga (NOL) CTD sections (Fig. 2.1). Values of T and S_p are binned to every 1 m of the water-column. CTD casts are taken from the sea surface to within a few metres of the seabed. Values of T and S_p are taken on the downcast only. There are 494 CTD casts in this dataset.

2.4 COMPARISON METHODS

Values of conservative temperature Θ, absolute salinity S_a and potential density ρ_w are calculated from both AMM7 model output and CTD observations using the Gibbs Seawater Matlab Toolbox (McDougall & Barker, 2011). Table 2.1 shows the specific functions called from the toolbox, and the variables that are obtained from using each function.

To assess the skill of AMM7, profiles of Θ and S_a were extracted from the operational model output in equivalent time and space to each of the 494 individual CTD casts. A 'nearest-neighbour' approach was used in the horizontal. This approach is justified because AMM7 operational model output is assumed to be valid for plus or minus half a grid cell in both the zonal and meridional dimensions (Mahdon *et al.*, 2015).

A 'mid-time' of each CTD cast was estimated because the recorded start time

of each CTD cast is often earlier than the time the observations are taken. A more suitable approximation would be the time at which observations are taken from the vertical centre of the CTD cast. To estimate the mid-time, 10 min were added to the recorded start time to account for the initial set-up of equipment. The downcast velocity is assumed to be $1\,\mathrm{m\,s^{-1}}$. The mid-time is then the time at which the equipment reaches half of the total observed depth range. The closest AMM7 model output time-step to the mid-time is used in the comparison with CTD observations.

To calculate absolute differences between AMM7 model output and CTD observations of Θ, S_a and ρ_w, a sub-sample of CTD observations are taken that match the vertical grid of the model. This is a reasonable representation of the full CTD dataset (see Section 2.6.1, Fig. 2.6). No comparisons are made deeper than 1000 m because no CTD stations are in waters deeper than 1500 m, which is the next deepest vertical level of the AMM7 model output.

In Section 2.6.3, the semidiurnal tidal variability of AMM7 model output is estimated by extracting 12 additional time-steps; 1–6 h before the mid-time of the CTD cast in hourly intervals; and 1–6 h after. This encapsulates the range of Θ, S_a and ρ_w over 13 h from AMM7 model output, which can be compared to absolute differences between AMM7 model output and CTD observations. Semidiurnal tidal variability is assumed to be depth-dependant.

2.5 PHYSICAL CHARACTERISTICS OF THE CHANNEL

Sections 2.5.1 and 2.5.2 describe the observed characteristics of the channel from several CTD section occupations.

2.5.1 CRUISES DURING MAY 2013 AND MAY 2014

In May 2013 and May 2014, the MRV Scotia [1] carried out section occupations of the FCW, FIM and NOL CTD sections. The May 2014 section occupations are shown in Fig. 2.2 (FCW), Fig. 2.3 (FIM) and Fig. 2.4 (NOL).

The maximum vertical gradients of Θ (thermocline), S_a (halocline) and ρ_w (pycnocline) occur several hundred metres below the sea surface, at approximately

[1] https://www2.gov.scot/Topics/marine/science/scienceops/vessels-technology/vessels/scotia

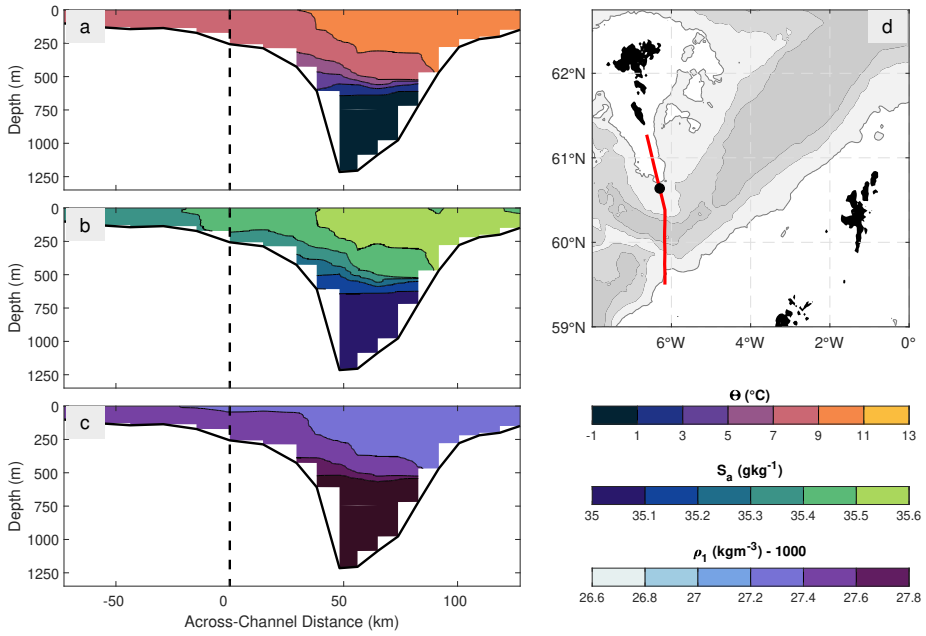

Figure 2.2: Across-channel stratification (FCW, May 2014). (**a**) Cross-section of conservative temperature (filled contours). Across-channel distance is relative to the Faroe shelf edge (black dashed line). (**b**) As (a) but for absolute salinity. (**c**) as (a) but for potential density. (**d**) CTD section location (red line) and location of the Faroe shelf edge (black dot). Bathymetry has a scale identical to Fig. 2.1.

400–600 m depth along the 2014 FCW section occupation and at approximately 300–500 m depth along both the FIM and NOL section occupations. Contours are closer together on the Shetland slope relative to on the Faroe slope, and are closer together along the FCW section occupation compared to the FIM or NOL section occupations. Contours of ρ_w that are closer together infer a stronger pycnocline and higher buoyancy frequency squared $N^2 = -(g/\rho_{ref})\partial\rho_w(z)/\delta z$, where g is gravitational acceleration, ρ_{ref} is the reference density at the seabed, $z < 0$ is depth, and $\partial\rho_w(z)/\delta z$ is the vertical potential density gradient.

A cool, fresh eddy-like structure can be seen along the FIM and NOL section occupations (Fig. 2.3 and Fig. 2.4). This takes the form of a vertical perturbation of property contours in the centre of the cross-sections, order 100 m shallower along the FIM section occupation and order 200 m shallower along the NOL section occupation. The eddy-like structure is not present along the FCW section occupation (Fig. 2.2). These vertical perturbations are likely the result of a semi-permanent mesoscale eddy passing through the channel, similar in size and location to previous observations

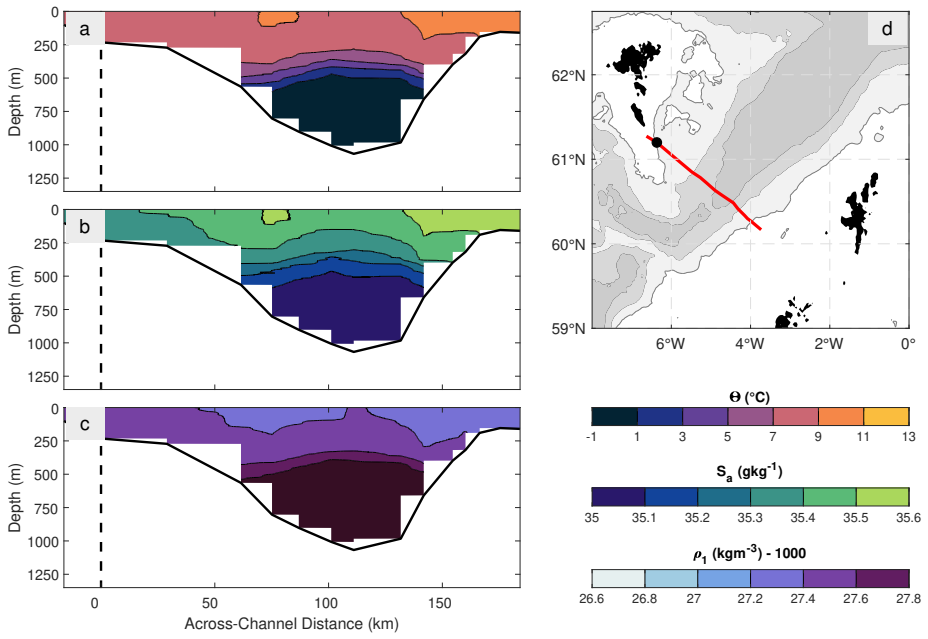

Figure 2.3: Across-channel stratification (FIM, May 2014). (**a**) Cross-section of conservative temperature (filled contours). Across-channel distance is relative to the Faroe shelf edge (black dashed line). (**b**) As (a) but for absolute salinity. (**c**) as (a) but for potential density. (**d**) CTD section location (red line) and location of the Faroe shelf edge (black dot). Bathymetry has a scale identical to Fig. 2.1.

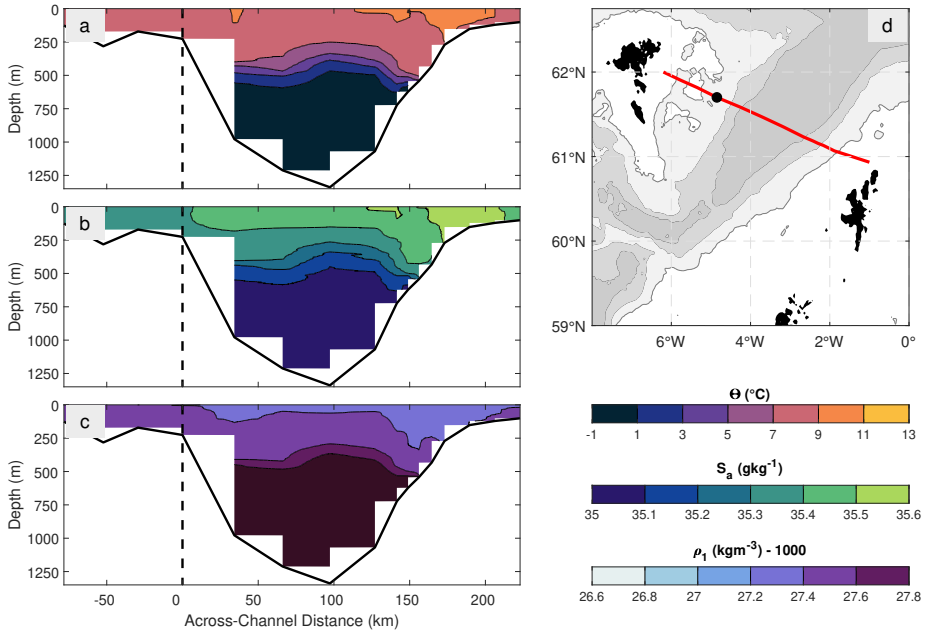

Figure 2.4: As Fig. 2.3, but for NOL, May 2014.

(Section 1.2.2; Sherwin *et al.*, 1999, 2006). The vertical perturbations are unlikely to be a result of internal wave or internal tide activity, because the amplitude of an internal wave in the FSC is typically order 50 m (Sherwin, 1991; Hosegood & van Haren, 2004; Hall *et al.*, 2011). Additionally, the transit time across either section occupation was 2–3 days; an internal wave in the FSC will typically oscillate at a frequency that is semidiurnal or faster.

SST is typically higher on the Shetland side of the channel compared to the Faroe side of the channel. This is the case along all three section occupations in either May 2013 or May 2014. The asymmetry in SST is a proxy for the Shetland shelf slope current, which transports NAW northward from the North Atlantic through the FSC and eventually into the Norwegian Sea. NAW is warmer and fresher than MNAW, which flows southward on the Faroe side of the channel. SST is also slightly lower along the 2014 NOL section occupation compared to along the 2014 FCW section occupation. This is probably a result of differential surface heading, because the CTD sections are separated by several degrees of latitude and longitude.

2.5.2 FIM AND NOL DURING SEPTEMBER AND DECEMBER

FIM and NOL section occupations during September 2014 and December 2014 are shown in Fig. B.1 (FIM, September), Fig. B.2 (FIM, December), Fig. B.3 (NOL, September) and Fig. 2.5 (NOL, December). Surface ρ_w is higher in December compared to in September along both section occupations (e.g. Fig. B.3c compared to Fig. 2.5c). The distribution of S_a near the surface remains quite similar for both times of year, whereas SST decrease by 1–2 °C. Therefore, the changes in surface ρ_w are primarily temperature-driven. Changes in SST could be due to decreased local surface forcing during Winter, or variability in surface transport.

The eddy-like structure seen in May 2014 is not present along either the FIM or NOL section occupations in either September or December, which suggests that it was not a permanent feature of the channel. A vertical perturbation gradients does exist along the NOL section in December (Fig. 2.5, approximately 50–100 km east of the reference position), where the property gradients are shallower on the Faroe side by approximately 200 m compared to on the Shetland side. Contours of Θ, S_a and ρ_w also appear to oscillate vertically over a smaller spatial scale. As a very rough estimate,

these oscillations are 20–50 m in amplitude, similar to earlier observations of internal waves in the FSC. Additionally, the oscillations are roughly semidiurnal when aliased on to the spatial section. With the CTD observations used in this analysis however, separating mesoscale activity from internal wave activity is not possible because the time-series is short and variable in space.

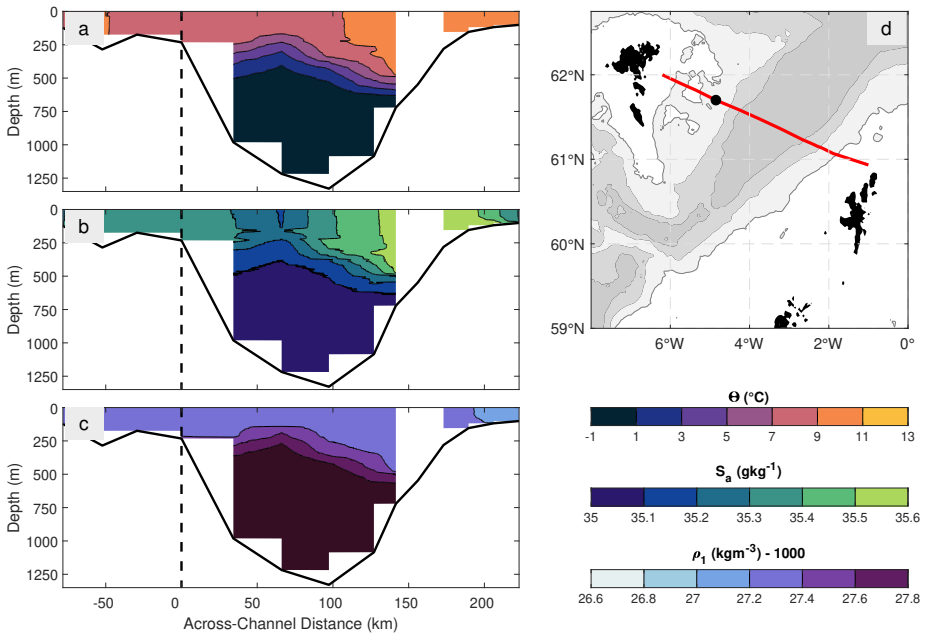

Figure 2.5: Across-channel stratification (NOL, December 2014). (**a**) Cross-section of conservative temperature (filled contours). Across-channel distance is relative to the Faroe shelf edge (black dashed line). (**b**) As (a) but for absolute salinity. (**c**) as (a) but for potential density. (**d**) CTD section location (red line) and location of the Faroe shelf edge (black dot). Bathymetry has a scale identical to Fig. 2.1.

2.6 MODEL-OBSERVATION COMPARISON

2.6.1 CHARACTERISTIC DIFFERENCES

Fig. 2.6 shows a representative example of a CTD cast taken on February 16th, 2014 in the central FSC, and the equivalent AMM7 model output profile. This example is used because it is representative of typical conditions in the deep (> 1000 m) FSC and shows the common characteristic model-observation differences found in this analysis.

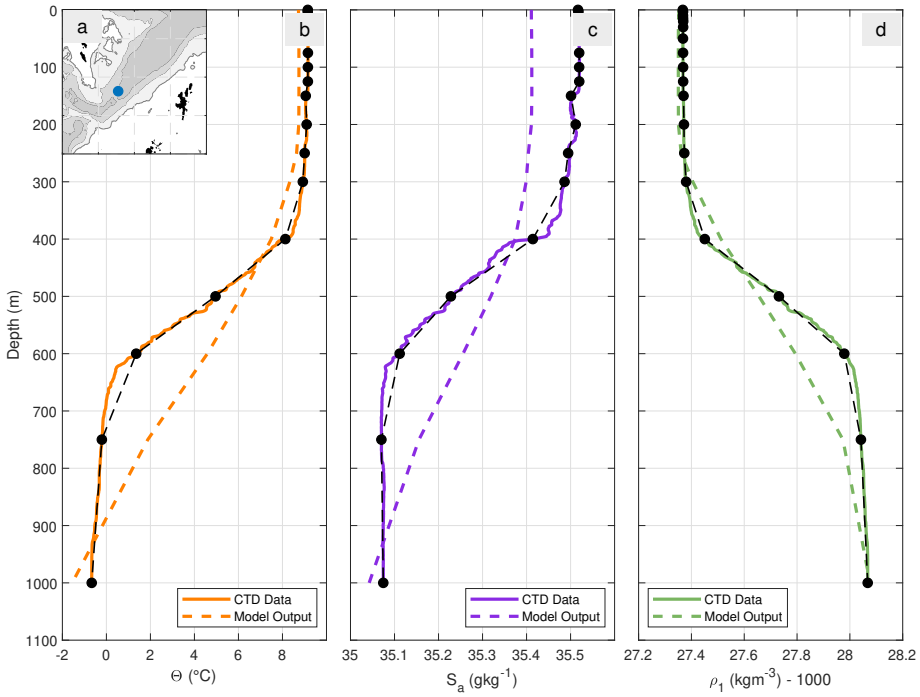

Figure 2.6: A representative CTD profile in the central FSC. (**a**) Location of the CTD cast (blue dot; February 16th, 2014). Bathymetry has a scale identical to Fig. 2.1. (**b**) Conservative temperature from AMM7 model output (coloured dashed line), observations (solid coloured line), and observations sub-sampled at model output depths (black dashed line; black dots). (**c**) As (b) but for absolute salinity. (**d**) As (b) but for potential density.

For the CTD cast, the water-column is approximately homogeneous from 0–400 m and 650–1000 m, with a strong density gradient from 400–650 m. Θ decreases from 8 °C at 400 m to 0 °C at 650 m, and S_a decreases from 35.4 g kg^{-1} at 400 m to 35.1 g kg^{-1} at 650 m. For the AMM7 model output profile, the water-column is approximately homogeneous from 0–250 m. Below this, property gradients are almost depth-uniform. Θ decreases from 8 °C at 250 m to −1 °C at 1000 m, and S_a decreases from 35.4 g kg^{-1} at 250 m to 35.05 g kg^{-1} at 1000 m.

The difference in stratification between the CTD cast and the AMM7 model output profile leads to same-depth absolute property differences of up to 4 °C, 0.15 g kg^{-1}, and 0.2 kg m^{-3}. Maximum absolute property differences occur at 600–700 m depth. Absolute property differences for all CTD casts in the dataset are explored in Section 2.6.2.

A Θ-S_a plot of CTD observations from all 494 CTD casts (Fig. 2.7) agrees visually with earlier research (Turrell *et al.*, 1999; Mauritzen *et al.*, 2005). NSAIW can be seen in Fig. 2.7 from the presence of a salinity minimum at 0 °C (potential density anomaly

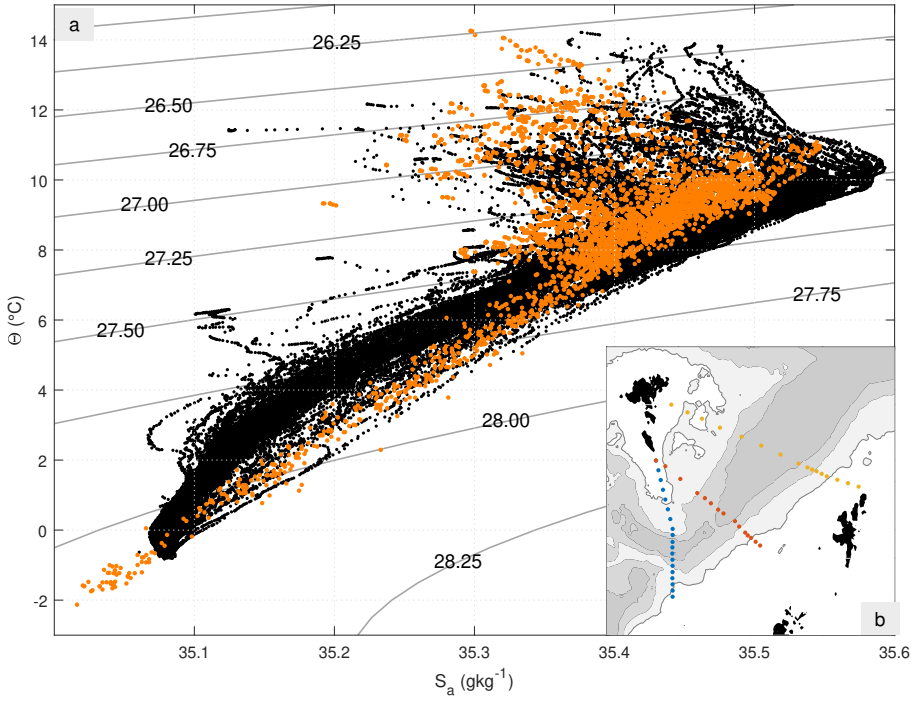

Figure 2.7: Θ-S_a plot of the CTD dataset. (**a**) Θ-S_a plot of unfiltered CTD data (black dots) and AMM7 output (orange dots) for all available data. Also shown are $\rho_1 - 1000$ contours (grey lines). (**b**) CTD station locations. Bathymetry has a scale identical to Fig. 2.1.

of $\approx 28\,\mathrm{kg\,m^{-3}}$). FSCBW is also visible, characterised by a higher S_a and a lower Θ than NSAIW. AMM7 model output does not appear to distinguish between these cool, fresh water masses that are typically found below the thermocline (> 600 m depth; Section 1.2.1). There is a linear relationship between S_a and Θ for density anomalies of > $27.5\,\mathrm{kg\,m^{-3}}$, and no salinity minimum at 0 °C. Minimum AMM7 model output Θ is cooler than observed Θ by order 1 °C, and minimum AMM7 model output S_a is cooler than observed S_a by order $0.05\,\mathrm{g\,kg^{-1}}$. The inability of AMM7 to distinguish between different water masses could be because of an exaggerated vertical mixing scheme in the model, or because of poor representation of large-scale circulation and water mass transport.

For potential density anomalies of 27.75–28 $\mathrm{kg\,m^{-3}}$, AMM7 model output is either too salty or too cold. AMM7 model output does replicate the high Θ, low S_a surface waters with potential density anomalies of < $27.25\,\mathrm{kg\,m^{-3}}$, but tends to slightly underestimate S_a. This can also be seen from the same-depth differences of the representative profile at < 400 m in Fig. 2.6c). The high Θ, low S_a near-surface waters are likely the result of increased solar radiation during Spring and Summer.

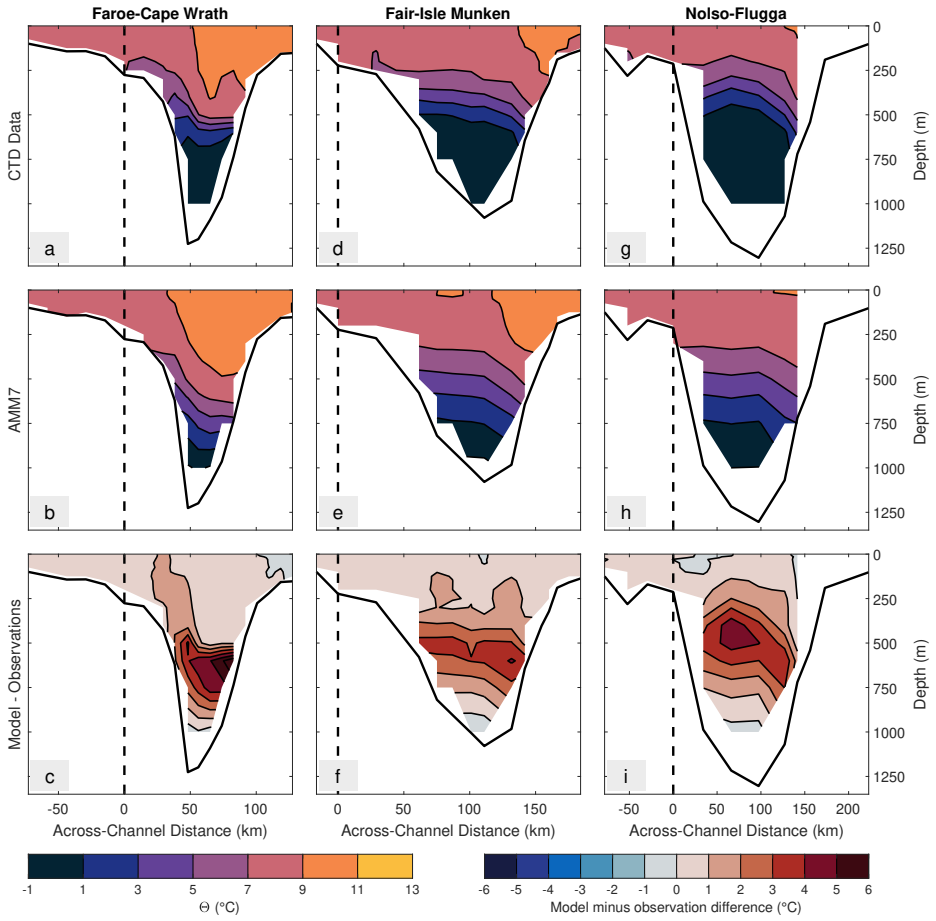

Figure 2.8: Comparison between AMM7 output and CTD observations (May 2013). (**a**) Cross-section of conservative temperature along the FCW CTD section from CTD data. Across-channel distance is relative to the Faroe shelf edge. (**b**) As (a) but from AMM7 output. (**c**) As (a) but for the model-minus-observation temperature difference. (**d, e, f**) As (a, b, c) but along the FIM CTD section. (**g, h, i**) As (a, b, c) but along the NOL CTD section.

2.6.2 ABSOLUTE DIFFERENCES IN Θ, S_a AND ρ_w

From the May 2013 and May 2014 occupations of the FCW, FIM and NOL CTD sections, CTD observations show that Θ is 7–11 °C at the surface (with warmer temperatures on the Shetland slope), decreasing to −1–1 °C at 1000 m depth. The May 2013 cross-sections of observed Θ are shown in Fig. 2.8a, d, g, and the May 2014 cross-sections of observed Θ are shown in Fig. 2.9a, d, g. AMM7 model output (Fig. 2.8b, e, h and Fig. 2.9b, e, h) appears to replicate the top-to-bottom temperature range well, in addition to the across-channel temperature asymmetry. However, the AMM7 model output is much warmer at 250–750 m depth (Fig. 2.8c, f, i and Fig. 2.9c, f, i). In May 2013, AMM7 model output Θ is up to 6 °C warmer than observed Θ along

the FCW section occupation, and up to 5 °C warmer along both the FIM and NOL section occupations. In May 2014, AMM7 model output Θ is up to 4 °C warmer than observed Θ along the FCW section occupation, and up to 6 °C warmer along both the FIM and NOL section occupations. These same-depth differences are large because of the linear temperature gradients from the AMM7 model output at 400–1000 m depth (Fig. 2.6b).

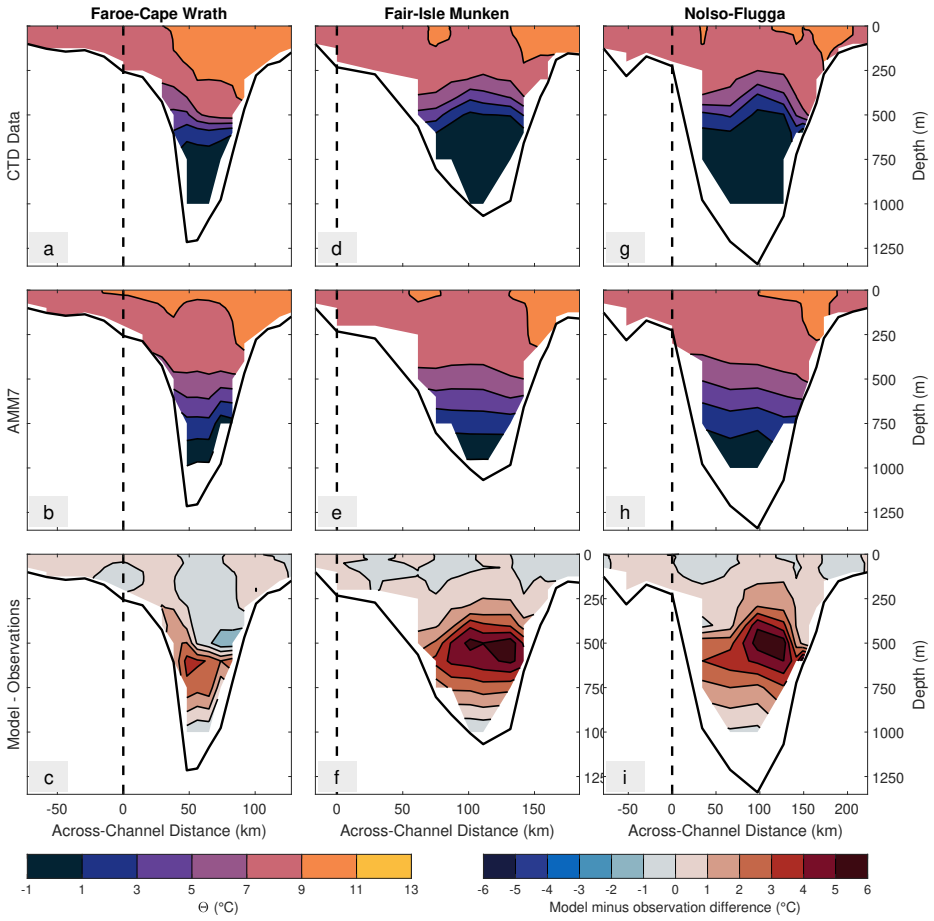

Figure 2.9: Comparison between AMM7 output and CTD observations (May 2014). (**a**) Cross-section of conservative temperature along the FCW CTD section from CTD data. Across-channel distance is relative to the Faroe shelf edge. (**b**) As (a) but from AMM7 output. (**c**) As (a) but for the model-minus-observation temperature difference. (**d, e, f**) As (a, b, c) but along the FIM CTD section. (**g, h, i**) As (a, b, c) but along the NOL CTD section.

AMM7 model output Θ is typically within 1 °C of observed Θ near the surface and at 1000 m depth. Along the May 2014 NOL section occupation, the model is too warm by > 1 °C in the central channel at > 200 m (Fig. 2.9i). Whilst CTD observations show an eddy-like structure here (Section 2.5.1), AMM7 model output does not. The

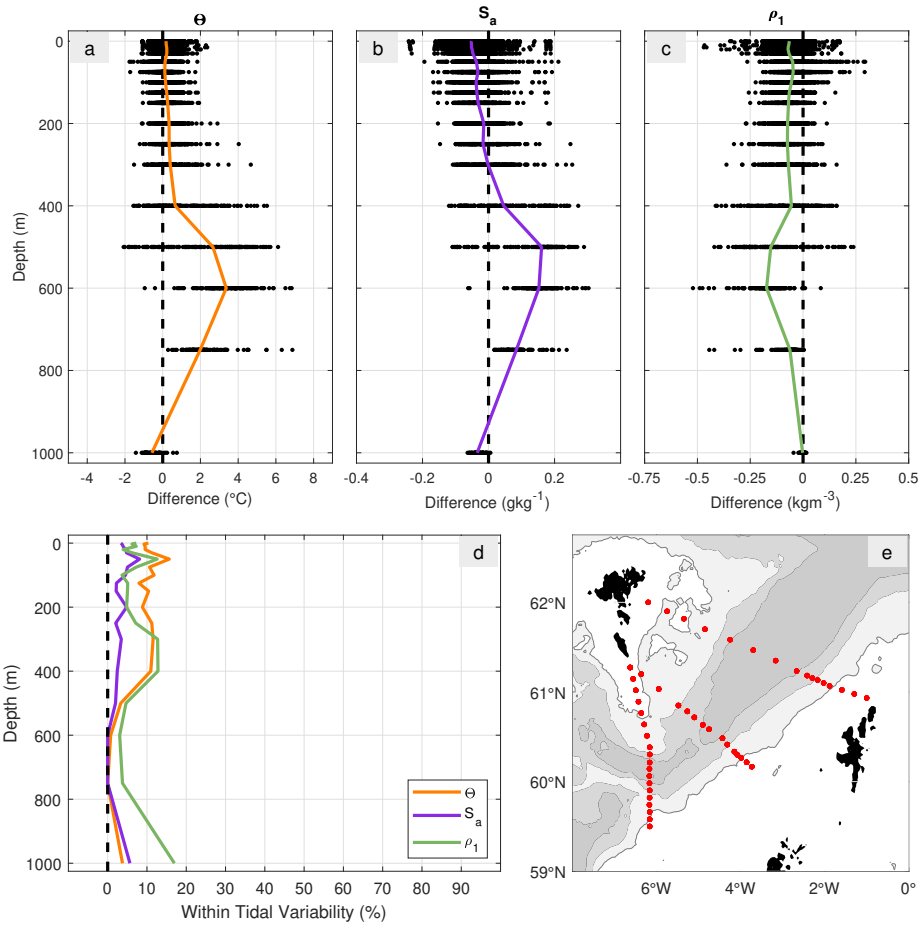

Figure 2.10: Model-minus-observation property differences. (**a**) Model-minus-observation differences for conservative temperature for all observations along the FCW, FIM and NOL CTD sections. Black dots show individual point comparisons, with the median difference shown as a coloured line. (**b**) As (a) but for absolute salinity. (**c**) As (a) but for potential density. (**d**) Proportion of observations that are within the semidiurnal tidal range of the model. (**e**) Location of CTD stations used in the analysis. Bathymetry has a scale identical to Fig. 2.1.

horizontal resolution of AMM7 model output (7 km) is too coarse to permit mesoscale eddies (≤ 2 km; Oey, 1998) and is also coarser than the Rossby radius of deformation (approximately 4 km at 60°N), so it is not surprising that the eddy-like feature is not resolved. AMM7 model output is also > 1 °C warmer than CTD observations at the surface along the May 2013 FCW section occupation (Fig. 2.8c). Here, CTD observations show a 9 °C contour of Θ almost perpendicular to isoclines from 0–400 m depth 50 km east of the reference position (Fig. 2.8a). AMM7 model output (Fig. 2.8b) is more parallel to isoclines, causing the difference in Θ. Although not investigated in this thesis, the temperature difference might be due to differences in the position of the Shetland slope current.

The dataset of CTD observations used for this analysis comprises of 494 CTD casts along the three CTD sections that have previously been discussed. An analysis of the full dataset reveals a systematic positive bias of Θ and S_a at 300–750 m depth (Fig. 2.10a, b). AMM7 model output is up to 7 °C warmer and 0.3 g kg^{-1} saltier than CTD observations at 600 m depth. At 500–750 m depth, median differences in Θ and S_a are 2–4 °C and 0.05–0.15 g kg^{-1}, respectively. AMM7 model output is also less salty than CTD observations at 0–200 m depth. The model-minus-observation differences in Θ and S_a result in differences in calculated ρ_w, and AMM7 model output is less dense than CTD observations at 0–750 m. Maximum model-minus-observation differences of ρ_w are order 0.5 kg m^{-3} at 400–750 m (typical depth of the pycnocline).

2.6.3 SEMIDIURNAL MODEL VARIABILITY

In this section, a comparison is made between the absolute values of the CTD observations, and the semidiurnal range of Θ, S_a and ρ_w from equivalent AMM7 model output profiles (method described in further detail in Section 2.4).

The proportions of CTD observations that are within the range of the semidiurnal model variability are shown in Fig. 2.10d as a function of depth. The lowest proportions of observed Θ, S_a and ρ_w within the range of semidiurnal model variability occur at 500–750 m depth. At 300 m and deeper, the proportions of observed ρ_w within the range of semidiurnal model variability are higher than for either Θ or S_a. For example, at 750 m, 0% of observed Θ and S_a values are within the range of the semidiurnal model variability, but 4.6% of observed ρ_w values are. The increased skill of AMM7 for ρ_w is because positive biases of Θ and S_a contribute to negative and positive biases of ρ_w, respectively, and so somewhat cancel out. This results in values of ρ_w that are closer to reality than either of the two original variables.

Over all depths, < 10% of CTD observations are within the range of semidiurnal model variability (9.78% for Θ, 3.90% for S_a and 6.72% for ρ_w). This suggests that the model-minus-observation differences are not a result of a phase difference in the semidiurnal tidal cycle, and could instead be because of other processes such as water mass circulation or mesoscale variability.

2.7 DISCUSSION

In this chapter, AMM7 model output is compared against CTD observations taken during 2013 and 2014 in the FSC. AMM7 performs poorly, and the thermocline, halocline and pycnocline are all too weak. This results in considerable same-depth differences in T, S_p and ρ_w. The tidal variability of AMM7 is minor compared to absolute model-observation differences. These results will guide the choice of parameter space for the idealised plume modelling performed in Chapter 3.

2.7.1 HOW WELL DO THE CTD OBSERVATIONS REPRESENT THE FSC?

CTD casts are regularly performed in the FSC and are well-documented for the past several decades. Along the NOL CTD section, the dataset used in this analysis shows similar characteristics to earlier observations (Turrell *et al.*, 1999). Similarities include the horizontal temperature asymmetry between the Shetland side and Faroe side of the channel, and a thermocline at roughly 400 m depth. Horizontal temperature asymmetry is also present in a long-term (1995-2009) average along the FIM CTD section (Berx *et al.*, 2013). Turrell *et al.* (1999) also show a vertical temperature perturbation in the centre of the channel, similar to the eddy-like structures in this dataset that can be seen in e.g. Fig. 2.4a and Fig. 2.5a. This vertical perturbation is not present in the 1995-2009 average along the FIM CTD section (Berx *et al.*, 2013). The FIM and NOL CTD sections are both situated in areas of high eddy kinetic energy (Sherwin *et al.*, 2006), so the presence of an eddy-like structure along these CTD sections is not particularly unexpected.

2.7.2 WHAT CAUSES POOR AMM7 MODEL PERFORMANCE?

A possible reason for the poor representation of Θ and S_a in the FSC is poorly resolved water mass circulation (compare Fig. 2.11a with Fig. 2.12). The Shetland slope current in AMM7 model output along the FIM CTD section is similar to the 1995-2009 average from observations (Berx *et al.*, 2013; Fig. 2.11a, 0–400 m depth on the Shetland side of the channel with mean surface velocities of $> 0.2\,\mathrm{m\,s^{-1}}$) (Berx *et al.*,

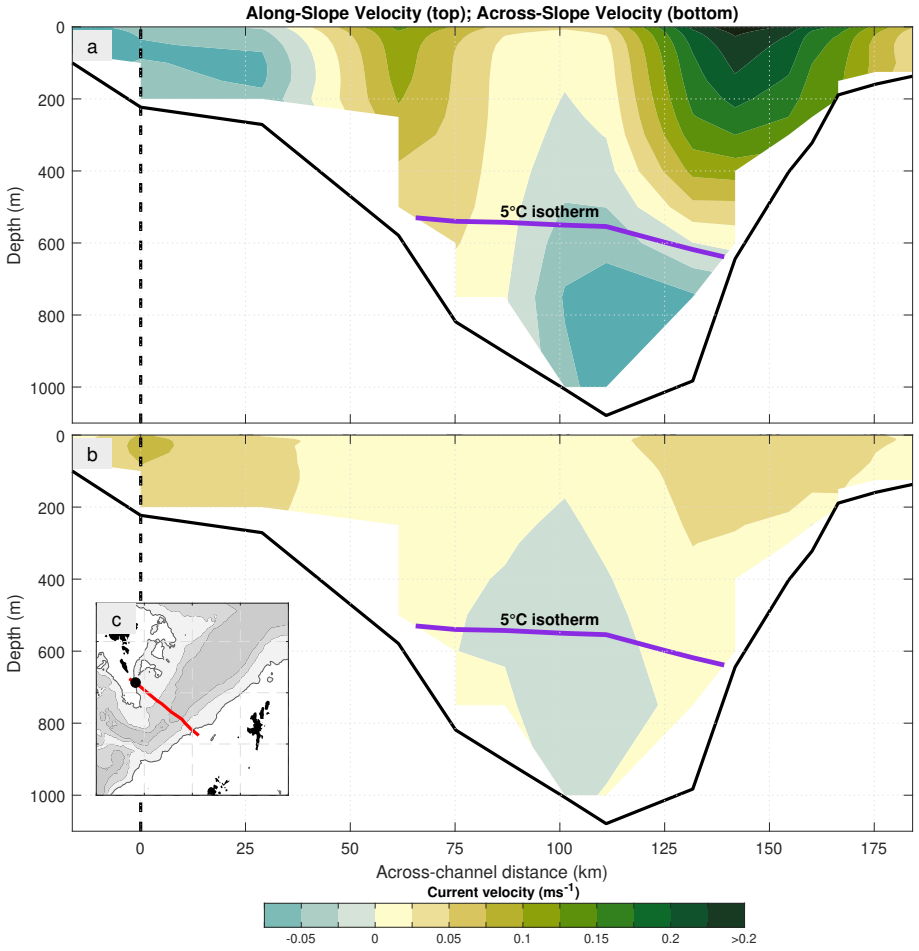

Figure 2.11: 2014 annual mean AMM7 model output along-slope and across-slope velocity for the FIM CTD section. (**a**) Along-slope velocity (coloured contours, positive-north-eastward). Also shown is the channel bathymetry (black solid line), reference position (black dashed line) and 5 °C potential temperature isotherm. (**b**) As (a) but for across-slope velocity (positive-south-westward). (**c**) CTD section location (red line) and location of the reference position (black dot). Bathymetry has a scale identical to Fig. 2.1.

2013). Additionally, the 5 °C in-situ temperature isotherm[2] separates the northward slope current from the southward bottom current, which is of a similar magnitude to the 1995-2009 average ($\approx$0.05 m s^{-1} at 700 m and deeper). However, the depth of the 5 °C in-situ temperature isotherm is approximately 100 m deeper than the 1995-2009 observed average. Furthermore, AMM7 model output shows a northward current across most of the channel near the surface, extending to up to 750 m on the Faroe side of the channel. In the 1995-2009 observed average, a weak southward current exists here instead. The excessive northward transport in AMM7 probably contributes

[2] Berx *et al.* (2013) do not explicitly state the type of temperature used (T, θ or Θ); it is assumed that T is used in the paper.

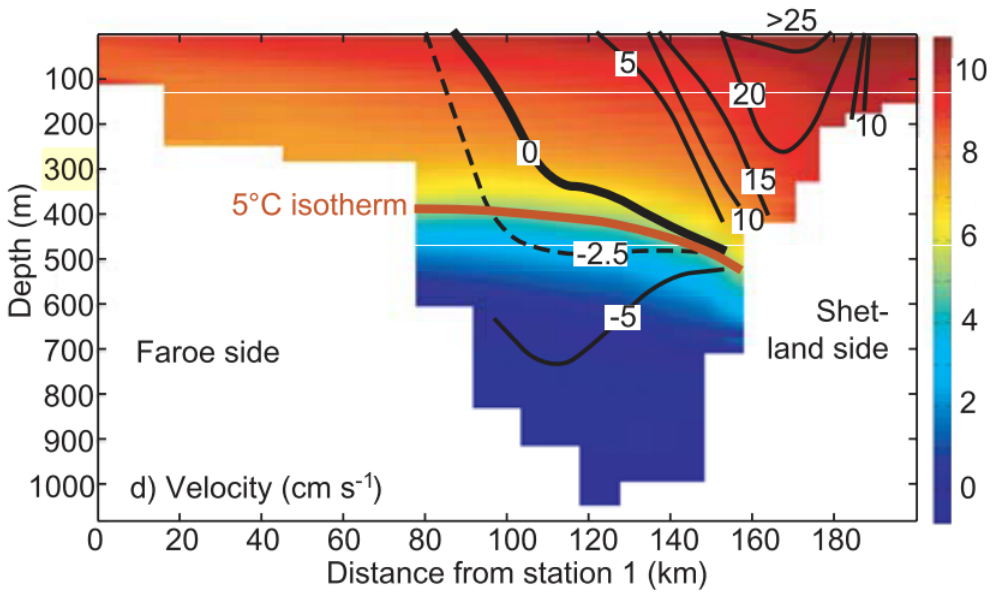

Figure 2.12: 1995-2009 average of along-slope velocities in the FSC (black contours) and θ (colour scale). Adapted from Berx *et al.* (2013).

to too much NAW in the channel and temperature biases that are typically positive (Fig. 2.10a).

Vertical property gradients from AMM7 model output are more linear compared to the CTD observations used for this analysis. An exaggerated vertical diffusivity scheme can potentially cause this. AMM7 uses the Generic Length Scale model (Umlauf & Barchard, 2003). A length scale limitation causes the vertical diffusivity of θ and S_p to be inversely proportional to buoyancy frequency N (Holt & Umlauf, 2008). The largest differences between AMM7 model output and CTD observations occur where the observed density gradients are highest (and thus N is highest), so an exaggerated vertical diffusivity is the least likely to occur here.

Coarse vertical resolution may contribute to the poor performance of AMM7. The scale of shear-flow and the vertical stacking of different water masses is order 100 m (Section 1.2.1), so it is possible that operational AMM7 vertical resolution, which is also order 100 m at 300–1000 m depth, is too coarse to correctly represent this. AMM7 is initially run with 51 vertical levels, and a finer operational output vertical resolution may help to alleviate the issue.

2.7.3 IMPLICATIONS FOR OIL SPILL BEHAVIOUR

Differences between AMM7 model output and CTD observations are likely to alter the behaviour of an oil plume in the FSC. The strength of the density gradient can change the trapping depth of a subsurface plume, and trapping is likely to occur near or below the pycnocline (Johansen, 2000b; Yapa & Chen, 2004). The density gradient is too high at depth in AMM7 model output, which could lead to plume trapping that is too deep.

Absolute differences in temperature will change the depth in which gas hydrates shed or form (Table 1.1). The water-column in AMM7 is typically too warm, which will cause gas hydrates to shed at a greater depth. At the surface, changes in SST could influence the rate of oil evaporation. AMM7 output SST performs relatively well compared to temperatures at intermediate depths (400–750 m; Fig. 2.10a), and so the rate of oil evaporation in OSCAR is probably not a considerable issue.

3

PHYSICAL CONTROLS ON DEEP-SEA SPILLS I: STRATIFICATION

3.1 INTRODUCTION

In Chapter 2, substantial differences between CTD observations and AMM7 model output were outlined. These differences took the form of biases in temperature and salinity, which together form the stratification structure of the water-column. Stratification will influence plume dynamics because the density of entrained water will change, which will affect the buoyancy of the plume. Stratification can influence the terminal layer of plume thickness (TLPD) and subsequent horizontal advection by ocean currents.

In this chapter, the DeepBlow component of OSCAR is used to investigate the sensitivity of plume dynamics to different vertical profiles of temperature and salinity. These profiles are modelled based on typical conditions found within the FSC. The release characteristics are based on a recent accidental seabed release on the west Shetland shelf (Section 1.1.3). The parameter space explored is guided by the differences found between CTD observations and AMM7 model output. These differences include the depth and strength of the thermocline, and the same-depth model-minus-observation temperature differences. The focus is on temperature because of the associated influence on gas hydrate shedding.

The aim of this chapter is to define and isolate individual characteristics of stratification, in order to better understand how buoyancy frequency and temperature affect a deep (≥ 500 m) seabed release in the FSC. Section 3.2 describes how the DeepBlow model handles key physical processes associated with an oil plume. Section 3.3 describes how the idealised stratification profiles are defined within the DeepBlow model as initial conditions for each release, and Section 3.4 outlines the release parameters. Sections 3.5, 3.6, 3.7 and 3.8 show the results of this idealised modelling study, and Section 3.9 discusses the broader implications of the sensitivity of a plume to stratification.

3.2 MODELLING THE PLUME

Plume behaviour can be approximated by assuming a pure plume model. This is in contrast to a lazy plume (Hunt & Kaye, 2005) or forced plume (Morton, 1959), which respectively have a deficit or excess of buoyancy flux compared to a pure plume. Consider a radially symmetric oil plume of density ρ_p within seawater of density $\rho_w(z)$, released at $z = -H$ where $\rho_0 = \rho_w(z = -H)$ is the seawater density at the seabed and H is the depth of the water-column. The plume has radius $r(z)$ and vertical velocity $w(z)$. A pure plume can be modelled by making three assumptions:

1. Differences in seawater density are negligible compared to the difference between seawater density and oil density, or $\rho_w(z) \approx \rho_0$. This is known as the Boussinesq approximation (Boussinesq, 1903).

2. In the horizontal, self-similarity exists for w and for the buoyancy force $g' = g(\rho_0 - \rho_p)/\rho_w(z)$.

3. The vertical plume velocity w is proportional to the seawater entrainment velocity $u_E = \alpha w$, where $\alpha \approx 0.1$. This is known as the entrainment assumption (Morton *et al.*, 1956). $\alpha > 0.1$ for a lazy plume, and $\alpha < 0.1$ for a forced plume.

Mass, momentum, and buoyancy conservation are respectively

$$\left[\rho_p \pi r^2 w\right]_{z+dz} = \left[\rho_p \pi r^2 w\right]_z + \left[\rho_0 2\pi r u_E\right] dz, \tag{3.1}$$

$$\left[\rho_p \pi r^2 w^2\right]_{z+dz} = \left[\rho_p \pi r^2 w^2\right]_z + \left[\rho_w g' \pi r^2\right] dz, \tag{3.2}$$

$$\left[\pi r^2 w g(\rho_w - \rho_p)\right]_{z+dz} = \left[\pi r^2 w g(\rho_w - \rho_p)\right]_z + \left[2\pi r u_E g(\rho_w - \rho_0)\right] dz. \tag{3.3}$$

If the Boussinesq approximation is true, Eq. 3.1, Eq. 3.2 and Eq. 3.3 can be respectively reduced to

$$\frac{d}{dz}\left(r^2 w\right) = 2\alpha w r, \tag{3.4}$$

$$\frac{d}{dz}\left(r^2 w^2\right) = g' r^2, \tag{3.5}$$

$$\frac{d}{dz}\left(r^2 w g\right) = -N^2 r^2 w, \tag{3.6}$$

where N^2 is the buoyancy frequency squared. This analysis is concerned with the sensitivity of the TLPD to N^2.

The DeepBlow model (Johansen, 2000a) was initially developed as a response to proposed deep-sea (> 500 m) drilling activity in the Norwegian sea. It builds on the above theory by considering processes that are not implemented in earlier plume models (e.g. SINTEF's BLOW model; Rye, 1994), which include:

- Depth-variable currents
- Dissolution of gas into seawater
- Gas hydrate formation and shedding
- Non-ideal gas behaviour at pressures where compressibility is significant (typically deeper than 500 m)

Sections 3.2.1 to 3.2.3 describe the DeepBlow model in more detail.

3.2.1 PLUME DENSITY

The volume of the plume calculated as

$$V_p = \sum \frac{G_i}{\rho_i}, \tag{3.7}$$

where G_i and ρ_i are the masses and densities of different constituents i of the plume, respectively. Constituents include seawater, gas hydrates, gas bubbles, and oil. Gas hydrates and oil are presumed to be incompressible. The density of oil is typically 850–900 $\mathrm{kg\,m^{-3}}$, depending on its chemical composition. Methane gas is used for all the releases that are modelled in this analysis; methane hydrates have a density of 900 $\mathrm{kg\,m^{-3}}$ in the DeepBlow model.

Gas bubble density is calculated from the compressibility equation of state

$$\rho_b = \frac{p}{ZRT_b}, \tag{3.8}$$

where p is hydrostatic pressure, T_b is the in-situ temperature of the gas bubbles, $R = 8314\ \mathrm{J\,mol^{-1}\,K^{-1}}$ is the ideal gas constant and Z is the compressibility factor. $Z = 1$ if gas behaves in an ideal manner, and $Z < 1$ when gas becomes compressed.

Seawater density is calculated empirically from T and S_p using SM 2520C (Millero & Poisson, 1981). ρ_w and N^2 are

$$\rho_w = \rho_0 + AS_p + BS_p^{3/2} + CS_p^2, \tag{3.9}$$

$$N^2 = -\frac{g}{\rho_0}\frac{d\rho_w}{dz}, \tag{3.10}$$

where ρ_0, A and B are functions of T, and C is a constant;

$$\begin{aligned}\rho_0 = 999.842\,594 + 6.793\,952\times10^{-2}T - 9.095\,290\times10^{-3}T^2 \\ +1.001\,685\times10^{-4}T^3 - 1.120\,083\times10^{-6}T^4 + 6.536\,332\times10^{-9}T^5,\end{aligned} \tag{3.11}$$

$$\begin{aligned}A = 8.244\,93\times10^{-1} - 4.0899\times10^{-3}T + 7.6438\times10^{-5}T^2 \\ -8.2467\times10^{-7}T^3 + 5.3875\times10^{-9}T^4,\end{aligned} \tag{3.12}$$

$$B = -5.72466 \times 10^{-3} + 1.0227 \times 10^{-4} T - 1.6546 \times 10^{-6} T^2, \tag{3.13}$$

$$C = 4.8314 \times 10^{-4}. \tag{3.14}$$

3.2.2 GAS DISSOLUTION

Dissolved gas contributes to the mass of the plume but not its volume, consequently acting to increase ρ_p and reduce plume buoyancy. The dissolution rate of gas bubbles into seawater is

$$\frac{dG_b}{dt} = -\frac{6kG_b}{D_b}\frac{s}{\rho_b}, \tag{3.15}$$

where G_b is the mass of undissolved gas, ρ_b is the gas bubble density, k is the mass transfer coefficient, s is the solubility of gas bubbles in seawater, and D_b are the gas bubble droplet diameters. Gas bubble (and oil) droplet diameters are estimated using a droplet size distribution (for full details, see Johansen *et al.*, 2013).

3.2.3 GAS HYDRATES

The formation and shedding of gas hydrates causes a change in plume volume, where

$$\Delta V_H = \frac{\Delta G_1}{\rho_w} + \frac{\Delta G_b}{\rho_b} - \frac{\Delta G_1 + \Delta G_g}{\rho_H}. \tag{3.16}$$

$\Delta G_1 = X_1 \Delta G_b$ and $\Delta G_b = X_H G_b$ are changes in the masses of water and gas in the hydrate, respectively. ρ_H is the gas hydrate density, X_H is the fraction of gas mass turned into hydrate, and X_1 is the mass ratio between water and gas in the hydrate, which is about 17:3 (Reed *et al.*, 1995).

3.3 STRATIFICATION PROFILES

To investigate the influence of stratification on the TLPD, stratification profiles are created using an idealised in-situ temperature profile

$$T(z) = \phi_A + \phi_B(z+H) + \phi_C\left(1+\tanh\left(2\pi\phi_D\left(1+\frac{2(z-\phi_E)}{H}\right)\right)\right), \tag{3.17}$$

and depth-uniform practical salinity

$$S_p = 35. \tag{3.18}$$

ϕ_A (units of °C) is equal to $T(z=-H)$. ϕ_B (units of °C m^{-1}) is a background depth-uniform temperature gradient. ϕ_C (units of °C) is the 'strength' of the thermocline when $\phi_B = 0$, where strength is defined as the middle temperature between $T(z=-H)$ and $T(z=0)$. ϕ_D (dimensionless) is a control on thermocline thickness. ϕ_E (units of m) is the vertical displacement of the thermocline relative to $H/2$.

By assuming the water-column is 1000 m deep, Eq. 3.17 can be re-written as

$$T(z) = \phi_A + \phi_B(z+1000) + \phi_C\left(1+\tanh\left(2\pi\phi_D\left(1+\frac{z-\phi_E}{500}\right)\right)\right). \tag{3.19}$$

This analysis will test the sensitivity of the TLPD to each of ϕ_A, ϕ_B, ϕ_C, ϕ_D, ϕ_E.

3.3.1 ZERO N^2

Oil will be released in the absence of a density gradient with depth-uniform T, where $\phi_B = \phi_C = \phi_D = \phi_E = 0$, $0 \le \phi_A \le 10$. Eq. 3.19 becomes

$$T = \phi_A. \tag{3.20}$$

These profiles are defined in Table 3.1 as *a01-a05*.

3.3.2 DEPTH-UNIFORM dT/dz

To introduce a density gradient, oil will be released in the presence of depth-uniform dT/dz, where $\phi_A = \phi_C = \phi_D = \phi_E = 0$, $0.001 \leq \phi_B \leq 0.02$. Eq. 3.19 becomes

$$T(z) = \phi_B(z + 1000). \tag{3.21}$$

These profiles are defined in Table 3.1 as *b01-b05*.

3.3.3 DEPTH-UNIFORM N^2

It is clear from Eq. 3.9 and 3.10 that uniform dT/dz is not equivalent to uniform N^2, because there is a non-linear relationship between T and ρ_w. To eliminate N^2 as a depth-dependant variable, mean N^2 is calculated from profiles *b01-b05*. By keeping the surface and bottom temperatures constant, equivalent profiles *f01-f05* can be created (not shown in Table 3.1), with depth-uniform N^2 and $\phi_B = \phi_B(z)$.

3.3.4 NON-LINEAR N^2

The stratification profiles defined below are more representative of conditions in the FSC, because they are characterised by non-linear temperature gradients with pycnoclines that are near to $H/2$. These profiles are shown in Fig. 3.1 (profiles of T) and Fig. 3.2 (profiles of N^2).

CONTROL RUN

A control profile is defined with $\phi_A = \phi_B = \phi_E = 0$, $\phi_C = 5$, $\phi_D = 1$. This profile has a region of zero N^2 near the surface and at depth, and a 10 °C difference in temperature between 0 m (10 °C) and 1000 m (0 °C). Eq. 3.19 becomes

$$T(z) = 5 + 5\tanh\left(2\pi\left(1 + \frac{z}{500}\right)\right). \tag{3.22}$$

This profile is defined in Table 3.1 as *control*, and shown in Fig. 3.1a and 3.2a.

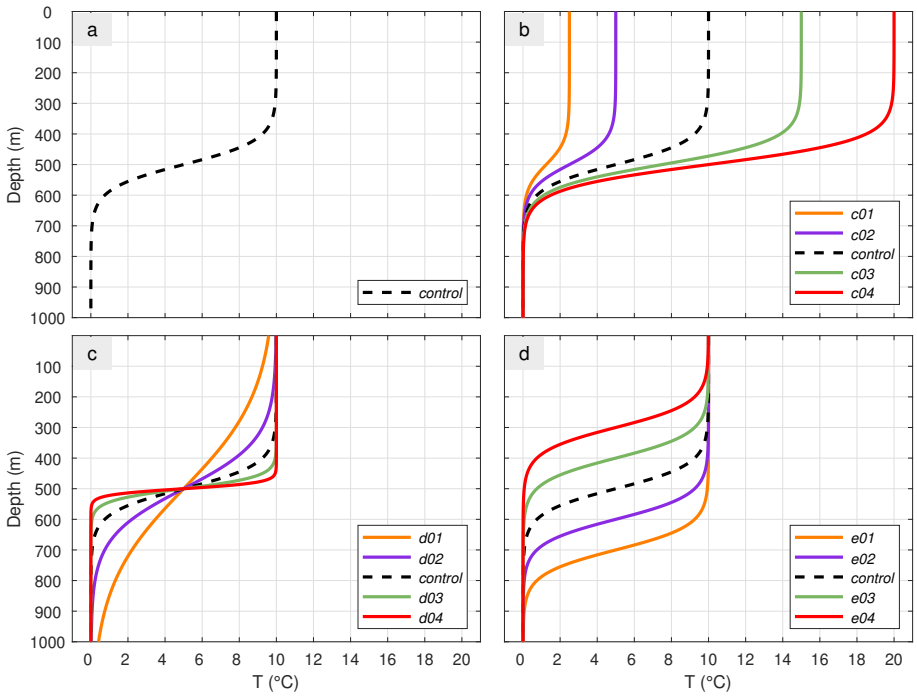

Figure 3.1: Non-linear T profiles. (**a**) The *control* profile (black dashed line). (**b**) Profiles *c01-c04* (solid coloured lines) alongside the *control* profile (black dashed line). (**c**) As (b) but for profiles *d01-d04*. (**d**) As (b) but for profiles *e01-e04*.

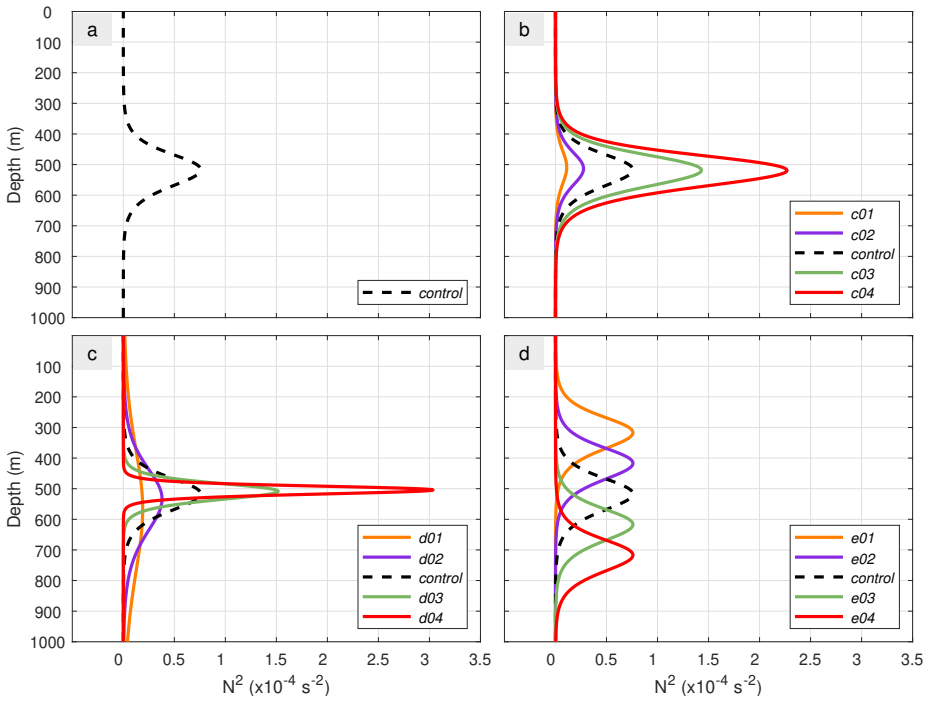

Figure 3.2: As Fig. 3.1 but for N^2.

THERMOCLINE STRENGTH

A key result from Chapter 2 was that N^2 at the thermocline (typically 400–750 m depth) was too weak from AMM7 model output. To investigate the influence of maximum N^2 on the TLPD, profiles based on the *control* are defined with $\phi_A = \phi_B = \phi_E = 0$, $1.25 \leq \phi_C \leq 10$, $\phi_D = 1$. Eq. 3.19 becomes

$$T(z) = \phi_C\left(1 + \tanh\left(2\pi\left(1 + \frac{z}{500}\right)\right)\right). \tag{3.23}$$

These profiles are defined in Table 3.1 as *c01-c04*, and shown in Fig. 3.1b and 3.2b. SST in the FSC is typically 8–12 °C, but the range of SST in profiles *c01-c04* is 2.5–20 °C, which is unrealistic. However, the intention here is to keep the same shape of the thermocline in the *control* profile whilst altering the value of N^2. Additionally, the behaviour of an oil plume may not necessarily be temperature-dependant.

THERMOCLINE THICKNESS

Although N^2 at the thermocline from AMM7 model output was too weak, the temperature range from the surface to the seabed was similar to CTD observations. This means that AMM7 model output was too homogeneous in terms of the vertical distribution of N^2. The homogeneity, or 'thickness', of the thermocline is controlled by ϕ_D, and so to test the sensitivity of a plume to this the *control* profile was modified by using $\phi_A = \phi_B = \phi_E = 0$, $\phi_C = 5$, $0.25 \leq \phi_D \leq 4$. Eq. 3.19 becomes

$$T(z) = 5 + 5\tanh\left(2\pi\phi_D\left(1 + \frac{z}{500}\right)\right). \tag{3.24}$$

These profiles are defined in Table 3.1 as *d01-d04*, and shown in Fig. 3.1c and 3.2c.

THERMOCLINE DEPTH

Another key difference between AMM7 model output and CTD observations was that the depth of the thermocline varied by order 100 m. A change in depth of the thermocline can be investigated by vertically displacing the *control* profile, with $\phi_A = \phi_B = 0$, $\phi_C = 5$, $\phi_D = 1$, $-200 \leq \phi_E \leq 200$. Eq. 3.19 becomes

$$T(z) = 5 + 5\tanh\left(2\pi\left(1 + \frac{z - \phi_E}{500}\right)\right). \tag{3.25}$$

These profiles are defined in Table 3.1 as *e01-e04*, and shown in Fig. 3.1d and 3.2d.

Table 3.1: Parameters used for each idealised stratification profile. n is the number of depth levels the profile is interpolated on to, and *res* is a control on mixed layer depth.

Profile	ϕ_A	ϕ_B	ϕ_C	ϕ_D	ϕ_E	n	*res*
control	0	0	5	1	0	40	0.05
a01	0	0	0	0	0	2	0
a02	2.5	0	0	0	0	2	0
a03	5	0	0	0	0	2	0
a04	7.5	0	0	0	0	2	0
a05	10	0	0	0	0	2	0
b01	0	0.001	0	0	0	2	0
b02	0	0.002	0	0	0	2	0
b03	0	0.005	0	0	0	2	0
b04	0	0.01	0	0	0	2	0
b05	0	0.02	0	0	0	2	0
c01	0	0	1.25	1	0	40	0.0125
c02	0	0	2.5	1	0	40	0.025
c03	0	0	7.5	1	0	40	0.075
c04	0	0	10	1	0	40	0.1
d01	0	0	5	0.25	0	40	0
d02	0	0	5	0.5	0	40	0.05
d03	0	0	5	2	0	40	0.05
d04	0	0	5	4	0	40	0.05
e01	0	0	5	1	-200	40	0.05
e02	0	0	5	1	-100	40	0.05
e03	0	0	5	1	+100	40	0.05
e04	0	0	5	1	+200	40	0.05

3.4 MODEL SET-UP

An ensemble of 12 oil spill simulations are carried out for each of the stratification profiles defined in Table 3.1. The depth of the release is varied (500 m, 600 m, 700 m, 800 m, 900 m and 1000 m depth), and each simulation was performed once with oil released on its own, and a second time with the addition of methane. There are many other variables that can influence the behaviour of a subsurface plume, including the release rate, oil type, release orifice diameter and gas-oil ratio (GOR). Because this thesis is concerned with how hydrodynamic processes influence the behaviour of oil and gas specifically in the FSC, most of these variables are held constant and are

Table 3.2: Notable DeepBlow model parameters.

Name	Value
DeepBlow time-step	1.5 s
DeepBlow output interval	9 s
Release depths	500–1000 m
Release amount	106 m^3
Release duration	1 h
Release rate	0.029 $m^3 s^{-1}$
Oil type	Clair (Table A.1)
Oil density	893.8 $kg m^{-3}$
Oil-water interfacial tension	0.007 $N m^{-1}$
Gas-Oil Ratio	200
Gas type	Methane
Release orifice diameter	0.1 m
Currents	None
Wind	None
Air temperature	10 °C
Initial bubble diameter	0.01 m
Max. bubble diameter	0.02 m
Max. bubble velocity	0.3 $m s^{-1}$
α	0.1

chosen based on their regional relevance. A summary of notable release parameters is given in Table 3.2.

OSCAR is not an open-source modelling system, and consequently the way in which it functions cannot be changed externally. One limitation of the DeepBlow model is that there is an upper limit of 6000 time-steps. The DeepBlow model was initially run with the default time-step of 0.5 s, which limits the total simulation time to 3000 s. This was not long enough to fully resolve the plume dynamics for some simulations. Therefore, the time-step was changed to 1.5 s, which increases the maximum time to 9000 s. Plume behaviour in the first 3000 s was not sensitive to the change in time-step.

Release characteristics such as release duration, release amount and oil type are based on the 2016 Clair platform seabed release (Section 1.1.3). These characteristics are therefore representative of a potential future spill in the FSC. For simulations where methane is present, a GOR of 200 is used because it is similar to earlier

modelling work (Reed *et al.*, 2000; Johansen, 2000b; Yapa & Chen, 2004). The release rate is 0.029 $m^3 s^{-1}$, which is between the low and high release rates used during the DeepSpill field experiment (Johansen, 2000b).

To isolate the influence of stratification on the plume, no currents are used to force the DeepBlow model. The influence of ocean currents is explored through idealised modelling in Chapter 4, and in a regional context in Chapters 5 and 6.

The 3-D Fates model is used for simulations using profiles *a01-a05* to assess the influence of temperature on the mass distribution of oil shortly after the beginning of the release (12 h). The air temperature will influence evaporation and is 10 °C for all simulations. The 3-D Fates model time-step is 60 s, with 1000 m horizontal resolution and 25 m vertical resolution. 1000 methane particles, 1000 liquid/solid particles and 1000 dissolved particles are used to track oil and methane in the far-field. In an operational context, order 10^4 particles of each type would be used. However, the short duration of the 3-D Fates model and absence of advection by winds or ocean currents justifies the lower number. Particle number has no influence on the behaviour of the plume or the mass balance after 12 h.

3.4.1 INCLUSION OF STRATIFICATION

Another limitation of the DeepBlow model is that there is an upper limit of 40 depth levels that can be used to represent an interpolated stratification profile. This is not an issue for S_p because it is depth-uniform. However, the method of interpolation is important for the representation of T. There are two possible methods of interpolation; mapping values of T onto prescribed values of z, or mapping values of z onto prescribed values of T. The second method is preferable here because many of the stratification profiles have large depth ranges where dT/dz is negligible, and there is no benefit in prescribing the same value of T onto more than two values of z.

To interpolate each stratification profile, two variables n and res are prescribed (Table 3.1). n defines the number of depth levels to interpolate onto, where $n \leq 40$. For profiles *a01-a05* and profiles *b01-b05*, $n = 2$ (values prescribed at 0 m and 1000 m) because dT/dz is either zero or depth-uniform. For all other profiles, $n = 40$. res is a control on where a mixed layer (depth-uniform T and S_p) is assumed, where $0 \leq res \leq 1$. Mixed layers are prescribed both above and below the thermocline.

For profiles *c01-c04*, *d02-d04*, *e01-e04* and the *control* profile, $res = \phi_C/100$. For example, for the *control* profile where $\phi_C = 5$, mixed layers are assumed where T is 0–0.05 °C (710–1000 m) and 9.95–10 °C (0–290 m). For these depth ranges, constant temperatures of 0 °C and 10 °C are prescribed, respectively. For *a01-a05*, *b01-b05* and *d01*, $res = 0$ either because there is no temperature gradient or no mixed layer.

The next four sections detail the results of this analysis.

3.5 RESULTS - ZERO N^2

In this section, Eq. 3.20 is used to force depth-uniform T in the water-column, for values of ϕ_A of 0 °C, 2.5 °C, 5 °C, 7.5 °C and 10 °C (profiles *a01-a05*). As both T and S_p are depth-uniform, it can be inferred from Eq. 3.9 and 3.10 that $d\rho_w/dz = N^2 = 0$.

In this chapter, three terms are used to describe the vertical position of oil in the water-column:

- **Depth** - the vertical distance from the sea surface to the location that is referred to (positive-downwards).
- **Release depth** - the depth at which the oil is released.
- **Plume height** - the vertical distance from the release depth to the top of the plume (positive-upwards).

3.5.1 OIL-ONLY RELEASES

Fig. 3.3a, b, c, d shows a time evolution of an oil-only plume released in profile *ao1* from 1000 m, and Fig. 3.4 shows vertical profiles of w and r in profile *a01* for each of the six oil-only releases (release depths of 500 m, 600 m, 700 m, 800 m, 900 m and 1000 m)[1]. In the first 100 m above each release depth, w decreases substantially, from 0.43 m s^{-1} to 0.18 m s^{-1} (Fig. 3.4a). w continues to decrease but never reaches zero, even from a release depth of 1000 m. The plume will always be buoyant because each component of the plume is either of equal or lower density compared to the surrounding ambient conditions, and so $\rho_p < \rho_w$. r increases linearly with plume

[1] To re-emphasise, the y-axis in Fig. 3.4 shows oil released at **different depths relative to the sea surface**.

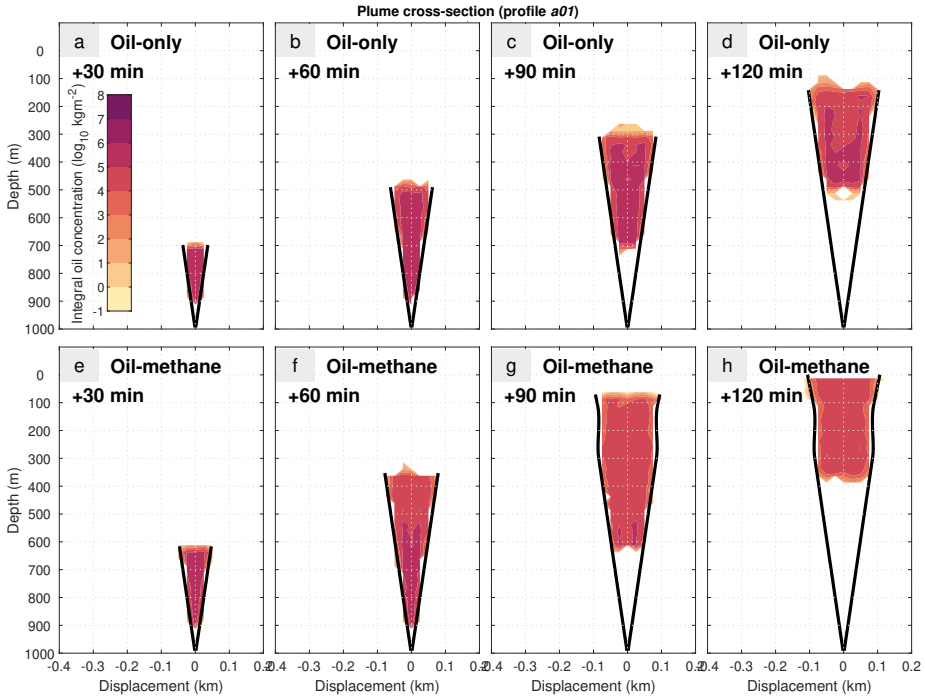

Figure 3.3: Plume development for an oil-only plume and oil-methane plume released from 1000 m depth in profile *a01*. (**a**) An oil-only plume 60 min after the beginning of the release. Contours show the log zonal integral of oil concentration. Also shown is the plume profile at the same point in time (solid black line). (**b**) As (a) but 75 min after the beginning of the release. (**c**) As (a) but 90 min after the beginning of the release. (**d**) As (a) but 105 min after the beginning of the release. (**e-h**) As (a-d) but for an oil-methane plume.

height, because the plume can only change volume as a result of the entrainment of seawater, and the rate of entrainment of seawater is proportional to w (Section 3.2). r increases by 0.12 m for every 1 m of vertical rise (Fig. 3.4b).

In the absence of methane, ϕ_A has no effect on plume development. The only variable affected is oil temperature, which attenuates to ϕ_A within 30 s. ρ_p is not sensitive to ϕ_A, and so both the volume and buoyancy of the plume are also not sensitive to ϕ_A.

The volume distribution of oil 12 h after the beginning of the 1 h release is a function of both release depth and ϕ_A. The total subsurface volume includes oil in the form of dissolved or liquid droplets and oil that has biodegraded. Total subsurface volume does not substantially change with ϕ_A but increases by 25% between oil released from 500 m (6 m^3) and oil released from 1000 m (7.5 m^3). The rate of biodegradation increases with a deeper release depth and with a higher ϕ_A, due to longer surfacing times and higher productivity rates, respectively. The total

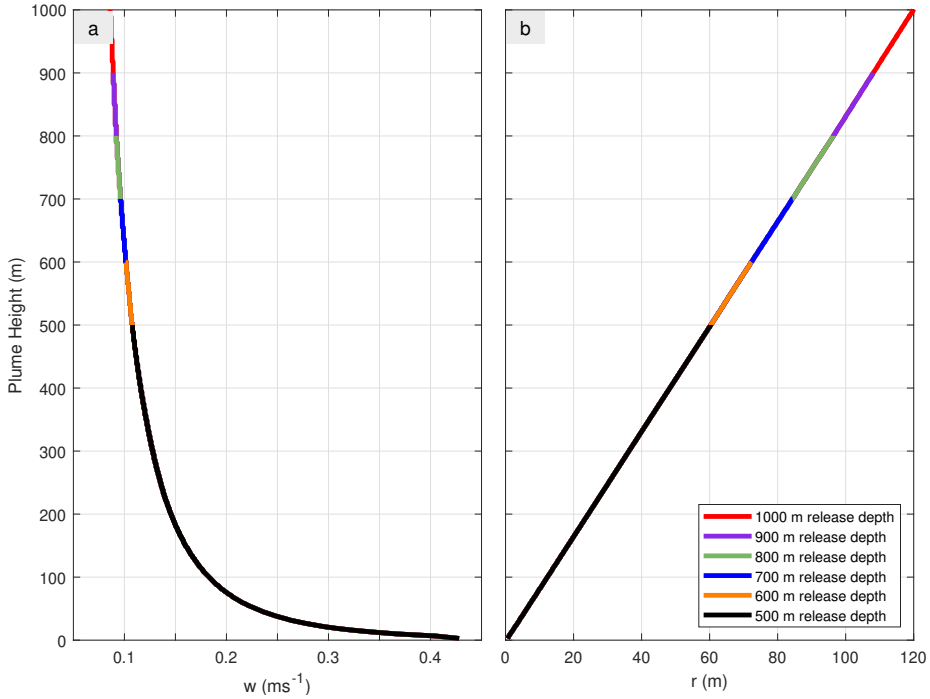

Figure 3.4: Oil-only plume dynamics for profile *a01*. (**a**) Vertical plume velocity for oil released at 500 m, 600 m, 700 m, 800 m, 900 m and 1000 m. (**b**) As (a) but for plume radius.

surfaced volume includes oil residing on the sea surface, and oil that has evaporated. Evaporation is enhanced by a shallower release depth and consequently a longer residence time on the sea surface. Evaporation also increases with ϕ_A.

3.5.2 OIL-METHANE RELEASES

The addition of methane causes the behaviour of the plume to change compared to an equivalent oil-only release (Fig. 3.3e, f, g, h; Fig. 3.5). For an oil-methane release, the plume can typically be divided into three phases (a simulation in profile *a01* with a release depth of 1000 m is used here as an example):

1. **1000-300 m depth**: methane exists in the plume exclusively as an incompressible gas hydrate. Because the density of the hydrate (900 kg m^{-3}) is less than seawater, the buoyancy of the plume is higher than the equivalent oil-only release.

2. **300-100 m depth**: when the ambient pressure is low enough, methane hydrates begin to shed into methane bubbles. Methane bubble density is lower than methane hydrate density, so the buoyancy of the plume increases further. w

increases as hydrate shedding occurs (Fig. 3.5a), and r decreases (Fig. 3.3g). Methane bubbles within the plume can now dissolve into any entrained water.

3. **100-0 m depth**: eventually, all methane becomes dissolved into the entrained water. Dissolved methane contributes to plume mass but not plume volume (Johansen, 2000a), and the plume is less buoyant than it would otherwise be with only oil and water present.

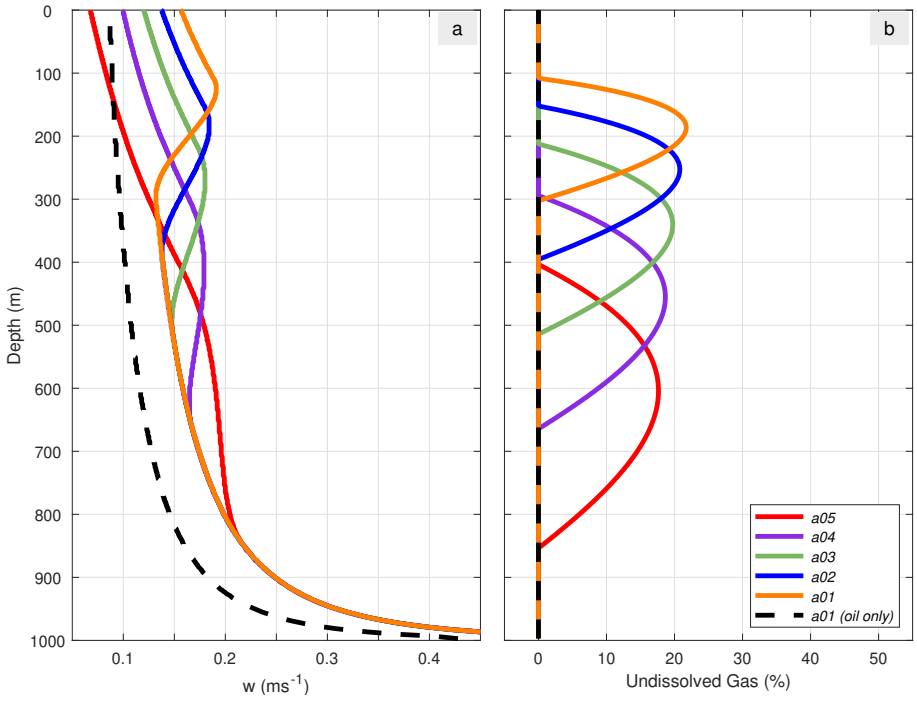

Figure 3.5: Oil-methane plume dynamics for profiles *a01-a05*. (**a**) Vertical plume velocity for oil released at 1000 m in different profiles with methane (solid coloured lines), and without methane (black dashed line). (**b**) As (a) but for the proportion of gas that is undissolved.

By changing ϕ_A, these three phases occur at different depth ranges. For the example given, the presence of methane results in a surfacing time that is 30% quicker than the equivalent oil-only release. All other oil-methane releases also had quicker surfacing times than the equivalent oil-only releases. For profile *a05* ($\phi_A = 10$ °C), an oil-methane release from 1000 m depth had a lower w than the equivalent oil-only release at 0–150 m (Fig. 3.5a), due to early methane dissolution.

3.5.3 KEY POINTS

1. A density gradient is required for trapping to occur.
2. In the absence of gas, plume behaviour is independent of pressure and T.
3. Increasing ϕ_A leads to increased rates of biodegradation and evaporation, but no notable difference in the amount of oil that has reached the surface.
4. Gas hydrates and gas bubbles increase the buoyancy of a plume. Gas that has dissolved into any entrained water decreases the buoyancy of a plume.

3.6 RESULTS - DEPTH-UNIFORM dT/dz

In this section, Eq. 3.21 is used to force depth-uniform dT/dz, for values of ϕ_B of 0.001 °C m^{-1}, 0.002 °C m^{-1}, 0.005 °C m^{-1}, 0.01 °C m^{-1} and 0.02 °C m^{-1} (profiles *b01*-*b05*). SST is 1 °C, 2 °C, 5 °C, 10 °C and 20 °C, respectively. Depth-uniform dT/dz is not equivalent to depth-uniform N^2 (Eq. 3.9), which is explored in Section 3.7.

3.6.1 OIL-ONLY RELEASES

In a stratified water-column, relatively dense water is entrained into the plume and advected into relatively less dense water. Eventually the TLPD is reached, where $\rho_p = \rho_w$ and $w = 0$ (e.g. after 90 min in profile *b01*; Fig. 3.6c). The TLPD occurs for all values of ϕ_B tested and varies considerably; when $\phi_B = 0.001$ °C m^{-1} (profile *b01*) the TLPD is approximately 600 m, but when $\phi_B = 0.02$ °C m^{-1} (profile *b05*), the TLPD is approximately 900 m. At the TLPD, r increases substantially, but maximum r does not appear to be related to any other physical parameter.

Following the termination of the plume, oil continues to ascend in the water-column as individual droplets, distributed evenly across the radial cross-section by 105 min after the beginning of the simulation from 1000 m depth in profile *b01* (Fig. 3.6d). Oil is typically buoyant and will eventually reach the sea surface, but some may dissolve or biodegrade, remaining submerged indefinitely.

There is a non-linear relationship between depth-mean N^2 and plume height (Fig. 3.7). Depth-mean N^2 is calculated between the release depth and the TLPD for

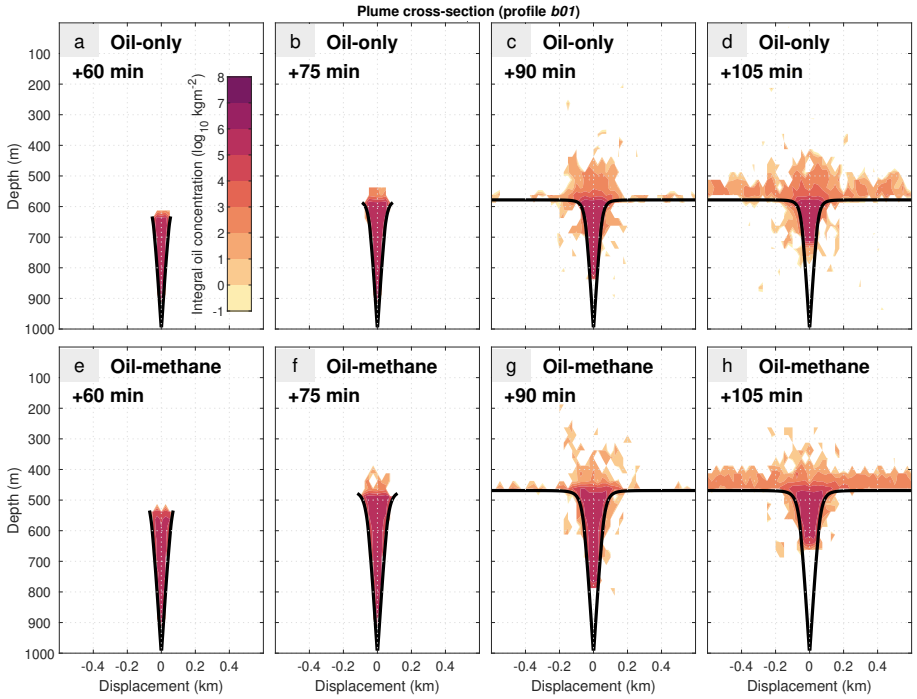

Figure 3.6: Plume development for an oil-only plume and oil-methane plume released from 1000 m depth in profile *b01*. (**a**) An oil-only plume 60 min after the beginning of the release. Contours show the log zonal integral of oil concentration. Also shown is the plume profile at the same point in time (solid black line). (**b**) As (a) but 75 min after the beginning of the release. (**c**) As (a) but 90 min after the beginning of the release. (**d**) As (a) but 105 min after the beginning of the release. (**e-h**) As (a-d) but for an oil-methane plume.

each individual simulation. The relationship between depth-mean N^2 and plume height appears to be asymptotic to both axes. For a small amount of time near the well-head, the release behaves like a jet and does not interact with the surrounding seawater. There will therefore always be a small distance that can be travelled before trapping occurs, even for unrealistically large density gradients. When $N^2 = 0$, there is no mechanism to cause trapping and the plume can rise all the way to the surface, because ρ_p is always lower than ρ_w.

3.6.2 OIL-METHANE RELEASES

Methane is a universal buoyancy aid from any release depth and for all values of ϕ_B, resulting in a shallower TLPD (Fig. 3.6g; Fig. 3.7). The time taken to reach the TLPD is almost identical between equivalent oil-only and oil-methane releases. As an example, when $\phi_B = 0.002$ °C m^{-1} (profile *b02*) the TLPD is shallower relative to the equivalent oil-only release by approximately 200 m if hydrate shedding does occur

(release depths of 500 m, 600 m and 700 m), and by approximately 100 m if hydrate shedding does not occur (release depths of 800 m, 900 m and 1000 m). For all values of ϕ_B, hydrate shedding leads to more substantial differences in the TLPD.

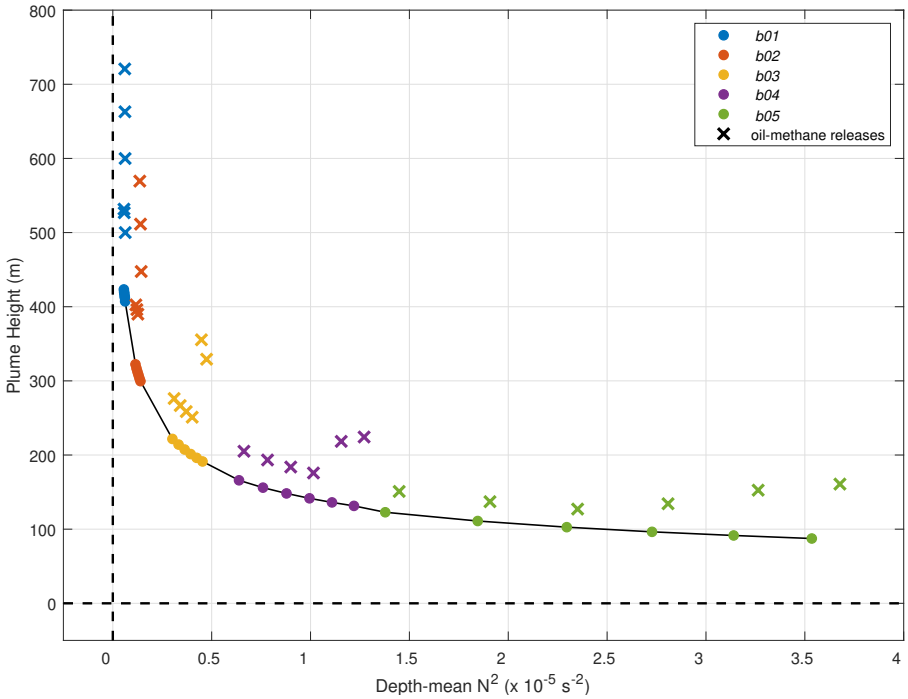

Figure 3.7: Plume height as a function of mean N^2 for profiles *b01-b05*. Shown are oil-only (dots) and oil-methane (crosses) releases in profiles *b01-b05* released at 500 m, 600 m, 700 m, 800 m, 900 m and 1000 m. Different profiles are indicated by different colours. The black dashed lines show zero stratification (vertical line) and the release depth (horizontal line).

3.6.3 KEY POINTS

1. Even a small amount of stratification (e.g. $\phi_B = 0.001$ °C m^{-1}) causes plume trapping and the formation of a TLPD.

2. There is a non-linear relationship between plume height and depth-mean N^2.

3. Methane is a universal aid to plume buoyancy and leads to a shallower TLPD.

3.7 RESULTS - DEPTH-UNIFORM N^2

In this section, plume heights and plume trapping times from Section 3.6 (profiles *b01-b05*) are compared against equivalent profiles *f01-f05*. For both profile sets, values of T at 0 m and 1000 m are identical, but with depth-uniform temperature gradients dT/dz in profiles *b01-b05* and depth-uniform buoyancy frequencies N^2 in profiles *f01-f05*. This analysis has been carried out to deduce if it is a reasonable assumption that depth-uniform dT/dz is a suitable approximation of depth-uniform N^2.

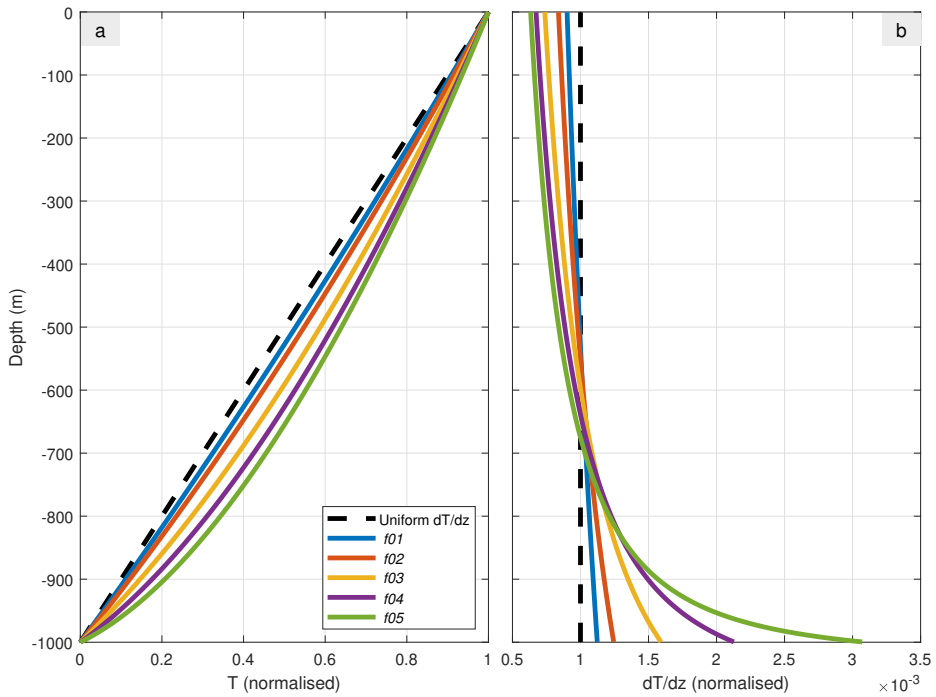

Figure 3.8: Vertical profiles of depth-uniform N^2 and depth-uniform dT/dz. (**a**) Normalised (0–1) T profiles for depth-uniform dT/dz (dashed line) and profiles *f01-f05* (coloured lines). (**b**) As (a) but for the vertical temperature gradient.

3.7.1 TEMPERATURE PROFILES

Fig. 3.8 shows normalised temperature profiles and normalised temperature gradients for a profile of uniform dT/dz and for profiles *f01-f05*. At approximately 0–650 m depth, the normalised gradients for profiles *f01-f05* are less than 1. At approximately 650–1000 m depth, the normalised gradients for profiles *f01-f05* are more than 1. The difference between depth-uniform N^2 and depth-uniform dT/dz

Table 3.3: Oil-only plume heights for profiles *b01-b05* and *f01-f05*. Considerable (≥ 5%) differences are highlighted in green (positive).

Depth	**Type**	*b01, f01*	*b02, f02*	*b03, f03*	*b04, f04*	*b05, f05*
500 m	dT/dz	407	300	191	131	87
	N^2	415	307	197	136	90
	Δ	-2.0%	-2.4%	-3.0%	-3.2%	-3.1%
600 m	dT/dz	412	303	196	136	92
	N^2	417	307	198	136	90
	Δ	-1.2%	-1.3%	-1.0%	0.0%	1.4%
700 m	dT/dz	414	308	201	142	96
	N^2	416	308	198	136	90
	Δ	-0.3%	0.0%	1.7%	4.5%	6.9%
800 m	dT/dz	418	312	207	148	103
	N^2	415	307	197	136	90
	Δ	0.7%	1.9%	5.3%	9.3%	13.6%
900 m	dT/dz	420	317	214	156	111
	N^2	416	308	197	135	90
	Δ	1.1%	2.9%	8.5%	15.3%	23.1%
1000 m	dT/dz	423	322	222	166	123
	N^2	416	307	197	135	89
	Δ	1.8%	5.1%	12.8%	22.7%	37.5%

increases with the stratification strength. At the extreme, profile *f05* has a temperature gradient three times as large at 1000 m, and four times as small at the sea surface.

The assumption that depth-uniform dT/dz is equivalent to depth-uniform N^2 may therefore lead to an overestimated plume height for deeper releases, but an underestimated plume height for shallower releases. This could subsequently affect the depth and direction of horizontal advection by ocean currents, particularly if there is a cross-flow such as in the FSC. The temperature of the water-column is also warmer for uniform N^2 (Fig. 3.8a), which could lead to methane hydrates shedding into methane bubbles earlier (Sloan & Koh, 2007; Table 1.1).

Table 3.4: Oil-methane plume heights for profiles *b01-b05* and *f01-f05*. Considerable (≥ 5%) differences are highlighted in green (positive) and red (negative).

Depth	Type	*b01, f01*	*b02, f02*	*b03, f03*	*b04, f04*	*b05, f05*
500 m	dT/dz	500	448	329	224	161
	N^2	500	454	331	234	187
	Δ	n/a	-1.4%	-0.6%	-4.1%	-14.0%
600 m	dT/dz	600	511	355	218	153
	N^2	600	517	373	233	158
	Δ	n/a	-1.1%	-4.7%	-6.1%	-3.3%
700 m	dT/dz	663	569	251	176	134
	N^2	668	574	248	170	145
	Δ	-0.7%	-0.9%	1.1%	3.5%	-7.6%
800 m	dT/dz	721	390	259	184	127
	N^2	724	387	248	170	113
	Δ	-0.5%	0.9%	4.4%	8.0%	12.5%
900 m	dT/dz	527	396	267	193	137
	N^2	523	387	249	170	113
	Δ	0.7%	2.4%	7.3%	13.6%	21.3%
1000 m	dT/dz	532	403	276	205	151
	N^2	523	387	248	170	112
	Δ	1.6%	4.0%	11.2%	20.9%	34.4%

3.7.2 COMPARISON WITH DEPTH-UNIFORM dT/dz

Differences in plume height between oil released in a profile of depth-uniform dT/dz and oil released in a profile of depth-uniform N^2 depend on both the stratification strength and the release depth. For oil-only releases (Table 3.3), there are considerable (>5%) differences between equivalent profiles for release depths of 700 m or deeper, and where stratification is 0.002 °C m^{-1} or stronger. In these conditions, depth-uniform N^2 leads to a lower plume height and a deeper TLPD. The absolute differences in plume heights (5–25 m) are unlikely to be physically significant, since the change in magnitude and direction of ocean currents in the FSC vary by order 100 m (Section 1.2.1). Percentage differences are larger when the release depth is deeper and when the stratification is stronger. For releases at 500 m and 600 m depth, profiles of depth-uniform N^2 typically cause shallower trapping than equivalent profiles of depth-uniform dT/dz.

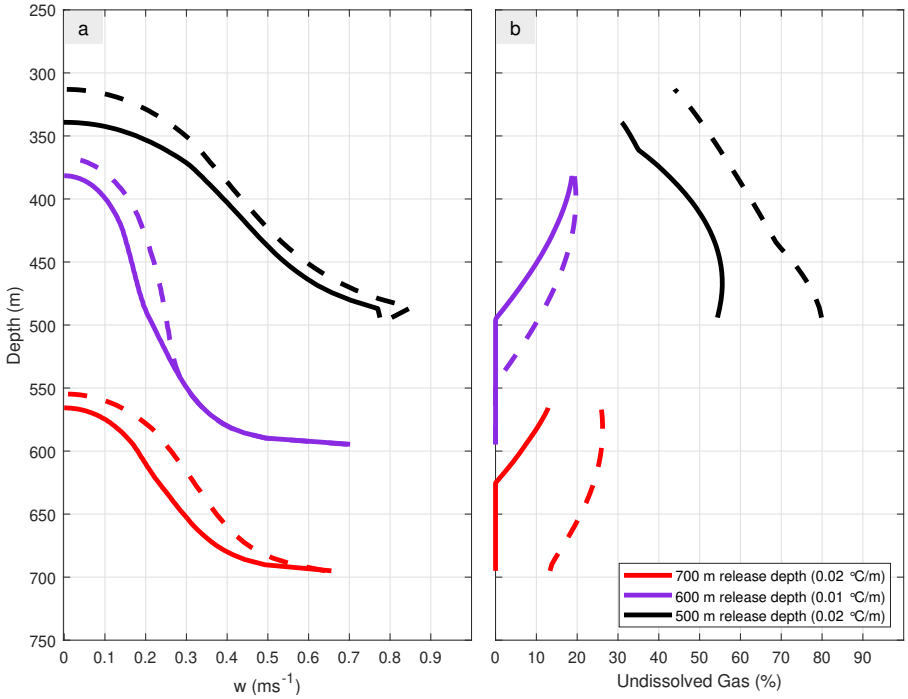

Figure 3.9: Oil-methane plume dynamics comparison for depth-uniform N^2 and depth-uniform dT/dz. (**a**) Vertical plume velocity for oil released at 700 m (*b05* and *f05*), 600 m (*b04* and *f04*) and 500 m (*b05* and *f05*). Solid lines indicate profiles of depth-uniform dT/dz, and dashed lines indicate profiles of depth-uniform N^2. (**b**) As (a) but for the proportion of gas that is undissolved.

When methane is released alongside oil, the relationship between profiles of depth-uniform N^2 and profiles of depth-uniform dT/dz becomes more complex (Table 3.4). Depth-uniform N^2 still causes considerably lower plume heights and a deeper TLPD, but only for release depths of 800 m or deeper and where stratification strength is 0.005 °C m^{-1} or stronger. Considerable negative differences also occur for release depth of 500–700 m; methane hydrates shed earlier in uniform N^2 because the temperature is typically higher (Fig. 3.8a). There is therefore a higher proportion of methane that is undissolved when oil is released (Fig. 3.9b), causing a higher plume buoyancy and vertical plume velocity (Fig. 3.9a), and subsequently a shallower TLPD.

In summary, depth-uniform dT/dz is not necessarily a suitable approximation for depth-uniform N^2, if the stratification is strong enough or if the release is deep enough. Differences in plume behaviour between equivalent profiles can also emerge when hydrate shedding occurs, which depends on the temperature and pressure.

3.7.3 TIME TAKEN TO REACH THE TLPD

For oil-methane releases from 1000 m depth (Fig. 3.10a), methane only ever exists in hydrate form, and there is no change in the density of either methane or oil during the ascent of the plume. From this release depth, both the oil-only releases and the oil-methane releases take the same amounts of time to reach the TLPD for all stratification strengths. w is also approximately 30% higher for an oil-methane release compared to an oil-only release. This relationship between an oil-methane release and an oil-only release can be explained using the pure plume model defined in Section 3.2.

Consider time $t = t_x$ shortly after the beginning of the release at $t = 0$, where the plume is sufficiently far away from any pressure forces at the well-head. Two different plumes have vertical velocities w_1 and w_2 such that

$$w_1 = f w_2, \tag{3.26}$$

where f is a constant. The plume radius can be described by $r(h) = d + \gamma h$, where d is the release orifice diameter, h is the vertical distance from the release depth (positive-upwards), and γ is a constant (Section 3.5; $\gamma \approx 0.12$). At $t > t_x$, $d << r$ and so $r(h) \approx \gamma h$. Considering Eq. 3.26, it can therefore be assumed that $r_1 = f r_2$ at $t > t_x$. If $u_E = \alpha w$ is the entrainment velocity (Section 3.2; $\alpha \approx 0.1$), then the mass flux of ambient water entrained into the plume is

$$F = z \rho_w 2\pi r u_E, \tag{3.27}$$

where ρ_w is the density of the surrounding seawater, and z is some small vertical distance. It is clear from Eq. 3.26 that $u_{E1} = f u_{E2}$, and by assuming that $\rho_{a1} \approx \rho_{a2}$, Eq. 3.27 shows that

$$F_1 = f^2 F_2. \tag{3.28}$$

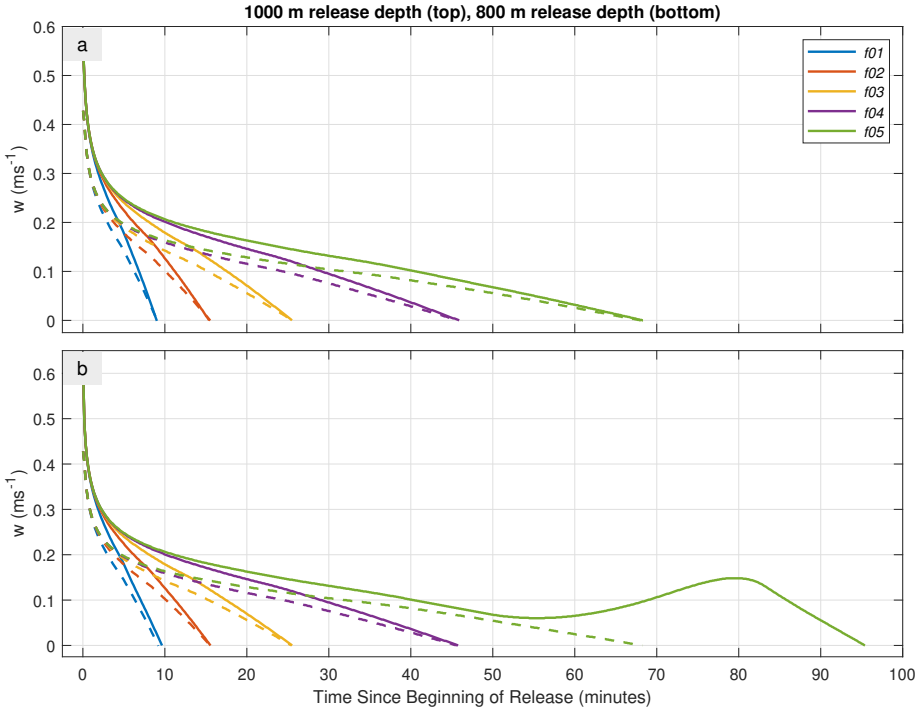

Figure 3.10: Vertical plume velocity in profiles *f01-f05* (1000 m and 800 m release depths). (**a**) Vertical plume velocity as a function of time for profiles *f01-f05* for oil-only releases (dashed lines) and oil-methane releases (solid lines) from1000 m. (**b**) As (a) but for 800 m.

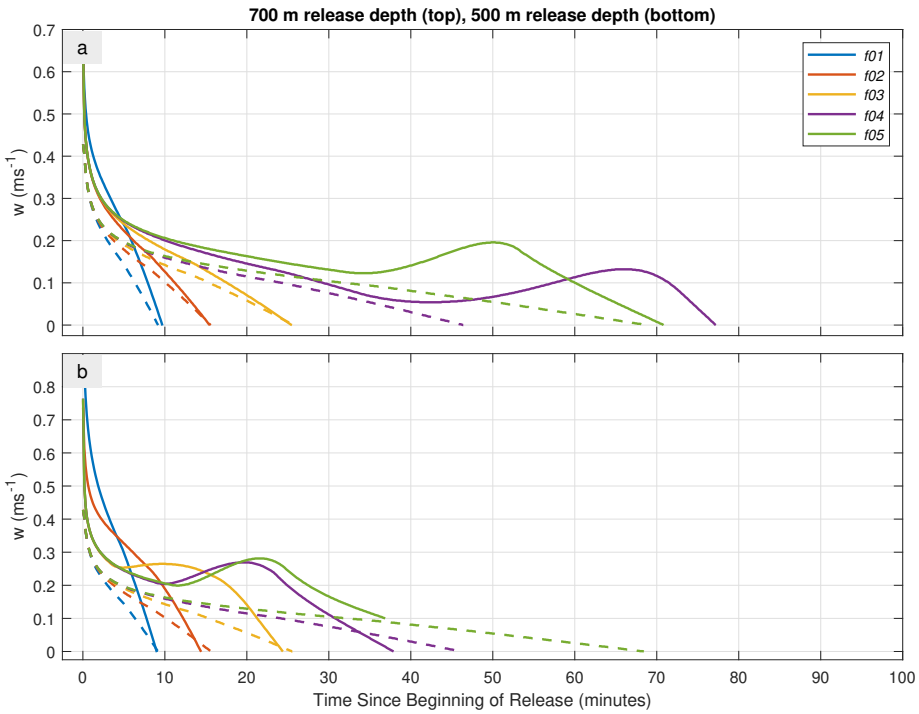

Figure 3.11: As Fig. 3.10 but for 700 m and 500 m release depths.

Momentum flux is defined as

$$M = \rho_p \pi r^2 w^2. \tag{3.29}$$

Assuming $\rho_{p1} \approx \rho_{p2}$, then $M_1 = f^4 M_2$. Also consider that the energy required to elevated 1 kg of ambient water by Δh is

$$e = \frac{g}{\rho_w} \Delta\rho_w \Delta h. \tag{3.30}$$

Over a small amount of time Δt, $\Delta h_1 = f\Delta h_2$. Assuming a depth-uniform N^2, $\Delta\rho_{a1} = f\Delta\rho_{a2}$. Thus, the total energies E_1 and E_2 lost through the entrainment of ambient water, where $E = eF$, are related by

$$\Delta E_1 = f^4 \Delta E_2. \tag{3.31}$$

Assuming a closed system of energy, the reduction in momentum flux ΔM will be proportional to ΔE;

$$\Delta M = \beta \Delta E, \tag{3.32}$$

where β is a constant. Therefore, $\Delta M_1 = f^4 \Delta M_2$, and

$$\frac{\Delta M_1}{M_1} = \left(\frac{f^4}{f^4}\right) \frac{\Delta M_2}{M_2}. \tag{3.33}$$

This means that the rate of change of momentum in the plume is proportional to the magnitude of the momentum of the plume. At $t > t_x$, $M_1(t) = f^4 M_2(t)$ and $w_1(t) = f\, w_2(t)$, inferring that trapping time, where $M = w = 0$, is the same for both releases in a profile of depth-uniform N^2.

When released from 800 m depth, the oil-methane plume in the weakest stratification (profile *f01*) reaches a depth where temperature and pressure are sufficient to allow for hydrate shedding and methane bubble formation 60 min after the beginning of the release. This enhances the buoyancy of the plume, leading to an increase in w (Fig. 3.10b). However, as gas dissolution occurs, the buoyancy of the plume decreases, which leads to a more rapid deceleration relative to an equivalent oil-only plume. In this instance, the plume's trapping time increases by approximately one-third.

For a release from 700 m depth (Fig. 3.11a), hydrate shedding and gas dissolution occur at an earlier stage in profile *f01*. Compared to the release in the same profile from 800 m, the trapping time is reduced by order 30 min. Shedding and dissolution also occur for a release in profile *f02*.

For a release from 600 m depth (not shown) or from 500 m depth (Fig. 3.11b), the oil-methane release surfaces in profile *f01*. Oil-methane releases that do not surface become trapped more rapidly than the equivalent oil-only releases, because hydrate shedding and gas dissolution occur almost immediately after the releases begin, and gas inhibits the buoyancy of the plume once dissolved. It is important to note that the inclusion of methane still leads to a shallower TLPD for any release in depth-uniform N^2.

3.7.4 KEY POINTS

1. Depth-uniform dT/dz is not necessarily a suitable approximation for depth-uniform N^2.

2. Time taken to reach the TLPD in depth-uniform N^2 is independent of plume buoyancy if hydrate shedding does not occur.

3.8 RESULTS - NON-LINEAR N^2

3.8.1 CONTROL RUN

The *control* profile is characterised by a vertically symmetric thermocline at 500 m depth, with boundary conditions of 0 °C at 1000 m and 10 °C at 0 m. The water-column is homogeneous from 0–290 m and from 710–1000 m. Trapping heights from releases in the *control* profile can be viewed in Table 3.5 ($\phi_C = 5$ °C), Table 3.6 ($\phi_D = 1$) or Table 3.7 ($\phi_E = 0$ m).

A release deeper than the thermocline (500 m) is also trapped[2] deeper than the thermocline. This is the case for both oil-only releases and for oil-methane releases. The TLPD is also always shallower than the deep homogeneous layer (710 m). For an oil-methane release, the TLPD is shallower by approximately 20 m compared to the

[2]Here, 'trapped' is analogous to the depth of the TLPD.

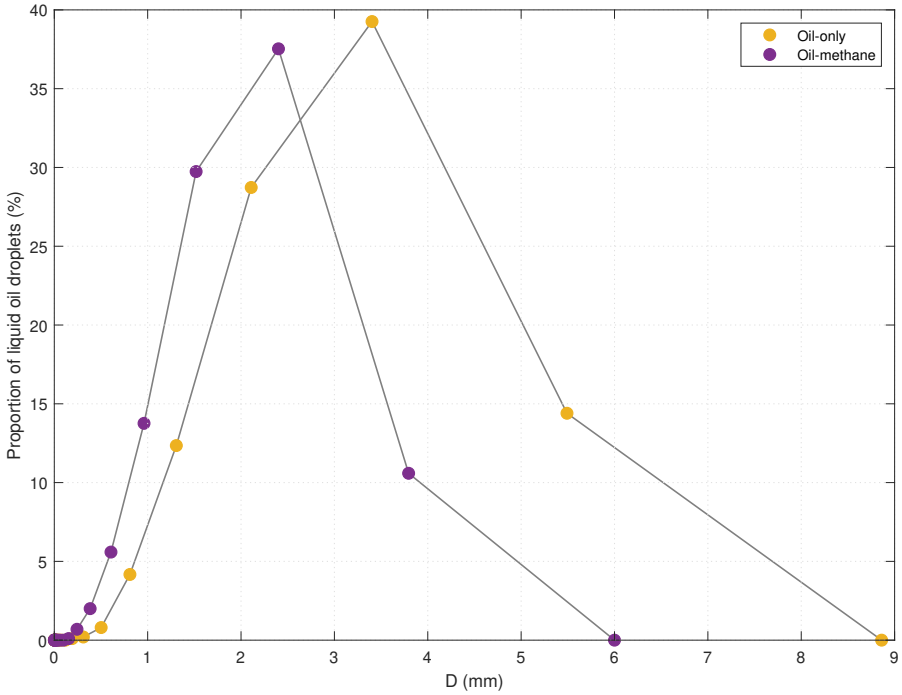

Figure 3.12: Droplet size distribution of subsurface liquid oil droplets at the end of the release period (1 h) for the *control* profile when oil is released at 1000 m depth. Shown are both the oil-only and oil-methane releases

equivalent oil-only release when released from 600 m and deeper (N^2 increases as the plume rises), but more than doubles when released from 500 m (N^2 decreases as the plume rises). The more substantial difference between releases from 500 m is partly because hydrate shedding occurs (and does not occur for deeper releases), and partly because N^2 decreases as the plume ascends.

Stratification in the FSC is controlled by the direction of ocean currents; oil below the thermocline is likely to be advected westward and into the open North Atlantic, whereas oil above the thermocline is likely to be advected north-eastward towards the Norwegian Sea. Buoyant oil droplets will continue to rise after trapping occurs, but very small droplets and dissolved oil may be trapped indefinitely at a depth similar to the TLPD. The TLPD is therefore a good indicator of the direction of advection in the FSC. These results suggest that if oil is released below the thermocline, at least some of it will be transported westward. For an oil-methane release, the droplet size distribution is smaller than for an oil-only release (Fig. 3.12), and so a larger proportion of the oil will remain below the surface.

The rest of the results for this analysis (Sections 3.8.2 to 3.8.4) explore how

Table 3.5: Plume heights for profiles *c01-c04* with and without methane. Considerable (≥ 5%) differences are highlighted in green (positive).

Depth	Type	$\phi_C = 1.25$	$\phi_C = 2.5$	$\phi_C = 5$	$\phi_C = 7.5$	$\phi_C = 10$
500 m	oil	360	118	69	52	43
	gas	500	346	148	103	88
	Δ	n/a	193.6%	115.9%	98.5%	104.9%
600 m	oil	145	110	85	73	65
	gas	182	131	99	85	75
	Δ	25.6%	19.0%	17.0%	16.0%	15.8%
700 m	oil	194	167	143	130	121
	gas	221	187	160	145	136
	Δ	13.8%	12.3%	11.8%	11.9%	12.0%
800 m	oil	268	241	215	201	190
	gas	293	263	235	220	210
	Δ	9.6%	9.1%	9.3%	9.8%	10.0%
900 m	oil	351	323	297	282	271
	gas	376	346	319	303	292
	Δ	7.2%	7.1%	7.3%	7.7%	7.9%
1000 m	oil	439	411	384	370	360
	gas	464	435	407	391	380
	Δ	5.7%	5.7%	5.9%	5.9%	5.7%

modifying the strength, thickness, and depth of the thermocline in the *control* profile influences the location of the TLPD.

3.8.2 THERMOCLINE STRENGTH

Thermocline strength is controlled in Eq. 3.23 by ϕ_C. For profiles *c01-c04*, values of ϕ_C of 1.25 °C, 2.5 °C, 7.5 °C and 10 °C are used. The *control* profile has a value of ϕ_C of 5 °C.

OIL-ONLY RELEASES

Like an oil-only plume in the *control* profile, an oil-only plume that is released below the thermocline (500 m) will also become trapped below the thermocline. An exception to this rule occurs when oil is released from 600 m and when ϕ_C = 1.25 °C or ϕ_C = 2.5 °C. Plume heights for these releases are respectively 145 m and 110 m

(TLPDs occur at 455 m depth and 490 m depth). For any particular release depth, a higher value of ϕ_C (stronger thermocline) leads to deeper trapping. This is because the shapes of profiles *c01-c04* are identical to the *control* profile when normalised between 0 and 1. Therefore, at any particular depth a higher value of ϕ_C leads to a larger local stratification strength. As previously outlined in Section 3.5, the absolute temperature of the water-column is not physically relevant for the behaviour of an oil-only plume.

OIL-METHANE RELEASES

Plume height for an oil-methane release is considerably larger than for an oil-only release for all results presented in Table 3.5. The plume height is greater by 5–6% when released from 1000 m, 7–8% from 900 m, 9–10% from 800 m, 11–14% from 700 m, 18–26% from 600 m and 100–200% from 500 m. Percentage differences are not influenced by the value of ϕ_A. The releases from 500 m for ϕ_C = 1.25 °C could not be compared because the oil-methane release surfaced. The much larger percentage differences for releases from 500 m compared to deeper releases are due to hydrate shedding and the associated increased buoyancy. The exact nature of shedding seen in these simulations is not expected to occur within the FSC because of the unrealistic surface temperatures. The *control* profile (ϕ_C = 5 °C) is the most appropriate representation of the FSC. Nevertheless, results for other values of ϕ_C highlight the large variability associated with the dependence of hydrate shedding on temperature and pressure.

3.8.3 THERMOCLINE THICKNESS

Thermocline thickness is controlled in Eq. 3.24 by ϕ_D. For profiles *d01-d04*, values of ϕ_D of 0.25, 0.5, 2 and 4 are used. The *control* profile has a value of ϕ_D of 1

OIL-ONLY RELEASES

Plume height increases as the release depth increases (Table 3.6). This is except for a release from 500 m when ϕ_D = 4, where the plume ascends to over 400 m above the release depth (compared to 95 m when released from 600 m depth). The plume from this release could have trapped at a shallower depth, but the maximum number of model iterations was reached and the simulation ended at t = 9001.5 s. For this profile (*d04*), the water-column is mixed from 0–448 m and from 552–1000 m in the

Table 3.6: Plume heights for profiles *d01-d04* with and without methane. Considerable (≥ 5%) differences are shaded in highlighted (positive).

Depth	Type	$\phi_D = 0.25$	$\phi_D = 0.5$	$\phi_D = 1$	$\phi_D = 2$	$\phi_D = 4$
500 m	oil	112	86	69	60	401
	gas	199	161	148	190	277
	Δ	77.8%	87.1%	115.9%	214.9%	n/a
600 m	oil	116	95	85	88	95
	gas	159	114	99	98	101
	Δ	36.5%	20.8%	17.0%	11.2%	6.2%
700 m	oil	130	125	143	169	187
	gas	158	147	160	180	194
	Δ	22.0%	17.9%	11.8%	6.5%	3.3%
800 m	oil	151	170	215	259	284
	gas	182	197	235	271	290
	Δ	20.8%	15.7%	9.3%	4.4%	2.2%
900 m	oil	179	226	297	353	381
	gas	214	257	319	365	388
	Δ	19.8%	13.7%	7.3%	3.3%	1.6%
1000 m	oil	214	288	384	449	480
	gas	254	324	407	461	486
	Δ	18.6%	12.4%	5.9%	2.7%	1.3%

interpolated DeepBlow input. The initial momentum and buoyancy of the plume was large enough to escape the vertically confined thermocline into the shallow region of zero N^2. The plume will eventually trap because a small amount of water is entrained along the density gradient from 500–448 m. For releases from 500 m using profiles *d01-d03*, the plume did escape into zero N^2 before trapping.

For releases from 700 m and deeper, a higher value of ϕ_D leads to shallower trapping. For releases from 600 m and shallower, a higher value of ϕ_D leads to deeper trapping. The cause of this is particularly clear between $\phi_D = 0.25$ and $\phi_D = 1$. As ϕ_D increases, N^2 becomes increasingly small near the surface and bottom (0–400 m and 600–1000 m), but increasingly large near the thermocline (400–600 m; Fig. 3.13). The difference between stratification profiles is analogous to the model-observation differences between AMM7 output and CTD observations (Chapter 2). Our results therefore suggest that deep-seabed releases using AMM7 model output will lead to

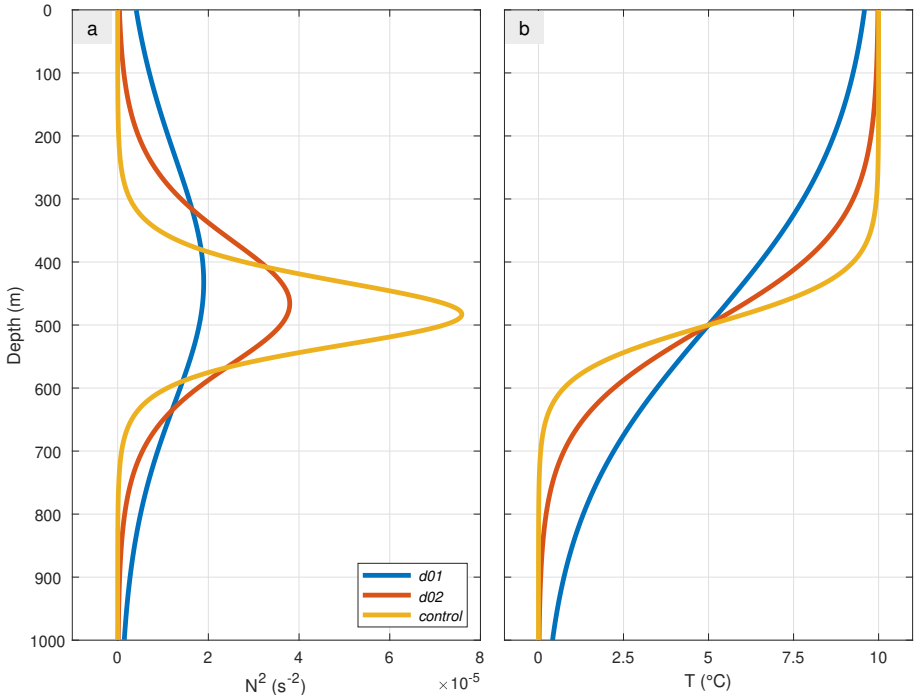

Figure 3.13: Vertical profiles of N^2 and T for profile *d01*, profile *d02* and the *control* profile. (**a**) Buoyancy frequency squared. (**b**) In-situ temperature.

deeper-than-expected plume trapping.

OIL-METHANE RELEASES

The inclusion of methane leads to considerably shallower trapping for many of the releases. A lower value of ϕ_D and a shallower release leads to a larger percentage difference. Gas universally enhances plume buoyancy and trapping height, with the exception of the release from 500 m when $\phi_D = 4$. Here, dissolved gas has a large enough negative influence on plume buoyancy to trap the plume at least 125 m deeper than the equivalent oil-only release.

Table 3.7: Plume heights for profiles *e01-e04* with and without methane. Considerable (≥ 5%) differences are highlighted in green (positive).

Depth	Type	$\phi_E = -200$	$\phi_E = -100$	$\phi_E = 0$	$\phi_E = 100$	$\phi_E = 200$
500 m	oil	500	500	69	85	143
	gas	500	500	148	99	159
	Δ	n/a	n/a	115.9%	16.4%	11.5%
600 m	oil	600	69	85	143	215
	gas	489	141	99	159	235
	Δ	n/a	105.2%	17.0%	11.7%	9.3%
700 m	oil	69	85	143	215	297
	gas	104	100	160	235	319
	Δ	51.5%	17.3%	11.8%	9.3%	7.3%
800 m	oil	85	143	215	297	384
	gas	100	160	235	319	407
	Δ	17.5%	11.9%	9.3%	7.3%	5.9%
900 m	oil	143	215	297	384	475
	gas	160	235	319	407	498
	Δ	12.0%	9.4%	7.3%	5.9%	4.8%
1000 m	oil	215	297	384	475	569
	gas	235	319	407	498	591
	Δ	9.4%	7.3%	5.9%	4.8%	3.9%

3.8.4 THERMOCLINE DEPTH

Thermocline depth is controlled in Eq. 3.25 by ϕ_E. For profiles *e01-e04*, values of ϕ_E of between −200 m and 200 m are used. The *control* profile has a value of ϕ_E of 0 m.

The thermocline depth was varied to capture the order 100 m variability of the maximum property gradients seen in the CTD observations (Section 2.5). Changing the thermocline depth has the effect of reducing or increasing the distance to maximum N^2 for a release from any particular depth. If the thermocline is deepened compared to the *control* profile (profiles *e01* and *e02*), the plume will meet the thermocline with a higher vertical velocity. However, an increase in w does not result in plume trapping above the thermocline if the release depth is at least 100 m below it. Releases at least 100 m above the thermocline result in the plume surfacing (see Table 3.7; this occurs for release depths of 500 m and 600 m when $\phi_E = -200$ m, and for a release depth of 500 m when $\phi_E = -100$ m). This is except for an oil-methane release

from 600 m depth when $\phi_E = -200$ m, because of the negative influence dissolved gas will have had on the buoyancy of the plume. Overall, these results suggest that the depth of the thermocline in the FSC is not important in determining whether a plume is trapped below it, but the release depth relative to the thermocline is.

3.8.5 KEY POINTS

1. Methane is still a universal aid to plume buoyancy in the presence of non-linear stratification.

2. Oil released below the thermocline does not typically pass through the thermocline before trapping occurs. Exceptions to this can occur when gas is released alongside oil, or when the thermocline strength is reduced.

3. The TLPD is particularly sensitive to the thermocline thickness (ϕ_D). The difference in thermocline thickness between AMM7 and reality will lead to a TLPD that is too deep if oil is released below the maximum temperature gradient, and too shallow if oil is released above the maximum temperature gradient.

3.9 DISCUSSION

In this chapter, an oil release with characteristics similar to what has previously occurred on the west Shetland Shelf was modelled as a deep-sea spill in the FSC, using different idealised stratification profiles. This included profiles of zero N^2, depth-uniform dT/dz, depth-uniform N^2, and numerous examples of regionally-relevant non-linear N^2. It was found that a plume will become trapped within the water-column even in the presence of a small density gradient (1 °C temperature change over 1000 m depth), and will be trapped below the thermocline in almost all cases. The results show that the depth distribution of N^2 is a critical control on the depth of the TLPD, which may later determine the vertical distribution of oil in the far-field.

3.9.1 COMPARISON WITH PREVIOUS LITERATURE

Yapa & Chen (2004) show how plume behaviour changes between a release in typical conditions found within the GoM, and a release in typical conditions found within the FSC[3]. The FSC water-column is well mixed from 700–1000 m depth, whilst there is a small temperature change (1 °C) over this depth range in the GoM water-column. Our results suggest that the TLPD should be shallower for the FSC release compared to the GoM release, but Yapa & Chen (2004) find that the opposite is true. This could be because the authors also included currents in their spill simulations, and at 1000 m depth the current speed in the FSC water-column (≈ 0.1 m s^{-1}) was higher than the current speed in the GoM water-column (≈ 0 m s^{-1}). A higher current velocity is likely to cause deeper trapping (Johansen, 2000b), and so this probably explains the difference to the results presented in this chapter.

Johansen (2000b) performed a series of plume simulations with the DeepBlow model from 1000 m depth in conditions representative of the FSC and similar to the *control* profile used in this chapter. There is also a small temperature gradient present in their stratification profiles of approximately 0.5 °C from 1000–600 m, which is a similar strength to either profile *b01* or profile *f01*. Releases were simulated alongside a variety of different stratification and current profiles. For low current speeds ($<$ 0.05 m s^{-1}), the TLPD is on average 600 m, which is similar to the TLPD for an oil-

[3] Yapa & Chen (2004) refer to these conditions as the 'North Sea', but the stratification profile is very similar to the observations presented in Chapter 2 in the central FSC.

methane release from 1000 m in the *control* profile (593 m). Higher current speeds resulted in a deeper TLPD. The TLPD always occurs below the thermocline in the results of Johansen (2000b), which is analogous to the conclusions drawn from the results in this chapter. Reed *et al.* (2000) also found that the TLPD is 700–800 m if oil is released in the central FSC from 1200 m depth, when simulating the plume in the DeepBlow model.

Other oil spill modelling studies using FSC ocean conditions only focus on far-field advection, and do not consider the potential role of near-field plume dynamics. Main *et al.* (2017) predict the trajectory of oil originating from a spill in the FSC using neutrally-buoyant particle tracking. The authors suggest where oil could be advected in the horizontal at different depths, but are not able to approximate the proportion of oil originating from a seabed release at each of these depths. The plume modelling presented in this chapter gives us an initial idea of the depth-distribution of oil from a release in the FSC by predicting the location of the TLPD. This understanding could be further improved by assessing the influence of currents representative of conditions in the FSC, which is the focus of Chapter 4.

In this analysis, the TLPD was chosen as the most important variable for assessing the sensitivity of an oil plume to stratification. A second variable that is sensitive to stratification is the trapping time, defined as time it takes a plume to reach the TLPD. Trapping time varies by up to order 1 h between simulations. However, the response of industry to a seabed release and the clean-up can take weeks or months (Beyer *et al.*, 2016; Gallego *et al.*, 2018), so a difference in trapping time is not particularly important here. On the other hand, the location of the TLPD is likely to determine the depth oil is dissolved, trapped and advected, which is particularly important in the FSC where a shear-flow exists between the upper and lower water-column.

3.9.2 IMPLICATIONS FOR REALISTIC STRATIFICATION

The stratification profiles used for this analysis are modelled in an idealised manner using Eq. 3.19. However, ocean stratification is often more complex than this, as is clear from both CTD observations and AMM7 model output. To assess whether the idealised modelling results can describe plume behaviour in non-idealised stratification, oil-methane plumes were simulated with initial conditions of either the

representative CTD observations sub-sampled at AMM7 model output depths, or the equivalent AMM7 model output stratification (see Fig. 2.6 for vertical profiles of Θ, S_a and ρ_w). The release depth is between 200–1000 m, in 100 m increments. Oil spill characteristics are identical to those described in Section 3.4. Plume velocity as a function of depth can be viewed in Fig. 3.14a, and N^2 profiles of both stratification profiles can be viewed in Fig. 3.14b.

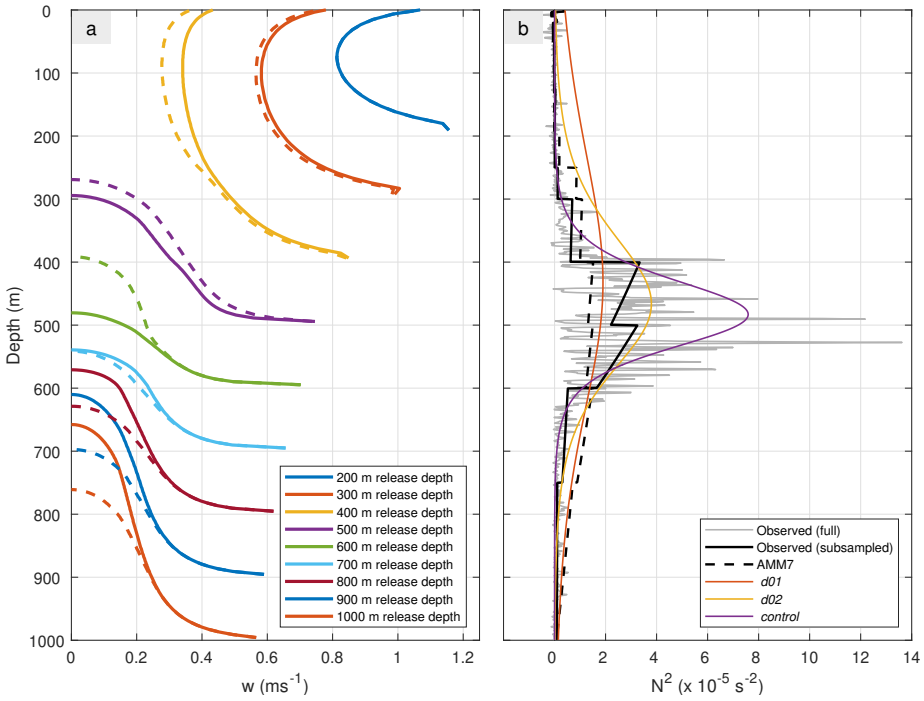

Figure 3.14: Oil-methane plume dynamics in profiles of observed stratification and AMM7 output stratification. (**a**) Vertical plume velocity profiles for releases at different depths in observed stratification (solid lines) and AMM7 output stratification (dashed lines). (**b**) Vertical N^2 profiles for AMM7 model output (dashed black line), observations sub-sampled to model depths (solid black line), raw observations (grey solid line), and idealised stratification profiles (*d01*, *d02* and the *control* profile; solid coloured lines).

Idealised stratification profile *d01* is most representative of AMM7 model output stratification, while profile *d02* is most representative of the sub-sampled CTD observations. Maximum N^2 in the full CTD observations (see the peaks in the grey solid line in Fig. 3.14b) is not represented by profile *d02*, and the *control* profile better represents this. Overall, the difference between profile *d01* and profile *d02* is the most analogous to the difference between AMM7 model output and CTD observations, because the *control* profile overestimates N^2 between 450–550 m depth.

For releases from 800 m or deeper, the sub-sampled CTD observations produce a

shallower TLPD than the AMM7 model output stratification. For releases from 500 m and 600 m the opposite is true. The plume surfaces in both stratification profiles when oil is released from 400 m or shallower. For a release from 1000 m, the TLPD is 746 m in profile *d01*, compared to 760 m in the AMM7 model output stratification. From the same release depth, the TLPD is 677 m in profile *d02*, compared to 658 m in the sub-sampled CTD observations. Therefore, the differences in plume behaviour between the two realistic profiles are approximated well by the differences in plume behaviour between profiles *d01* and *d02*.

Oil spill characteristics such as gas behaviour, release orifice diameter and release rate can vary from what has been modelled here. Whilst hydrate shedding has been switched on in the DeepBlow model in this analysis, observations suggest that gas hydrates do not necessarily form at depth (> 800 m; Johansen *et al.*, 2003). An oil spill from 1000 m depth in the representative sub-sampled CTD observations produces a TLPD at 658 m if hydrate formation is switched on, and 591 m if hydrate formation is switched off. The shallower TLPD occurs because gas bubbles have a lower density than gas hydrates. Additionally, Johansen (2000b) found that the TLPD decreased by order 50 m when hydrate formation was switched off. The release rate also influences the TLPD; doubling or halving the release rate of 106 $m^3 h^{-1}$ used in this analysis leads to TLPDs of 695 m and 622 m, respectively. The release orifice diameter has no substantial impact on the TLPD; a diameter of 0.05 m results in a TLDP of 660 m, and a diameter of 0.5 m results in a TLPD of 657 m.

4

PHYSICAL CONTROLS ON DEEP-SEA SPILLS II: CURRENTS

4.1 INTRODUCTION

The sensitivity of an oil plume to ocean stratification was investigated in Chapter 3, guided by the parameter space of the model-observation differences in Θ and S_a described by Chapter 2. Plume dynamics were sensitive to the strength of stratification and the type of release (oil-only or oil-methane). Plume dynamics, in addition to the far-field advection of oil and its eventual fate, may also be influenced by ocean currents. In the FSC, currents are comprised of large-scale water mass transport, smaller-scale mesoscale processes, and tides that are predominantly semidiurnal (Section 1.2). Earlier modelling of oil spills in the FSC suggests that the opposing flows of the near-surface Shetland slope current and FSC bottom current can lead to large differences in horizontal advection, depending on the depth the oil resides at (Main *et al.*, 2017).

In this chapter, both the DeepBlow and 3-D Fates components of OSCAR are used to investigate how barotropic (depth-uniform) and baroclinic (depth-varying) currents influence both near-field plume development and far-field oil advection. Three different stratification profiles are used from Chapter 3; a profile of zero N^2 (profile *a01*); a profile of uniform N^2 (profile *f01*); and a profile of non-linear N^2

(the *control* profile). The oil release characteristics are identical to the characteristics that are used in Chapter 3. Releases are simulated in the presence of time-constant barotropic currents of different magnitudes, and over a semidiurnal rectilinear barotropic tidal cycle with velocity amplitudes that are typically found within the FSC. The uniform N^2 and non-linear N^2 stratification profiles are also used to compute dynamic modes of horizontal velocity, which represent different baroclinic shear-flows.

The aim of this chapter is to provide a better understanding of how the individual components of currents representative of the FSC act to disperse and advect oil. This chapter expands on the previous work presented in Chapter 3 by investigating how far-field oil advection might be controlled by near-field plume dynamics. Section 4.2 describes the 3-D Fates component of OSCAR, and how the far-field distribution of oil is modelled. Sections 4.3 and 4.4 describe the stratification and current profiles used, respectively. Section 4.5 describes the release parameters and model set-up. Section 4.6 presents results for barotropic currents, and Section 4.7 presents results for baroclinic currents. Section 4.8 concludes the chapter by discussing the broader implications of this idealised modelling.

4.2 MODELLING FAR-FIELD OIL ADVECTION

In this chapter, both the DeepBlow (Section 3.2) and 3-D Fates models are used to show how oil is transported vertically and horizontally in the first 24 h after the beginning of a release from the seabed. The DeepBlow model essentially supplies a forcing input to the 3-D Fates model, where plume profiles provide initial conditions for the depth distribution and droplet size distribution of oil droplets. The 3-D fates model then predicts the advection and weathering of oil and gas over larger-scales of time and distance.

The 3-D Fates model solves the generalised transport equation

$$\frac{\delta C}{\delta t} + \vec{V} \cdot \vec{\nabla} C = \vec{\nabla} \cdot k_D \vec{\nabla} C + \sum_{j=1}^{n} R_j C, \tag{4.1}$$

where C is the concentration of each component of the oil (e.g. the components defined in Table A.1 for the Clair oil type), $\vec{V}$ is an advective transport vector, $\vec{\nabla}$ is a

gradient operator, k_D is the turbulent dispersion coefficient and R_j are process rates. Processes solved by Eq. 4.1 in the 3-D Fates model include:

- Surface and subsurface advection
- Dispersion
- Emulsification
- Vertical entrainment and re-surfacing
- Dissolution
- Evaporation
- Biodegradation
- Oil that reaches the coast (beaching)

These processes are all represented by R_j. Processes are described in Section 1.3 and defined mathematically in further detail by Reed *et al.* (1995). The 3-D Fates model can also simulation different clean-up operations.

The 3-D Fates model computes the distribution of oil using a particle tracking algorithm. A nearest-neighbour method is used to estimate the horizontal extension of mass around each particle. The 3-D Fates model domain includes a 2-D surface grid and 3-D subsurface grid. Oil can transition between grids through vertical plume entrainment, vertical advection of buoyant oil droplets, or dissolution.

Currents act to horizontally displace oil in both the DeepBlow and 3-D Fates models, and are a dominant advection process in the far-field alongside the buoyancy-driven vertical rise of individual oil droplets. The horizontal advection of oil in the surface grid is calculated as the current velocity plus 3.6% of the surface wind velocity (Reed *et al.*, 1995). The horizontal advection of oil in the subsurface grid is calculated as the current velocity only (although currents may be partially wind-driven in the Ekman layer of the hydrodynamic forcing). In this analysis, in addition to in Chapters 5 and 6, direct wind forcing is not used.

4.3 STRATIFICATION PROFILES

To provide consistency between Chapter 3 and Chapter 4, three idealised stratification profiles used in Chapter 3 have been chosen for this analysis; profile *a01*, profile *f01*, and the *control* profile (Table 3.1). The vertical T and N^2 structures of these profiles are shown in Fig. 4.1.

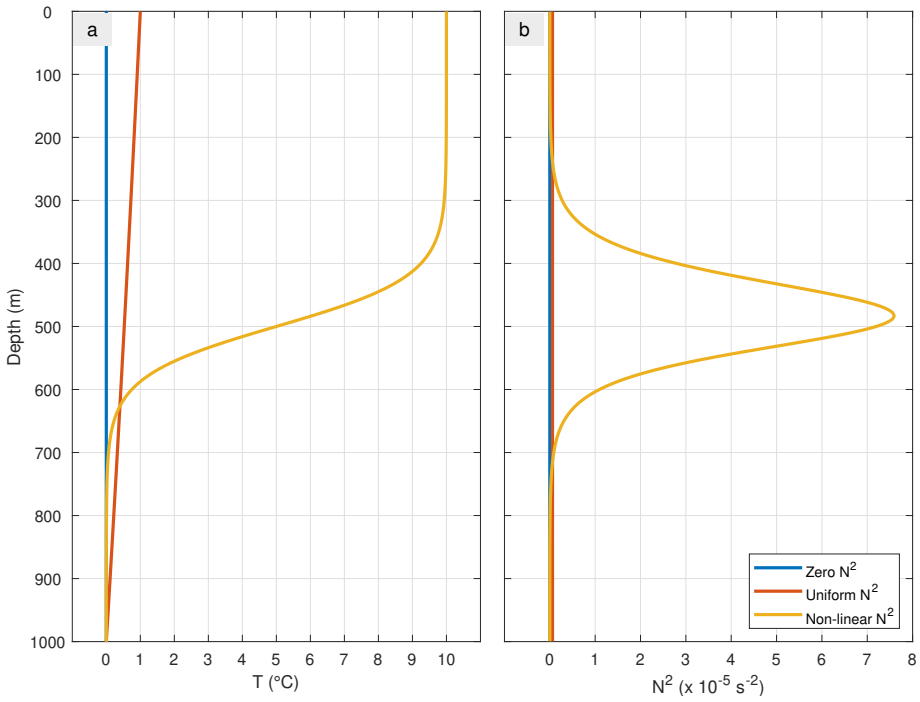

Figure 4.1: Vertical profiles of T and N^2 for zero N^2, uniform N^2 and non-linear N^2. (**a**) In-situ temperature for each profile. (**b**) As (a) but for N^2.

All three stratification profiles have depth-uniform $S_p = 35$. Profile *a01* is a water-column with depth-uniform $T = 0$ °C (Eq. 4.2). This profile was chosen because $N^2 = 0$ everywhere[1], and the influence of currents can therefore be isolated from the influence of a density gradient. This profile is hereafter referred to as the 'zero N^2' profile, and the vertical T structure can be expressed mathematically as

$$T = 0. \tag{4.2}$$

[1]The method used by the DeepBlow model to compute N^2 (SM 2520C; Section 3.2.1) ignores the effects of a changing potential temperature.

Profile *f01* is a water-column with depth-uniform N^2, and boundary conditions of 0 °C at 1000 m and 1 °C at 0 m . The weakest profile of depth-uniform N^2 used in Chapter 3 has been chosen because it causes plume trapping in the absence of currents, whilst showing a larger plume height compared to profiles *f02-f05*. A profile of depth-uniform dT/dz will produce comparable results to a profile of depth-uniform N^2 (Section 3.7). This profile is hereafter referred to as the 'uniform N^2' profile.

The *control* profile is more representative of ocean stratification within the FSC. The *control* profile has a lower N^2 than the uniform N^2 profile from 0–250 m and from 700–1000 m, but a much higher N^2 from 240–720 m (Fig. 4.1b). This profile is hereafter referred to as the 'non-linear N^2' profile, and the vertical T structure can be expressed mathematically as

$$T(z) = 5 + 5\tanh\left(2\pi\left(1 + \frac{z}{500}\right)\right). \tag{4.3}$$

These stratification profiles are used as initial conditions in the DeepBlow model, in combination with various idealised barotropic and baroclinic currents. These currents are described in Sections 4.4.1 and 4.4.2.

4.4 CURRENT PROFILES

4.4.1 BAROTROPIC CURRENTS

The most basic example of current forcing is barotropic, where the current direction and magnitude is uniform with depth. Oil spills are modelled using constant barotropic currents of different magnitudes (residual currents), and over semidiurnal rectilinear tidal cycles with velocity amplitudes typically found within the FSC. Time-variable currents are not used in this chapter because only time-constant currents can be used as a forcing input to the DeepBlow model. Time-variable currents are used as a forcing input to the 3-D Fates model in Chapters 5 and 6.

RESIDUAL CURRENTS

To isolate the effect of changing the current magnitude on the behaviour of a plume, oil spills are modelled alongside barotropic currents with magnitudes of 0–1.5 $\mathrm{m\,s^{-1}}$

($0.01\,m\,s^{-1}$ increments from 0–$0.2\,m\,s^{-1}$, and $0.1\,m\,s^{-1}$ increments from 0.2–$1.5\,m\,s^{-1}$). The current direction is northward for all releases, and each simulation is repeated for profiles of zero N^2, uniform N^2 and non-linear N^2, and with or without methane.

RECTILINEAR SEMIDIURNAL TIDAL CYCLES

The variability of oil advection over a semidiurnal tidal cycle will also be tested in this analysis, in the context of tidal velocity amplitudes typically expected within the FSC. Hall (2008) showed from a repeat station on the west Shetland slope at 680 m depth that barotropic tidal velocity amplitude is approximately $0.12\,m\,s^{-1}$. However, the short time-series (approximately 24 h) results in some uncertainty as to whether the tide was observed during the spring phase or neap phase of the spring-neap cycle. Barotropic M_2 tidal velocity amplitude in the central FSC (4°W, 61°N) is approximately $0.15\,m\,s^{-1}$ if extracted from the TPXO European Shelf tidal solution (Egbert & Erofeeva, 2000). On the other hand, several observations suggest that the semidiurnal tidal velocity amplitude will be larger than $0.15\,m\,s^{-1}$. Several studies suggest that an M_2 tidal amplitude of $0.3\,m\,s^{-1}$ is typical in the FSC (Gould, 1984; Mauritzen *et al.*, 2005), by analysing historical current meter data. Other tidal components may also substantially increase the overall tidal velocity amplitude; Gould (1984) suggests that the S_2 and N_2 tides have amplitudes of $0.1\,m\,s^{-1}$ and $0.05\,m\,s^{-1}$, respectively. This disparity in the literature may be due to differences in the spring-neap phase, or because of spatial variability.

As a result of the conflicting literature, two different semidiurnal (12 h) rectilinear (north-south) tidal cycles with velocity amplitudes of $0.15\,m\,s^{-1}$ and $0.3\,m\,s^{-1}$ will be used as forcing inputs to the DeepBlow and 3-D Fates models. Barotropic velocities are calculated over the tidal cycle in regular intervals of 30 min from 0–3 h after the beginning of the cycle. Since the tide is symmetric and rectilinear, barotropic velocities at 3–6 h will be a time-reversal of the velocities at 0–3 h. Subsequent 6 h time periods will be identical in structure and magnitude to one another, but either northward or southward. Therefore, simulations in the first 3 h can be extrapolated to supply all the information for the entire 12 h cycle. Each simulation is repeated for profiles of zero N^2, uniform N^2 and non-linear N^2, and with or without methane.

4.4.2 BAROCLINIC CURRENTS

Currents in the FSC also have a baroclinic component, where a shear-flow exists and there is a resultant change in current magnitude or direction with depth. Current shear in the FSC is typically associated with the stratification structure, for example when considering the opposing flows of the shelf slope current and FSC bottom current (Section 1.2.1). For this analysis, the three stratification profiles outlined in Section 4.3 are used to guide the choice of baroclinic currents by using dynamic modes of horizontal velocity. Internal wave variability is not investigated here; dynamic modes are only used to represent a shear-flow with different numbers of vertical layers.

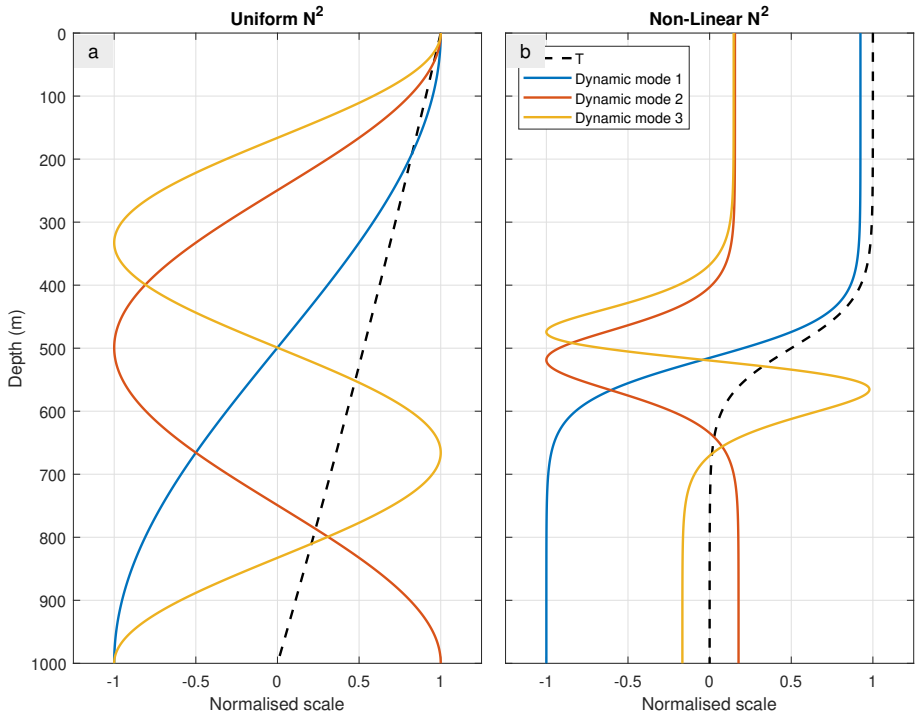

Figure 4.2: Vertical profiles of T and current velocity for different baroclinic dynamic modes. (**a**) Dynamic modes 1, 2 and 3 computed from the profile of uniform N^2 (solid coloured lines), and the temperature profile (black dashed line). The scale is normalised between -1 and 1. (**b**) As (a) but from the profile of non-linear N^2.

In order to compute the dynamic modes of the water-column with a pre-defined stratification structure, the Matlab function *dynmodes.m* (Klinck, 1999) is used. *dynmodes.m* computes vertical modes of horizontal velocity and vertical displacement from input N^2 and pressure p, assuming a frictionless bottom boundary and zero vertical displacement at the seabed and surface. Output modes

are normalised between −1 and 1, with mean integral horizontal velocity set to zero. The velocity structure is then scaled to have maximum velocity amplitudes of $0.02\,\mathrm{m\,s^{-1}}$, $0.05\,\mathrm{m\,s^{-1}}$, $0.1\,\mathrm{m\,s^{-1}}$, $0.15\,\mathrm{m\,s^{-1}}$, $0.2\,\mathrm{m\,s^{-1}}$ and $0.3\,\mathrm{m\,s^{-1}}$. These values are chosen in order to represent the full parameter space over the largest rectilinear tide described in Section 4.4.1. The first three modes were computed for profiles of uniform N^2 (Fig. 4.2a) and non-linear N^2 (Fig. 4.2b). For a dynamic mode to exist $N^2 > 0$, and so the analysis was not repeated for the profile of zero N^2. Oil spills were simulated both with and without the presence of methane.

4.5 MODEL SET-UP

For all simulations, the release depth is 1000 m. Each case study (different initial conditions of stratification and/or a different current forcing) was simulated with oil-only, and with methane released alongside oil. The GOR is 200, as in Chapter 3. Other DeepBlow model parameters are identical to those used in Chapter 3 (for full details, refer to Section 3.4 and Table 3.2), which are based on the 2016 Clair oil spill (Section 1.1.3). This isolates the influence of ocean conditions on the behaviour of an oil plume, so direct comparisons can be made between Chapters 3 and 4.

For most of the DeepBlow simulations performed in this analysis, a proportion of oil escapes from the plume due to horizontal plume advection and subsequent plume bending. Plume bending is defined as a plume with a trajectory that is not entirely vertical. In some simulations, current velocities are large enough for most, and occasionally all, of the oil to escape the plume. Because of this behaviour, 'termination depth' is defined in this chapter as the deepest depth in which at least one of the following criteria are first met:

1. The vertical plume velocity reaches zero (the TLPD, as in Chapter 3).

2. More than 95% of oil has escaped the plume.

One limitation of the DeepBlow model is the inability to include time-varying currents as forcing input for an individual plume simulation. If time-varying currents are used as a forcing input to the DeepBlow model, a separate plume profile per time-step of the input currents will be outputted. For each of these profiles, the current structure stays constant in time for the duration of the plume. This is not a substantial

Table 4.1: Notable 3-D Fates model parameters.

Name	Value
3-D Fates time-step	1 min
3-D Fates output interval	5 min
3-D Fates model duration	24 h
Release depth	1000 m
Release amount	106 m^3
Release duration	1 h
Oil Type	Clair (Table A.1)
Currents	Variable
Wind	None
Air temperature	10 °C
Liquid/solid particles	5000
Dissolved particles	5000
Gas particles	5000
Zonal grid resolution	1 km
Meridional grid resolution	100 m
Vertical grid resolution	25 m
Grid dimensions	4 × 60 × 1 km

limitation to the study, since the rate of change of the plume dynamics is faster than the rate of change of the hydrodynamics.

Notable 3-D Fates model parameters used in this analysis are summarised in Table 4.1. To investigate the sensitivity of oil advection to the barotropic tidal cycle, and to baroclinic dynamic modes, the 3-D Fates model was run for 24 h with a 1 min time-step and 5 min output interval. 5000 methane particles, 5000 liquid/solid particles and 5000 dissolved particles are used to represent oil distribution in the surface and subsurface grids. This is five times more than what has been used in Chapter 3, because oil advection will be caused by meridional current velocities. The number of particles is still less than the order 10^4 typically used for regional spill simulations, but our simulations are shorter (24 h, compared to weeks or months). Additionally, zonal current velocities are zero, thereby limiting the advection and dispersion of oil.

The domain extends to 2 km east/west and 30 km north/south of the release location. Assuming a maximum current speed of 0.3 $m\,s^{-1}$, the maximum possible oil advection away from the release location is 25.92 km north/south, and 0 km

east/west. The 3-D Fates model horizontal grid resolution is 1 km (zonal) and 100 m (meridional). The zonal and meridional resolutions are identical for both the surface and subsurface grids. A coarser zonal resolution is used, since no zonal advection is expected to take place in any of the simulations and variability does not need to be resolved in this dimension. The vertical resolution of the subsurface grid is 25 m.

4.5.1 INCLUSION OF CURRENTS AND STRATIFICATION

Stratification is incorporated into the DeepBlow model using SM 2520C and the methods described in Section 3.4.1. Current input takes the form of NetCDF files, and currents are interpolated using a nearest-neighbour method from the input NetCDF grid to the surface and subsurface 3-D Fates model grids.

4.6 RESULTS - BAROTROPIC CURRENTS

Section 4.6.1 describes the influence of plume bending on the proportion of oil that can escape a plume. Sections 4.6.2 and 4.6.3 discuss the influence of barotropic currents on the behaviour of an oil plume and the subsequent far-field advection.

4.6.1 PLUME BENDING

To visualise how oil escapes from the plume in the DeepBlow model to the subsurface grid in the 3-D Fates model, two more simulations were performed. For these simulations, a residual current of 0.1 $m\,s^{-1}$ is used as a forcing input, and the profile of zero N^2 is used as an initial condition for the DeepBlow model. The model is run once for an oil-only release, and a second time for an oil-methane release. Compared to other simulations performed in this analysis, a finer zonal resolution (250 m, compared to 1 km) and finer meridional resolution (25 m, compared to 100 m) is used, to capture the far-field distribution of oil in more detail.

'Plume bending' is defined as a plume with a trajectory that is not entirely vertical, and occurs in the presence of a horizontal current. The largest, most buoyant oil droplets can escape the plume if enough plume bending occurs and w is negligible compared to the horizontal advection. For the oil-only release, > 95% of oil escapes

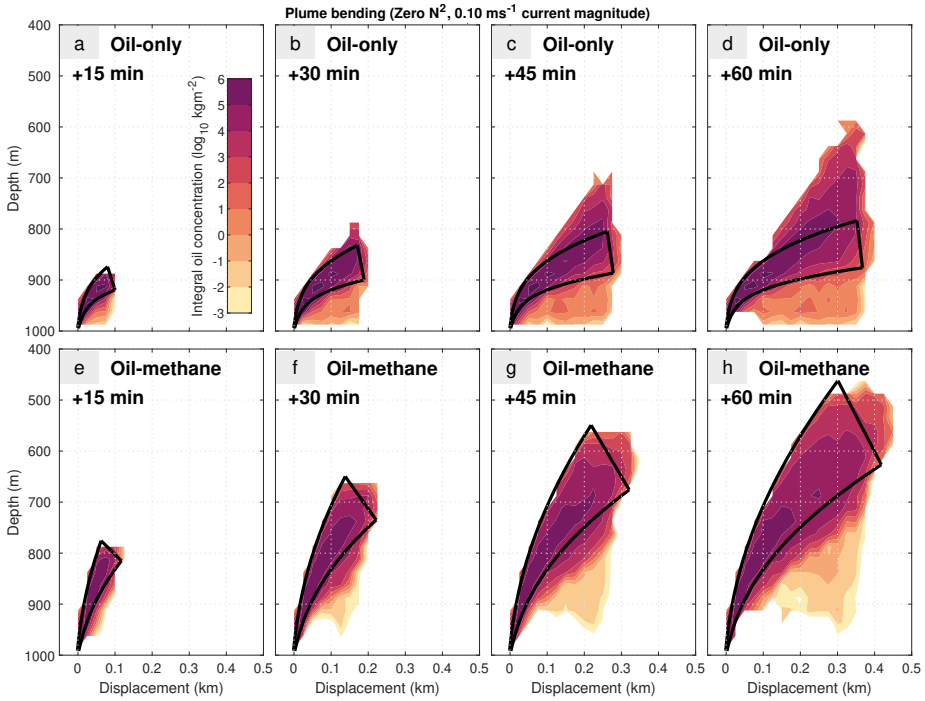

Figure 4.3: Plume development for an oil-only plume and oil-methane plume in zero N^2 with a residual current of magnitude 0.10 m s^{-1}. (**a**) An oil-only plume 15 min after the beginning of the release. Contours show the log zonal integral of oil concentration. Also shown is the plume profile at the same point in time (solid black line). (**b**) As (a) but 30 min after the beginning of the release. (**c**) As (a) but 45 min after the beginning of the release. (**d**) As (a) but 60 min after the beginning of the release. (**e-h**) As (a-d) but for an oil-methane plume.

the plume in this manner 15 min after the beginning of the release (Fig. 4.3a)[2]. A significant amount of oil has advected to depths order 100 m shallower than the plume profile after 60 min (Fig. 4.3d).

For the equivalent oil-methane release, oil is not advected to depths shallower than the plume profile. 45% of oil has escaped the plume after 15 min (Fig. 4.3e) , and 80% of oil has escaped the plume after 60 min (Fig. 4.3h). The lower proportion of escaped oil for the oil-methane release is partly a result of a smaller droplet-size distribution compared to the oil-only release (Fig. 3.12), and therefore a reduction in average droplet buoyancy. Additionally, w is higher for the oil-methane release, and so for any given horizontal current magnitude less plume bending will occur compared to an equivalent oil-only release. It is also clear that oil can ascend more rapidly within a plume compared to as individual droplets (e.g. by comparing the shallowest depths oil exists at in Fig. 4.3d and Fig. 4.3h).

[2]Although a plume profile is still outputted by the DeepBlow model after 15 min, the plume is considered terminated by the definition used in this chapter.

4.6.2 RESIDUAL CURRENTS

A higher barotropic current velocity typically leads to a deeper termination depth. This is the case for all releases (both oil-only and oil-methane; Fig. 4.4 and 4.5), with an exception from 0–0.06 m s^{-1} for an oil-methane release in the non-linear N^2 profile (Fig. 4.5a). Here, a higher current speed leads to a shallower termination depth. However, this variability is order 1 m and does not bear any physical significance.

For both oil-only releases and oil-methane releases, plumes have shallower termination depths in the zero N^2 profile compared to in the uniform N^2 profile or non-linear N^2 profile. This suggests that currents and stratification independently influence plume behaviour. Below 710 m depth, termination depths for plumes released in both the non-linear N^2 and zero N^2 profiles are numerically identical. This is because the interpolated non-linear N^2 profile has a constant temperature of 0 °C at 710–1000 m, and Eq. 4.2 therefore describes the non-linear N^2 profile in this depth range. There is a deeper plume termination depth for a release in uniform N^2 compared to a release in non-linear N^2 for most current velocities. However, at low current velocities the opposite is true, and there is a shallower plume termination depth in uniform N^2. This trend reversal occurs at approximately 625 m for both the oil-only and oil-methane releases. This depth is also where the temperature of the non-linear N^2 profile becomes greater than the temperature of the uniform N^2 profile (Fig. 4.1).

When methane is released alongside oil, w is higher because methane hydrates contribute to a decrease in plume density ρ_p, and thus an increase in plume buoyancy. This leads to less plume bending (a plume profile closer to vertical), and subsequently a lower proportion of oil escaping for any given current speed (compare the proportions of escaped oil in Fig. 4.4 with the proportions of escaped oil in Fig. 4.5). For an oil-only release, > 95% of oil escapes the plume in the presence of just a few cm s^{-1} of current forcing (0.02–0.03 m s^{-1} for zero N^2, 0.03–0.04 m s^{-1} for uniform N^2, and 0.04–0.05 m s^{-1} for non-linear N^2). As a result of this, the relationship between plume termination depth and current velocity becomes dependant entirely on the rate of oil escaping the plume; a higher current velocity leads to increased plume bending (a plume profile closer to horizontal), a more rapid rate of escape, and therefore less time taken to reach the 95% threshold and a deeper termination depth.

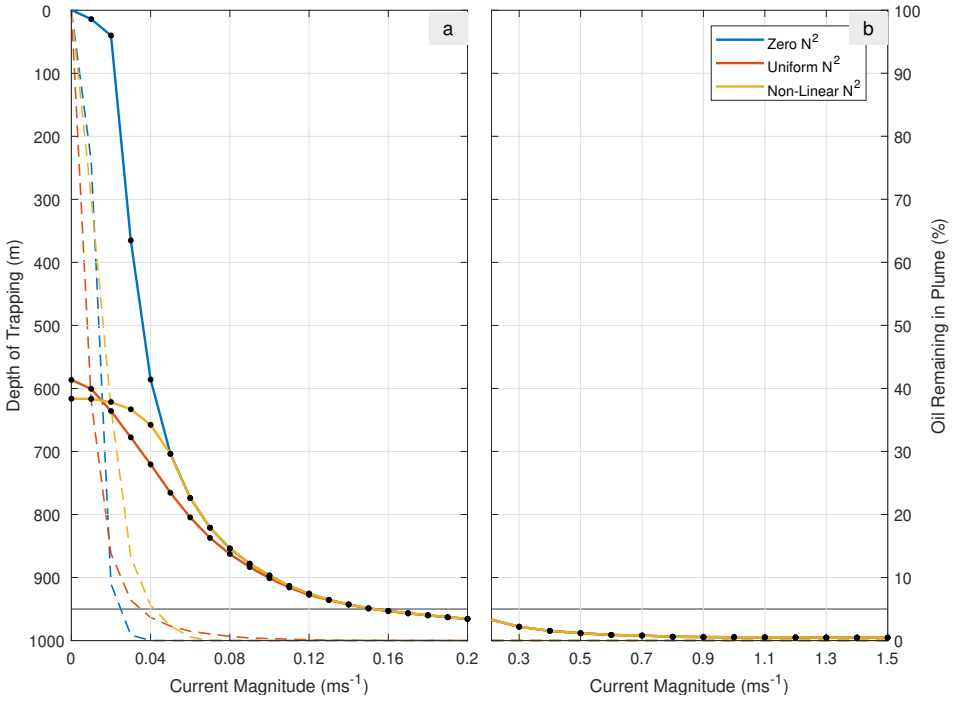

Figure 4.4: Oil-only plume termination heights for barotropic currents. (**a**) Termination depth as a function of barotropic velocity (0–0.2 m s^{-1}) for profiles of zero N^2, uniform N^2 and non-linear N^2 (coloured solid lines). Also shown are the percentages of oil remaining in the plumes for the last time-step of the DeepBlow simulation (coloured dashed lines) and the percentage threshold where > 95% of oil has escaped the plume (grey solid line). (**b**) As (a) but for 0.2–1.5 m s^{-1}.

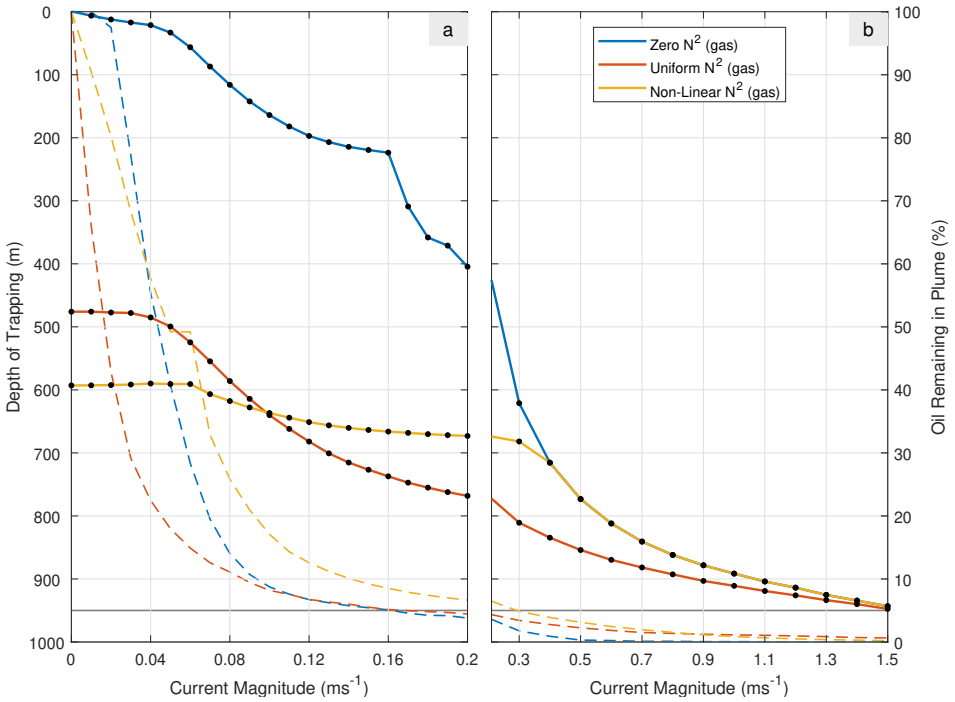

Figure 4.5: As Fig. 4.4 but for oil-methane releases.

This threshold is reached at considerably higher current velocities for the oil-methane releases (0.16–0.17 m s^{-1} for zero N^2 and uniform N^2, 0.2–0.3 m s^{-1} for non-linear N^2).

4.6.3 RECTILINEAR SEMIDIURNAL TIDAL CYCLE

Over the barotropic tidal cycle, it is clear from Section 4.6.2 that several parameters influence the plume termination depth. Firstly, a higher current velocity leads to a deeper plume termination depth. This is shown in Section 4.6.2 but is also reflected by the variability of currents over the semidiurnal rectilinear tidal cycle (Fig. 4.6c, d and C.1c, d; Table 4.2). Secondly, the inclusion of methane alongside oil results in a shallower plume termination depth, because of a decrease in ρ_p. This is true for all ocean states used for this analysis. Stratification acts as a third independent control on plume termination depth. Density gradients from either the uniform N^2 or non-linear N^2 stratification profiles lead to a deeper or equal plume termination depth compared to the profile of zero N^2.

These three independent controls on subsurface plume development result in a highly variable termination depth over the tidal cycle. At the extreme, in the profile of zero N^2 an oil-only plume surfaces when there are no currents, but is terminated 51 m above the release depth in the presence of a 0.15 m s^{-1} current (Fig. 4.6c), and 22 m above the release depth in the presence of a 0.30 m s^{-1} current (Fig. C.1c). This difference contributes to a standard deviation of > 300 m (Table 4.2).

The plume termination depth is less variable in the presence of a density gradient. Where $N^2 > 0$ (profiles of uniform N^2 and non-linear N^2), plume buoyancy is inhibited by the entrainment and subsequent vertical advection of dense water into less dense water, which increases ρ_p. This provides a limit on how far the plume can rise, regardless of how weak the currents are. In the profile of zero N^2 and in the absence of currents, the limit on how far the plume can rise is determined exclusively by the vertical distance to the sea surface.

Plume termination depth is also less variable when methane is released alongside oil, and shallower than an equivalent oil-only release on average by 200 m when $N^2 > 0$ and 600 m when $N^2 = 0$. A probable reason for the reduced variability is that for oil-methane releases, the rate of oil escaping the plume is much lower compared to equivalent oil-only releases. For current speeds of 0.16 m s^{-1} or less, all of the

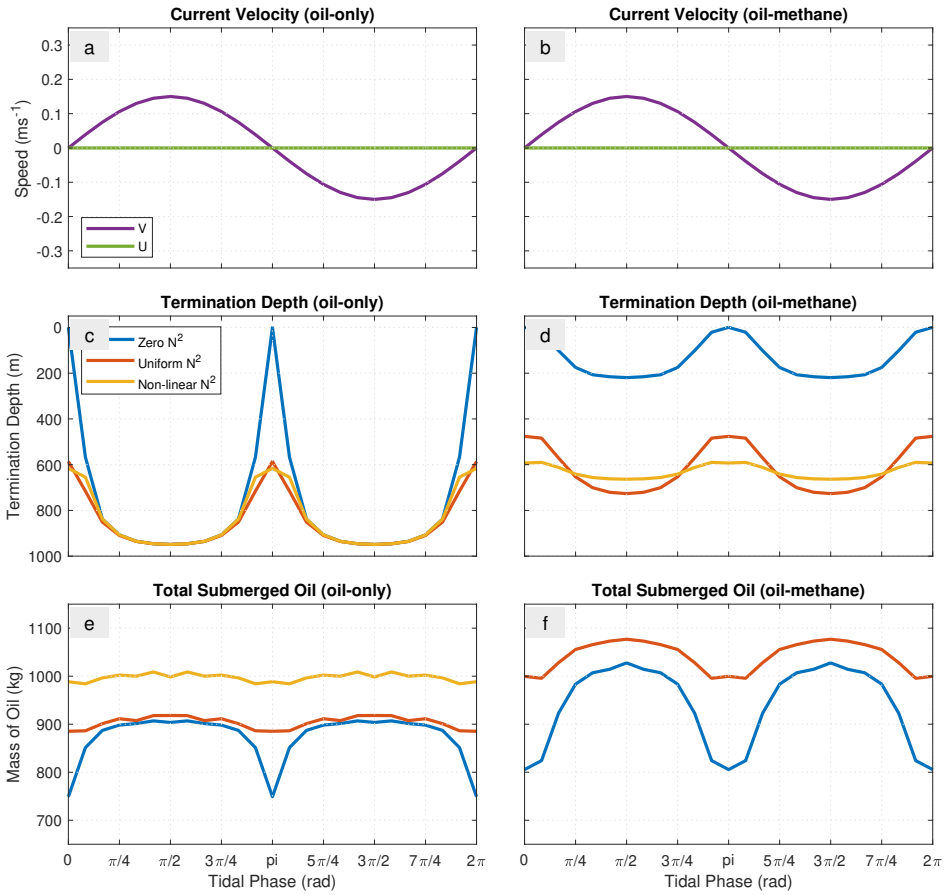

Figure 4.6: Variability of an oil spill over a semidiurnal tidal cycle of 0.15 m s^{-1} velocity amplitude. (**a**) U (zonal) and V (meridional) components of the current from 0–2π rad for oil-only releases. (**b**) As (a) but for oil-methane releases. (**c**) Plume termination depths for oil-only releases in profiles of zero N^2, uniform N^2 and non-linear N^2 (coloured solid lines). (**d**) As (c) but for oil-methane releases. (**e, f**) As (c, d) but for the total submerged oil mass after 24 h.

simulated plumes retain at least 5% of the initial oil volume (Fig. 4.5a). Therefore, plume termination depths for oil-methane releases when forced by the 0.15 m s^{-1} velocity amplitude tide are always defined as the depth where $w = 0$ (the TLPD). For the profile of non-linear N^2, plume termination depth must be shallower than 710 m, because no density gradient exists deeper than this in the interpolated input profile. It must also be deeper than ≈600 m, where the vertical plume velocity reaches zero in the absence of currents (Fig. 4.5a).

The amount of oil that remains below the surface after 24 h is sensitive to the current velocity, the inclusion of methane, and the plume termination depth, which is in itself sensitive to the former two parameters. The stratification structure does not

Table 4.2: Minimum, maximum, mean, and standard deviation over the semidiurnal tidal cycle for plume termination depth and the proportion of subsurface oil after 24 h. Shown are values from both oil-only and oil-methane releases for profiles of zero N^2, uniform N^2 and non-linear N^2. Values are for tidal velocity amplitudes of [0.15 (**0.3**)] $\mathrm{m\,s^{-1}}$.

Termination Depth (m)	min	max	mean	std.
Zero N^2				
oil-only	0 (**0**)	949 (**978**)	747 (**832**)	311 (**317**)
oil-methane	0 (**0**)	219 (**621**)	133 (**358**)	76 (**231**)
Uniform N^2				
oil-only	586 (**586**)	949 (**978**)	844 (**905**)	126 (**127**)
oil-methane	476 (**476**)	727 (**811**)	616 (**712**)	99 (**119**)
Non-linear N^2				
oil-only	616 (**616**)	949 (**978**)	835 (**906**)	131 (**119**)
oil-methane	590 (**593**)	664 (**682**)	630 (**656**)	30 (**11**)
Submerged Oil (%)	min	max	mean	std.
Zero N^2				
oil-only	6.68 (**6.68**)	8.60 (**8.85**)	8.11 (**8.22**)	0.62 (**0.61**)
oil-methane	7.08 (**7.10**)	9.17 (**9.49**)	8.17 (**8.76**)	0.69 (**0.75**)
Uniform N^2				
oil-only	7.95 (**8.24**)	8.43 (**8.68**)	8.28 (**8.48**)	0.16 (**0.15**)
oil-methane	9.26 (**9.45**)	10.60 (**11.12**)	9.97 (**10.54**)	0.51 (**0.57**)
Non-linear N^2				
oil-only	7.94 (**7.68**)	8.57 (**8.79**)	8.25 (**8.46**)	0.21 (**0.36**)
oil-methane	9.39 (**9.72**)	10.39 (**10.72**)	9.97 (**10.28**)	0.36 (**0.32**)

directly influence the advection of oil in the far-field, because individual oil droplets retain a constant density in the 3-D Fates model. For all simulations, only a small proportion of the total oil volume (6–11%) does not surface.

Current velocity determines the depth oil droplets escape from the plume, and this is likely the associated mechanism that causes the variability in the volume of submerged oil. A higher current velocity results in oil escaping from the plume at an earlier stage, and therefore at a greater depth. The vertical transport of escaped oil is exclusively controlled by the droplet size and buoyancy of individual droplets, and not from the buoyancy and vertical momentum of the plume itself. An oil droplet of specified diameter D will therefore take longer to reach the surface if it escapes at a

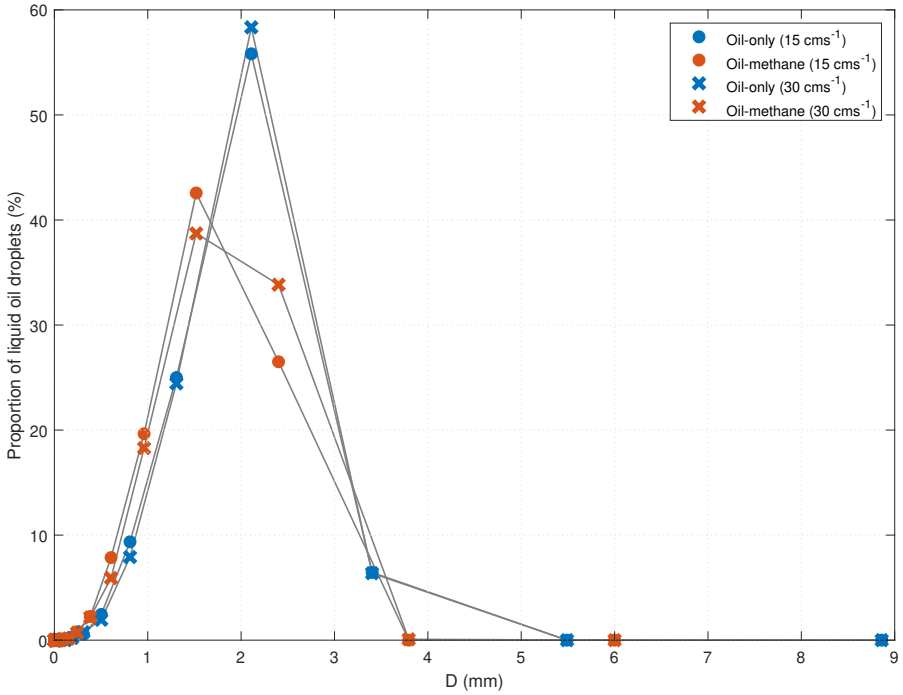

Figure 4.7: Droplet size distribution of subsurface liquid oil droplets in $0.15\,\mathrm{m\,s^{-1}}$ and $0.3\,\mathrm{m\,s^{-1}}$ barotropic currents. Shown are both the oil-only (blue) and oil-methane (red) releases for a $0.15\,\mathrm{m\,s^{-1}}$ current (dots) and a $0.3\,\mathrm{m\,s^{-1}}$ currents (crosses).

greater depth. Droplet size does not influence the vertical velocity of oil within the plume (Yapa *et al.*, 2012). A longer residence time of a droplet below the surface also allows more time for processes such as dissolution and biodegradation to occur. The droplet size distribution is not as sensitive to the current speed compared to whether methane is released alongside oil (Fig. 4.7).

The inclusion of methane leads to considerable (> 5%) increases in the amount of submerged oil (Table 4.2). This is despite a shallower plume termination depth and is instead due to a smaller droplet size distribution compared to an oil-only release (Fig. 4.7). The smaller droplet sizes are due to a higher initial vertical velocity at the well head ($6.4\,\mathrm{m\,s^{-1}}$ for an oil-methane release, compared to $3.7\,\mathrm{m\,s^{-1}}$ for an oil-only release), leading to the increased turbulent breakup and mechanical dispersion of liquid oil.

4.6.4 KEY POINTS

1. A deeper plume termination depth can be caused by higher current velocities, the presence of a density gradient, or the presence of methane hydrates within the plume.

2. Oil can escape the plume if plume bending occurs. For oil-only releases, > 95% of oil escapes when just a few $cm\,s^{-1}$ of current forcing is present ($\leq 0.05\,m\,s^{-1}$). For oil-methane releases, this increases to $\geq 0.16\,m\,s^{-1}$.

3. The amount of oil remaining below the surface can be determined by the current velocity, the plume termination depth, or the presence of methane. These parameters influence the depth of escaped oil and the droplet size distribution, which directly control the proportion of oil that surfaces over time and the rates of dissolution and biodegradation.

4.7 RESULTS - BAROCLINIC CURRENTS

The simplest case of a baroclinic flow is a two-layer shear-flow. This type of flow is represented by the first dynamic mode of either the uniform N^2 or non-linear N^2 stratification profiles (Fig. 4.2). It is important to clarify here that dynamic modes are being used in this chapter to represent multi-layer shear-flows, and not to show internal tide or internal wave variability. A current velocity of $0.15\,m\,s^{-1}$ is used for the basis of the presentation of the results.

For dynamic mode 1, Fig. 4.8, 4.9, 4.10 and 4.11 all show that subsurface far-field oil transport separates into two distinct vertical pathways of integral concentration. It is important to emphasise here is that oil is only released during the first hour of the simulation, and oil that can be seen near the seabed in these figures is trapped and not newly-released. Most oil is transported to the surface, and the trajectories are shown by the pathways with relatively high integral concentrations that are displaced less by ocean currents (i.e. remain closer to the horizontal position of the release). Output from OSCAR does not include location-specific droplet size distributions. However, these more rapidly ascending integral concentration pathways almost certainly consist of larger and undissolved oil droplets.

This argument is further supported by how the droplet size and volume

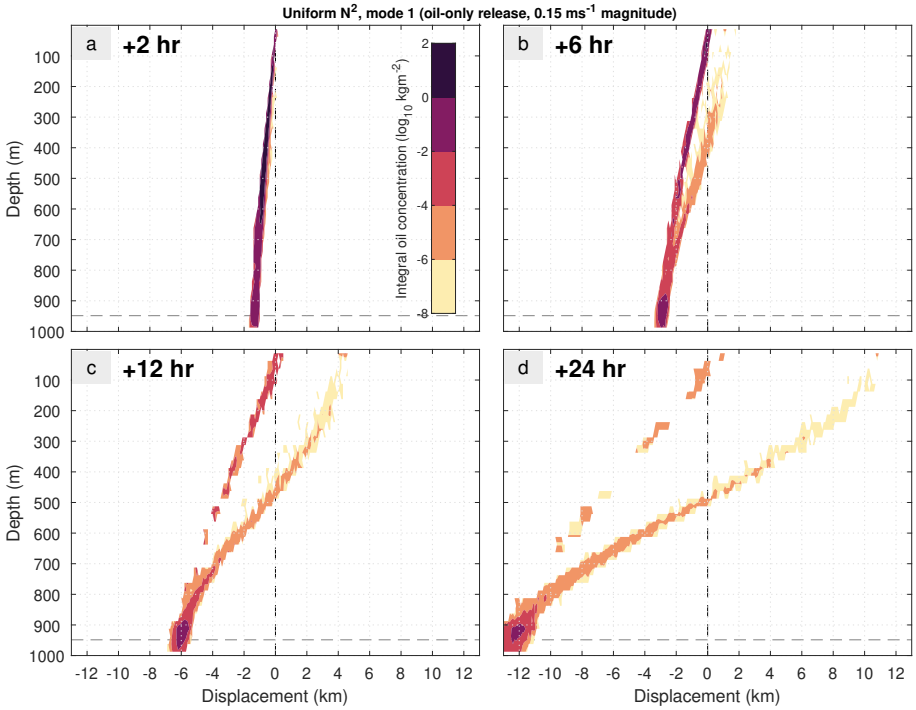

Figure 4.8: Oil-only plume development for a plume in uniform N^2 and dynamic mode 1 with a maximum amplitude of $0.15\,\mathrm{m\,s^{-1}}$. (**a**) Cross-section of oil distribution 2 h after the beginning of the release. Coloured contours show the log zonal integral of oil concentration. Also shown are the release location (black dashed line) and plume termination depth (grey dashed line). (**b**) As (a) but 6 h after the beginning of the release. (**c**) As (a) but 12 h after the beginning of the release. (**d**) As (a) but 24 h after the beginning of the release.

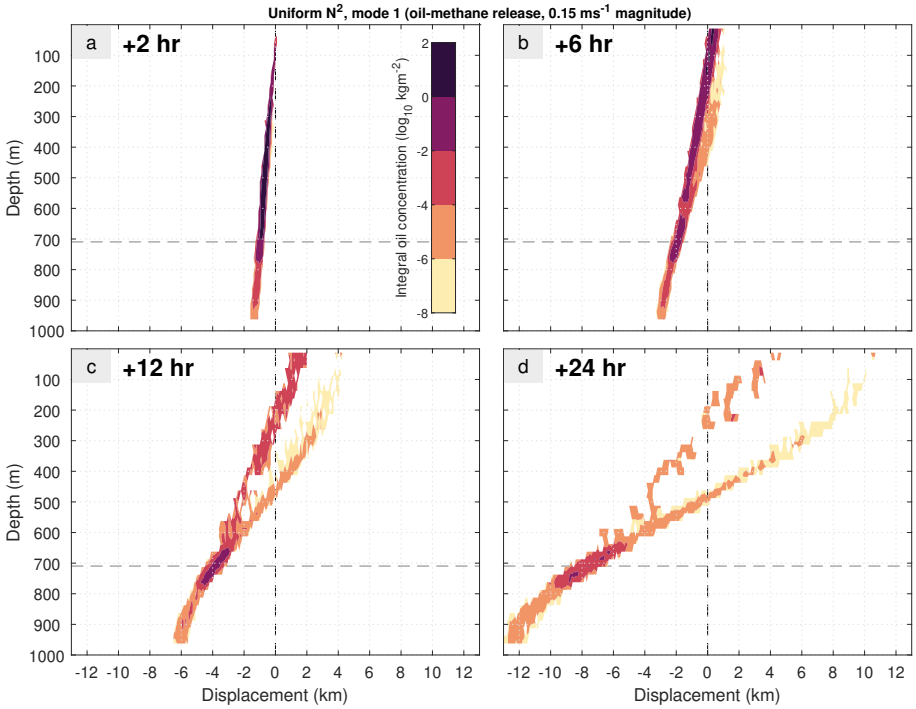

Figure 4.9: As Fig. 4.8 but for an oil-methane release.

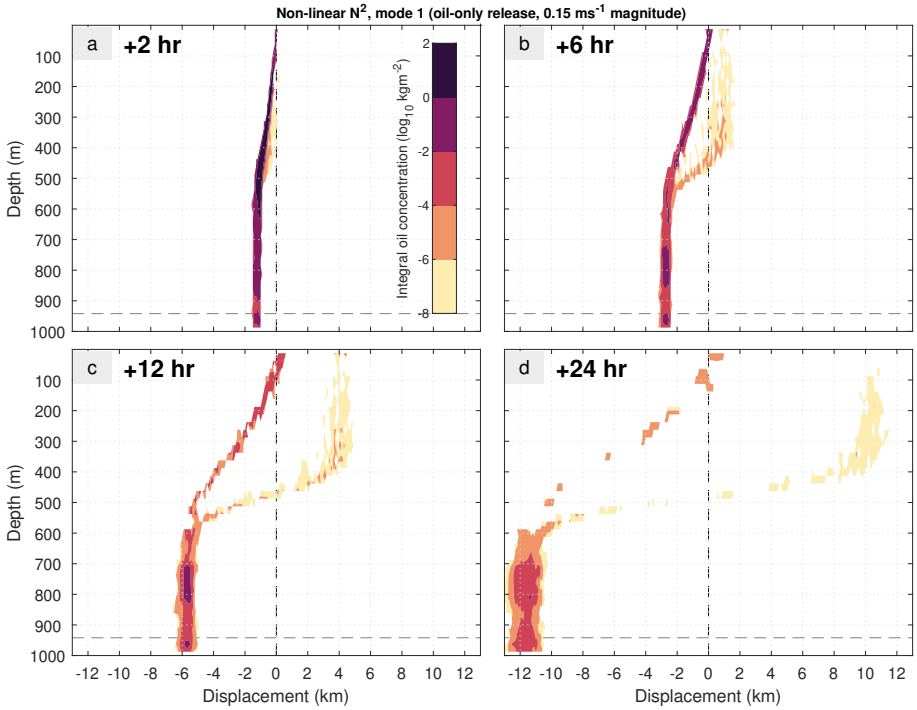

Figure 4.10: Oil-only plume development for a plume in non-linear N^2 and dynamic mode 1 with a maximum amplitude of $0.15\,\mathrm{m\,s^{-1}}$. (**a**) Cross-section of oil distribution 2 h after the beginning of the release. Coloured contours show the log zonal integral of oil concentration. Also shown are the release location (black dashed line) and plume termination depth (grey dashed line). (**b**) As (a) but 6 h after the beginning of the release. (**c**) As (a) but 12 h after the beginning of the release. (**d**) As (a) but 24 h after the beginning of the release.

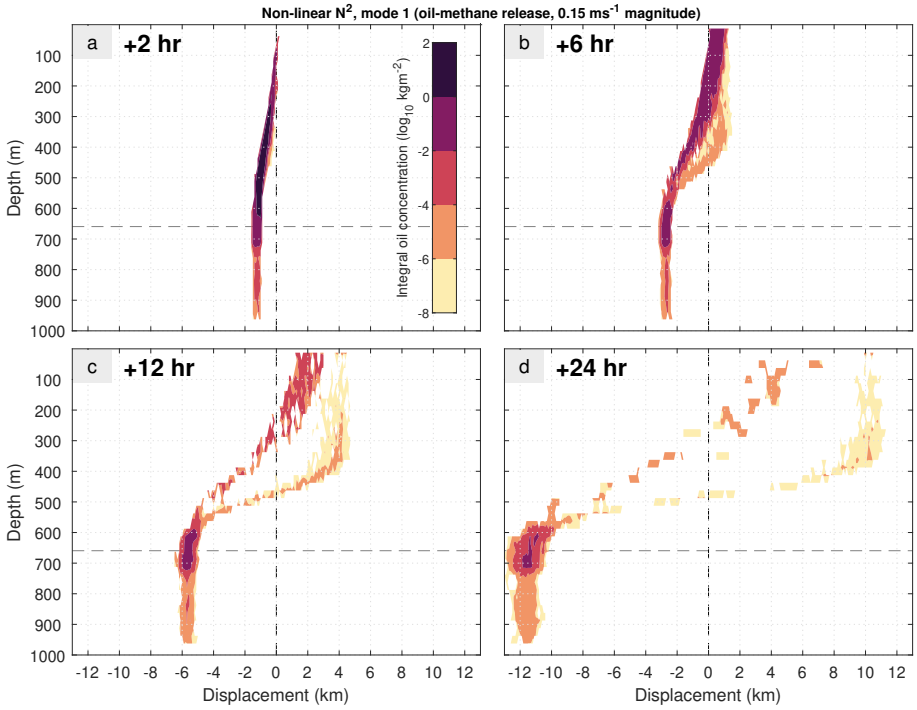

Figure 4.11: As Fig. 4.10 but for an oil-methane release.

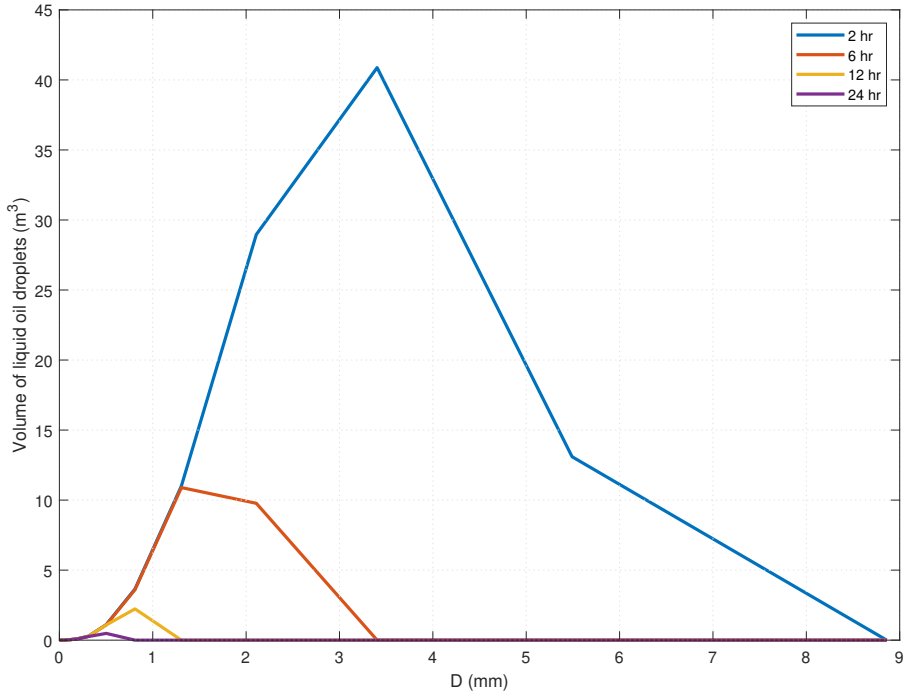

Figure 4.12: Volume distribution of subsurface liquid oil droplets in uniform N^2 stratification and dynamic mode 1 currents (0.15 m s^{-1} velocity amplitude) for an oil-only release. Shown are the volume distributions 2 h, 6 h, 12 h and 24 h after the beginning of the release.

distribution of liquid oil droplets changes over time. Fig. 4.12 shows a representative distribution from an oil-only release in uniform N^2 and dynamic mode 1. The most common droplet diameter reduces by an order of magnitude, from 3.4 mm after 2 h to 0.5 mm after 24 h. The reduction in droplet size is due to a combination of more buoyant droplets surfacing, and oil droplets partially dissolving or biodegrading. After 24 h only 10% of the remaining submerged oil volume exists as liquid droplets, with the rest either biodegraded (11.3%) or dissolved (78.7%).

A secondary pathway of oil advection exists for each simulation, with lower integral concentrations than the more rapidly ascending pathways. These profiles will consist of smaller liquid oil droplets that are neutrally-buoyant, or dissolved oil that is trapped indefinitely. After 24 h, the shape of the less buoyant profiles are close approximations of the dynamic mode horizontal displacement structures. The distinction between transport pathways of high and low buoyancy oil is also prevalent in the results for dynamic modes 2 and 3 (Fig. C.2-C.9).

For dynamic mode 1, termination depths for oil-only releases in both uniform N^2 and non-linear N^2 are 940–950 m. For equivalent oil-methane releases, termination

depths are much shallower (650–710 m). Near to each termination depth, there is an enhanced area of integral concentration even 24 h after the beginning of the release (Fig. 4.8d-4.11d). An exception occurs for an oil-only release in non-linear N^2, where after 24 h the area of enhanced integral concentration is distributed evenly from 700–1000 m depth (i.e. below the density gradient; Fig. 4.10d).

Higher dynamic modes represent more complex shear-flows (Fig. 4.2). For the uniform N^2 profile, dynamic modes 2 and 3 represent three-layer and four-layer shear-flows respectively, distributed over the entire water-column. For the non-linear N^2 profile, dynamic modes 2 and 3 represent three-layer and four-layer shear-flows respectively, with stronger currents confined to near the thermocline and weaker currents deeper and shallower than this. Since the currents below the thermocline are weak for non-linear N^2 dynamic modes 2 and 3 ($< 0.05\,\mathrm{m\,s^{-1}}$; Fig. 4.2b), both the oil-only and oil-methane releases have similar plume termination depths (600–650 m) that are caused by trapping of the plume, rather than 95% or more of oil escaping the plume. This leads to similar meridional distributions of submerged oil (compare Fig. C.4 with Fig. C.5, and compare Fig. C.8 with Fig. C.9). However, because of the mechanisms discussed in Section 4.6.3 the oil-methane releases have smaller droplet size distributions, leading to more oil submerged after 24 h for the oil-methane releases in dynamic modes 2 and 3 (9.4–9.8%) compared to the equivalent oil-only releases (7.6–7.8%). These proportions are lower than for the same magnitude barotropic tide (Table 4.2).

4.7.1 KEY POINTS

- Most oil released in the presence of a shear-flow will surface in the day following a 1 h release and will surface near to the horizontal position of the well-head.
- A small amount of oil (order 10% of the total volume) will become trapped within the water-column, taking the form of small neutrally-buoyant liquid droplets and dissolved oil. The advection pathway of this oil replicates the horizontal current structure.
- The termination depth determines the vertical position of maximum subsurface integral oil concentration, and subsequently the proportion of oil advected by each layer of a shear-flow.

4.8 DISCUSSION

In this chapter, oil plumes were simulated with several of the idealised stratification profiles used in Chapter 3, alongside different idealised barotropic and baroclinic current profiles. Currents fundamentally change the behaviour of a plume, because oil can prematurely escape and ascend through the water-column as individual droplets with different diameters and buoyancies. The rate of oil that escapes a plume depends on the current magnitude, type of stratification, and whether methane is present. By modelling a baroclinic shear-flow representative of the FSC, results suggest that submerged oil could be transported both north-eastward by the Shetland slope current, as well as westward by the bottom current that eventually flows into the open North Atlantic through the FBC. Overall, this analysis shows that the advection of oil from a seabed release in the FSC will be sensitive to the direction and strength of ocean currents and tides, and that it is crucial that operational hydrodynamic models are skilful at representing them. The presence of gas leads to plume trapping that is considerably shallower, and prevents the break-up of a plume until much stronger currents are present, relative to when oil is released on its own.

4.8.1 COMPARISON WITH PREVIOUS LITERATURE

Yapa & Chen (2004) use the CDOG model to show how plume development is influenced by ocean currents, by releasing oil at 1000 m and at 500 m in conditions representative of the GoM and the FSC. For a 1000 m release the GoM plume has a shallower trapping depth than the FSC release, but for a 500 m release the GoM plume has a deeper trapping depth than the FSC plume. Current magnitude used for the GoM release is smaller than for the FSC release at 1000 m, but at 500 m the opposite is true. Yapa & Chen (2004) therefore suggest that lower current velocities lead to a shallower trapping depth. However, the authors do not isolate the influence of currents from the influence of stratification. Johansen (2000b) do isolate the influence of ocean currents by repeating DeepBlow simulations of oil plumes with the same stratification profile but with different current forcing inputs. They show that a higher current velocity leads to deeper trapping. For example, a plume that traps in typical FSC stratification at 500–600 m depth in currents of 0.05 $\mathrm{m\,s^{-1}}$ will trap at 700–800 m

depth in currents of $0.2\,\mathrm{m\,s^{-1}}$.

DeepBlow has also been used to recreate observed plume development from the DeepSpill field experiment (Johansen *et al.*, 2003). The observed release formed a plume that was advected 300 m horizontally in 36 min, terminating 150 m above the release depth. This gives an average current velocity of $0.13\,\mathrm{m\,s^{-1}}$, assuming that the horizontal current velocity is equal to the horizontal plume velocity. In the non-linear N^2 stratification profile, our results suggest that when forced with a residual current of $0.13\,\mathrm{m\,s^{-1}}$, an oil-only plume will terminate 75 m above the release depth (Fig. 4.4a) and an oil-methane plume will terminate 350 m above the release depth (Fig. 4.5a). Differences in stratification, release rate and the type of oil used will contribute to the differences between the observations from the DeepSpill experiment and the results from this chapter.

The separation of oil advection into two different transport pathways (see Section 4.7) has been previously modelled with the CDOG model (Yapa *et al.*, 2012). The authors found that the surfacing location of oil droplets was dependant on the droplet size. Larger (> 1 mm) droplets surfaced 500–1000 m horizontally away from the release location, while smaller (< 1 mm) droplets surfaced 2000 m horizontally away from the release point. The results in this chapter show that the same mechanism occurs with a baroclinic shear-flow of several layers.

4.8.2 HOW REPRESENTATIVE ARE THE IDEALISED CURRENT PROFILES?

In this analysis, barotropic currents are used to show the sensitivity of an oil plume to both residual current magnitude and semidiurnal tidal variability. However, the FSC is host to baroclinic processes such as internal waves (Sherwin, 1991; Hosegood & van Haren, 2004; Hall *et al.*, 2011, 2019) and shear-flows (Turrell *et al.*, 1999; Berx *et al.*, 2013). A barotropic current is thus not particularly representative of conditions within the FSC. The results from the barotropic part of this analysis (Section 4.6) should therefore be seen as an idealised modelling study that tests the sensitivity of a plume to current magnitude, rather than suggesting realistic FSC plume development.

By estimating volume transport of T and S_p through the FIM CTD section, Berx *et al.* (2013) shows that currents at the FSC seabed are approximately $0.05\,\mathrm{m\,s^{-1}}$ on average between 1995-2009. The baroclinic mode 1 shear-flows used in this

chapter may therefore be too strong below the thermocline ($0.15\,m\,s^{-1}$). Furthermore, currents above the thermocline can be stronger than $0.15\,m\,s^{-1}$; the Shetland slope current, for example, can exceed $1\,m\,s^{-1}$ (Hopkins, 1991; Sherwin *et al.*, 1999). On the other hand, the size of the 1995-2009 average surface-to-seabed shear is similar to our results ($0.3\,m\,s^{-1}$; Berx *et al.*, 2013).

In reality a no-slip condition will exist at the seabed, where horizontal current velocity is zero. At some shallower depth, the seabed will have no considerable influence on the current velocity. This is known as the bottom Ekman layer, which has a thickness of approximately 80 m at the FBC outflow (Darelius *et al.*, 2011). The Ekman layer thickness is determined by a spatially variable drag coefficient in AMM7 (Madec, 2016). Oil spills do not necessarily originate from the seabed and can occur along a pipe at any depth, so the representation of the bottom Ekman layer is not necessarily important for a spill simulation. However, incorporating a no-slip condition should be considered in future work to determine its impact on the first stages of plume development from a seabed release.

4.8.3 IMPLICATIONS FOR FAR-FIELD ADVECTION

The first dynamic mode of the non-linear N^2 stratification profile is the most representative of ocean currents and stratification within the central FSC, because it represents a two-layer shear flow separated by a mid-water-column thermocline. For the oil-only release in these ocean conditions (Fig. 4.10), 88% of the submerged oil is trapped below the thermocline after 24 h, and 12% is trapped above it. For the oil-methane release (Fig. 4.11), these values are 82% and 18%, respectively. This suggests that most submerged oil will be advected westward if released in the central FSC. However, the depth distribution of submerged oil could change over longer periods of time. Additionally, only a small proportion of the total release volume (approximately one-tenth) remains submerged after 24 h, so surface currents and surface winds will determine the trajectory of most of the oil.

The dynamic mode 1 non-linear N^2 current structure overestimates typical FSC current velocities in the lower water-column but underestimates typical FSC current velocities in the upper water-column (Section 4.8.2). To assess whether this is important, the mode 1 non-linear N^2 oil-methane simulation was modified

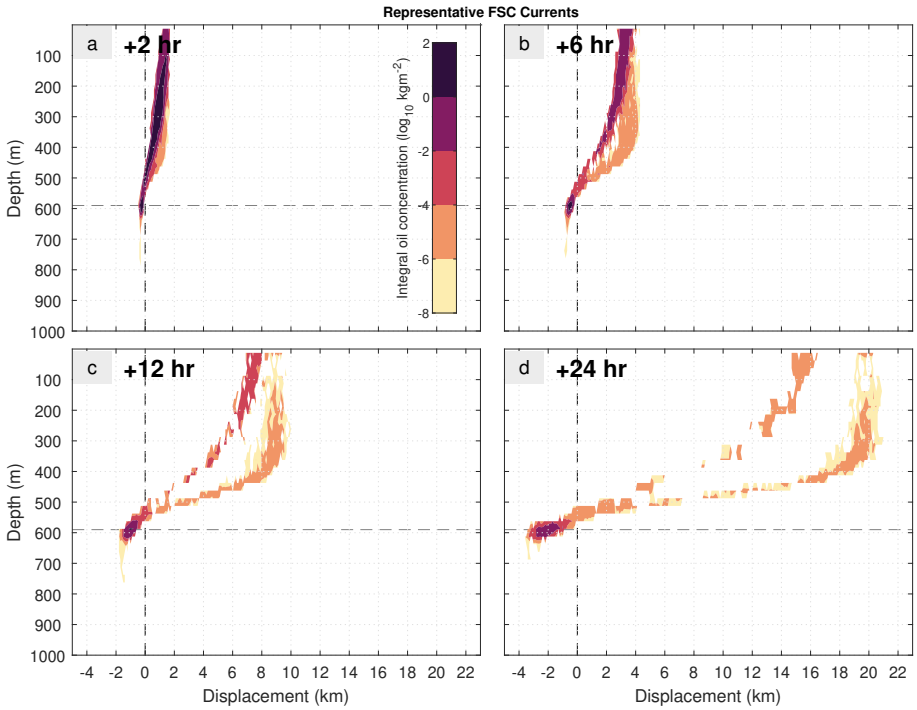

Figure 4.13: Oil-only plume development for a plume in non-linear N^2 and representative FSC currents. (**a**) Cross-section of oil distribution 2 h after the beginning of the release. Coloured contours show the log zonal integral of oil concentration. Also shown are the release location (black dashed line) and plume termination depth (grey dashed line). (**b**) As (a) but 6 h after the beginning of the release. (**c**) As (a) but 12 h after the beginning of the release. (**d**) As (a) but 24 h after the beginning of the release.

by superposing a northward barotropic current velocity of $0.1\,\mathrm{m\,s^{-1}}$. The current velocity for this modified simulation is $0.05\,\mathrm{m\,s^{-1}}$ southward at 1000 m (compared to $0.15\,\mathrm{m\,s^{-1}}$ southward for the unmodified simulation), and $0.25\,\mathrm{m\,s^{-1}}$ northward at the sea surface (compared to $0.15\,\mathrm{m\,s^{-1}}$ northward). Oil transport still splits into two different advection pathways (Fig. 4.13). 77% of the submerged oil is trapped below the thermocline after 24 h, compared to 82% for the unmodified simulation. The submerged oil in the lower water-column also becomes confined to 700 m or shallower (Fig. 4.13d).

The role of hydrate formation was not investigated in this analysis. If methane hydrates do not form, the rate of oil escaping a plume might reduce, because w will increase and less plume bending will occur. However, gas bubbles can potentially escape the plume in the same manner as oil droplets, which will reduce the plume buoyancy and increase the escape rate of oil. This mechanism has not been investigated in this thesis, but future modelling work should focus on how a plume

behaves in the deep FSC if hydrates do not form (e.g. in the case of the DeepSpill field experiment; Johansen *et al.*, 2003).

5

REGIONAL MODELLING OF OIL SPILLS FROM THE SEABED

5.1 INTRODUCTION

Chapter 3 outlined the sensitivity of an oil plume to ocean stratification, and Chapter 4 showed how ocean currents can influence the trajectory of oil in both the near-field and the far-field. In both of these chapters, oil spills were simulated with idealised ocean stratification and currents, so that the individual characteristics of ocean hydrodynamics could be isolated. In reality the ocean does not behave in this way, and realistic ocean hydrodynamics are more complex. This is particularly true in the FSC, where large-scale circulation, smaller-scale mesoscale variability, stratification and tides are superposed (see Section 1.2). To appreciate the full significance of a large seabed release in the FSC, it is therefore useful to force oil spill simulations by a regional hydrodynamic model that attempts to resolve these processes.

In this chapter, both the DeepBlow and 3-D Fates components of OSCAR are used to simulate the trajectory of oil spills originating from the seabed in the FSC. The current state-of-the-art operational forecasting model for the north-west European shelf is used to supply inputs of stratification and currents into the OSCAR system. The size of the oil spill is guided by release flow rate and volume estimates by Gallego *et al.* (2018). The simulations are run for long enough to account for a

typical response time (30 days). Several simulations are carried out with different environmental characteristics by varying the time of year, the release location, and whether stratification is from the hydrodynamic model or from CTD observations.

The aim of this chapter is to show how these environmental characteristics change the fate and trajectory of oil in the FSC, and to explain this variability using the conclusions from Chapters 3 and 4. Section 5.2 describes how the DeepBlow and 3-D Fates models are configured. Chapter 6 uses very similar methodology to what is described here but is treated as a separate piece of work for publication. Section 5.3 describes the hydrodynamic model used in this analysis and discusses the different forcing fields and initial conditions that are used. Sections 5.5, 5.4 and 5.6 respectively show the results of changing the time of year, release location, and stratification forcing. Section 5.7 summarises the chapter by discussing the limitations and implications of this analysis.

5.2 MODELLING THE OIL SPILLS

In this chapter, a total of five seabed oil spill simulations are performed with different release locations (Fig. 5.1), at different times of the year, and with different stratification profiles. The *control* simulation is characterised by a release in the central FSC (61.07°N, 4.055°W), using February 2017 AMM15 currents and stratification. Two more simulations are performed at the same release location. The first of these simulations uses August 2017 AMM15 currents and stratification (hereafter referred to as the *August* release). The second of these simulations uses February AMM15 currents, but with observations of T and S_p taken in February 2014 from the CTD dataset used in Chapter 2 (hereafter referred to as the *CTD* release).

A further two simulations are carried out using February AMM15 currents and stratification, but with a release location in the Wyville-Thomson Basin (60.2°N, 6.6°W) and on the west Shetland shelf (60.69°N, 2.545°W) These releases are hereafter referred to as the *basin* release and the *shelf* release, respectively. Both the central FSC and west Shetland shelf locations have been chosen because they are active areas of oil and gas development (Fig. 5.1) and will show the difference between a shallow (< 200 m) and deep (> 1000 m) release. The Wyville-Thomson Basin location has been chosen because it is a similar depth to the central FSC, but the dominant

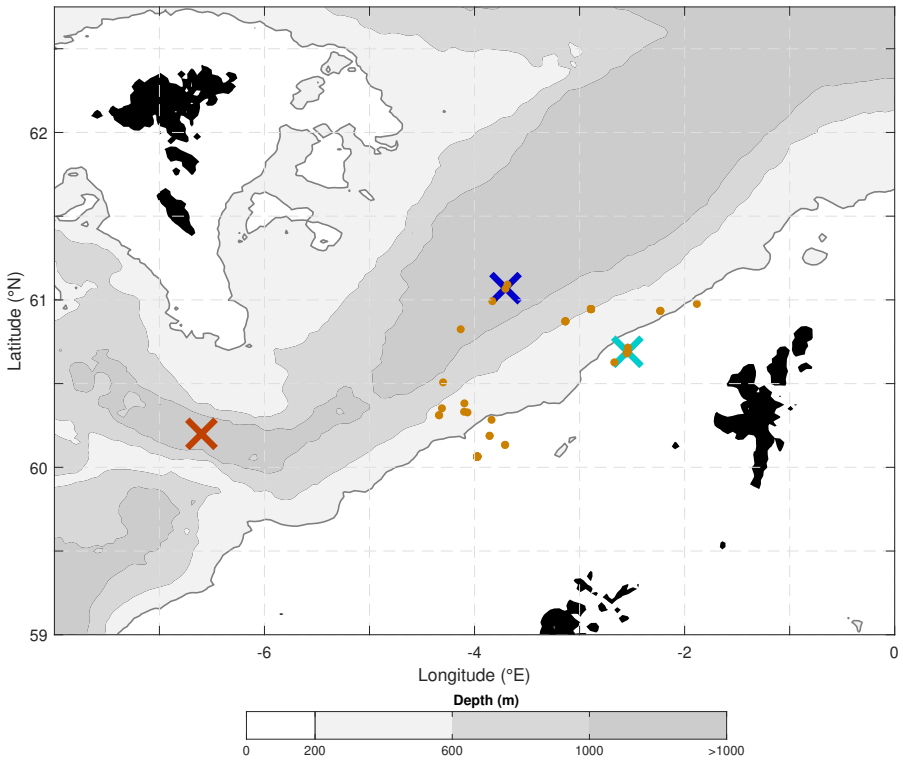

Figure 5.1: Locations of the simulated seabed releases. Active well head locations as of August 2018 are indicated by yellow dots (source: UK Oil and Gas Authority). Crosses indicate the locations of the *control*, *August* and *CTD* releases (dark blue), *shelf* release (light-blue) and *basin* release (brown). Bathymetry is from Smith & Sandwell (1997).

hydrodynamic processes are likely to be different.

5.2.1 DETAILS OF THE DEEPBLOW MODEL

A summary of notable DeepBlow model parameters is given in Table 5.1. Oil is released from the seabed in all simulations. The release depth is 1122 m for the *control*, *August* and *CTD* releases. The depth of the *basin* release is 1187 m, and the depth of the *shelf* release is 164 m. Oil is released at a constant rate of $0.130\,\mathrm{m^3\,s^{-1}}$, which is consistent with the upper flow rate estimate by Gallego *et al.* (2018). Over a release period of nine days, this results in a total volume of oil of $100\,700\,\mathrm{m^3}$.

The release orifice diameter is 0.1 m, which is identical to what was used in Chapters 3 and 4. The release rate is higher than in these two previous chapters, so the expulsion velocity at the well head will be higher and the droplet size distribution will probably be smaller as a result. The Clair oil type is used, and for all simulations methane gas is released with a GOR of 200. Hydrate formation is switched on in the

Table 5.1: Notable DeepBlow model parameters.

Name	Value
DeepBlow time-step	5 s
DeepBlow output interval	30 s
Release depths	1122 m 1187 m 184 m
Release amount	100 700 m^3
Release duration	9 days
Release rate	0.130 $m\,s^{-1}$
Oil type	Clair (Table A.1)
Oil density	893.8 $kg\,m^{-3}$
Gas-Oil Ratio	200
Gas type	Methane
Release orifice diameter	0.1 m

DeepBlow model, and methane hydrates have a constant density of 930 $kg\,m^{-3}$ in the model.

The DeepBlow model time-step is 5 s, and plume dynamics were not sensitive to a time-step more frequent than this. Plume termination is calculated in the same way as in Chapter 4, but the higher release rate results in only small proportions (< 5%) of oil escaping the plume before the trapping depth is reached.

5.2.2 DETAILS OF THE 3-D FATES MODEL

A summary of notable 3-D Fates model parameters is given in Table 5.2. The release period is 9 days. Releases that take place in February 2017 begin on February 1st, 0000 UTC and end on February 10th, 0000 UTC. The 2017 *August* release begins on August 1st, 0000 UTC and ends on August 10th, 0000 UTC. The subsurface and surface grid domains are 12°W-6°E, 57°N-62.75°N. The release locations are close (1–3 degrees) to the northern boundary of the hydrodynamic model domain, which is also 62.75°N. In an operational context, a combination of hydrodynamic models would be used to force the 3-D Fates model, for example AMM15 model output surrounded by the global Met Office model output. The horizontal grid resolution is 1.5 km, to capture the variability of oil transport on the same spatial scale as the hydrodynamic forcing

Table 5.2: Notable 3-D Fates model parameters.

Name	**Value**
3-D Fates time-step	10 min
3-D Fates output interval	60 min
3-D Fates model duration	30 days
Currents	AMM15 (February) AMM15 (August)
Wind	none
Air temperature	Equal to SST
Liquid/solid particles	30 000
Dissolved particles	30 000
Gas particles	30 000
Model domain	57°N-62.75°N; 12°W-6°E
Zonal grid resolution	1.5 km
Meridional grid resolution	1.5 km
Vertical grid resolution	50 m

model.

The total model duration is 30 days, which is equivalent to a typical response time for the region (Gallego *et al.*, 2018) and allows for three weeks of additional transport following the end of the release period (9 days). The output interval is 60 min so that semidiurnal variability can be resolved. With a typical maximum current velocity of $1\,\mathrm{m\,s^{-1}}$, a model time-step of 10 min will displace oil by no more than 600 m, which is less than the horizontal grid resolution (1.5 km) and ensures numerical stability.

No direct wind forcing is used in the simulations, because the intention is to isolate the influence of ocean currents. Biodegradation is also switched off. The influences of these additional processes are discussed in Section 5.7.

5.3 DETAILS OF THE HYDRODYNAMIC MODEL

In November 2018, an updated version of AMM7 was released for public operational usage. This model is the Met Office Forecasting Ocean Assimilation Model 1.5 km Atlantic Margin Model of the North-West European Shelf (FOAM AMM15 NWS, hereafter referred to as AMM15; Graham *et al.*, 2018; Tonani *et al.*, 2019). AMM15 is based on NEMO v3.6 (Madec, 2016) and output is available to download in NetCDF format from the CMEMS website (EU Copernicus Marine Services Information, 2018b). The AMM15 domain extends from 16°W-10°E and 46°N-62.75°N, which is slightly smaller than the domain of AMM7. The model is one-way nested with both the Met Office North Atlantic $\frac{1}{12}°$deep ocean model (Storkey *et al.*, 2010) and the Copernicus operational Baltic Sea model.

AMM15 is forced using surface wind fields, surface pressure fields, and heat/moisture fluxes as described for AMM7 in Section 2.2. AMM15 is assimilated with SST and SSH from a combination of in-situ and satellite observations. Unlike the NEMO v3.4 version of AMM7 used in Chapter 2, vertical profiles of T and S_p from CTD observations are used as part of the assimilation process (King *et al.*, 2018), which may alleviate some of the issues found with AMM7 model output at intermediate depths (400–750 m). AMM15 is also forced with river discharge data from a climatology of 279 rivers. Bathymetry is from EMODnet (described in more detail by Graham *et al.*, 2018), which is initially obtained at a finer resolution than the AMM15 grid and then interpolated onto each grid cell. The finer resolution bathymetry (compared to AMM7) improves the representation of internal wave generation from topography (Tonani *et al.*, 2019). Increased model resolution has also been found to improve the representation of small-scale processes along the shelf break (Aslam *et al.*, 2018), but has not yet been tested between AMM15 and AMM7 model outputs. Tidal forcing is via the same method as AMM7 (Section 2.2).

AMM15 model output has a horizontal resolution of 1.5 km. This is significantly finer than the AMM7 model output (7 km), and finer than the resolution needed to explicitly resolve mesoscale activity in the FSC (< 2 km; Oey, 1998). AMM15 is initially run with 51 vertical levels on the same s-σ-z^* co-ordinate system as AMM7, but interpolated onto a finer vertical grid of 33 isobaths for the operational output (0 m, 3 m, 5 m, 10 m, 15 m, 20 m, 25 m, 30 m, 40 m, 50 m, 60 m, 75 m, 100 m, 125 m, 150 m,

175 m, 200 m, 225 m, 250 m, 300 m, 350 m, 400 m, 450 m, 500 m, 550 m, 600 m, 750 m, 1000 m, 1500 m, 2000 m, 3000 m, 4000 m and 5000 m). At the time of writing, AMM15 is not currently used by spill responders (AMM7 is still widely used). A comparison between oil spill simulations forced by AMM7 and AMM15 is carried out in Chapter 6.

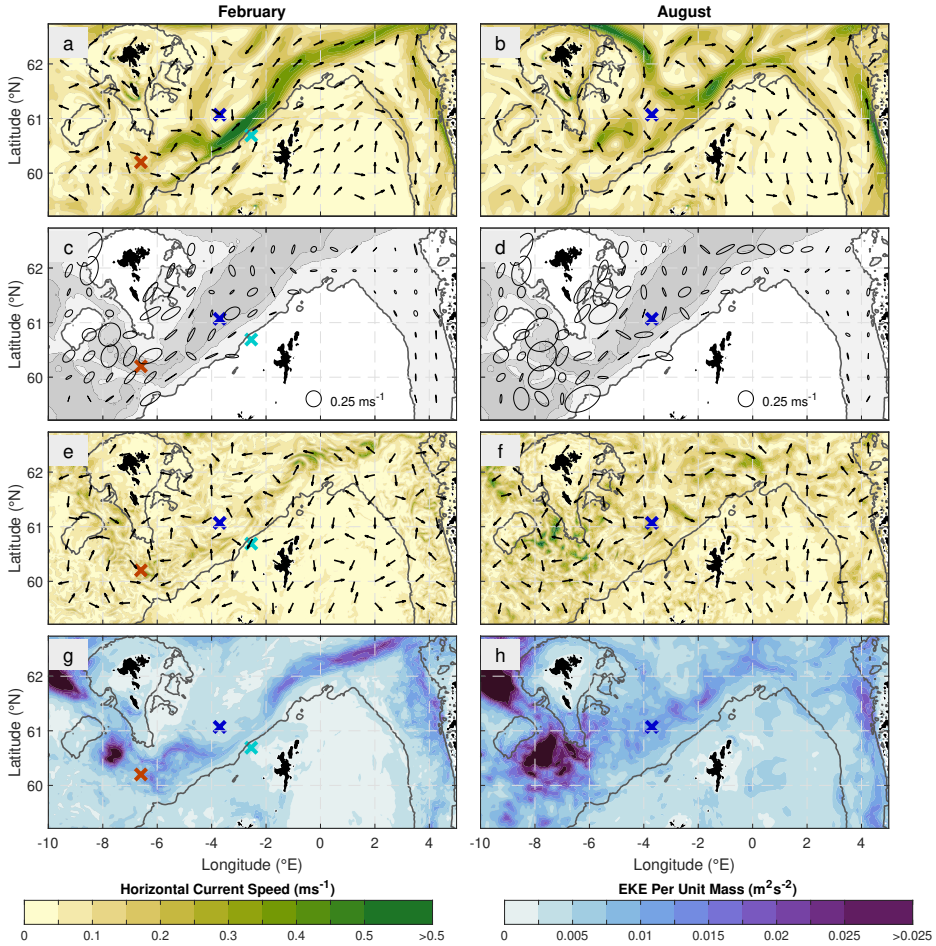

Figure 5.2: Surface current decomposition from February 2017 and August 2017 AMM15 model output. (**a, b**) Thirty-day mean surface current velocity, with magnitude shown as filled contours, and direction shown by arrows. (**c, d**) M_2 tidal ellipses, masked on the shelf (< 200 m). (**e, f**) Residual surface current velocities at the end of the release period on February 10th, 2017. (**g, h**) Thirty-day surface mean eddy kinetic energy (EKE) per unit mass. The shelf edge (200 m isobath) is shown as a dark grey contour, and release locations are shown as coloured cross. Bathymetry has a scale identical to Fig. 5.1.

5.3.1 CURRENT FORCING

Two 30-day periods of AMM15 model output are used in this analysis, to investigate how the same release might vary at different times of the year. The different times are used to show a change in currents and stratification for an identical release location and using the same hydrodynamic model. This analysis does not attempt to derive typical seasonal differences. For releases using 2017 February AMM15 model output, hourly instantaneous horizontal currents are used from 1 February 0000 UTC until March 3rd, 0000 UTC. For the *August* release, 2017 AMM15 model output of hourly instantaneous horizontal currents are used from August 1st, 0000 UTC until August 31st, 0000 UTC.

Fig. 5.2 shows a decomposition of surface currents for both the February and August AMM15 model outputs. The instantaneous model output currents are decomposed as

$$\underbrace{\boldsymbol{u}(x,y,z,t)}_{\text{total}} = \overbrace{\underbrace{\overline{\boldsymbol{u}}(x,y,z)}_{\text{mean}} + \underbrace{\overleftarrow{\boldsymbol{u}}(x,y,z)}_{\text{trend}}}^{\text{time-constant}} + \overbrace{\underbrace{\sum_{n=1}^{35} \boldsymbol{u_n}(x,y,z,t)}_{\text{tides}} + \underbrace{\boldsymbol{u}'(x,y,z,t)}_{\text{residual}}}^{\text{time-variable}}. \tag{5.1}$$

The Python 3 implementation of Utide (Codiga, 2011) is used to perform a harmonic analysis of $\boldsymbol{u}$ over both 30-day periods, in order to de-tide the current field and separate different tidal constituents. For the harmonic analysis, the default value of the noise-modified Rayleigh criterion of 1 is used. Constituents are selected automatically, and 35 tidal constituents (with time-varying velocities of $\boldsymbol{u_n}$) are resolved. Resolving different combinations of tidal constituents results in a redistribution of the tidal amplitudes and energies. However, the velocity amplitudes and phases of the dominant tidal constituents (M_2, S_2, N_2, K_1) did not change by more than 5% when solved for individually, or when the noise-modified Rayleigh criterion was increased to 1.5. M_2 tidal ellipses are shown in Fig. 5.2c, d. The linear trend of the AMM15 output velocities ($\overleftarrow{\boldsymbol{u}}$) at each grid point was also computed to better separate the tidal variability from the long-term (monthly) variability.

Mean surface current velocities ($\overline{\boldsymbol{u}}$; Fig. 5.2a, b) are calculated by averaging $\boldsymbol{u}$ over each 30-day period. Residual currents ($\boldsymbol{u}'$) can then be calculated for each time-step of the AMM15 model outputs by re-arranging Eq. 5.1 and subtracting the

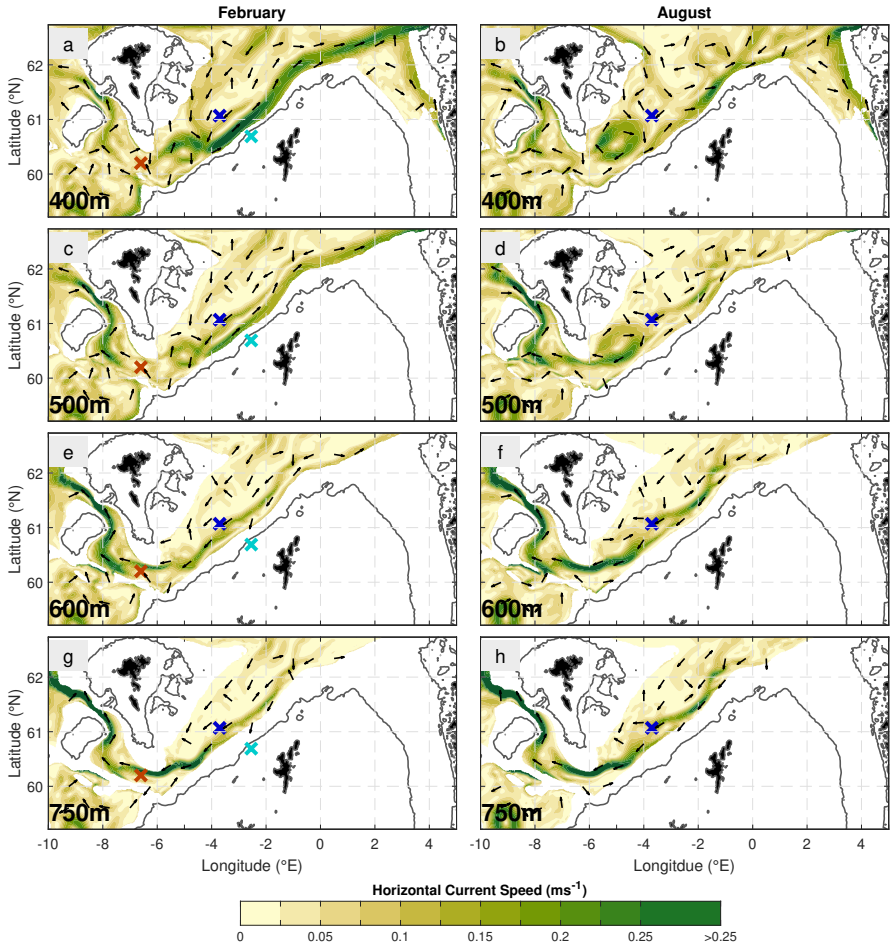

Figure 5.3: Monthly mean current velocities at different depths from February 2017 and August 2017 AMM15 model output. (**a, b**) 400 m. (**c, d**), 500 m (**e, f**) 600 m. (**g, h**) 750 m. The shelf edge (200 m) is shown as a dark grey contour, and release locations are shown as a coloured crosses. Bathymetry has a scale identical to Fig. 5.1.

mean current velocities, 35 tidal velocities and model trends from $\boldsymbol{u}$. The residual currents will show any model variability that is separate from the long-term mean and short-term tidal variability. This residual variability is defined here as the 'mesoscale' variability. Mesoscale Eddy Kinetic Energy (EKE) per unit mass is then calculated $EKE = 1/2(u'^2 + v'^2)$, where u' and v' are the zonal and meridional velocity components of $\boldsymbol{u}'$, respectively. This is performed for each time-step and averaged over the same period as the mean surface currents (30 days). Mean surface EKE is shown in Fig. 5.2g, h. The analysis was also repeated at depths of 400 m, 500 m, 600 m and 750 m (see Fig. 5.3 and 5.4).

Three-dimensional, hourly instantaneous horizontal current velocities from AMM15 model output are used as a forcing input to the 3-D Fates model, and

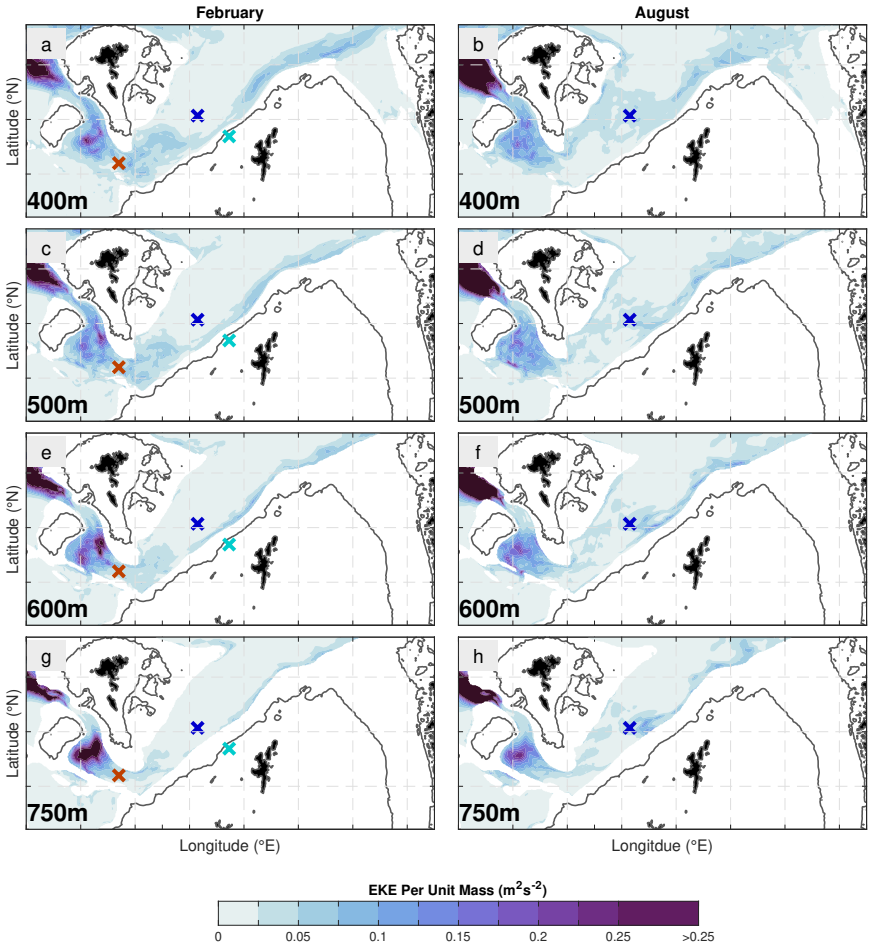

Figure 5.4: Monthly mean EKE per unit mass at different depths for February 2017 and August 2017. (**a, b**) 400 m. (**c, d**), 500 m (**e, f**) 600 m. (**g, h**) 750 m. Current magnitude is shown as coloured contours, and direction is shown by arrows. The shelf edge (200 m) and coastal outlines (0 m) are shown as dark grey contours, and release locations are shown as coloured crosses. Bathymetry has a scale identical to Fig. 5.1.

interpolated onto the subsurface and surface grids using a nearest-neighbour method. The DeepBlow model outputs a plume profile once per hour, using a vertical profile of current velocities from each AMM15 time-step that coincides with the release period. The profile is estimated at the release location from the AMM15 forcing input by using values from the nearest AMM15 grid-point.

5.3.2 STRATIFICATION

Each of the five oil spill simulations in this analysis use different stratification profiles (Fig. 5.5). The *control*, *basin* and *shelf* releases use AMM15 model output stratification, taken from the nearest grid point to the release locations on February

1st, 2017, 0000 UTC. The *August* release uses AMM15 model output stratification taken from the same location as the *control* release, but on 1 August 2017, 0000 UTC. The *CTD* release, which occurs in the same location and at the same time as the *control* release, uses CTD observations that were taken on February 2nd, 2014, 1300 UTC, which is in the same month but in a different year and at a different location. The CTD cast is located 80 km to the south-west of the release location (60.63°N, 4.9°W; see Fig. 5.1). Observations are sub-sampled onto AMM15 model output depths. Only time-constant profiles of T and S_p can be used as input for the DeepBlow model, and so each stratification profile stays constant for the duration of the release periods (9 days).

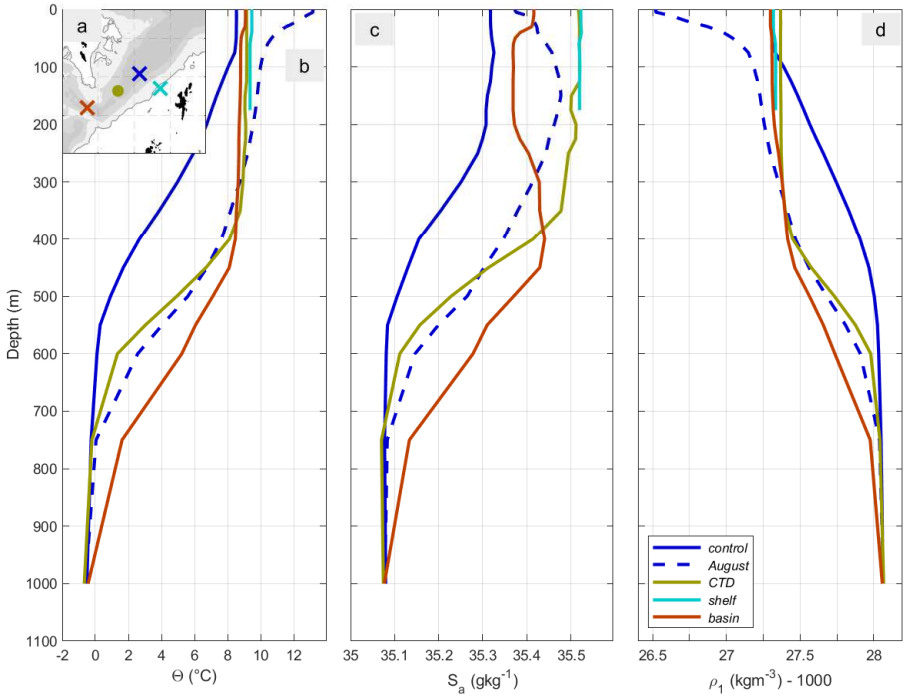

Figure 5.5: Stratification profiles used for the regional oil spill simulations. (**a**) Location of the release locations (dark blue cross: *control*, *August* and *CTD* releases; light blue cross: *shelf* release; brown cross: *basin* release). Also shown is the location of the CTD cast used for the *CTD* release (yellow dot). Bathymetry has a scale identical to Fig. 5.1. (**b**) Conservative temperature for the *control* release (dark blue solid line), *August* release (dark blue dashed line), *CTD* release (yellow solid line), *basin* release (brown solid line) and *shelf* release (light blue solid line). (**c**) As (b) but for absolute salinity. (**d**) As (b) but for potential density.

5.4 RESULTS - SEASONAL VARIABILITY

5.4.1 SURFACE TRANSPORT

For the *control* release, the surface emulsion is initially advected to the north-east. This singular band of emulsion begins to split into two distinct advection pathways after nine days; a pathway to the east, and a pathway to the west (Fig. 5.6a). Surface emulsion continues to be advected to the north-east but is not transported onto either the Shetland shelf or the Faroe shelf (Fig. 5.6c, e, g). The distribution of the slick becomes increasingly complex and breaks up into numerous smaller patches over time. By the end of the simulation, a small amount of oil has escaped the model domain, and in reality will continue to travel into the Norwegian Sea.

For the *August* release, the surface emulsion is initially advected to the south. After nine days, some oil is trapped by an eddy-like structure to the south-west of the release location (Fig. 5.6b) and stays there for at least two weeks (Fig. 5.6d, f). Most of the surface emulsion is advected to the north-east, and some is transported onto the Shetland shelf north of the Shetland islands. Some of the surface emulsion also follows the 200 m isobath clockwise around the Shetland Islands and subsequently towards the Norwegian coastline (Fig. 5.6h).

Most of the differences in surface transport between the *control* release and the *August* release can be accounted for by differences in the mean surface currents. In February, surface transport within the central FSC is dominated by a strong slope current on the Shetland slope with a magnitude of approximately $0.5\,\mathrm{m\,s^{-1}}$ (Fig. 5.2a). This current is present from directly west of the Shetland Islands (4°W, 60.5°N) until the northern boundary of the model domain (3°E, 62.75°N). Water entering the channel from the north recirculates to join this slope current around the south of the release location. In August however, recirculation is instead to the north of the release location (Fig. 5.2b). Consequently, mean surface currents in August show a cyclonic eddy with a centre at 3°W, 62°N. Further to the south-west, mean surface currents also show an anti-cyclonic eddy with a centre at 5°W, 60.5°N. These two eddies occur at two areas of enhanced EKE that have previously been observed within the channel (locations 'b' and 'e' from Figure 9 by Sherwin *et al.*, 2006). The anti-cyclonic eddy explains the trapping of oil to the south-west of the release location.

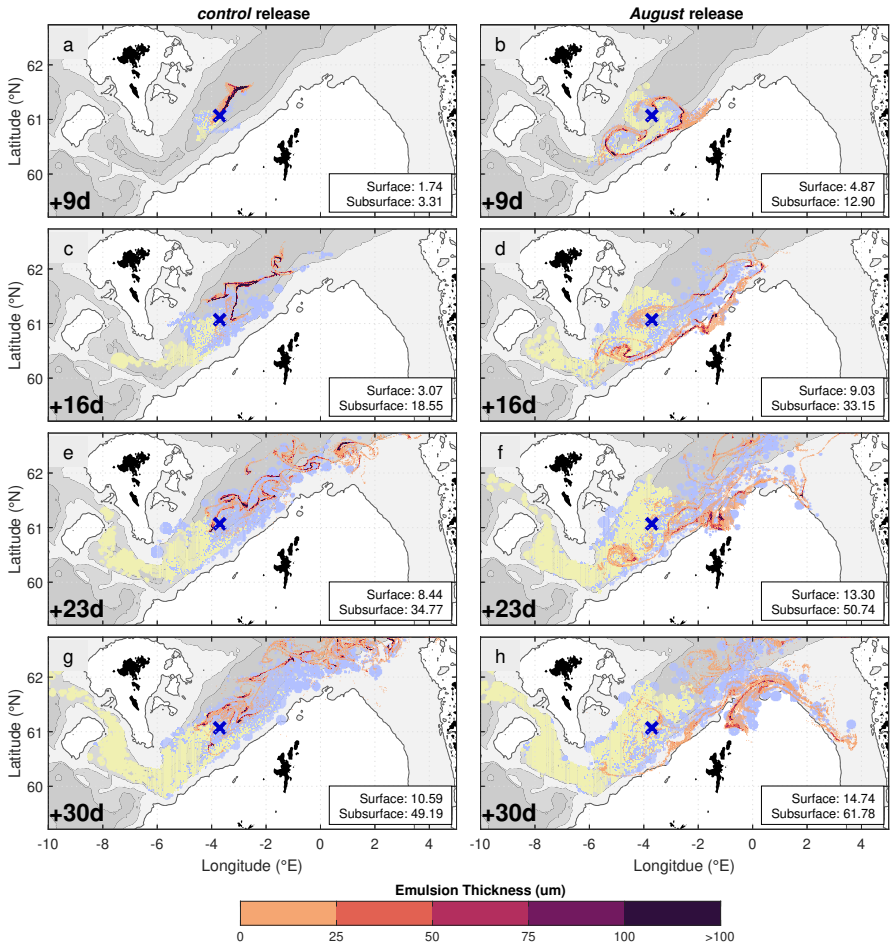

Figure 5.6: Far-field transport of pollutant for the *control* and *August* releases. It is important to clarify here that the *August* release refers to currents of August 2017, and not a climatological mean. The comparison is intended to be between two 'representative' current fields that were assessed subjectively. (**a, b**) Surface emulsion thickness nine days after the beginning of the release (colour scale). Light blue and yellow both show where depth-integrated subsurface pollutant exceeds 5 kg km^{-2}, but with maximum concentration above and below 500 m, respectively. (**c, d**) As (a, b), but 16 days after the beginning of the simulation. (**e, f**) As (a, b), but 23 days after the beginning of the simulation. (**g, h**) As (a, b), but 30 days after the beginning of the simulation. Release location is shown as a blue cross. Units of surface and subsurface coverage are 10^9 m^2. Bathymetry has a scale identical to Fig. 5.1.

In both February and August, a mean surface current exists that flows clockwise around the north of the Shetland Islands, acting to transport water from the central FSC towards the Norwegian coastline. In February, the magnitude of this current is 0.05–0.1 m s^{-1}, but in August this increases to 0.1–0.2 m s^{-1}. Conversely, the slope current north of 62°N has a magnitude of 0.3–0.4 m s^{-1} in February, but 0.1–0.2 m s^{-1} in August. These differences explain why some oil is advected towards the Shetland Islands and Norway for the *August* release, but not for the *control* release.

Table 5.3: Percentage mass balance for different model components at the end of the simulation period (30 days) for the *control* and *August* releases.

Component	***control*** **(%)**	***August*** **(%)**
On surface	68.78	64.35
Evaporated	13.24	16.19
Submerged	12.26	12.76
Biodegraded	0.00	0.00
In sediment	0.15	0.07
Escaped	5.57	6.64

After 30 days, the total amount of oil that has surfaced is approximately 87.5% for both the *control* release and the *August* release (Table 5.3). Total surfaced mass is calculated as the sum of the oil that is either on the sea surface forming an emulsion, oil that has evaporated, and oil that has escaped outside of the model domain. Escaped oil is assumed to be part of the surfaced mass because only the surface emulsion reaches the domain boundary for either of these two releases. The amount of escaped oil is similar for both releases (5.57% for the *control* release and 6.64% for the *August* release). A larger amount of oil evaporates in the *August* release (16.19%, compared to 13.24% for the *control* release). This could partly be because of the higher spatial coverage of oil at the surface in the *August* release (lower right panels in Fig. 5.6), but the primary cause will be the higher SST and air temperature in August (13 °C, compared to 9 °C in February). Mass residing on the surface (that is not outside the model domain) is subsequently lower for the *August* release (Table 5.3).

Surface spatial coverage is higher for the *August* release throughout the 30-day simulation period. This difference is largest after 16 days (Fig. 5.6c, d), where surface coverage for the *August* release is higher by a factor of 2.9 compared to the *control* release. After 30 days (Fig. 5.6g, h), surface coverage for the *August* release is higher by a factor of 1.2. The higher spatial coverage could be due to higher surface EKE in August (Fig. 5.2g, h). This is particularly true near the release location and on the Shetland shelf. Oil from the *August* release is advected into both of these areas. On the other hand, oil from the *control* release is initially advected into a region of relatively low surface EKE. Higher surface EKE suggests more variable and energetic surface instantaneous currents, which could lead to higher rates of horizontal dispersion.

5.4.2 SUBSURFACE TRANSPORT

For both the *control* release and the *August* release, one-eighth (12.26–12.76%) of oil remains below the surface after 30 days (Table 5.3). Approximately nine-tenths of the remaining submerged mass has been dissolved into the water-column and will remain this way indefinitely. The remaining submerged oil consists of neutrally-buoyant liquid droplets that have not yet been degraded. Liquid oil droplets within the water-column are subject to several possible fates, and can biodegrade, surface after a period of weeks or months, mix with sediment or dissolve (Beyer *et al.*, 2016).

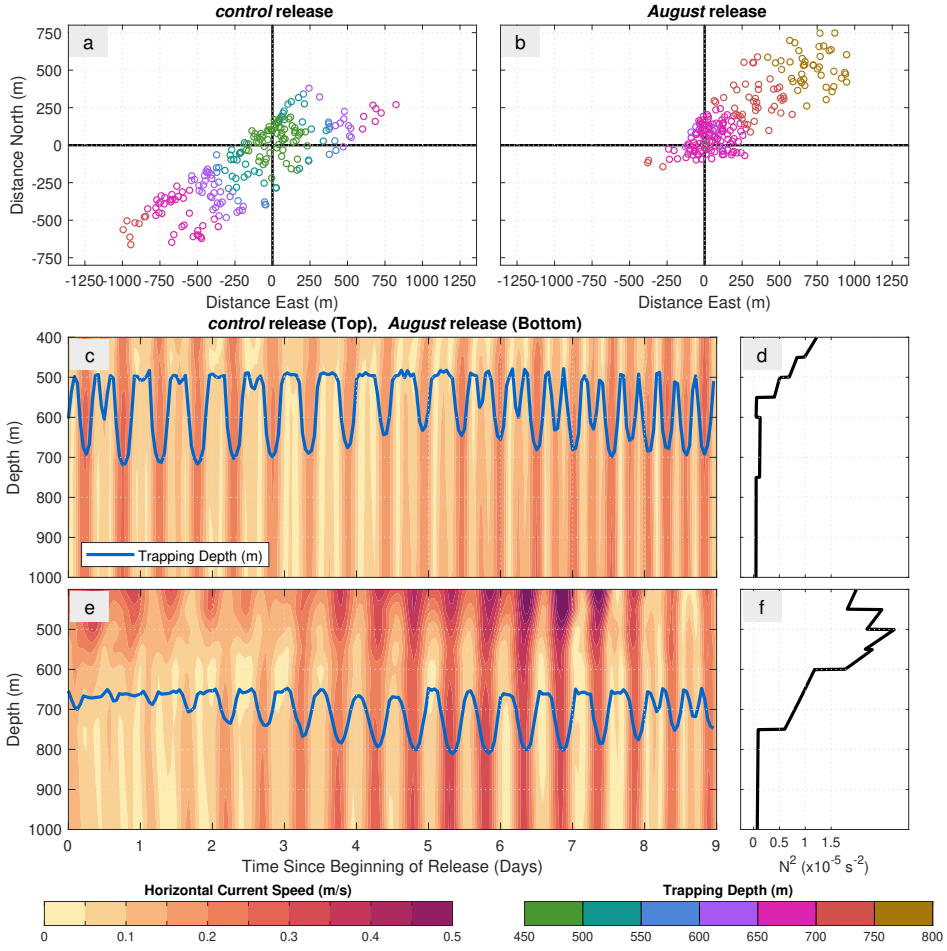

Figure 5.7: Plume dynamics for the *control* and *August* releases. (**a, b**) Trapping location of the subsurface plume for the *control* release and *August* release (right), relative to the release location. (**c**) Contoured current speed from the *control* release location, where the blue line indicates trapping depth. (**d**) Buoyancy frequency squared used by OSCAR for the *control* release. (**e, f**) As (c, d), but for the *August* release.

For all plume profiles outputted by the DeepBlow model, the plume is trapped because of zero vertical plume velocity (Fig. 5.7c, e). For the *control* release, the trapping depth is between 478 m and 718 m, with an average of 574 m. For the *August* release, the trapping depth is between 647 m and 811 m, with an average of 711 m. From the analysis presented in Chapter 4, it is reasonable to assume that the shallowest trapping depth is approximately the depth the plume would reach in the absence of currents. Therefore, a major cause of the difference in trapping depths between the *control* release and the *August* release will be the stratification structure (Fig. 5.5), because the shallowest trapping depths are different by 169 m. In February the water-column is almost mixed from 1122–550 m (Fig. 5.7d), but in August the water-column is almost mixed from 1122–750 m (Fig. 5.7d). The onset of a density gradient shallower than these depths will promote plume trapping. The current magnitude is also larger at 3–8 days after the beginning of the release in August compared to in February (Fig. 5.7c, e), which will also act to deepen the depth of trapping compared to the *control* release (see Section 4.6.2).

The trapping depth and horizontal plume displacement are sensitive to the semidiurnal tide (Fig. 5.7a, b). A deeper trapping depth correlates with a larger horizontal plume displacement and faster current velocities. For the *control* release, the horizontal displacement is rectilinear (north-east to south-west, parallel to the Shetland slope), with a slight bias to the south-west of the release location. For the *August* release, the horizontal displacement is almost exclusively to the north-east of the release location.

Following the termination of the plume, subsurface transport can be broadly divided into two pathways (Fig. 5.2). Shallower oil (maximum concentration is < 500 m) is advected to the north-east and tends to correlate with the position of the surface emulsion. Deeper oil (maximum concentration is > 500 m) is advected in the opposite direction, westward through the Faroe Bank Channel and towards the western boundary of the model domain (the open North Atlantic). This depth-dependency occurs for both the *control* release and the *August* release, and is probably because the current shear is similar in both February and August, where currents near the Shetland slope change direction from north-eastward (< 500 m; Fig. 5.3c, d) to south-westward (> 600 m; Fig. 5.3e, f). The magnitude of the currents at 600–750 m are also similar for both times of year (Fig. 5.3e, f, g, h).

Similar to the surface spatial coverage, the subsurface spatial coverage is higher for the *August* release compared to the *control* release (lower right panels in Fig. 5.2). Subsurface EKE is greater in August at 400–750 m depth along the Shetland slope and extends further into the centre of the FSC compared to in February (Fig. 5.4). Subsurface EKE is also higher near the release location in August, which suggests that more energy is available to disperse oil in the early stages of the spill. Furthermore, the eddies to the north and south of the release location in August are both visible at up to 500 m depth (Fig. 5.3b, d). Although these eddies do not coincide with areas of enhanced EKE calculated in Section 5.3.1, they are likely to increase horizontal stirring and dispersion. The disparity between the visible eddies and calculated mesoscale variability may be due to the residence time of the eddies, and is discussed in Section 5.7.

5.4.3 KEY POINTS

- Most oil from a deep-sea release in the central FSC will reach the surface. The resultant surface emulsion is predominantly advected north-eastward and breaks into patches that become increasingly small and numerous.
- Oil that remains below the surface will either be advected north-eastward (upper water-column) or westward (lower water-column), resulting in potentially far-reaching effects of a spill.
- Higher EKE appears to result in increased spatial coverage of an oil spill both at and below the sea surface.
- Eddy-like structures can trap oil for several weeks.
- More work is needed to deduce whether the differences between the August and February forcing fields are representative of typical seasonal differences, because only a single example of either time of year is used for this analysis.

5.5 RESULTS - RELEASE LOCATION

5.5.1 WYVILLE-THOMSON BASIN

For the *basin* release, surface emulsion is initially advected to the north-east into the central FSC (Fig. 5.8a). A very small amount of surface oil is also advected to the west. Subsurface oil in the first nine days is either advected to the east for shallower subsurface oil, or to the west for deeper subsurface oil. Oil continues to be advected in this depth-dependant manner for the rest of the simulation; surface and shallower subsurface oil is advected to the north-east through the central FSC, and deeper oil is guided by currents and bathymetry westward through the FBC (Fig. 5.8c, e, g). Like the *control* and *August* releases discussed in Section 5.4, the surface emulsion breaks up over time into separate patches that become increasingly thin, small, and numerous.

After 30 days, 10.13% of oil has escaped the model domain. The majority of this is from surface emulsion reaching the northern model boundary, but a smaller amount of subsurface oil also escapes through the western model boundary at 62°N out into the open North Atlantic.

Throughout the simulation, a small amount of shallower subsurface oil is present to the west of the release location (6.6°W or further west). Monthly mean currents at the surface (Fig. 5.2a) and at up to 500 m depth (Fig. 5.3a, c) show exclusively eastward currents in the Wyville-Thomson Basin and FBC (roughly 10°W-4°W, 60°N-62°N). It is therefore unlikely that oil was advected by the currents at this depth. Instead, the shallower subsurface oil likely exists here because of buoyant droplets slowly rising within the water-column after being transported by the strong mean westward currents seen at 600–750 m depth (Fig. 5.3e, g). Although not shown in the monthly mean values, current velocities of up to 0.7 $m\,s^{-1}$ are present at the release location during the first nine days of the simulation (Fig. 5.9e).

The total surfaced mass (including oil that has evaporated and oil that has escaped) is 86.78%. This is similar to both the *control* release (87.59%) and the *August* release (87.18%), but is a slight overestimation because a small amount of the escaped oil is from below the surface. Compared to the *control* release, a higher proportion of oil from the *basin* release has evaporated (15.90% compared to 13.24%). The reason

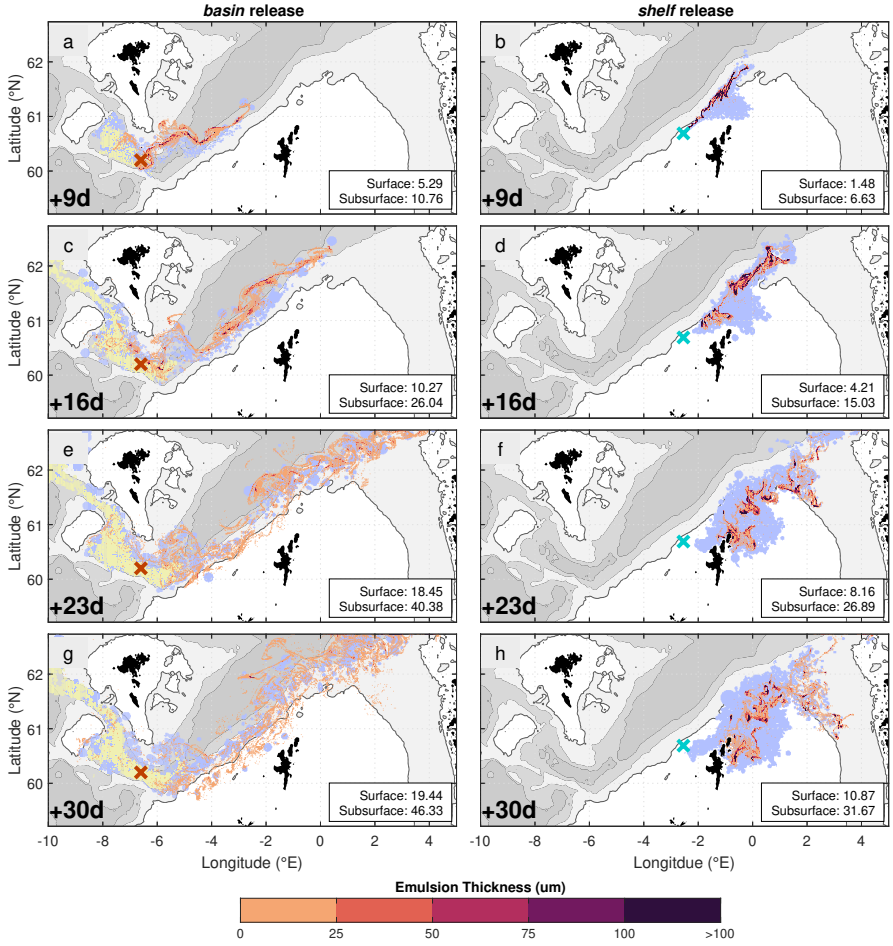

Figure 5.8: Far-field transport of pollutant for the *basin* and *shelf* releases. (**a, b**) Surface emulsion thickness nine days after the beginning of the release (colour scale). Light blue and yellow both show where depth-integrated subsurface pollutant exceeds 5 kg km^{-2}, but with maximum concentration above and below 500 m, respectively. (**c, d**) As (a, b), but 16 days after the beginning of the simulation. (**e, f**) As (a, b), but 23 days after the beginning of the simulation. (**g, h**) As (a, b), but 30 days after the beginning of the simulation. Release location is shown as a blue cross. Units of surface and subsurface coverage are 10^9 m^2. Bathymetry has a scale identical to Fig. 5.1.

for this increase is because the surface spatial coverage is much greater than the *control* release (e.g. by a factor of 1.9 after 30 days).

For the *basin* release, the plume trapping depth is between 738 m and 934 m, with an average of 881 m (Fig. 5.9e). This is deeper than either the *control* release or the *August* release. There are three reasons for this. Firstly, the pycnocline is deeper in the Wyville-Thomson Basin; high N^2 begins at 750 m compared to at 500 m in the central FSC during February. The maximum density gradient is also much higher than in the central FSC during either February or August. Secondly, much stronger

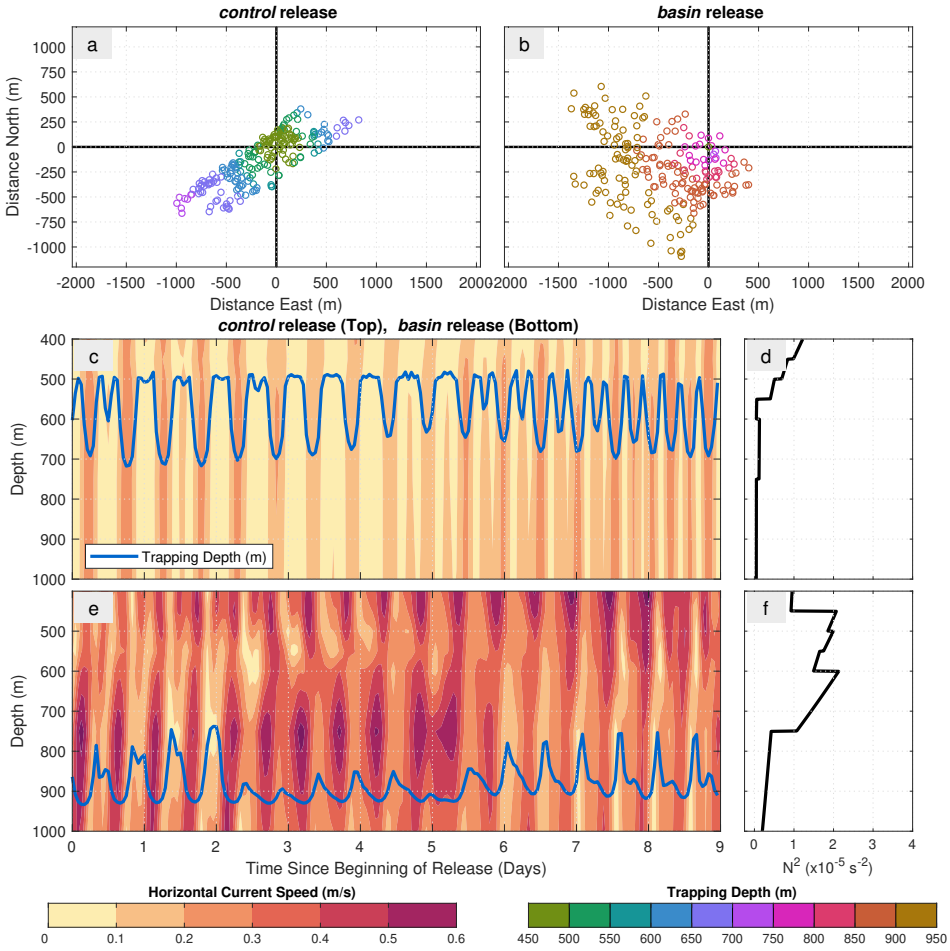

Figure 5.9: Plume dynamics for the *control* and *basin* releases. (**a, b**) Trapping location of the subsurface plume for the *control* release (left) and the *basin* release (right), relative to the release location. (**c**) Contoured current speed from the *control* release location, where the blue line indicates trapping depth. (**d**) Buoyancy frequency squared used by OSCAR for the *control* release. (**e, f**) As (c, d), but for the *basin* release.

currents are present in the Wyville-Thomson Basin (up to 0.7 m s^{-1}, compared to up to 0.3–0.5 m s^{-1} in the central FSC, depending on the time of year). The effect of these stronger currents is most notable at 2–6 days, where the shallowest trapping depths for the *basin* release are order 100 m deeper than they are at 0–2 days and 6–9 days. Thirdly, the release depth is slightly deeper (1187 m, compared to 1122 m in the central FSC).

Despite a deeper average trapping depth, a similar proportion of oil remains submerged within the water-column after 30 days when compared to the *control* release (Table 5.4). This suggests that a change in plume trapping depth does not influence the total amount of subsurface oil, but could influence the subsequent

Table 5.4: Percentage mass balance for different model components at the end of the simulation period (30 days) for the *control*, *basin* and *shelf* releases.

Component	***control*** (%)	***basin*** (%)	***shelf*** (%)
On surface	68.78	60.73	76.15
Evaporated	13.24	15.90	17.77
Submerged	12.26	12.83	4.02
Biodegraded	0.00	0.00	0.00
In sediment	0.15	0.41	0.02
Escaped	5.57	10.13	2.04

direction of advection when taking into account the cross-flows found within the FSC.

5.5.2 ON-SHELF

The *shelf* release is notably different from any of the other simulated releases in this analysis, because the release depth is much shallower (< 200 m, compared to > 1000 m). From 0–200 m depth, the flow is equivalent barotropic. The surface emulsion is initially advected to the north-east in a continuous band that closely follows the 200 m isobath (Fig. 5.8b). Subsurface oil, which resides no deeper than 150 m, is advected in a similar direction, but propagates further to the east compared to the surface emulsion, reaching as far as the northern tip of the Shetland Islands. In subsequent weeks, oil is either advected by the slope current further north-east or is transported further onto the Shetland Shelf (Fig. 5.8d, f, h). Some surface emulsion also continues to follow the 200 m isobath clockwise around the Shetland Islands and towards the Norwegian coastline, similar to the *August* release. No oil is advected to the west or south-west of the release location, because mean surface currents are north-eastward on-shelf (Fig. 5.2a). Additionally, since subsurface oil is only advected at depths shallower than 150 m, the cross-flow at 500–600 m depth (Fig. 5.3c, e) that influences subsurface oil advection for other releases does not influence oil advection for the *shelf* release.

After 23 days (Fig. 5.8f), oil encounters the north Shetland coastline. The bathymetry used by the 3-D Fates model does not recognise either the Faroe Islands or Shetland Islands as land masses, and so the beaching of oil is not numerically recognised in the model output. However, results suggest that a considerable

proportion of surface emulsion will contaminate the north and west Shetland coastlines by the end of the simulation period (Fig. 5.8h). The source of this surface emulsion could be either already surfaced pollutant, or from subsurface liquid oil droplets that have recently surfaced. The proportion of subsurface oil-only decreases by order 1% between the end of the release period (9 days) and the end of the simulation period (30 days), and so the source is almost definitely from existing surface emulsion.

All plume profiles outputted by the DeepBlow model for the *shelf* release reach the surface within 2 min. This is partly because of the shallow release depth, and partly because water-column temperature and pressure are sufficient for gas bubble formation[1]. The presence of gas bubbles enhances plume buoyancy compared to the presence of gas hydrates (see Section 3.5.2). As a result of rapid plume surfacing, there is negligible (< 35 m) horizontal plume displacement. Due to the prevailing currents at the release location, any plume displacement is primarily eastward.

The difference in release depths on-shelf, compared to release depths in the central FSC and Wyville-Thomson Basin locations, lead to a difference in the mass balance (Table 5.4). For any of the other releases in this analysis, approximately 12.5% of oil remains below the surface after 30 days. For the *shelf* release however, only 4.02% of oil does not surface. The subsequent higher proportion of oil that does surface leads to increased amounts of evaporated oil compared to the *control* release, due to a larger surface area of interface between oil and the atmosphere. The surface spatial coverage after 30 days is similar (10.87×10^9 m^2, compared to 10.59×10^9 m^2 for the *control* release), so this is not a contributing factor.

The subsurface spatial coverage after 30 days for the *shelf* release (31.67×10^9 m^2) is lower compared to the *control* release (49.19×10^9 m^2), the *August* release (61.78×10^9 m^2), or the *basin* release (46.33×10^9 m^2). This is probably because subsurface oil from the *shelf* release is only advected in one direction (to the north-east) and is therefore more confined. Additionally, there is much less oil below the surface compared to any of the other releases.

[1] Assuming a temperature of 9 °C, methane hydrates will only form at approximately 750 m and deeper.

5.5.3 KEY POINTS

- A release on-shelf increases the proportion of oil that has surfaced compared to a deep (> 1000 m) release, evidenced by the lack of plume trapping that occurs for the *on-shelf* release in the results from this chapter.
- Increased evaporation rates can be caused by a higher SST, a thinner emulsion or an increased proportion of oil that has surfaced. The specific reason depends on the conditions of the release. Respectively, these three mechanisms can be seen in Sections 5.4, 5.5.1 and 5.5.2.
- A deep release in the Wyville-Thomson Basin still results in a splitting of subsurface oil transport into deeper westward advection and shallower north-eastward advection. This is likely to occur for most releases of a similar depth in the FSC area, because of the consistent presence of a two-layer cross-flow.
- The Shetland islands are at risk of contamination when oil is released on the Shetland shelf.

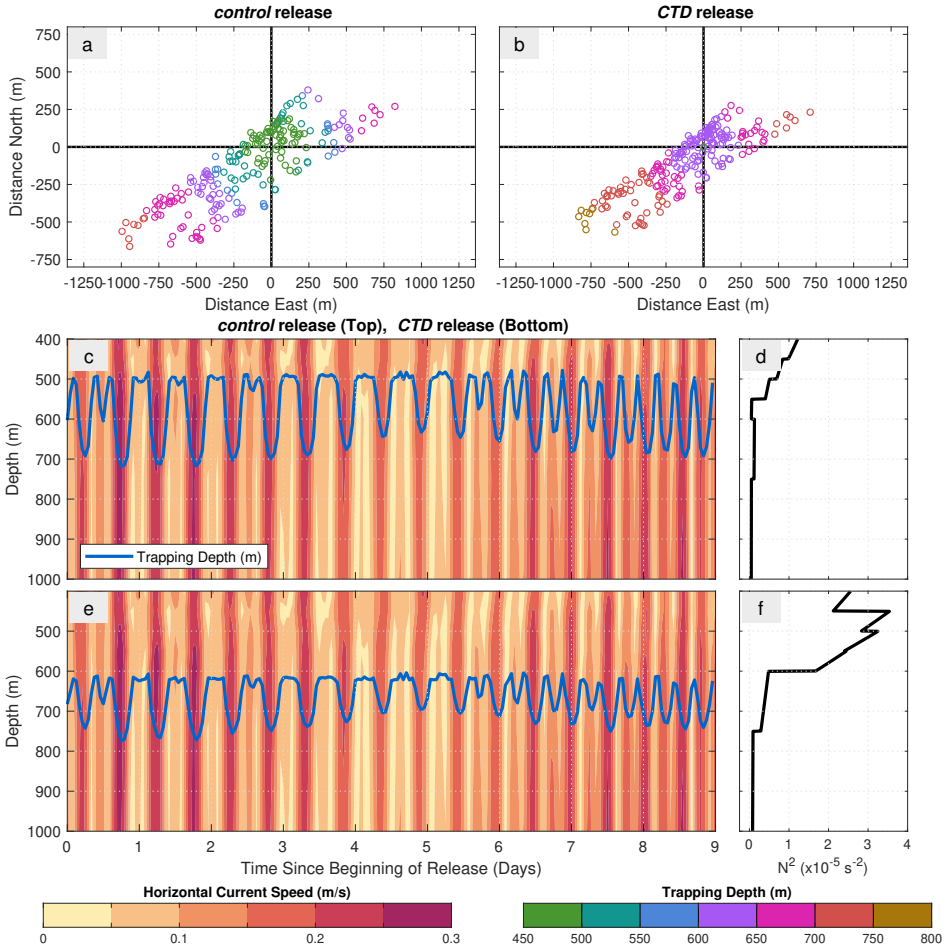

Figure 5.10: Plume dynamics the *control* and *CTD* releases. (**a, b**) Trapping location of the subsurface plume for the *control* release (left) and the *CTD* release (right), relative to the release location. (**c**) Contoured current speed from the *control* release location, where the blue line indicates trapping depth. (**d**) Buoyancy frequency squared used by OSCAR for the *control* release. (**e, f**) As (c, d), but for the *CTD* release.

5.6 RESULTS - INCLUSION OF OBSERVED STRATIFICATION

For both the *CTD* release and the *control* release, the DeepBlow model is forced with the same AMM15 model output of horizontal ocean currents. The only difference in input between both releases is the stratification profile; both are from February, but in different years and 80 km apart from each other. The profile obtained from CTD observations has a pycnocline order 100 m deeper than the AMM15 model output (Fig. 5.5d. Additionally, the maximum density gradient is much stronger from the CTD observations, with higher N^2 at 400–600 m (Fig. 5.10d, f). The higher N^2 in

the CTD profile leads to deeper plume trapping for the *CTD* release compared to the *control* release. For the *CTD* release, the trapping depth is between 603 m and 774 m, with an average of 666 m. This average is order 100 m deeper than the average trapping depth for the *control* release (574 m).

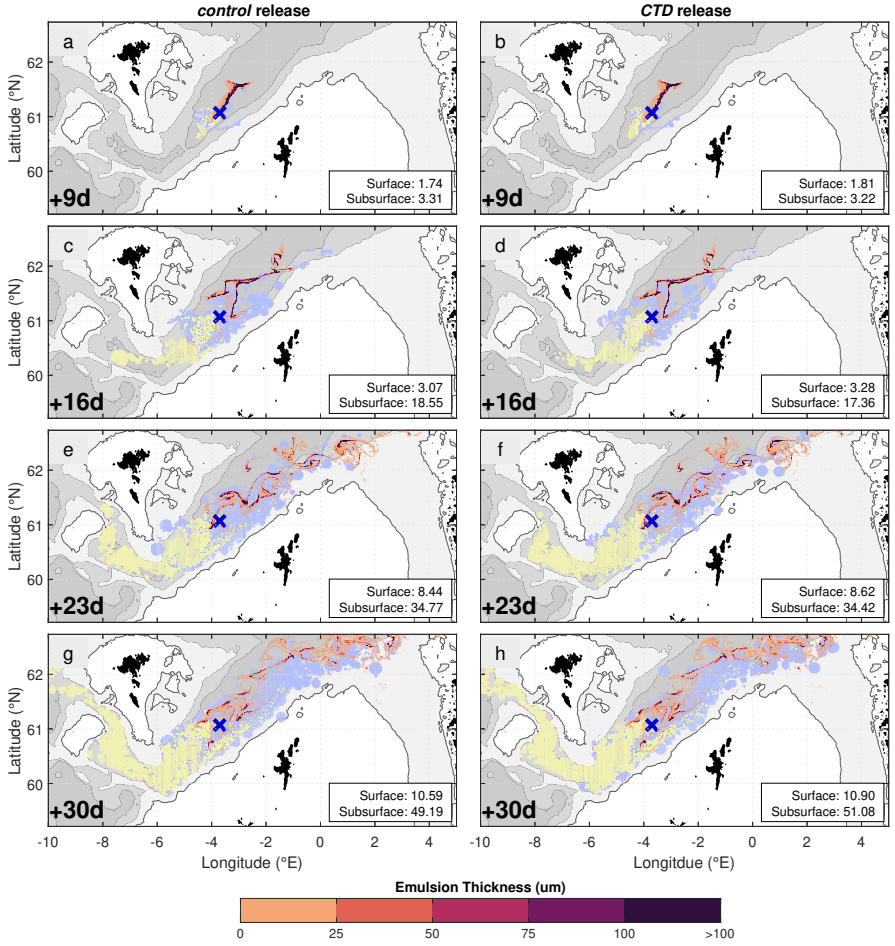

Figure 5.11: Far-field transport of pollutant for the *control* and *CTD* releases. (**a, b**) Surface emulsion thickness nine days after the beginning of the release (colour scale). Light blue and yellow both show where depth-integrated subsurface pollutant exceeds 5 kg km^{-2}, but with maximum concentration above and below 500 m, respectively. (**c, d**) As (a, b), but 16 days after the beginning of the simulation. (**e, f**) As (a, b), but 23 days after the beginning of the simulation. (**g, h**) As (a, b), but 30 days after the beginning of the simulation. Release location is shown as a blue cross. Units of surface and subsurface coverage are 10^9 m^2. Bathymetry has a scale identical to Fig. 5.1.

The differences in plume dynamics between the *CTD* release and the *control* release do not lead to any notable differences in the far-field advection and dispersion of oil (Fig. 5.11). The surface and subsurface spatial distributions are schematically identical throughout the simulation period. The surface spatial coverage after 30 days

Table 5.5: Percentage mass balance for different model components at the end of the simulation period (30 days) for the *control* and *CTD* releases.

Component	***control*** **(%)**	***CTD*** **(%)**
On surface	68.78	68.59
Evaporated	13.24	13.50
Submerged	12.26	12.61
Biodegraded	0.00	0.00
In sediment	0.15	0.19
Escaped	5.57	5.10

for the *CTD* release is higher than for the *control* release by a factor of 1.04 (Fig. 5.11g, h. This coincides with a slightly higher proportion of oil that has evaporated (13.50%, compared to 13.24% for the *control* release), but this difference is negligible and does not provide confidence for a causal link. The total amount of oil that has surfaced is 87.19% for the *CTD* release (compared to 87.59% for the control release). The 0.4% difference is smaller than the difference in the proportion of escaped oil (0.47%; Table 5.5).

5.6.1 KEY POINTS

- Differences between observed and modelled stratification lead to differences in plume dynamics.
- Differences in plume dynamics do not lead to notable differences in far-field advection when the same current forcing is used.

5.7 DISCUSSION

In this chapter, large oil spills originating from the FSC were simulated using realistic ocean currents and stratification. Several simulations were performed using different release locations, different times of the year, and with either modelled or observed stratification. Surfaced oil and submerged oil in the upper water-column (< 500 m depth) will predominantly be advected north-eastward through the central FSC and into the Norwegian sea. Submerged oil in the lower water-column (> 500 m depth) will predominantly be advected westward through the FBC and into the open North Atlantic. Plume behaviour is sensitive to the local currents and density gradient (as was also shown in Chapters 3 and 4), but this does not influence the proportion of oil that reaches the surface after 30 days unless the release depth changes considerably (e.g. in the case of the *shelf* release).

The mesoscale variability of the current field has an influence on the total surface and subsurface spatial coverage, and varies between the February and August current forcing fields. Physical processes visible in the 30-day mean current fields, such as the Shetland slope current and several semi-permanent eddy-like features, can have a major influence on oil advection. Furthermore, both the north Shetland coastline and the south-west Norwegian coastline are at considerable risk of contamination from the *August* and *shelf* releases, where oil is advected onto the Shetland shelf. Overall, this analysis shows that whilst the idealised results of Chapters 3 and 4 can partly explain the behaviour of a spill in a regional context, non-idealised physical processes can also have a substantial influence on far-field fate and trajectory.

5.7.1 HOW REPRESENTATIVE IS THE CALCULATION OF EDDY-KINETIC-ENERGY?

For the August current forcing field, the semi-permanent eddy-like features described in Section 5.4 are visible in the mean surface currents (Fig. 5.2b), but do not correlate with areas of calculated mean surface EKE (Fig. 5.2h). Mesoscale eddies act to disperse water through horizontal stirring (Quadfasel & Käse, 2007; Seim *et al.*, 2010; Voet *et al.*, 2010), and are therefore likely to enhance the entrainment and dispersion of oil. EKE is calculated in this analysis by subtracting various components of the

current field from $\boldsymbol{u}$ to determine $\boldsymbol{u}'$, including the 30-day mean $\overline{\boldsymbol{u}}$. It is therefore unsurprising that the eddy-like features are only visible in one of these fields. The two eddy-like features identified in August do however correspond to areas of enhanced EKE from earlier drifter observations (letters 'b' and 'e' in Fig. 5.12; Sherwin *et al.*, 2006). As these semi-permanent eddy-like features are useful for characterising the behaviour of an oil spill, it would probably be more useful in future calculations of EKE to use a longer time-series of currents, to capture processes that occur in the channel on inter-monthly scales.

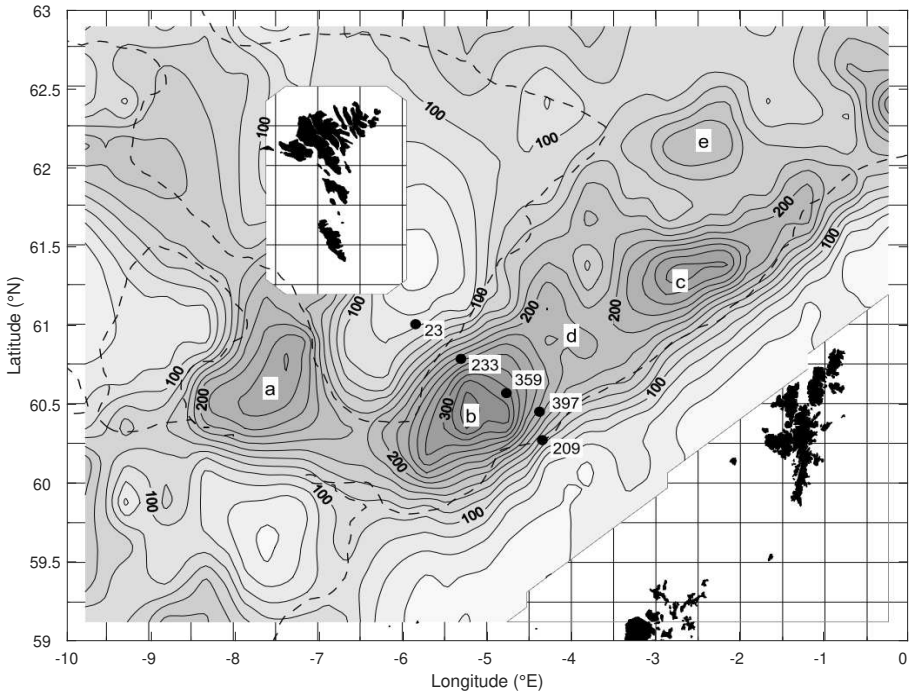

Figure 5.12: Observed EKE from drifters. Adapted from Sherwin *et al.* (2006). Solid contours are surface EKE ($\mathrm{cm^2\,s^{-2}}$), and dashed contours are the 500 m isobath. Letters 'a-e' correspond to enhanced areas of EKE.

5.7.2 POTENTIAL EFFECTS OF SURFACE WINDS AND BIODEGRADATION

Direct wind forcing was not included for any of the simulations in this analysis, because the intention was to isolate the influence of ocean currents. However, indirect wind forcing is present because AMM15 is forced by surface wind fields (Tonani *et al.*, 2019), and will therefore exhibit a surface Ekman layer. Typical wind speeds in the FSC are $10\,\mathrm{m\,s^{-1}}$ in February and $7\,\mathrm{m\,s^{-1}}$ in August (Gallego *et al.*, 2018). For this range of wind speeds, the surface Ekman layer at 60°N will be 50–100 m deep.

Oil advection and dispersion below the Ekman layer will not be directly or indirectly influenced by surface wind fields.

Direct wind forcing influences surface advection, which is calculated in the 3-D Fates model as the surface current velocity plus 3.6% of the surface wind velocity (Reed *et al.*, 1995). The results from this analysis inform us of the sensitivity of oil advection to ocean currents, but do not necessarily accurately predict the dispersion of oil in the real world. Direct wind forcing will probably be significant in the FSC; a wind speed of $10\,\mathrm{m\,s^{-1}}$ will contribute to $0.36\,\mathrm{m\,s^{-1}}$ of advection, which is often higher than the surface current velocity. Surface winds also influence emulsification and evaporation, and this analysis likely underestimates both the proportion of evaporated oil and the amount of surface spatial coverage. Future work should focus on incorporating climatological wind speed magnitude and variability, for example by using the 30-year monthly mean climatology presented by Gallego *et al.* (2018). A further improvement would be to provide wind as 6-hourly fields, as this will avoid the issue of averaging out extreme values of wind speed (and thus oil transport) from storms, for example.

Biodegradation is a second process that is not considered in this analysis (but is considered in Chapters 3 and 4). The rate of biodegradation is dependent on several factors including the ambient temperature[2], availability of light and nutrients, local bacterial colonies, and the chemical composition of the oil that is released (Beyer *et al.*, 2016). Biodegradation is likely to limit the extent of oil transport away from the FSC, but oil could still reach as far west as Greenland or as far north as the Arctic Circle before fully degrading (Main *et al.*, 2017). The rate of biodegradation will probably be higher for the *August* release due to a higher water-column temperature (Fig. 5.5b), and will probably be lower for the *shelf* release because of less oil submerged in the water-column compared to other releases (Table 5.4).

The idealised spill simulation performed in this thesis that is most representative of conditions in the FSC is the modified non-linear N^2 mode 1 simulation (Section 4.8.3). After 24 h, one-eighth of the total amount of submerged oil has biodegraded. However, for the regional simulations the release rate is greater ($0.130\,\mathrm{m^3\,s^{-1}}$, compared to $0.03\,\mathrm{m^3\,s^{-1}}$ used in Chapter 4). An increased release rate decreases

[2]Primary productivity is proportional to temperature for the same bacteria. However, it is likely that bacterial colonies will have adapted to their local conditions, and so ambient temperature may not be a major control.

the mean droplet diameter (Fig. 5.13) which will increase the rate of biodegradation because of a higher surface area to volume ratio.

5.7.3 IMPLICATIONS OF CHANGING THE RELEASE RATE

The release rate might change the trapping depth of a plume (Section 3.9.2), and might also alter the droplet size distribution of liquid oil in the water-column because of a different expulsion velocity at the well-head. To investigate whether changing the release rate has any notable influence on a regional spill, the first nine days of the *control* release was repeated, but with an identical release rate to what was used in Chapters 3 and 4. This release is hereafter referred to as the *reduced* release.

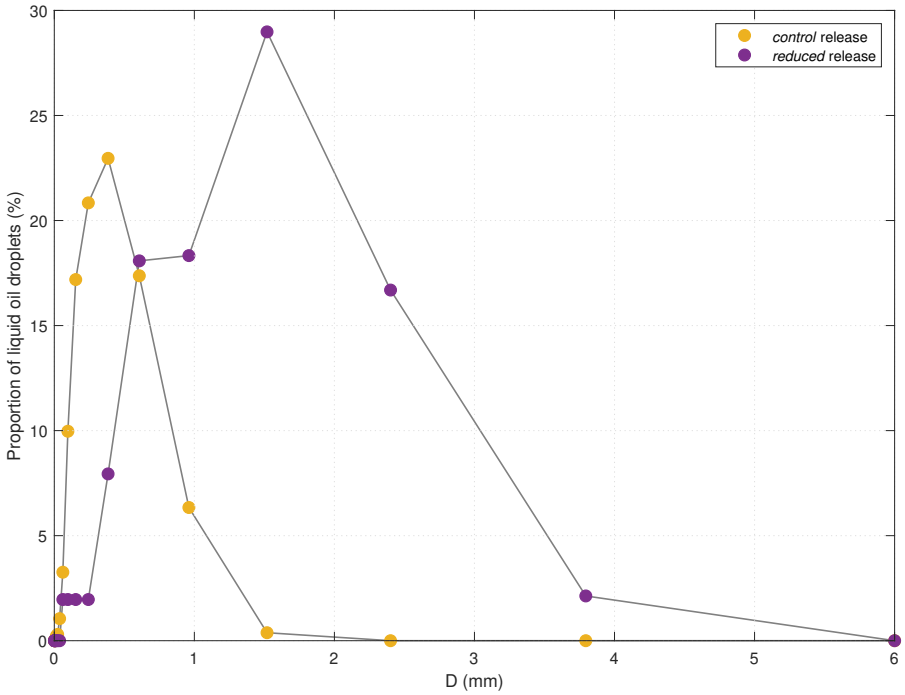

Figure 5.13: Droplet size distribution of subsurface liquid oil droplets at the end of the release period (9 days) for the *control* release and *reduced* release.

For the *reduced* release, the trapping depth is between 614 m and 886 m (compared to 478–718 m for the *control* release), with an average of 757 m (compared to 574 m). After nine days, 12% of the total volume of released oil remains below the surface for the *reduced* release (compared to 21% for the *control* release), despite an order 100 m deeper trapping depth. The lower proportion of submerged oil is because of a larger droplet size distribution (Fig. 5.13), which increases the average droplet

buoyancy and reduces the time taken to surface. Larger droplets will also take more time to fully dissolve into the water-column, which will act to decrease the proportion of submerged oil after a longer period (i.e. after 30 days).

5.7.4 IMPLICATIONS FOR THE EVENTUAL FATE OF OIL

Our results are similar to earlier regional modelling of oil spills originating from the FSC. Main *et al.* (2017) show that oil shallower than 400 m is advected predominantly north-eastward, and that oil deeper than this is advected predominantly westward. The authors suggest that when temperature-dependent biodegradation is considered, oil could travel as far north as the Arctic Circle, or as far west as Greenland. Main *et al.* (2017) have likely overestimated this extent, since local bacterial colonies will have adapted to local ocean conditions. Although the analysis presented in this chapter is not on a global scale, advection differences between deep and shallow oil suggests a similar longer-term fate. The advantage to the analysis in this chapter is that mesoscale processes such as eddies have been explicitly resolved (the horizontal resolution of AMM15 is 1.5 km, whereas the horizontal resolution of the global NEMO configuration used by Main *et al.* (2017) is 1/12°, or approximately 7 km). Mesoscale eddies can act to trap oil for several weeks, since water tends to continuously recirculate around the eddy core.

A trade-off of using a higher model resolution is that the model domain is restrictive and some oil escapes. Escaped oil is exclusively from surface emulsion through the north-east model boundary for all releases, excluding the basin release where a very small amount of submerged oil escapes through the west model boundary. The amount of evaporated oil after 30 days is an underestimation, because the process of evaporation does not take place for oil that is no longer considered in the simulation. However, oil escapes the model domain only during the final five days of the simulation period, and the total amount of escaped oil after 30 days is small (11% of the total volume or less). Therefore, this underestimation is not a substantial one.

Within the model domain, this analysis suggests that currents in the FSC can advect oil towards the north Shetland islands and the south-west Norway. With the addition of wind, oil could potentially be advected and dispersed towards other land

masses. Throughout the year, surface winds are typically north-eastward (Gallego *et al.*, 2018). This will help to deflect oil away from the north Shetland coastline, but will promote the beaching of oil onto the Norwegian coastline, particularly in June where surface winds are predominantly eastward.

As more time than 30 days passes, oil will continue to evaporate, reducing the volume of oil that needs to be manually removed from the sea surface. At the same time, the viscosity of the surface emulsion will increase, providing a greater challenge for recovery equipment. Additionally, the surface and subsurface spatial coverages and extents will almost certainly continue to increase due to dispersion by currents, making it logistically more difficult to contain any oil. Tracking of the surface slick will also become more difficult over time as the average thickness of the emulsion decreases.

6

INCREASED DISPERSION OF OIL FROM A DEEP-WATER SEABED RELEASE BY ENERGETIC MESOSCALE EDDIES[1]

6.1 ABSTRACT

In addition to surface winds, hydrodynamics play a critical role in determining the trajectory of an oil spill. Currents, stratification and mesoscale processes all contribute to how a spill behaves. Using an industry-leading oil spill model, we compare forecasts of oil dispersion when forced with two different hydrodynamic models of the North-West European Shelf (7 km and 1.5 km horizontal resolution). This demonstrates how the trajectory of a deep-sea (> 1000 m) release in the central Faroe-Shetland Channel is influenced by explicitly resolving mesoscale variability. The finer resolution hydrodynamic model dramatically enhances the horizontal dispersion of oil, altering surface emulsion characteristics and transporting pollutant farther afield. This is a consequence of higher mesoscale variability. Stratification influences the depth of subsurface plume trapping and subsequently the far-field

[1] This work has previously been submitted in its current form for peer-review in Geophysical Research Letters (initial submission of May 29th, 2019). I acknowledge the contributions of the co-authors of this submission; Robert Hall, John Bacon, Jon Rees, and Jennifer Graham. It is currently being revised for resubmission. Please note that because this version was written before final thesis re-drafts, there may be inconsistent terminology between this chapter and the other chapters.

transport of oil. These results demonstrate that the choice of hydrodynamic model resolution is crucial when designing particle tracking experiments.

6.1.1 KEY POINTS

1. An oil spill is simulated in the Faroe-Shetland Channel, forced by hydrodynamic models with different horizontal resolutions.

2. Explicitly resolving mesoscale eddies leads to dramatically increased horizontal pollutant dispersion at and below the surface. However, the accuracy of the eddy field is also likely to be an important control, and so data assimilation should be considered for future simulations.

3. A change in stratification leads to differences in subsurface plume trapping depth and subsequent far-field transport.

6.1.2 PLAIN LANGUAGE SUMMARY

The Deepwater Horizon oil spill in the Gulf of Mexico was one of the worst environmental disasters in history. In order to increase preparedness and minimize the potential impacts, we use numerical modelling to predict the trajectory and fate of a potential spill, to inform us where the clean-up should take place. The behaviour of oil in water is complicated, with temperature, salinity and currents all influencing its dispersion, in addition to surface winds. This study gives us an insight into how a large spill in the Faroe-Shetland Channel (North Atlantic), a region of active drilling in UK waters, might behave when we include smaller ocean processes such as mesoscale eddies. By including these processes, we discover that oil is dispersed over a much larger area both at the surface and within the water-column, and can travel either north-eastward towards the Nordic Seas, or westward into the open North Atlantic, depending on the depth at which it resides. We use the same spill and hydrodynamic models that are utilized by emergency response, so lessons learnt from this work can be directly applied to industry.

6.2 INTRODUCTION

Oil spills from seabed releases are a worldwide risk to the marine environment, and drilling is gradually pushing into deeper waters as a result of resource discovery and technological innovation (Burgherr, 2007; Gallego *et al.*, 2018). Deepwater Horizon (DWH) is the highest profile example of a deep-seabed release, costing BP $145 billion (Lee *et al.*, 2018) and spilling 700 000–800 000 m^3 of oil over 86 days (Camilli *et al.*, 2010; Crone & Tolstoy, 2010; McNutt *et al.*, 2012; Joye *et al.*, 2016). Deep-water drilling also occurs in the Faroe-Shetland Channel (FSC, Fig. 6.1) in the North Atlantic, which has been a region of UK oil and gas development since the early 1990s (Smallwood & Kirk, 2005). As of August 2018, there were 162 active well heads in the FSC (source: UK Oil and Gas authority), three-quarters of which were deeper than 200 m. A spill in the FSC lasting for 30 days could result in up to 3.4×10^5 m^3 of oil released (Gallego *et al.*, 2018).

The FSC is a hydrodynamically complex and energetic environment. A strong slope current (up to 1 $m\,s^{-1}$) along the west Shetland slope transports warm, saline surface water north-eastward towards the Norwegian Sea and eventually into the Arctic. Near the seabed at > 1000 m depth, a bottom current transports relatively cold, fresh deep-water south-westward, which either follows bathymetry through the Faroe Bank Channel (FBC) into the open North Atlantic, or overflows the Wyville-Thomson Ridge (WTR) into the Rockall Trough (Turrell *et al.*, 1999; Sherwin *et al.*, 2008). Mesoscale eddies can extend across the width of the channel and south of the Faroe Islands near the FBC (Sherwin *et al.*, 1999, 2006; Darelius *et al.*, 2011). Large internal tides and non-linear internal waves have been observed in the region, which can act to increase turbulent mixing rates (Sherwin, 1991; Hosegood & van Haren, 2004; Hall *et al.*, 2011, 2019). A unique stratification structure is also present, where the thermocline typically resides at several hundred meters below the sea surface and separates the exchanging water masses (Berx *et al.*, 2013; Fig. 6.1c, d, e).

The behaviour of oil from a seabed release depends on ocean currents and stratification, in addition to properties of the oil such as viscosity, temperature, gas-oil ratio (GOR), flow rate and orifice diameter (Yapa & Chen, 2004). Previous plume modelling suggests that oil will be trapped at 650–800 m depth from a 1000 m release in the FSC, depending on the release rate and ambient ocean conditions (Johansen,

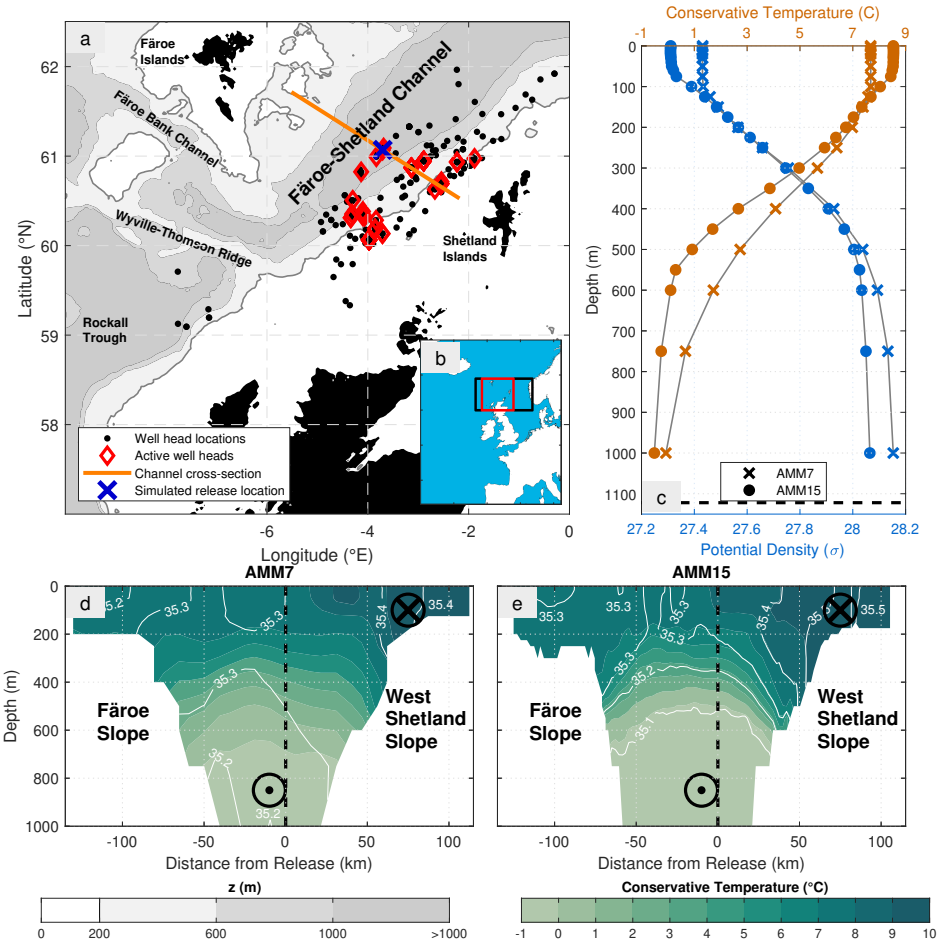

Figure 6.1: Overview of the Faroe-Shetland Channel (FSC). (**a**) Well head locations in the FSC (source: UK Oil and Gas Authority), with active well heads shown as red diamonds, and the simulated release location shown as a blue cross. Bathymetry is from Smith & Sandwell (1997). (**b**) Location of the FSC as shown in (a) (red box), and the spill model domain (black box). (**c**) Profiles of potential density (blue) and conservative temperature (red) at the release location from both hydrodynamic models. Release depth is indicated by a black dashed line. (**d, e**) Representative cross-channel sections of conservative temperature (filled contours, °C) and absolute salinity (white contours, $g kg^{-1}$) from AMM7 (left) and AMM15 (right), along the orange line in (a). Release location is indicated by a black dashed line. Also shown are approximate locations and directions of the slope current and bottom current. Typical currents in the FSC are discussed in Section 2.7. For clarity, 1995-2009 averaged along-slope currents are shown in Fig. 6.2.

2000b). Main *et al.* (2017) used a global ocean circulation model based on the Nucleus of European Modelling of the Oceans (NEMO; Madec, 2016) to predict the transport of oil from the FSC, and found that far-field oil transport was dependent on depth. Oil near the surface travelled north-eastward towards the Arctic Circle, whereas oil trapped at depth reached as far west as Greenland. However, they did not consider the influence plume dynamics might have on the vertical distribution of pollutant,

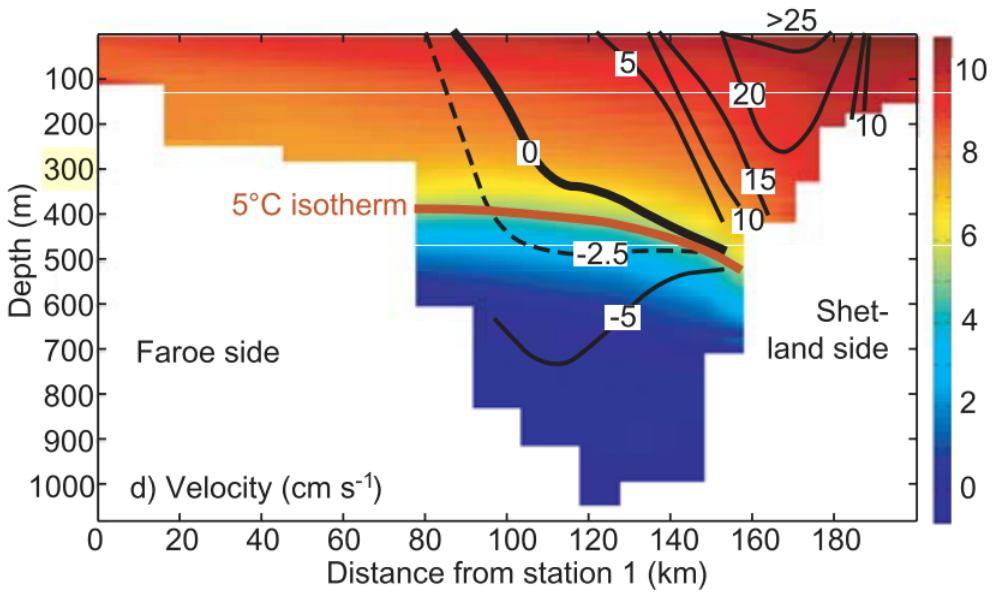

Figure 6.2: 1995-2009 average of along-slope velocities in the FSC (black contours) and θ (colour scale). Adapted from Berx *et al.* (2013). Repeated from Section 2.7.

or the role of surface weathering processes such as evaporation and emulsification. Additionally, the horizontal resolution of the model (1/12°) was coarser than required to explicitly resolve mesoscale eddies in the FSC region (2 km or less; Oey, 1998).

Oil Spill Contingency and Response (OSCAR) is the modelling system typically used by institutions such as OSRL and Cefas to predict the fate and trajectory of a release during emergency response. OSCAR comprises of a 3-D fates model (Reed *et al.*, 1995, 2000), near-field plume model (Johansen, 2000a) and droplet breakup model (Johansen *et al.*, 2013), and is typically forced with velocities from an operational hydrodynamic ocean model. OSCAR has been well-validated from historical emulsion observations (Abascal *et al.*, 2010) and from the DeepSpill field experiment (Johansen *et al.*, 2003).

In this study, OSCAR is used to consider how oil from a seabed release in the FSC could be transported by hydrodynamic processes, and how an increase in hydrodynamic model resolution influences dispersion. We demonstrate that enhanced mesoscale variability leads to a dramatic increase in horizontal dispersion, and that stratification influences the depth of trapping and subsequent far-field transport. These results will help guide the choice of hydrodynamic forcing for emergency spill forecasting.

6.3 HYDRODYNAMIC FORCING

To force OSCAR, both Oil Spill Response (OSRL) and the UK Centre for Environment, Fisheries and Aquaculture Science (Cefas) currently use operational ocean forecasts based on the UK Met Office 7 km horizontal resolution Atlantic Margin Model of the North-West European Shelf (FOAM AMM7 NWS, hereafter referred to as AMM7; Edwards *et al.*, 2012; O'Dea *et al.*, 2012). In November 2018, an updated version of this model became available to use operationally (FOAM AMM15 NWS, hereafter referred to as AMM15; Graham *et al.*, 2018; Tonani *et al.*, 2019). Both models are based on NEMO v3.6. They are forced using surface pressure and wind fields, and assimilated with sea surface temperature, sea surface height and temperature/salinity profiles using the methods described in King *et al.* (2018). Operational output is available from EU Copernicus Marine Services Information (2018a,b). This paper provides a comparison of these two hydrodynamic models when they are used to force an oil spill simulation.

AMM15 has a finer horizontal resolution of 1.5 km, which is high enough to explicitly resolve mesoscale eddies within the FSC. Resolving bathymetry at 1.5 km also provides a mechanism for increased internal wave generation (Guihou *et al.*, 2017). AMM7 and AMM15 are both run with 51 vertical levels, but the operational output of AMM15 is finer (33 vertical levels from 0–5000 m, compared with 24 for AMM7). Tonani *et al.* (2019) show that AMM15 performs better than AMM7 against ocean glider observations of density, and against HF radar observations of surface currents.

A 30 day period (1 February, 2017 to 3 March, 2017) is analysed, as outputs are available from both hydrodynamic models. Three-dimensional, hourly instantaneous current velocities are used to force both the 3-D fates model and plume model. Due to limitations in the plume model, only time-constant, single-point-profiles of temperature and salinity can be used to represent stratification. These are taken from the nearest hydrodynamic model grid-point to the release location on 1 February, 2017 (Fig. 6.1c). There is likely to be a systematic positive salinity bias in AMM7 of order 0.1 (Fig. 6.1d, e), but it is beyond the scope of this chapter as to why this may be the case.

Fig. 6.3 shows a surface current decomposition for both hydrodynamic models.

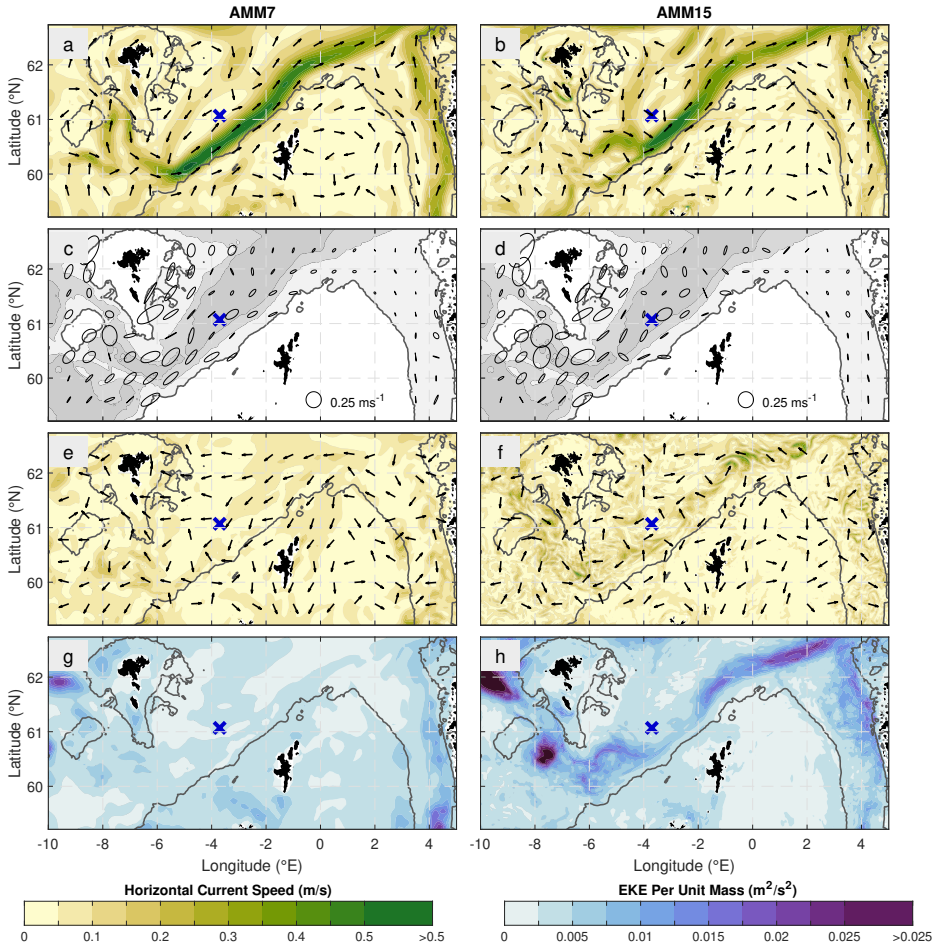

Figure 6.3: Surface current decomposition for AMM7 and AMM15. (**a, b**) Thirty-day mean surface current velocity, with magnitude shown as filled contours, and direction shown by arrows. (**c, d**) M_2 tidal ellipses, masked on the shelf (< 200 m). (**e, f**) Residual surface current velocities at the end of the release period on 10 February, 2017. (**g, h**) Thirty-day surface mean eddy kinetic energy (EKE) per unit mass. The shelf edge (200 m isobath) is shown as a dark grey contour, and release location is shown as a blue cross. Bathymetry has a scale identical to Fig. 6.1.

Semidiurnal (M_2) tidal ellipses are computed by harmonic analysis over 30 days using Utide (Codiga, 2011). Residual surface currents associated with the mesoscale eddy field are extracted by de-tiding, de-meaning and de-trending the instantaneous currents. Thirty-five tidal constituents are resolved using a minimum Rayleigh criterion of 1. Surface eddy kinetic energy (EKE) per unit mass is calculated $EKE = 1/2(u^2 + v^2)$, where u and v are the zonal and meridional components of the residual surface currents. EKE is calculated to quantify the mesoscale current variability of both hydrodynamic models and averaged over the 30 day period. Our calculations of monthly mean EKE for AMM15 (Fig. 6.3h) show that the locations of enhanced eddy

activity are similar to drifter observations (Sherwin *et al.*, 2006; 0.015–0.025 $m^2 s^{-2}$ within the central FSC and the FBC). Mean EKE in these locations for AMM7 is considerably lower (< 0.005 $m^2 s^{-2}$).

6.4 MODELLING THE OIL SPILL

Oil is released from the seabed (1122 m depth) on 1 February, 2017 for nine days at 61.07°N, 3.705°W. Nine days was chosen as it ensures project tractability whilst being within the range of the likely length of time of accidental leak (i.e. between 1 h for the CLAIR release, and 3 months for DWH). In reality, it is difficult to precisely predict the duration of the release. The location was chosen because it is in an area with several active wells (Fig. 6.1a). The simulation is run for 30 days, which accounts for the release period plus three weeks of further dispersion. A total of 100 700 m^3 of oil is released at a constant rate of 0.130 $m^3 s^{-1}$, guided by the estimate of Gallego *et al.* (2018). The oil exits from an orifice with diameter 0.1 m, similar to the DeepSpill field experiment (Johansen *et al.*, 2003) and subsurface plume modelling by Yapa & Chen (2004). Clair oil type is used, with a density of 893.8 $kg m^{-3}$ and initial temperature of 10 °C. Methane gas is released alongside oil with a GOR of 200, similar to previous studies (Yapa & Chen, 2004). Due to the high pressures and low temperatures associated with this release, only methane hydrates were present during the plume phase, which retain a constant density of 930 $kg m^{-3}$ (Johansen, 2000a).

The plume model time-step is 5 s, and the plume is terminated when the vertical velocity reaches zero. Plume profiles are computed hourly, to capture variability over the semidiurnal tidal cycle. The 3-D fates model time-step is 10 min. A total of 30 000 liquid/solid particles, 30 000 dissolved particles and 30 000 methane particles are used to track the far-field fate of the pollutant within the model domain (57–62°NN, 12°W-6°E). This domain is restrictive at the northern boundary due to the extent of the AMM15 domain. Oil that travels outside of the model domain is defined as 'escaped' and is almost exclusively from the surface. Vertical resolution is 50 m and horizontal resolution is 1.5 km for both simulations, ensuring that spill dynamics are captured on the same spatial scale as the highest resolution hydrodynamic model. Oil that reaches the surface is tracked and can emulsify with water or evaporate.

The hydrodynamic models are used as forcing only and are not coupled with

OSCAR. Horizontal current velocities are interpolated onto the 3-D fates model grid. In the plume model, standard method 2520C (Millero & Poisson, 1981) is used to calculate density and buoyancy frequency squared (N^2) from in-situ temperature and practical salinity. Practical salinity is a direct output of the hydrodynamic models; in-situ temperature is calculated from output potential temperature using the Gibbs Seawater oceanographic toolbox (McDougall & Barker, 2011). The operational outputs of AMM7 and AMM15 do not extend to the seabed, so values of temperature and salinity deeper than 1000 m are extrapolated using a nearest-neighbour method. Wind forcing and biodegradation are not considered in this study. Therefore, 'surface transport' is defined in this study as the transport of oil residing on the sea surface by ocean currents only.

6.5 RESULTS

6.5.1 SURFACE TRANSPORT

Pollutant at the surface for the AMM7 release resides close to, and slightly west of, the release location for approximately two weeks (Fig. 6.4a, c). The surface emulsion is then transported by the slope current in a continuous band north-eastward, parallel to the 600 m isobath (Fig. 6.4e, g). For the AMM15 release, initial surface transport is north-eastward, and the emulsion has already begun to diverge into two distinct branches by the end of the release period (Fig. 6.4b). The emulsion continues to travel along the channel in separate patches that become increasingly small and numerous (Fig. 6.4d, f, h). Some of the emulsion is transported by the slope current, but the majority resides farther west. Differences in surface transport between simulations can be partly accounted for by differences in the mean surface circulation (Fig. 6.3a, b); for both hydrodynamic models, a surface current recirculates water anti-clockwise around the south of the release location. The location of this recirculation is different for AMM7 and AMM15. There are relatively high velocities ($> 0.2\,\mathrm{m\,s^{-1}}$) close to the release location for AMM15, but a region of lower velocities ($< 0.05\,\mathrm{m\,s^{-1}}$) to the west for AMM7. This explains the initial retention of surface emulsion around the release location. It is difficult to say which model is more 'correct' in this instance, since the location of the mesoscale eddy cannot be verified by observation. The

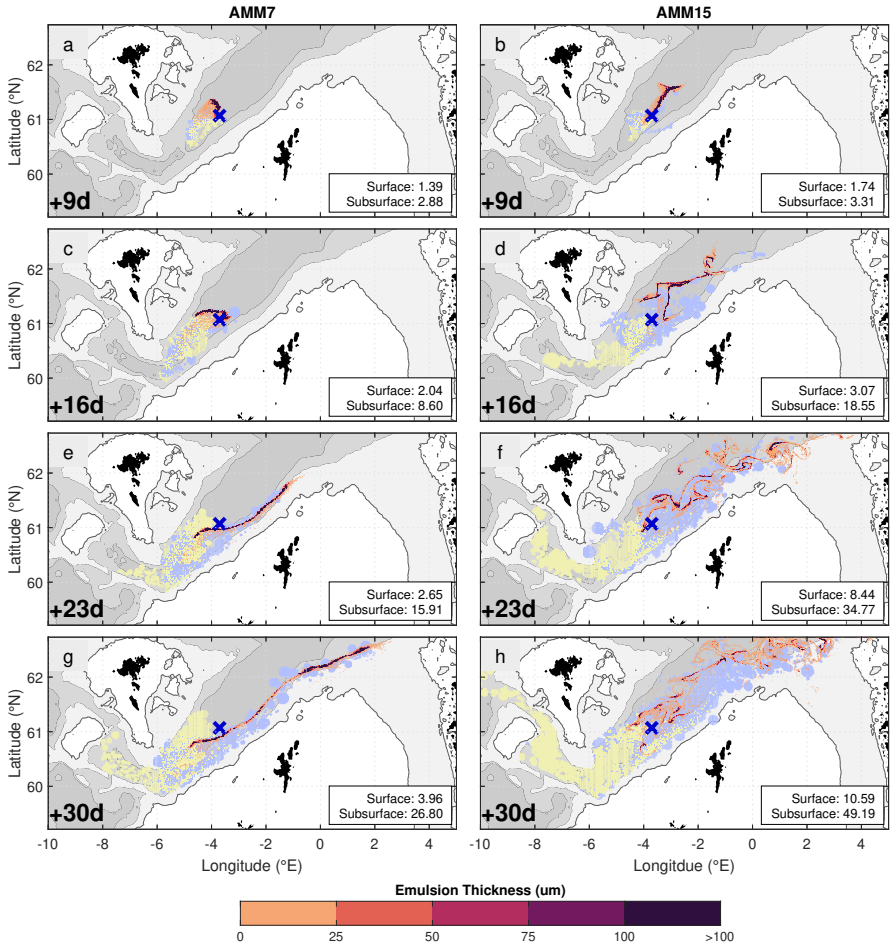

Figure 6.4: Far-field transport of pollutant for AMM7 and AMM15. (**a, b**) Surface emulsion thickness nine days after the beginning of the release (colour scale). Light blue and yellow both show where depth-integrated subsurface pollutant exceeds 5 kg km^{-2}, but with maximum concentration above and below 500 m, respectively. (**c, d**) As (a, b), but 16 days after the beginning of the simulation. (**e, f**) As (a, b), but 23 days after the beginning of the simulation. (**g, h**) As (a, b), but 30 days after the beginning of the simulation. Release location is shown as a blue cross. Units of surface and subsurface coverage are 10^9 m^2. Bathymetry has a scale identical to Fig. 6.1.

substantially higher surface *EKE* along the shelf slope for AMM15 (Fig. 6.3h) is a potential mechanism for diverting pollutant away from the primary slope current. No surface emulsion is transported onto the shelf (< 200 m) for either model run, but the distribution would likely change with the addition of wind forcing to the north-east, as is typical for the region during February (Gallego *et al.*, 2018).

For both releases, approximately 87.5% of oil surfaces after 30 days (Table 6.1). consisting of an oil-water emulsion (75%), and more volatile components that have evaporated (12.5%). For the AMM15 release, 5.6% of oil escapes the north-west

Table 6.1: Percentage mass balance for different model components at the end of the simulation period (30 days) for the AMM7 and AMM15 releases.

Component	**FOAM AMM7 NWS** (%)	**FOAM AMM15 NWS** (%)
On surface	74.69	68.78
Evaporated	12.67	13.24
Submerged	12.64	12.26
Biodegraded	0.00	0.00
In sediment	0.01	0.15
Outside model domain	0.00	5.57

boundary of the domain (compared to zero for AMM7), but this mass is assumed to be part of the surfaced mass because it escapes during the final five days and is almost exclusively from surface emulsions.

After nine days, surface coverage is a factor of 0.25 greater for the AMM15 release. The proportion of the total mass of oil residing on the sea surface at this time is 72% for both releases. The emulsion from the AMM15 release has not had sufficient time to break up into multiple patches, and the full effect of additional mesoscale variability cannot yet be seen quantitatively. After 30 days, surface coverage is a factor of 2.7 greater for the AMM15 release. The total mass of oil on the surface at the end of the simulation is similar, so cannot account for the increase. However, likely as a result of increased EKE availability, mean water content in the emulsion is higher (43.2% compared with 33.2% for AMM7), and the mean emulsion thickness is lower (14.0 µm compared with 31.1 µm). This means that there is a higher volume of emulsion that is spread out more thinly on the sea surface.

6.5.2 SUBSURFACE TRANSPORT

For both releases, approximately 12.5% of oil is trapped below the surface after 30 days. Most of this (90%) is dissolved into the water-column. The remaining mass consists of small (< 100 µm) liquid droplets, which have an almost neutral buoyancy. In reality, these droplets will either remain within the water-column indefinitely, slowly rise to the surface, mix with sediment, dissolve, or biodegrade (Beyer *et al.*, 2016).

Trapping depth, where vertical velocity of the plume reaches zero, is different

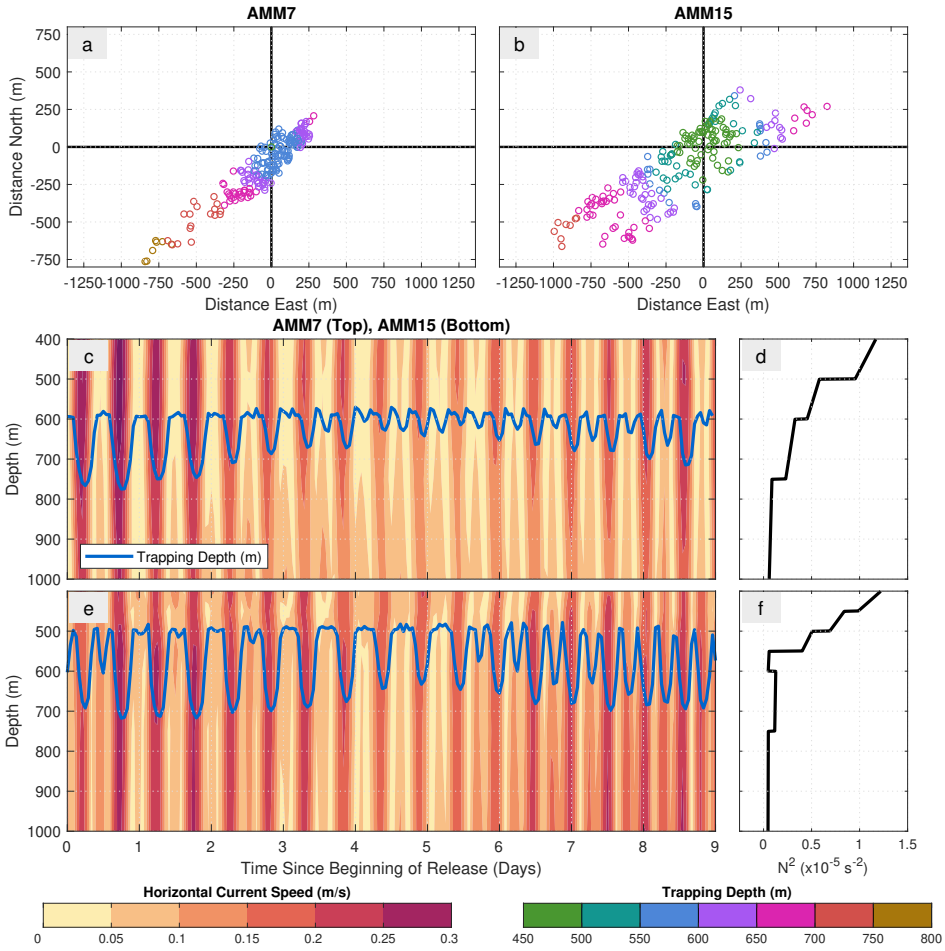

Figure 6.5: Plume dynamics for AMM7 and AMM15. (**a, b**) Trapping location of the subsurface plume for AMM7 (left) and AMM15 (right), relative to the release location. (**c**) Contoured current speed from AMM7 at the release location, where the blue line indicates trapping depth. (**d**) Buoyancy frequency squared used by OSCAR from AMM7. (**e, f**) As (c, d), but for AMM15.

for each simulation (Fig. 6.5). For the AMM7 release, trapping depth is 570–775 m, with an average of 622 m. For the AMM15 release, trapping depth is 478–718 m, with an average of 574 m. To separate the influence of stratification and currents, we repeated the simulations with the same AMM7 and AMM15 stratifications, but with current velocity set to zero for both cases (not shown). This leads to a trapping depth of 595 m and 497 m, respectively. The plume traps at a greater depth for the AMM7 release as a result of increased N^2 at 450–1000 m, and thus increased energy required to advect entrained water compared to the AMM15 release (Fig. 6.5d, f). This difference in N^2 is apparent across the channel (Fig. 6.1d, e). Current flow also acts to deepen the trapping depth, and this varies semidiurnally (Fig. 6.5c, e). The horizontal

distribution of trapping shows an asymmetric, approximately rectilinear tide parallel to the shelf slope and with a bias to the south-west (Fig. 6.5a, b). The maximum concentration of trapped oil at the end of the release period (not shown) is typically 75 m above the top of the plume, at 550 m (AMM7) and 500 m (AMM15).

Subsurface transport can be divided into two primary pathways. Deeper oil (maximum concentration at > 500 m) is transported westward through the FBC and restricted by the relatively shallow WTR. This transport is more rapid for the AMM15 release, with oil reaching the western boundary of the model domain. Shallower oil (maximum concentration at < 500 m) is transported north-eastward through the FSC along the continental slope, following a similar trajectory to the surface emulsion. Pollutant from the AMM7 release resides close to the shelf edge, but for AMM15 it is spread more broadly across the channel. Oil escapes from the surface at the northern boundary for the AMM15 release.

After nine days, the subsurface spatial coverage of oil is 15% higher for the AMM15 release than for the AMM7 release (Fig. 6.4a, b). This is partly a consequence of an increased spread of plume trapping locations (Fig. 6.5a, b). After 30 days, there is almost twice the amount of subsurface coverage. Higher EKE for AMM15 through the water-column may contribute to increased deep horizontal dispersion (Fig. 6.6). Enhanced mesoscale variability at up to 800 m depth has also been previously observed within the FSC (Dooley & Meincke, 1981; Sherwin *et al.*, 1999). A second contributing factor for increased dispersion for the AMM15 release could be higher mean current velocities at depth, particularly south of the Faroe Islands at 600 m and 750 m (Fig. 6.7), which will result in oil at these depths transported more rapidly away from the release location.

6.6 DISCUSSION

Oil transport from a deep-water release in the central FSC will divide into two main pathways. Oil that has reached the surface, in addition to oil trapped in the upper portion of the water-column, will predominantly travel north-eastward along the continental slope towards the Norwegian Sea. Deeper oil will be transported westward, advected by deep currents and guided by bathymetry through the FBC and eventually out into the open North Atlantic. No oil overflows the WTR into the

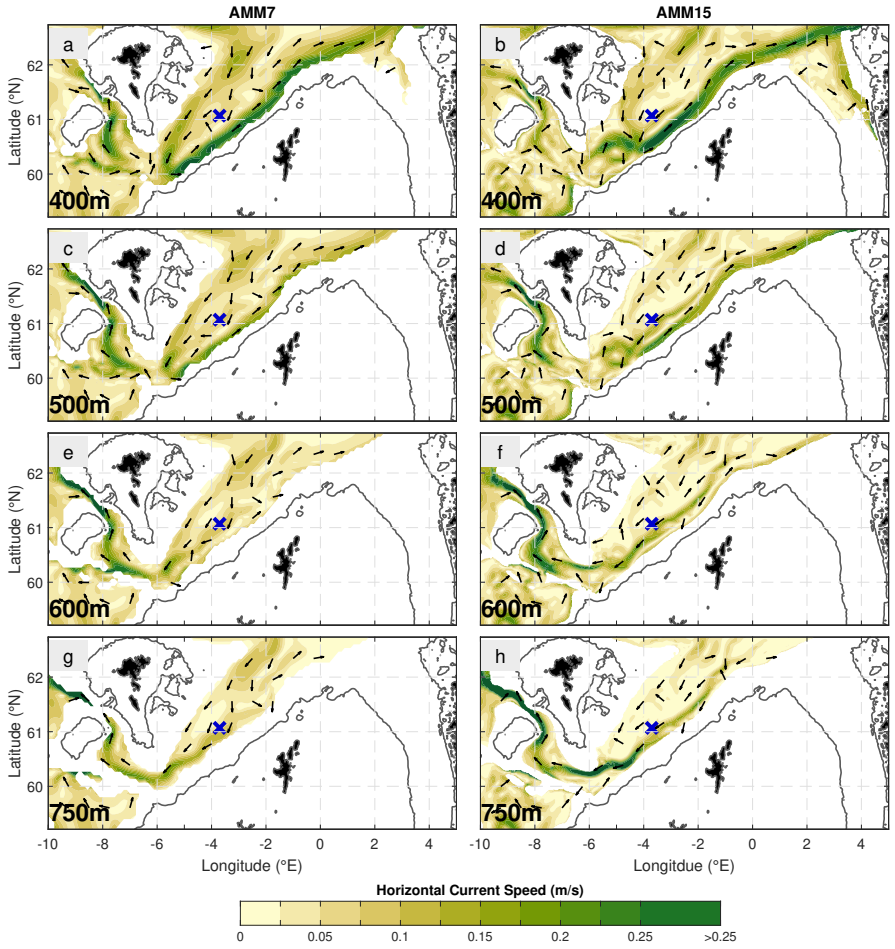

Figure 6.6: Monthly mean EKE per unit mass at different depths for AMM7 and AMM15. (**a, b**) 400 m. (**c, d**), 500 m (**e, f**) 600 m. (**g, h**) 750 m. The shelf edge (200 m) is shown as a dark grey contour, and release location is shown as a blue cross. Bathymetry has a scale identical to Fig. 6.1.

Rockall Trough in these simulations. A finer model resolution allowing for the explicit resolution of mesoscale processes increases the amount of EKE available for the horizontal dispersion of oil and its emulsification at the sea surface. This leads to increased spatial coverage, as well as a thinner emulsion with a higher water content.

The large-scale transport pathways highlighted in this study broadly agree with previous modelling work by Main *et al.* (2017), who found that oil transported at 400 m and shallower consistently reached the Norwegian Sea, whereas deeper transport was predominantly westward. Our study builds upon this research by considering the vertical distribution of oil from a plume model, the trajectory of particles that are not neutrally-buoyant, and smaller spatial scales that are more useful for emergency response. Emulsification and evaporation have also been considered, and have an

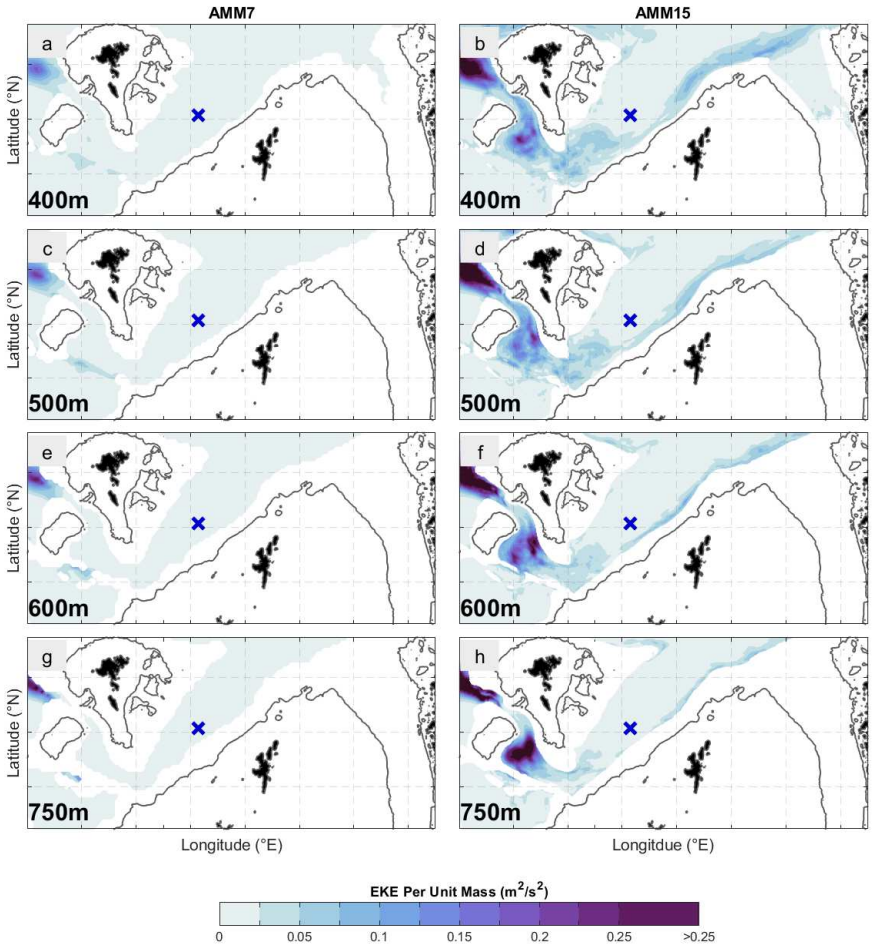

Figure 6.7: Monthly mean current velocities at different depths for AMM7 and AMM15. (**a, b**) 400 m. (**c, d**), 500 m (**e, f**) 600 m. (**g, h**) 750 m. Current magnitude is shown as coloured contours, and direction is shown by arrows. The shelf edge (200 m) is shown as dark grey contours, and release location is shown as a blue cross. Bathymetry has a scale identical to Fig. 6.1.

influence on the total mass of oil on the sea surface.

This study shows the likely range of depths that oil will become trapped at within the FSC, and the proportion of oil trapped within the water-column. A much higher proportion (at least 30%) of oil did not reach the surface during DWH, but this additional trapping was probably due to the application of dispersant at the well head continuously from early May until the well was capped, resulting in much of the oil being entrained in the plume as very small (< 70 µm), neutrally-buoyant droplets (Beyer *et al.*, 2016). No dispersants were simulated in our releases, resulting in a relatively high droplet size distribution, and a higher proportion of oil reaching the surface.

Plume modelling by Johansen (2000b) suggests oil will be trapped at 650–800 m depth from a 1000 m release in the FSC, depending on stratification, ocean currents and release rate. This is deeper than the average trapping depth for the AMM15 release by 150–300 m, but Johansen (2000b) uses a lower release rate range (0.018–0.035 $m^3 s^{-1}$ compared to 0.130 $m^3 s^{-1}$) and larger orifice diameter (0.29 m compared to 0.1 m), both of which will act to deepen the trapped plume (Johansen, 2000b; Yapa & Chen, 2004). Our results suggest that the trapping depth does not substantially influence the overall surfacing time or the proportion of oil trapped below the surface. Yapa & Chen (2004) make similar conclusions by comparing typical stratification and current profiles of the North Sea and the Gulf of Mexico. Our study builds on this previous plume modelling work by suggesting that a change in the depth of trapped oil has a subsequent influence on its trajectory in the far-field.

Neither oil biodegradation or the influence of wind forcing are considered here. The rate of oil biodegradation can depend on temperature, local bacterial colonies, and the chemical composition of the pollutant (Beyer *et al.*, 2016). Temperature is unlikely to be a major control, since local bacterial colonies are likely to have adapted to existing ocean conditions. Additionally, bacteria that reside near natural oil leaks in the area will have adapted to efficiently degrade that particular oil type. This means that biodegradation will likely play a key role in limiting the extent of subsurface transport in the FSC. Main *et al.* (2017) show that oil might reach west of Iceland and within the Arctic Circle before fully biodegrading, but only used a temperature-dependent degradation rate, thereby likely overestimating the transport extent of most oil components. The exception to this rule is for any non-biodegradable oil components.

Direct wind forcing is not included here because the intention is to show the exclusive influence of ocean currents. Surface oil trajectory is typically calculated as the current velocity plus 3.6% of the surface wind velocity (Reed *et al.*, 1995). Both AMM7 and AMM15 are forced by wind fields (Tonani *et al.*, 2019), so there is an indirect influence of the wind in the upper water-column. Wind will have no direct influence on subsurface transport below the Ekman layer, which is approximately 100 m deep at 60°N assuming a typical wind speed of 10 $m s^{-1}$ in February[2]. The presence of a wind field will also increase the proportion of oil that evaporates.

[2]It is important to note here that the Ekman layer depth depends on the vertical eddy viscosity, so this is an approximation.

This study provides an insight into how a hydrodynamic model with resolution fine enough to resolve mesoscale variability influences the predicted dispersion of oil from a deep-seabed release. The modelling systems used here are currently in use by spill responders; this study therefore serves to directly inform industry of what is missed by coarser resolution hydrodynamic models, and how that may impact real-world predictions. Additional hazards that have been uncovered include the potential for subsurface pollutant to travel rapidly from the release location, and increased spatial coverage of the surface emulsion. Both of these will increase the difficulty of a clean-up operation. Results from this research demonstrate how the choice of hydrodynamic model resolution can lead to substantially different outcomes, and can be applied to a wide range of particle tracking applications, for example marine plastic pollution or dispersion of benthic faunal larvae.

7

SYNTHESIS

7.1 INTRODUCTION

This thesis investigated the role of hydrodynamics on controlling the behaviour of a plume and the subsequent far-field advection and dispersion of oil. The research was performed using the oil spill models and hydrodynamic models commonly-used as part of UK emergency spill response. In Chapter 2, AMM7 model output of T and S_p were compared against CTD observations of the FSC from 2013 and 2014. Model-observation differences were then quantified and used to guide idealised oil plume simulations in Chapters 3 and 4 with the OSCAR modelling system. Regional oil spills originating from the FSC were then modelled in Chapters 5 and 6 with OSCAR by varying the time of year, release location, and type of hydrodynamic input. This work was performed in order to answer the six questions posed in Chapter 1, which are repeated here for clarity:

1. How well does a commonly-used operational hydrodynamic model represent the structure of the water-column in the FSC?

2. Do differences in stratification between model and observations substantially influence the behaviour of an oil plume?

3. How sensitive is the advection and dispersion of oil to the magnitude and structure of barotropic and baroclinic ocean currents?

4. Can we use the results from idealised spill simulations to make informed and accurate predictions on how pollutants behave in a regional simulation?

5. How does the advection of oil by ocean currents change with the location and depth of a release?

6. Does a change in hydrodynamic model resolution influence oil transport and dispersion?

Section 7.2 re-frames these six questions into answering the three main aims of the thesis, where each aim is a different sub-section. Recommendations for future scientific research are at the end of each of the three sub-sections. Section 7.3 concludes this thesis by suggesting changes industry could make in order to improve spill prediction effectiveness. Some of the conclusions from this research have also been written into an article for *Ocean Challenge* (Gilchrist, 2020; Appendix D).

7.2 SYNTHESIS

7.2.1 SUITABILITY OF AMM7 AND AMM15 FOR SPILL MODELLING

AMM7 is currently used by industry as a forcing input for predicting oil spills in the FSC. By using T and S_p as proxies, the work in this thesis shows that AMM7 is poor at representing temperature and salinity at intermediate depths (400–750 m). Mid-water-column property gradients are typically too weak, and there are large same-depth differences in Θ, S_a and ρ_w as a result. This is probably because of incorrectly resolved circulation. When these differences are quantified for idealised oil plume modelling, the trapping depth of a plume can change considerably. When oil is released from the seabed in the FSC (at 1000 m depth), the plume will trap order 100 m deeper using AMM7 model output compared to using CTD observations. An order 100 m difference in plume height does not influence the proportion of oil that has surfaced after 30 days, but can determine the depth distribution of neutrally-buoyant and dissolved oil. Differences in plume behaviour will be less pronounced for shallow

(< 400 m) releases, because the plume is likely to surface and the absolute differences between model output and CTD observations in this depth range are relatively small. SST is also well-resolved in AMM7, which will minimise uncertainty associated with the rate of oil evaporation. Overall, this version of AMM7 (using NEMO v3.4) may incorrectly predict plume trapping depth in areas of strong stratification such as the FSC and Norwegian Sea.

More recent versions of AMM7, in addition to AMM15, use NEMO v3.6. A major change compared to NEMO v3.4 is that the water-column is assimilated using CTD profiles of T and S_p. This assimilation will likely result in improved representation of the mid-water-column property gradients. Other parameters that may influence the representation of stratification at depth include the vertical resolution and the representation of ocean currents and water mass transport. A comparison between different versions of AMM7 or AMM15 was not possible to the CTD dataset used in Chapter 2 because outputs from the newer operational models start in 2015 or later. A comparison between all model versions could potentially be made with CTD observations from January 1st, 2017 or later.

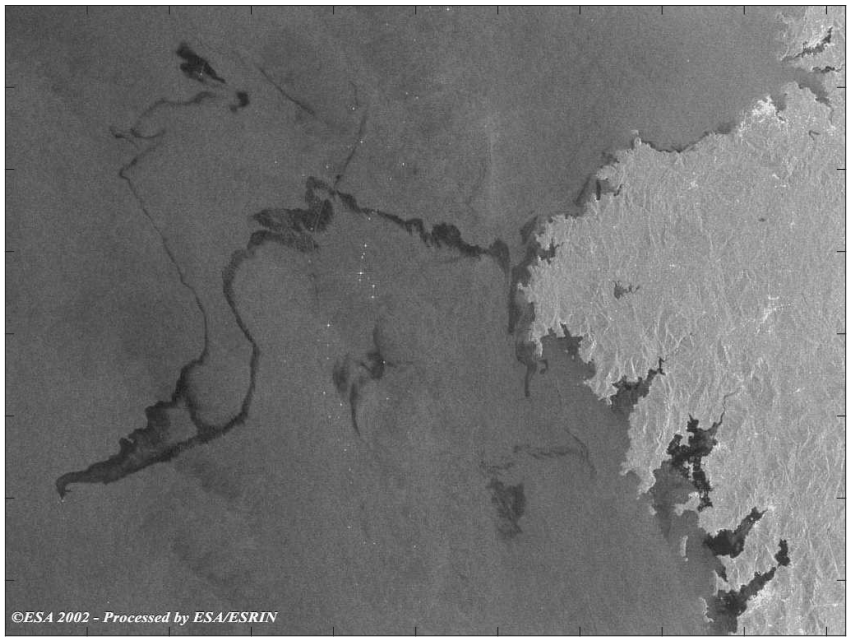

Figure 7.1: AVHRR image of the Prestige oil spill (Galicia, Spain) - European Space Agency (2002).

An advantage to using AMM15 compared to AMM7 for oil spill prediction is that

AMM15 explicitly represents mesoscale features such as eddies. These features are shown in Chapter 5 to be important controls on whether oil is recirculated and contained in the central FSC. Recirculation can occur for up to several weeks, which is on a similar time-scale to clean-up operations. It is however possible that the clean-up operation can last for months, rather than weeks. Areas of enhanced mesoscale activity in the AMM15 forcing fields tend to agree with previous observations (Sherwin *et al.*, 2006). AMM15 is therefore a more suitable hydrodynamic model than AMM7 for predicting far-field advection and dispersion. Using finer resolution models will also be important for other regions; small-scale processes can be seen to have influenced the trajectory and fate of historical releases such as the 2002 Prestige oil spill, off the Portuguese/Spanish coast (Fig. 7.1; European Space Agency, 2002).

Both AMM7 and AMM15 have northern boundaries close to the release locations considered in this thesis, at 65°N and 62.75°N, respectively. Surfaced oil is likely to be advected by the Shetland slope current north-eastward towards this boundary. Chapters 5 and 6 provide evidence that oil can take several weeks to reach the northern boundary of AMM15, but this could be sooner with a stronger slope current or a higher latitude release. To prevent oil escaping the 3-D Fates domain, a combination of operational hydrodynamic models could be used to force OSCAR, instead of only AMM7 or AMM15. The global Met Office model could be used, but a limitation of this is that the resolution is coarse compared to AMM15 (approximately 7 km, similar to AMM7). In the future, finer resolution global circulation models should be used to improve the representation of mesoscale processes in oil spill prediction.

RECOMMENDATIONS FOR FUTURE RESEARCH

- The representation of ocean currents in AMM7 and AMM15 should be compared against observations (e.g. ADCP moorings or Seaglider observations) to provide a more complete picture of how these operational models represent reality. The performance of model currents could also be compared against the performance of model stratification to test whether one is a proxy for the other.

- As more recent CTD observations become available, the analysis in Chapter 2 should be repeated for regional models based on NEMO v3.6, to test whether assimilation using CTD profiles improves the representation of mid-water-

column property gradients.

- To predict oil trajectory, an operational hydrodynamic model is typically used in conjunction with an operational atmospheric model. The skill of commonly-used atmospheric models should be assessed to provide an overall picture of the uncertainty associated with forcing inputs.

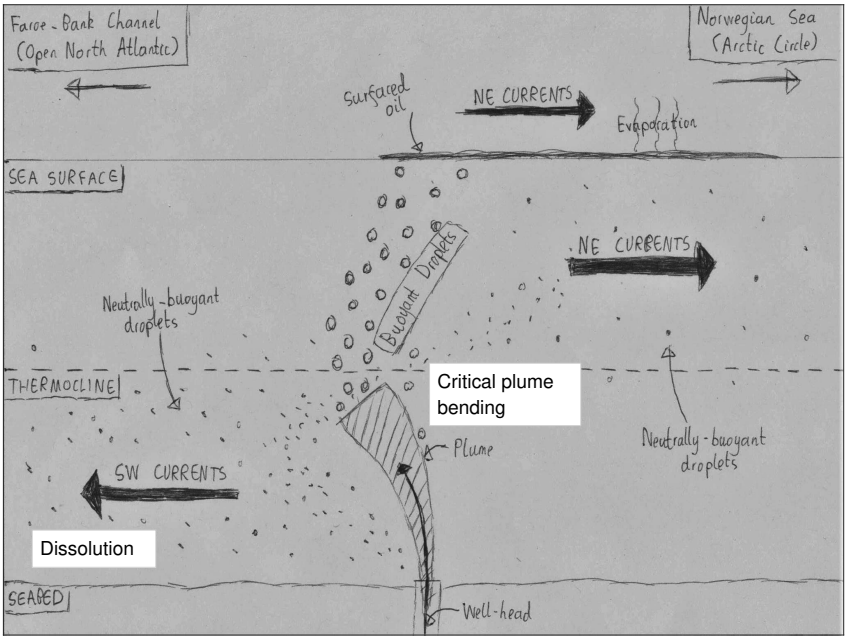

Figure 7.2: Schematic summary of oil spill dynamics from a seabed release in the central FSC.

7.2.2 SCHEMATIC BEHAVIOUR OF OIL RELEASED IN THE FSC

Schematic FSC oil spill dynamics are summarised in Fig. 7.2. If oil is released below the thermocline (typically 500 m depth), the plume will also become trapped below the thermocline. This broad conclusion agrees with previous regional-specific plume modelling (Reed *et al.*, 2000; Johansen, 2000b; Yapa & Chen, 2004) and is irrespective of thermocline strength, thickness, or depth. The results of this Thesis show that in the majority of scenarios, depth-uniform dT/dz is a suitable approximation of depth-uniform N^2. Assuming that the thermocline indicates the depth of the change in direction of shear-flow, this means that plume trapping will predominantly occur in the westward-flowing FSC bottom currents.

Ocean currents act to deepen the trapping depth, and deeper trapping correlates with stronger currents. This agrees with previous numerical modelling using OSCAR (Johansen, 2000b). Liquid oil droplets can escape the plume prematurely if enough plume bending occurs. Plume bending and the escape rate of oil are dependent on the current magnitude and the type of release (oil-only or oil-methane). Non-hydrodynamic controls on trapping depth include the presence of gas alongside oil, whether gas hydrates form, and the release rate. However, these additional parameters do not typically determine whether trapping occurs below or above the thermocline.

Following the termination of a plume, most oil from a deep-seabed release will reach the surface. For a release rate equivalent to the 2016 Clair oil spill, approximately 90% of oil will reach the surface after 24 h. For a release rate equivalent to upper flow rate estimates by Gallego *et al.* (2018), approximately 87.5% of oil will reach the surface after 30 days. Results therefore suggest that a higher release rate can lead to a higher proportion of submerged oil, and this is most likely due to a different droplet size distribution. Once at the surface, oil will be advected predominantly by the Shetland slope current towards the Norwegian Sea.

Most oil that does not reach the sea surface, excluding that removed by marine snow, will become trapped indefinitely in the lower water-column, consisting of neutrally-buoyant oil droplets and dissolved oil. Approximately four-fifths of the total submerged oil remains below the thermocline after a period of 24 h. This means that most submerged oil will be advected westward through the FBC and eventually into the open North Atlantic. The trapping of a plume below a thermocline is therefore a key control on the fate of submerged oil.

Modelling a seabed release in the presence of a baroclinic shear-flow shows that subsurface oil advection is divided into two pathways. Buoyant droplets will ascend and surface close to the release location, while less buoyant droplets and dissolved oil will be advected primarily in the horizontal. This division has also been modelled using CDOG (Yapa *et al.*, 2012), but this thesis expands on this previous research by showing that the same division occurs in shear-flows of more than two layers. Trapping depth and the amount of oil submerged within the water-column is also sensitive to a tidal cycle that is typical of the FSC. Tides in the FSC are semidiurnal and this variability will not have a substantial impact on a prolonged (more than 24 h)

spill. However, if a shorter release were to occur (e.g. 1 h), the phase of the tidal cycle will become important.

RECOMMENDATIONS FOR FUTURE RESEARCH

- Oil spills could be simulated non-ideally by directly comparing the CTD profiles and equivalent AMM7 model outputs in Chapter 2. This would give a more quantitative answer to question 2 defined in Section 7.1. Representative examples of this recommended future work are performed in Section 3.9.2 for AMM7 and Section 5.6 for AMM15.

- Monthly climatological CTD observations could be obtained to test the seasonal variability of plume trapping.

- Release characteristics such as orifice diameter, release rate, gas type, gas-oil-ratio and oil temperature can vary between individual releases. More simulations should be performed to fully assess the sensitivity of a release to these characteristics.

7.2.3 CONSEQUENCES OF A LARGE SEABED RELEASE

Idealised oil spill simulations show that surface and submerged oil in the upper water-column is predominantly advected north-eastward, and submerged oil in the lower water-column is predominantly advected westward. These results correctly summarise the behaviour of the non-idealised simulations performed in Chapters 5 and 6, as well as the only other research paper to model a spill originating from the FSC on a regional or global scale (Main *et al.*, 2017).

The consequences of a spill change depending on the hydrodynamic model resolution used. A finer resolution hydrodynamic model leads to increased oil dispersion and spatial coverage, likely as a result of explicitly resolving mesoscale activity. The overall schematic behaviour of oil (e.g. the east-west division of submerged oil) remains consistent between different hydrodynamic model resolutions, so broad clean-up decisions (e.g. where to direct surface recovery efforts) can be made robustly using either AMM7 or AMM15 as a forcing input. However, finer details such as the amount of equipment required and the best method of dealing with the slick (e.g. burning, manual removal, using of dispersants), will

change depending on which hydrodynamic model is used. For example, the slick in the AMM7 simulation in Chapter 6 would be much easier to contain using booms than the multiple patches present in the AMM15 simulation. The use of coarse hydrodynamic models may therefore lead to an underestimation of clean-up difficulty. Overall, and providing output can be obtained and used in a timely manner, a finer resolution model is more appropriate for spill response, as there is a reduced likelihood of underestimating the resources required during the clean-up process.

The consequences of a spill will also change depending on the release depth and the release location. A release on-shelf will lead to a higher proportion of surfaced oil, as well as a higher contamination risk for the coastlines of north Shetland and south-west Norway. Deeper releases reduce the risk of coastline contamination but will increase the risk of sedimentation if submerged oil comes into contact with the Shetland or Faroe shelf slopes, or the Faroe Bank. Additionally, the risks become more complex for a deep-sea release because submerged oil is advected in two opposing directions, compared to exclusively north-eastward in the case of the *shelf* release performed in Section 5.5. Westward advection could result in contamination as far west as Greenland (Main *et al.*, 2017).

The dispersion of oil in the FSC and surrounding region is likely to lead to environmental and economic damage. The region is a significant area of the Scottish core marine sector, with a turnover of £30 billion (Baxter *et al.*, 2011). Mackerel fishing occurs commercially in the central FSC, and crabs, mussels, kelp and scallops are all farmed around the Shetland islands. Fisheries are however more robust in the years following a spill, because over-fishing is reduced due to closures. The Shetland islands are also home to several sea-bird protected areas, and there is a marine special area of conservation for reefs on the WTR and Shetland shelf. Furthermore, the central and north-east FSC are host to sponge belt marine protected areas (Joint Nature Conservation Committee, 2014). Sponge belts provide zones at depth that support animals such as the ocean quahog. An oil spill in the FSC would put these areas at risk of contamination and could cause large amounts of economic and environmental damage. The work from this thesis better informs spill responders of the dynamics and impacts of oil spills from seabed releases, in order to minimise this damage.

RECOMMENDATIONS FOR FUTURE RESEARCH

- Neither wind or biodegradation were considered in any of the regional simulations performed in this thesis. Respectively, these processes will alter the surface emulsion and reduce the amount of submerged oil. These processes should be considered in the future work to provide a more accurate depiction of a real-world spill.

- Where possible, simulations should be run stochastically (i.e. many versions of the same oil spill with small variations in release orifice diameter, current forcing etc.). This would provide a 'percentage risk' for protected areas.

- Oil spills should be simulated using a larger domain than what is used in this thesis (e.g. with a combination of hydrodynamic forcing models discussed in Section 7.2.1), to quantify the risks to remote areas (e.g. north Norwegian coastlines, Greenland).

7.3 RECOMMENDATIONS FOR INDUSTRY

The concluding section of this thesis outlines four key recommendations that may be relevant to spill responders for a release in the FSC. These recommendations include implications of the results from the previous five chapters, and technical suggestions based on experience using the OSCAR modelling system:

1. ***Several limitations of the OSCAR modelling system should be lifted in order to improve the flexibility of the input hydrodynamic fields and overall model function.*** Firstly, the DeepBlow model has a hard limit of 6000 time-steps, which was encountered in Chapter 3 and resulted in the premature termination of a plume. Secondly, the DeepBlow model only accepts 1-D vertical profiles of time-constant temperature and salinity, whereas 3-D, time-varying fields are available to use and could provide better estimates of temperature-dependant processes such as evaporation and biodegradation. Thirdly, the stratification profile must be typed by hand into the DeepBlow model, which could take up valuable time during an emergency response.

2. ***AMM15 should replace AMM7 for the hydrodynamic input into OSCAR, but AMM7 should be an easy-to-implement backup.*** AMM15 explicitly permits features such as mesoscale eddies, which are shown in this thesis to be important controls on the advection and dispersion of oil. However, data assimilation is needed in the future to ensure that eddies are in the correct position and phase. Another consideration is that when retrieving AMM15 model output for Chapters 5 and 6, the online sub-sampling tool did not work and it took several days to download all of the required forcing fields. This is manageable during a PhD thesis but would be an unacceptable length of time during an emergency response. The sub-sampling issue was because AMM15 was released only a few days before the download was attempted (November 2018), and has likely since been resolved. In comparison, the AMM7 forcing fields took less than 15 minutes to download. The ability to implement multiple operational hydrodynamic models would considerably reduce the risk of similar issues in the future. Another consideration is that if the 3-D Fates grid matched the hydrodynamic model horizontal resolutions, a simulation using AMM7 would be more than 20 times as fast as a simulation using AMM15.

3. ***Where possible, real-time observations of ocean conditions from oil rigs should be used in place of hydrodynamic model output.*** This thesis shows that stratification is not represented well by AMM7 model output at 400–750 m depth. It has not yet been investigated whether AMM15 or the most recent version of AMM7 improves this representation. Another option is to use ocean observations made in real-time from most oil rigs (Transportation Research Board, 2016). This would provide an input that is much more representative of real-world conditions. If real-time data is not accessible in the public domain, an alternative could be to instead use historical CTD observations. It is also important to consider that stratification will influence plume trapping depth, but not necessarily the subsequent far-field horizontal transport. Therefore, a more important improvement to the hydrodynamic input would be suggestion (2), with particular attention to data assimilation of ocean currents.

4. ***Spill responders should aim to reduce the response time to a spill in the FSC to 15 days.*** A deep-sea spill in the FSC will lead to rapid oil advection towards both the open North Atlantic and the Norwegian Sea. This type of spill will be inherently difficult to contain, even without considering the often poor working conditions at the sea surface. A likely response time for an uncontrolled spill in the area is 30 days or less when taking into account mobilisation, deployment and unforeseen circumstances (estimated by Gallego *et al.*, 2018), but halving this to 15 days would result in most oil still contained within the central FSC by the time the clean-up effort begins. This would substantially reduce the amount of dispersant and equipment needed, and help to minimise cost to the environment.

BIBLIOGRAPHY

Abascal, A J, Castanedo, S, Medina, R, & Liste, M. 2010. Analysis of the reliability of a statistical oil spill response model. *Marine Pollution Bulletin*, **60**(11), 2099–2110.

Alford, M H. 2003. Redistribution of energy available for ocean mixing by long-range propagation of internal waves. *Nature*, **423**(6936), 159–162.

Alford, M H, Gregg, M C, Zervakis, V, & Kontoyiaanis, H. 2012. Internal wave measurements on the Cycladic Plateau of the Aegean Sea. *Journal of Geophysical Research: Oceans*, **117**(C1).

Antonio, F.J., Mendes, R.S., & Thomaz, S.M. 2011. Identifying and modeling patterns of tetrapod vertebrate mortality rates in the Gulf of Mexico oil spill. *Aquatic Toxicology*, **105**(1-2), 177–179.

Asaeda, T, & Imberger, J. 1993. Structure of bubble plumes in linearly stratified environments. *Journal of Fluid Mechanics*, **249**(apr), 35–57.

Aslam, T A, Hall, R A, & Dye, S. 2018. Internal tides in a dendritic submarine canyon. *Progress in Oceanography*, **169**(dec), 20–32.

Bandara, U C, & Yapa, P D. 2011. Bubble Sizes, Breakup, and Coalescence in Deepwater Gas/Oil Plumes. *Journal of Hydraulic Engineering*, **137**(7), 729–738.

Baxter, J M, Boyd, I L, Cox, M, Donald, A E, Malcolm, S J, Miles, H, Miller, B, & Moffat, C F. 2011. *Scotland's Marine Atlas: Information for the national marine plan*. Edinburgh: Marine Scotland.

Becker, G, & Hansen, B. 1988. *Modified North Atlantic Water*. International Council for the Exploration of the Sea (ICES).

Berx, B, Hansen, B, Østerhus, S, Larsen, K M, Sherwin, T J, & Jochumsen, K. 2013. Combining in situ measurements and altimetry to estimate volume, heat and salt

transport variability through the Faroe-Shetland Channel. *Ocean Science*, **9**(4), 639–654.

Beyer, J, Trannum, H C, Bakke, T, Hodson, P V, & Collier, T K. 2016. Environmental effects of the Deepwater Horizon oil spill: A review. *Marine Pollution Bulletin*, **110**(1), 28–51.

Blindheim, J. 1990. Arctic intermediate water in the Norwegian sea. *Deep Sea Research Part A. Oceanographic Research Papers*, **37**(9), 1475–1489.

Blindheim, J, & Borovkov, V. 1996. *Recent Upper Layer Cooling and Freshening in the Norwegian Sea*.

Boufadel, M C, Abdollahi-Nasab, A, Geng, X, Galt, J, & Torlapati, J. 2014. Simulation of the Landfall of the Deepwater Horizon Oil on the Shorelines of the Gulf of Mexico. *Environmental Science & Technology*, **48**(16), 9496–9505.

Boussinesq, J. 1903. Theórie analytiche de la chaleur mise en harmonie avec la thermodynamique et avec la théorie mécanique de la lumière. *Monatshefte für Mathematik und Physik*, **14**(1), A11———A12.

Brandvik, P J, Johansen, Ø, Leirvik, F, Farook, U, & Daling, P S. 2013. Droplet breakup in subsurface oil releases - Part 1: Experimental study of droplet breakup and effectiveness of dispersant injection. *Marine Pollution Bulletin*, **73**(1), 319–326.

Burgherr, P. 2007. In-depth analysis of accidental oil spills from tankers in the context of global spill trends from all sources. *Journal of Hazardous Materials*, **140**(1-2), 245–256.

Camilli, R, Reddy, C M, Yoerger, D R, van Mooy, B A S, Jakuba, M V, Kinsey, J C, McIntyre, C P, Sylva, S P, & Maloney, J V. 2010. Tracking Hydrocarbon Plume Transport and Biodegradation at Deepwater Horizon. *Science*, **330**(6001), 201–204.

Chafik, L. 2012. The response of the circulation in the Faroe- Shetland Channel to the North Atlantic Oscillation. *Tellus A*, **64**(1), 18423.

Codiga, D L. 2011. *Unified tidal analysis and prediction using the UTide Matlab functions*. Graduate School of Oceanography, University of Rhode Island Narragansett, RI.

Crone, T J, & Tolstoy, M. 2010. Magnitude of the 2010 Gulf of Mexico Oil Leak. *Science*, **330**(6004), 634.

Darelius, E, Fer, I, & Quadfasel, D. 2011. Faroe Bank Channel Overflow: Mesoscale Variability*. *Journal of Physical Oceanography*, **41**(11), 2137–2154.

Dasanayaka, L K, & Yapa, P D. 2009. Role of plume dynamics phase in a deepwater oil and gas release model. *Journal of Hydro-environment Research*, **2**(4), 243–253.

Diercks, A, Highsmith, R C, Asper, V L, Joung, D, Zhou, Z, Guo, L, Shiller, A M, Joye, S B, Teske, A P, Guinasso, N, Wade, T L, & Lohrenz, S E. 2010. Characterization of subsurface polycyclic aromatic hydrocarbons at the Deepwater Horizon site. *Geophysical Research Letters*, **37**(20).

Dooley, H D, & Meincke, J. 1981. Circulation and Water Masses in the Faroese Channels during Overflow '73. *Deutsche Hydrographische Zeitschrift*, **34**(2), 41–55.

Du, M, & Kessler, J D. 2012. Assessment of the Spatial and Temporal Variability of Bulk Hydrocarbon Respiration Following the Deepwater Horizon Oil Spill. *Environmental Science & Technology*, **46**(19), 10499–10507.

Duda, T F, Lynch, J F, Irish, J D, Beardsley, R C, Ramp, S R, Chiu, C S, Tang, T Y, & Yang, Y J. 2004. Internal Tide and Nonlinear Internal Wave Behavior at the Continental Slope in the Northern South China Sea. *IEEE Journal of Oceanic Engineering*, **29**(4), 1105–1130.

Edwards, K P, Barciela, R M, & Butenschön, M. 2012. Validation of the NEMO-ESEM operational ecosystem model for the North West European Continental Shelf. *Ocean Science*, **8**(6), 983–1000.

Edwards, M, Beaugrand, G, Reid, P C, Rowden, A A, & Jones, M B. 2002. Ocean climate anomalies and the ecology of the North Sea. *Marine Ecology Progress Series*, **239**(aug), 1–10.

Egbert, G D, & Erofeeva, S Y. 2000. Efficient Inverse Modeling of Barotropic Ocean Tides. *Journal of Atmospheric and Oceanic Technology*, **19**(1), 183–204.

EU Copernicus Marine Services Information. 2018a. *European North West Shelf – Ocean physics analysis: NORTHWESTSHELF_ANALYSIS_FORECAST_PHY_004_001_b*.

EU Copernicus Marine Services Information. 2018b. *European North West Shelf – Ocean physics analysis: NORTHWESTSHELF_ANALYSIS_FORECAST_PHY_004_13*.

European Space Agency. 2002. *Prestige oil spill (Galicia, Spain)*.

Fitzgerald, T P, & Gohlke, J M. 2014. Contaminant Levels in Gulf of Mexico Reef Fish after the Deepwater Horizon Oil Spill As Measured by a Fishermen-Led Testing Program. *Environmental Science & Technology*, **48**(3), 1993–2000.

Flather, R A. 1976. A tidal model of the north-west European continental shelf. *Memoires de la Societe Royale des Sciences de Liege*, **10**(6), 141–164.

Gallego, A, Murray, R, Berx, B, Turrell, W R, Beegle-Krause, C J, Inall, M E, Sherwin, T J, Siddorn, J R, Wakelin, S, Vlasenko, V, Hole, L R, Dagestad, K F, Rees, J, Short, L, Rønningen, P, Main, C E, Legrand, S, Gutierrez, T, Witte, U, & Mulanaphy, N. 2018. Current status of deepwater oil spill modelling in the Faroe-Shetland Channel, Northeast Atlantic, and future challenges. *Marine Pollution Bulletin*, **127**(feb), 484–504.

Geyer, F, Østerhus, S, Hansen, B, & Quadfasel, D. 2006. Observations of highly regular oscillations in the overflow plume downstream of the Faroe Bank Channel. *Journal of Geophysical Research*, **111**(C12).

Gilchrist, R M. 2020. The challenges of predicting the fate of oil from a spill in the Faroe-Shetland Channel. *Ocean Challenge*, **24**(1).

Gordon, R L, & Marshall, N F. 1976. Submarine canyons: Internal wave traps? *Geophysical Research Letters*, **3**(10), 622–624.

Gould, W J. 1984. The current regime on the continental slope north and west of the United Kingdom. *In: Society for Underwater Technology Conference*.

Graham, J A, O'Dea, E, Holt, J T, Polton, J, Hewitt, H T, Furner, R, Guihou, K, Brereton, A, Arnold, A, Wakelin, S, Sanchez, J M C, & Adame, C G M. 2018. AMM15: a new

high-resolution NEMO configuration for operational simulation of the European north-west shelf. *Geoscientific Model Development*, **11**(2), 681–696.

Guihou, K, Polton, J, Harle, J, Wakelin, S, O'Dea, E, & Holt, J T. 2017. Kilometric Scale Modeling of the North West European Shelf Seas: Exploring the Spatial and Temporal Variability of Internal Tides. *Journal of Geophysical Research: Oceans*, **123**(1), 688–707.

Hall, R A. 2008. *Internal waves and slope mixing in the Faroe-Shetland Channel*. Liverpool: University of Liverpool.

Hall, R A, Huthnance, J M, & Williams, R G. 2011. Internal tides , nonlinear internal wave trains , and mixing in the Faroe-Shetland Channel. *Journal of Geophysical Research*, **116**(C3).

Hall, R A, Huthnance, J M, & Williams, R G. 2013. Internal Wave Reflection on Shelf Slopes with Depth-Varying Stratification. *Journal of Physical Oceanography*, **43**(2), 248–258.

Hall, R A, Berx, B, & Damerell, G. 2019. Internal tide energy flux over a ridge measured by a co-located ocean glider and moored ADCP. *Ocean Science Discussions*, mar, 1–21.

Hansen, B, & Meincke, J. 1979. Eddies and meanders in the Iceland-Faroe Ridge area. *Deep Sea Research Part A, Oceanographic Research Papers*, **26**(9), 1067–1082.

Helfrich, K R, & Melville, W K. 2006. Long Nonlinear Internal Waves. *Annual Review of Fluid Mechanics*, **38**(1), 395–425.

Henkel, J R, Sigel, B J, & Taylor, C M. 2012. Large-Scale Impacts of the Deepwater Horizon Oil Spill: Can Local Disturbance Affect Distant Ecosystems through Migratory Shorebirds? *BioScience*, **62**(7), 676–685.

Hill, A E, & Mitchelson-Jacob, E G. 1993. Observations of a poleward-flowing saline core on the continental slope west of Scotland. *Deep Sea Research Part I: Oceanographic Research Papers*, **40**(7), 1521–1527.

Hoffman, A J, & Jennings, P D. 2011. The BP Oil Spill as a Cultural Anomaly? Institutional Context, Conflict, and Change. *Journal of Management Inquiry*, **20**(2), 100–112.

Holt, J, & Umlauf, L. 2008. Modelling the tidal mixing fronts and seasonal stratification of the Northwest European Continental shelf. *Continental Shelf Research2*, **28**(7), 887–903.

Hopkins, T S. 1991. The GIN Sea—A synthesis of its physical oceanography and literature review 1972–1985. *Earth-Science Reviews*, **30**(3-4), 175–318.

Hosegood, P, & van Haren, H. 2004. Near-bed solibores over the continental slope in the Faeroe-Shetland Channel. *Deep Sea Research Part II: Topical Studies in Oceanography*, **51**(25-26), 2943–2971.

Hosegood, P, van Haren, H, & Veth, C. 2005. Mixing within the interior of the Faeroe-Shetland Channel. *Journal of Marine Research*, **63**(3), 529–561.

Hotchkiss, F S, & Wunsch, C. 1982. Internal waves in Hudson Canyon with possible geological implications. *Deep Sea Research Part A. Oceanographic Research Papers*, **29**(4), 415–442.

Hunt, G R, & Kaye, N B. 2005. Lazy Plumes. *Journal of Fluid Mechanics*, **533**(jun).

Jayko, K, & Howlett, E. 1992. Oilmap: An Interactive Oil Spill Model. *In: OCEANS 92: Mastering the Oceans through Technology*. IEEE.

Johansen, Ø. 2000a. DeepBlow – a Lagrangian Plume Model for Deep Water Blowouts. *Spill Science & Technology Bulletin*, **6**(2), 103–111.

Johansen, Ø. 2000b. *Simulations of Near Field Spreading from Potential Blowouts in Deep Waters South of Faroe Islands*. Tech. rept. SINTEF Applied Chemistry, Trondheim.

Johansen, Ø, Jensen, H V, & Daling, P. 2001. *Deep Spill JIP Experimental Discharges of Gas and Oil at Helland Hansen - June 2000 Cruise Report*. Tech. rept. SINTEF, Trondheim.

Johansen, Ø, Rye, H, & Cooper, C. 2003. DeepSpill—Field Study of a Simulated Oil and Gas Blowout in Deep Water. *Spill Science & Technology Bulletin*, **8**(5-6), 433–443.

Johansen, Ø, Brandvik, P J, & Farooq, U. 2013. Droplet breakup in subsea oil releases – Part 2: Predictions of droplet size distributions with and without injection of chemical dispersants. *Marine Pollution Bulletin*, **73**(1), 327–335.

Joint Nature Conservation Committee. 2014. *Faroe-Shetland Sponge Belt Marine Protected Area*. Tech. rept. Joint Nature Conservation Committee, Peterborough.

Joye, S B, Bracco, A, Özgökmen, T M, Chanton, J P, Grosell, M, MacDonald, I R, Cordes, E E, Montoya, J P, & Passow, U. 2016. The Gulf of Mexico ecosystem, six years after the Macondo oil well blowout. *Deep Sea Research Part II: Topical Studies in Oceanography*, **129**(jul), 4–19.

Kelly, S M, Jones, N L, Nash, J D, & Waterhouse, A F. 2013. The geography of semidiurnal mode-1 internal-tide energy loss. *Geophysical Research Letters*, **40**(17), 4689–4693.

Kerry, C G, Powell, B S, & Carter, G S. 2013. Effects of Remote Generation Sites on Model Estimates of M2 Internal Tides in the Philippine Sea*. *Journal of Physical Oceanography*, **43**(1), 187–204.

Kessler, J D, Valentine, D L, Redmond, M C, Du, M, Chan, E W, Mendes, S D, Quiroz, E W, Villanuev, C J, Shusta, S S, Werra, L M, Yvon-Lewis, S A, & Weber, T C. 2011. A Persistent Oxygen Anomaly Reveals the Fate of Spilled Methane in the Deep Gulf of Mexico. *Science*, **331**(6015), 312–315.

King, R, While, J, Martin, M J, Lea, D, Lemiuex-Dudon, B, Waters, J, & O'Dea, E. 2018. Improving the initialisation of the Met Office operational shelf-seas model. *Ocean Modelling*, **130**(oct), 1–14.

Klinck, J. 1999. *Dynmodes.m—Ocean Dynamic Vertical Modes, Woods Hole Science Center - SEA-MAT - Matlab Tools for Oceanographic Analysis*.

Knudsen, M. 1911. *Danish hydrographical investigations at the Faroe Islands in the spring of 1910*. Reitzel.

Kunze, E, MacKay, C, McPhee-Shaw, E E, Morrice, K, Girton, J B, & Terker, S R. 2012. Turbulent Mixing and Exchange with Interior Waters on Sloping Boundaries. *Journal of Physical Oceanography*, **42**(6), 910–927.

Lane-Serff, G F, & Baines, P G. 1998. Eddy formation by dense flows on slopes in a rotating fluid. *Journal of Fluid Mechanics*, **363**(may), 229–252.

Lee, K, Nedwed, T, Prince, R C, & Palandro, D. 2013. Lab tests on the biodegradation of chemically dispersed oil should consider the rapid dilution that occurs at sea. *Marine Pollution Bulletin*, **73**(1), 314–318.

Lee, Y G, Garza-Gomez, X, & Lee, R M. 2018. Ultimate Costs of the Disaster: Seven Years After the Deepwater Horizon Oil Spill. *Journal of Corporate Accounting & Finance*, **29**(1), 69–79.

MacNaughton, S J, Stephen, J R, Venosa, A B, Davis, G A, Chang, Y, & White, D C. 1999. Microbial Population Changes during Bioremediation of an Experimental Oil Spill. *Applied Environmental Microbiology*, **65**(8), 3566–3574.

Madec, G. 2016. *NEMO ocean engine. Note du Pole de modélisation.* 27 edn. Institut Pierre-Simon Laplace.

Mahdon, R, Tonani, M, McConnel, N, O'Dea, E, King, R, & Martin, M J. 2015. *Product User Manual f or North-West Shelf Physical Forecast Product NORTHWESTSHELF _ FORECAST_ PHYS_ 004_ 001_ b.* Tech. rept. Copernicus Marine Environment Monitoring Service (CMEMS).

Main, C E, Yool, A, Holliday, N P, Popova, E E, Jones, D O B, & Ruhl, H A. 2017. Simulating pathways of subsurface oil in the Faroe–Shetland Channel using an ocean general circulation model. *Marine Pollution Bulletin*, **114**(1), 315–326.

Martin, J H A. 1993. Norwegian Sea intermediate water in the Faroe-Shetland Channel. *ICES Journal of Marine Science*, **50**(2), 195–201.

Mauritzen, C. 1996. Production of dense overflow waters feeding the North Atlantic across the Greenland-Scotland Ridge. Part 1: Evidence for a revised circulation scheme. *Deep Sea Research Part I: Oceanographic Research Papers*, **43**(6), 769–806.

Mauritzen, C, Price, J, Sanford, T, & Torres, D. 2005. Circulation and mixing in the Faroese Channels. *Deep Sea Research Part I: Oceanographic Research Papers*, **52**(6), 883–913.

McDougall, T J, & Barker, P M. 2011 (may). *Getting started with TEOS-10 and the Gibbs Seawater (GSW) oceanographic toolbox*. Tech. rept. SCOR/IAPSO.

McNutt, M K, Camilli, R, Crone, T J, Guthrie, G D, Hsieh, P A, Ryerson, T B, Savas, O, & Shaffer, F. 2012. Review of flow rate estimates of the Deepwater Horizon oil spill. *Proceedings of the National Academy of Sciences*, **109**(50), 20260–20267.

Meincke, J. 1978. On the distribution of low salinity intermediate waters around the faroes. *Deutsche Hydrographische Zeitschrift*, **31**(2), 50–64.

Michel, J, Owens, E H, Zengel, R, Graham, A, Nixon, Z, Allard, T, Holton, W, Reimer, P D, Lamarche, A, White, M, Rutherford, N, Childs, C, Mauseth, G, Challenger, G, & Taylor, E. 2013. Extent and Degree of Shoreline Oiling: Deepwater Horizon Oil Spill, Gulf of Mexico, USA. *PLoS ONE*, **8**(6), e65087.

Millero, F J, & Poisson, A. 1981. International one-atmosphere equation of state of seawater. *Deep Sea Research Part A. Oceanographic Research Papers*, **28**(6), 625–629.

MMO. 2014. *Mapping UK shipping density and routes from AIS*. Tech. rept. Marine Management Organisation.

Mogensen, K, Alonso, M, & Weaver, A. 2012 (feb). *The NEMOVAR ocean data assimilation system as implemented in the ECMWF ocean analysis for System 4*.

Morton, B R. 1959. Forced Plumes. *Journal of Fluid Mechanics*, **5**(1), 151.

Morton, B R, Taylor, G T, & Turner, J S. 1956. Turbulent gravitational convection from maintained and instantaneous sources. *Proceedings of the Royal Society A*, **234**(1196), 1–23.

Nash, J D, Kelly, S M, Shroyer, E L, Moum, J N, & Duda, T F. 2012. The Unpredictable Nature of Internal Tides on Continental Shelves. *Journal of Physical Oceanography*, **42**(11), 1981–2000.

National Research Council. 2003. *Oil in the Sea III.* Washington, DC: The National Academies Press.

Nixon, Z, Zengel, S, Baker, M, Steinhoff, M, Fricano, G, Rouhani, S, & Michel, J. 2016. Shoreline oiling from the Deepwater Horizon oil spill. *Marine Pollution Bulletin*, **107**(1), 170–178.

O'Dea, E, Arnold, A K, Edwards, K P, Furner, R, Hyder, P, Martin, M J, Siddorn, J R, While, J, Holt, J T, & Liu, H. 2012. An operational ocean forecast system incorporating NEMO and SST data assimilation for the tidally driven European North-West shelf. *Journal of Operational Oceanography*, **5**(1), 3–17.

Oey, L Y. 1998. Eddy energetics in the Faroe-Shetland channel: A model resolution study. *Continental Shelf Research*, **17**(15), 1929–1944.

Otto, L, & van Aken, H M. 1996. Surface circulation in the northeast Atlantic as observed with drifters. *Deep Sea Research Part I: Oceanographic Research Papers*, **43**(4), 467–499.

Quadfasel, D, & Käse, R. 2007. Present-day manifestation of the Nordic Seas overflows. *Pages 75–89 of: Ocean Circulation: Mechanisms and Impacts – Past and Future Changes of Meridional Overturning.* American Geophysical Union (AGU).

Rainville, L. 2010. Interference Pattern and Propagation of the M2 Internal Tide South of the Hawaiian Ridge. *Journal of Physical Oceanography*, **40**(2), 311–325.

Reed, M, Turner, C, & Odulo, N. 1994. The Role of Wind and Emulsification in Modelling Oil Spill and Surface Drifter Trajectories. *Spill Science & Technology Bulletin*, **1**(2), 143–157.

Reed, M, Rines, H, Drive, D K, & Rye, H. 1995. A Three-Dimensional Oil and Chemical Spill Model for Environmental Impact Assessment. *International Oil Spill Conference (IOSC)*, **1995**(1), 61–66.

Reed, M, Daling, P S, Brakstad, O G, Singsaas, I, Faksness, L G, Hetland, B, & Ekrol, N. 2000. OSCAR2000 : a multi-component 3-dimensional oil spill contingency and response model. *In: Proceedings of the 23. Arctic and Marine Oilspill Program*

(AMOP) Technical Seminar. Ottowa: International Nuclear Information System (INIS).

Rye, H. 1994. Model for calculation of underwater blow-out plume. *Page 849 of: Arctic and Marine Oilspill Program Technical Seminar*. Ministry of Supply and Services, Canada.

Rye, H, & Brandvik, P J. 1997. Verification of Subsurface Oil Spill Models. *International Oil Spill Conference (IOSC)*, **1997**(1), 551–558.

Rye, H, Brandvik, P J, & Reed, M. 1996. Subsurface oil release field experiment - observations and modelling of subsurface plume behaviour. *Pages 1417–1435 of: Proceedings of the 19. Arctic and Marine Oilspill Program (AMOP) Technical Seminar*. Ottowa: International Nuclear Information System (INIS).

Saunders, P M. 1990. Cold Outflow from the Faroe Bank Channel. *Journal of Physical Oceanography*, **20**(1), 29–43.

Seim, K S, Fer, I, & Berntsen, J. 2010. Regional simulations of the Faroe Bank Channel overflow using a σ-coordinate ocean model. *Ocean Modelling*, **35**(1-2), 31–44.

Sherwin, T J. 1991. Evidence of a deep internal tide in the Faeroe-Shetland channel. *Chap. 24, pages 469–488 of: Tidal Hydrodynamics*. John Wiley.

Sherwin, T J, Turrell, W R, Jeans, D R G, & Dye, S. 1999. Eddies and a mesoscale deflection of the slope current in the Faroe-Shetland Channel. *Deep Sea Research Part I: Oceanographic Research Papers*, **46**(3), 415–438.

Sherwin, T J, Williams, M O, Turrell, W R, Hughes, S L, & Miller, P I. 2006. A description and analysis of mesoscale variability in the Färoe-Shetland Channel. *Journal of Geophysical Research*, **111**(C3).

Sherwin, T J, Griffiths, C R, Inall, M E, & Turrell, W R. 2008. Quantifying the overflow across the Wyville Thomson Ridge into the Rockall Trough. *Deep Sea Research Part I: Oceanographic Research Papers*, **55**(4), 396–404.

Simmons, H L, & Alford, M H. 2012. Simulating the Long-Range Swell of Internal Waves Generated by Ocean Storms. *Oceanography*, **25**(2), 30–41.

Sloan, E D, & Koh, C A. 2007. *Clathrate Hydrates of Natural Gases*. Boca Raton: CRC Press.

Smallwood, J R, & Kirk, W J. 2005. Paleocene exploration in the Faroe-Shetland Channel: disappointments and discoveries. *Geological Society, London, Petroleum Geology Conference series*, **6**(1), 977–991.

Smith, P C. 1976. Baroclinic Instability in the Denmark Strait Overflow. *Journal of Physical Oceanography*, **6**(3), 355–371.

Smith, W H F, & Sandwell, D T. 1997. Global Sea Floor Topography from Satellite Altimetry and Ship Depth Soundings. *Science*, **277**(5334), 1956–1962.

Socolofsky, S A, Adams, E E, & Sherwood, C R. 2011. Formation dynamics of subsurface hydrocarbon intrusionsfollowing the Deepwater Horizon blowout. *Geophysical Research Letters*, **38**(9).

Spall, M A, & Price, J F. 1998. Mesoscale Variability in Denmark Strait: The PV Outflow Hypothesis. *Journal of Physical Oceanography*, **28**(8), 1598–1623.

Spaulding, M, Howlett, E, Anderson, E, & Jayko, K. 1992. OILMAP: a global approach to spill modeling. *In: 15th Arctic and Marine Oil Spill Program, Technical Seminar*.

Spaulding, M, Kolluru, V S, Anderson, E, & Howlett, E. 1994. Application of three-dimensional oil spill model (WOSM/OILMAP) to Hindcast the Braer spill. *Spill Science & Technology Bulletin*, **1**(1), 23–35.

Spier, C, Stringfellow, W T, Hazen, T C, & Conrad, M. 2013. Distribution of hydrocarbons released during the 2010 MC252 oil spill in deep offshore waters. *Environmental Pollution*, **173**(feb), 224–230.

Storkey, D, Blockley, E W, Furner, R, Guiavarch'h, C, Lea, D, Martin, M J, Barciela, R M, Hines, A, Hyder, P, & Siddorn, J R. 2010. Forecasting the ocean state using NEMO: The new FOAM system. *Journal of Operational Oceanography*, **3**(1), 3–15.

Swaters, G E. 1991. On the baroclinic instability of cold-core coupled density fronts on a sloping continental shelf. *Journal of Fluid Mechanics*, **224**(-1), 361–382.

Tanaka, K. 2006. Effects of the Earth's rotation and bottom slope on a density current descending a sloping bottom. *Journal of Geophysical Research*, **111**(C11).

Tanaka, K, & Akitomo, K. 2001. Baroclinic instability of density current along a sloping bottom and the associated transport process. *Journal of Geophysical Research: Oceans*, **106**(C2), 2621–2638.

Tonani, M, Sykes, P, King, R R, McConnel, N, Pequignet, A, O'Dea, E, Graham, J A, Polton, J, & Siddorn, J R. 2019. The impact of a new high-resolution ocean model on the Met Office North-West European Shelf forecasting system. *Ocean Science Discussion*, feb, 1–34.

Tran, T, Yazdanparast, A, & Suess, E A. 2014. Effect of Oil Spill on Birds: A Graphical Assay of the Deepwater Horizon Oil Spill's Impact on Birds. *Computational Statistics*, **29**(1-2), 133–140.

Transportation Research Board. 2016. *Application of Real-Time Monitoring to Offshore Oil and Gas Operations*. Washington, DC: The National Academies Press.

Turrell, W R, Slesser, G, Adams, R D, Payne, R, & GIllibrand, P A. 1999. Decadal variability in the composition of Faroe Shetland Channel bottom water. *Deep Sea Research Part I: Oceanographic Research Papers*, **46**(1), 1–25.

Umlauf, L, & Barchard, H. 2003. A generic length-scale equation for geophysical turbulence models. *Journal of Marine Research*, **61**(2), 235–265.

van Aken, H M. 1988. Transports of water masses through the Faroese Channels determined by an inverse method. *Deep Sea Research Part A. Oceanographic Research Papers*, **35**(4), 595–617.

van Aken, H M, & Eisma, D. 1987. The circulation between Iceland and Scotland derived from water mass analysis. *Netherlands Journal of Sea Research*, **21**(1), 1–15.

Voet, G, Quadfasel, D, Mork, K A, & Søiland, H. 2010. The mid-depth circulation of the Nordic Seas derived from profiling float observation. *Tellus A*, **62**(5), 516–529.

Walters, D N, Best, M J, Bushell, A C, Copsey, D, Edwards, J M, Falloon, P D, Harris, C M, Lock, A P, Manners, J C, Morcrette, C J, Roberts, M J, Stratton, R A, Webster, S,

Wilkinson, J M, Willett, M R, Boutle, I A, Earnshaw, P D, Hill, P G, MacLachlan, C, Martin, G M, Moafouma-Okia, W, Palmer, M D, Petch, J C, Rooney, G G, Scaife, A A, & Williams, K D. 2011. The Met Office Unified Model Global Atmosphere 3.0/3.1 and JULES Global Land 3.0/3.1 configurations. *Geoscientific Model Development*, **4**(2), 919–941.

Wunsch, C, & Webb, S. 1979. The climatology of deep ocean internal waves. *Journal of Physical Oceanography*, **9**(2), 235–243.

Yapa, P D, & Chen, F. 2004. Behavior of oil and gas from deepwater blowouts. *Journal of Hydraulic Engineering*, **130**(6), 540–553.

Yapa, P D, Wimalaratne, M R, Dissanayake, A L, & DeGraff, J A. 2012. How does oil and gas behave when released in deepwater? *Journal of Hydro-environment Research*, **6**(4), 275–285.

Youssef, M, & Spaulding, M. 1993. Drift current under the action of wind and waves. *Pages 587–615 of: Proceedings of the 16. Arctic and Marine Oilspill Program (AMOP) Technical Seminar*. Ottowa: International Nuclear Information System (INIS).

Zhao, Z, Alford, M H, Lien, R, Gregg, M C, & Glenn, S C. 2012. Internal tides and mixing in a submarine canyon with time-varying stratification. *Journal of Physical Oceanography*, **42**(12), 2121–2142.

Zheng, L, Yapa, P D, & Chen, F. 2003. A model for simulating deepwater oil and gas blowouts - Part I: Theory and model formulation. *Journal of Hydraulic Research*, **41**(4), 339–351.

A

CLAIR OIL PROPERTIES

Table A.1: Chemical composition of the Clair oil type.

Chemical component	**Proportion** (%)
C1-Benzene	0.3611
C2-Benzene	0.3725
C3-Benzene	1.9634
C4-Benzene	0.0510
Benzene	0.1644
C1-C4 gasses (dissolved in oil)	0.2454
Phenols (C0-C4)	3.2798
Naphthalenes (C0-C1)	0.1430
Naphthalenes (C2-C3)	0.5806
C5-saturates	0.3916
C6-saturates	0.9864
C7-saturates	1.3157
C8-Saturates	1.4232
C9-Saturates	1.5181
C10-Saturates	1.4796
C11-C12	2.0355
C13-C14	2.8644
C15-C16	8.0839
C17-C18	5.2604
C19-C20	4.0397
C21-C25	8.8912
C25+	53.8790
Unresolved chromatographic materials (C10-C36)	0.1067
PAH (Medium solubility)	0.3505
PAH (Low solubility)	0.2131

B

ADDITIONAL FIGURES FOR CHAPTER 2

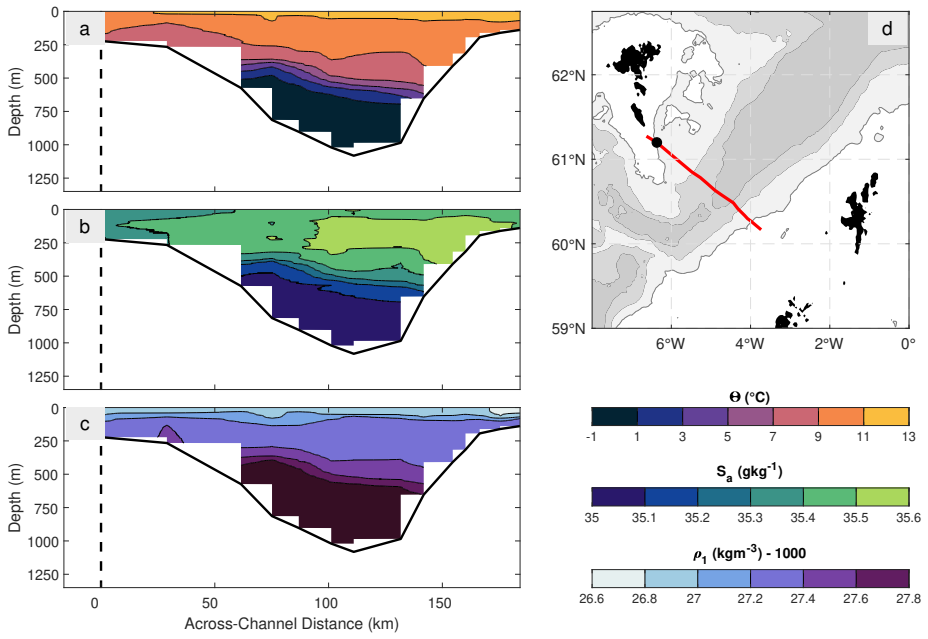

Figure B.1: Across-channel stratification (FIM, September 2014). (**a**) Cross-section of conservative temperature (filled contours). Across-channel distance is relative to the Faroe shelf edge (black dashed line). (**b**) As (a) but for absolute salinity. (**c**) as (a) but for potential density. (**d**) CTD section location (red line) and location of the Faroe shelf edge (black dot). Bathymetry is from Smith & Sandwell (1997).

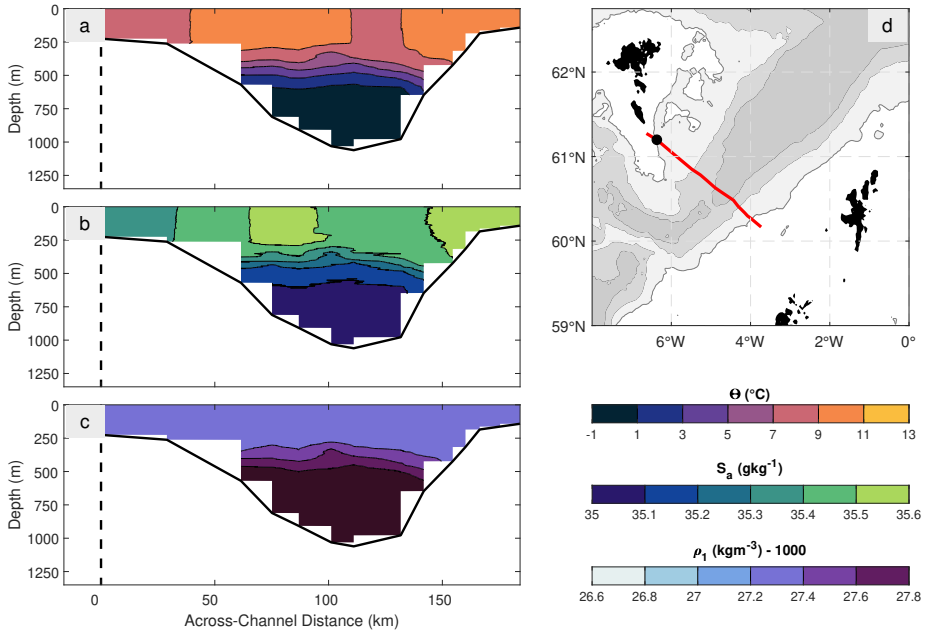

Figure B.2: As Fig. B.1, but for FIM, December 2014.

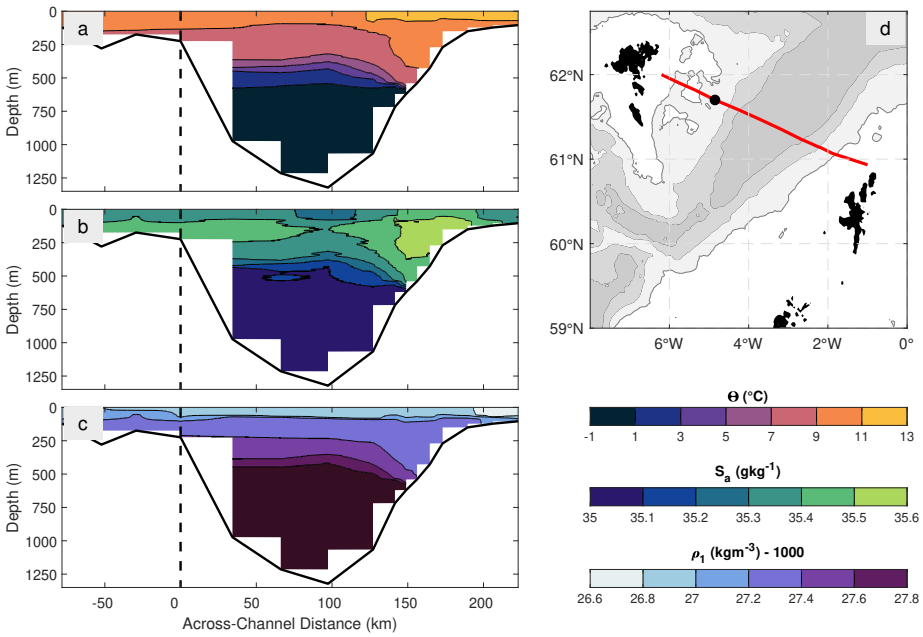

Figure B.3: Across-channel stratification (NOL, September 2014). (**a**) Cross-section of conservative temperature (filled contours). Across-channel distance is relative to the Faroe shelf edge (black dashed line). (**b**) As (a) but for absolute salinity. (**c**) as (a) but for potential density. (**d**) CTD section location (red line) and location of the Faroe shelf edge (black dot). Bathymetry has a scale identical to Fig. B.1.

C

ADDITIONAL FIGURES FOR CHAPTER 4

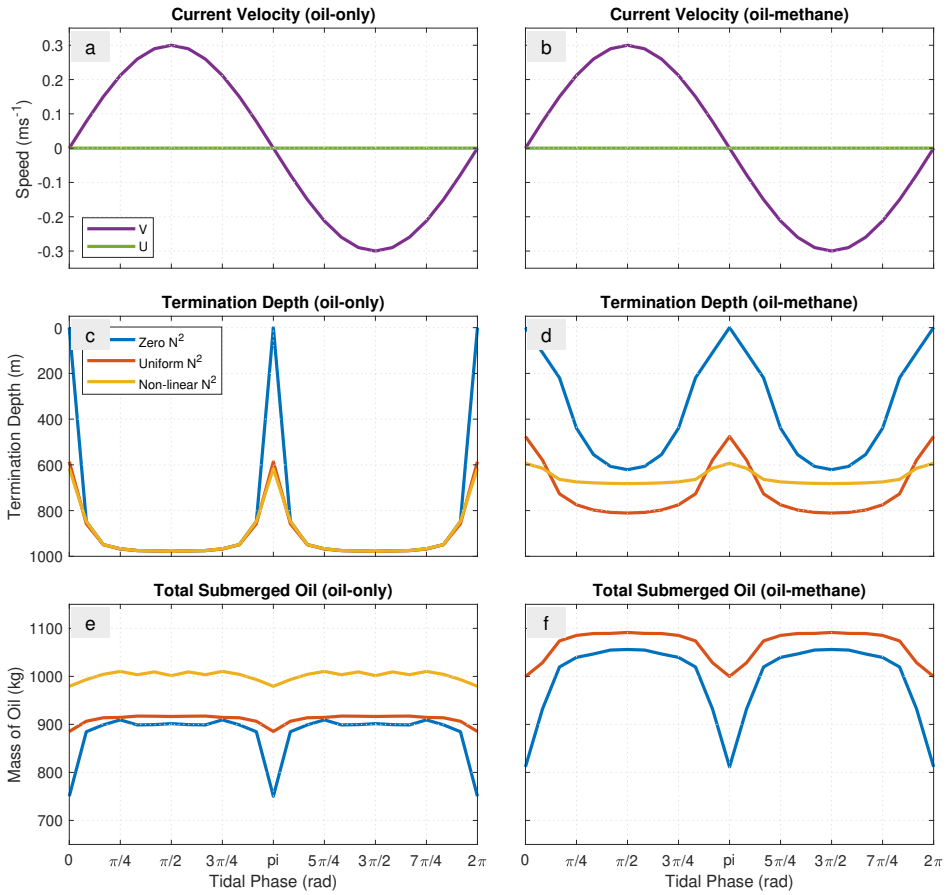

Figure C.1: Variability of an oil spill over a semidiurnal tidal cycle of $0.3\,\mathrm{m\,s^{-1}}$ velocity amplitude. (**a**) U (zonal) and V (meridional) components of the current from 0–2π rad for oil-only releases. (**b**) As (a) but for oil-methane releases. (**c**) Plume termination depths for oil-only releases in profiles of zero N^2, uniform N^2 and non-linear N^2 (coloured solid lines). (**d**) As (c) but for oil-methane releases. (**e, f**) As (c, d) but for the total submerged oil mass after 24 h.

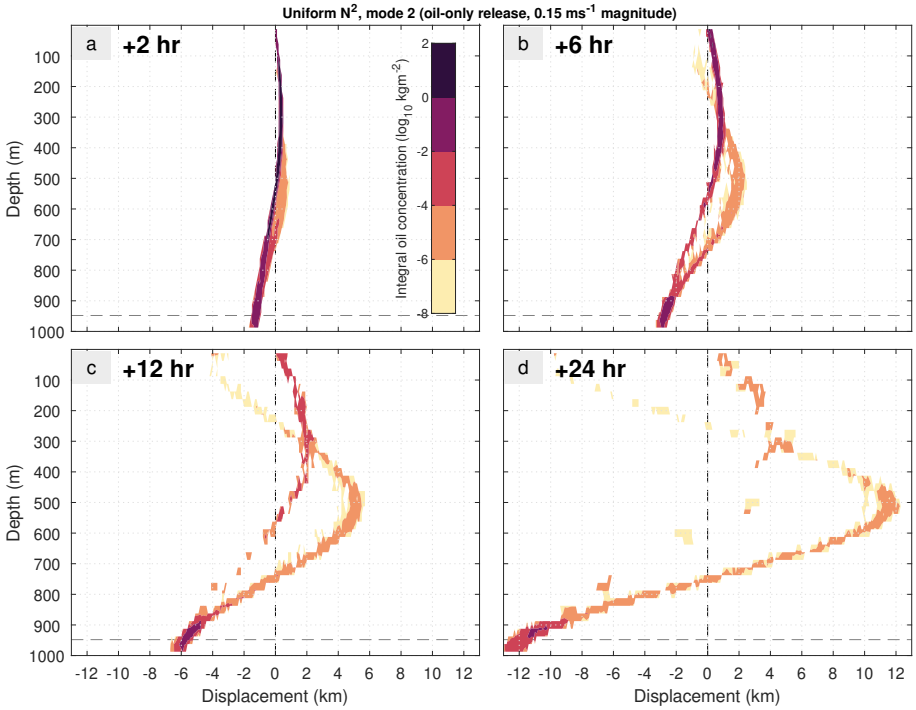

Figure C.2: Oil-only plume development for a plume in uniform N^2 and dynamic mode 2 with a maximum amplitude of $0.15\,\mathrm{m\,s^{-1}}$. (**a**) Cross-section of oil distribution 2 h after the beginning of the release. Coloured contours show the log zonal integral of oil concentration. Also shown are the release location (black dashed line) and plume termination depth (grey dashed line). (**b**) As (a) but 6 h after the beginning of the release. (**c**) As (a) but 12 h after the beginning of the release. (**d**) As (a) but 24 h after the beginning of the release.

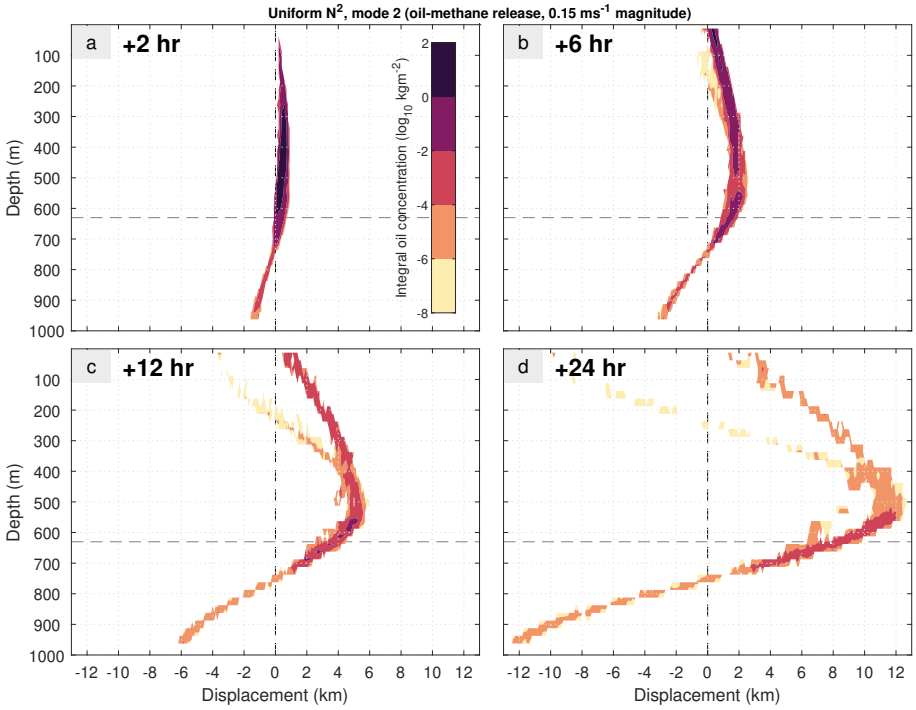

Figure C.3: As Fig. C.2 but for an oil-methane release.

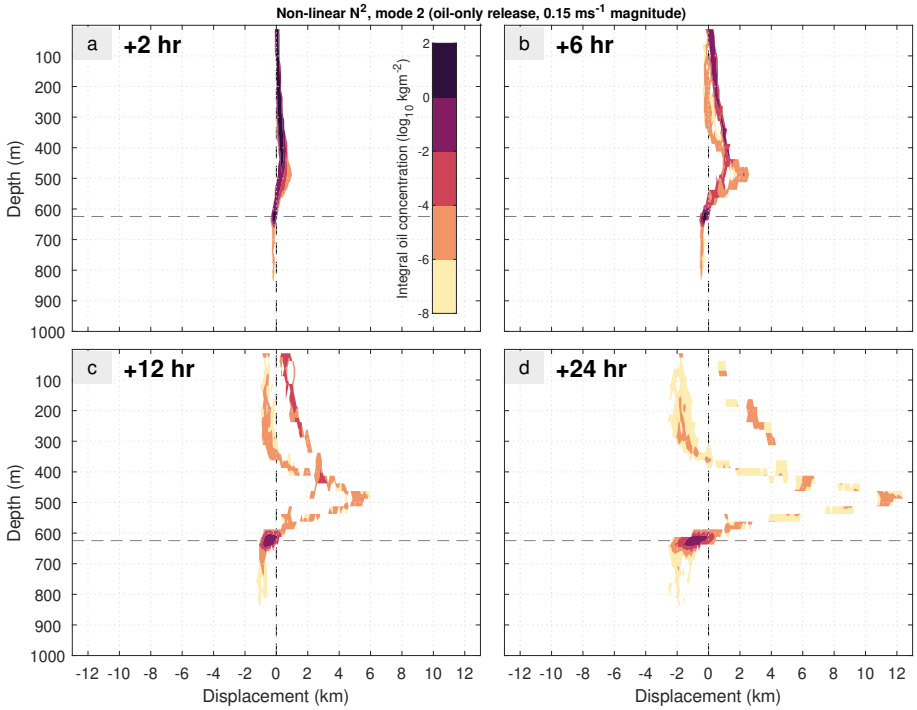

Figure C.4: Oil-only plume development for a plume in non-linear N^2 and dynamic mode 2 with a maximum amplitude of $0.15\,\mathrm{m\,s^{-1}}$. (**a**) Cross-section of oil distribution 2 h after the beginning of the release. Coloured contours show the log zonal integral of oil concentration. Also shown are the release location (black dashed line) and plume termination depth (grey dashed line). (**b**) As (a) but 6 h after the beginning of the release. (**c**) As (a) but 12 h after the beginning of the release. (**d**) As (a) but 24 h after the beginning of the release.

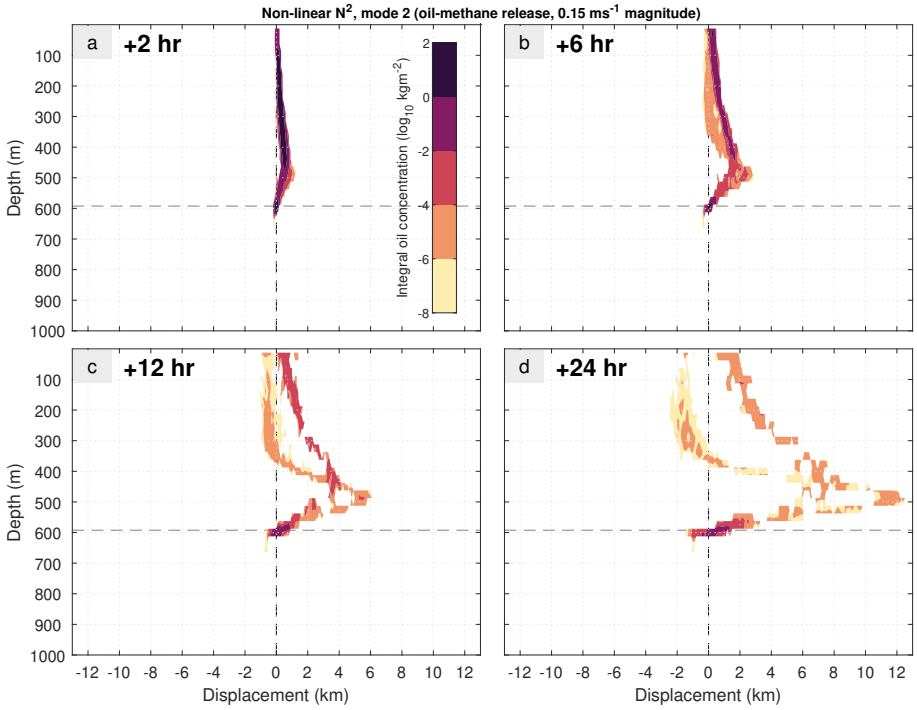

Figure C.5: As Fig. C.4 but for an oil-methane release.

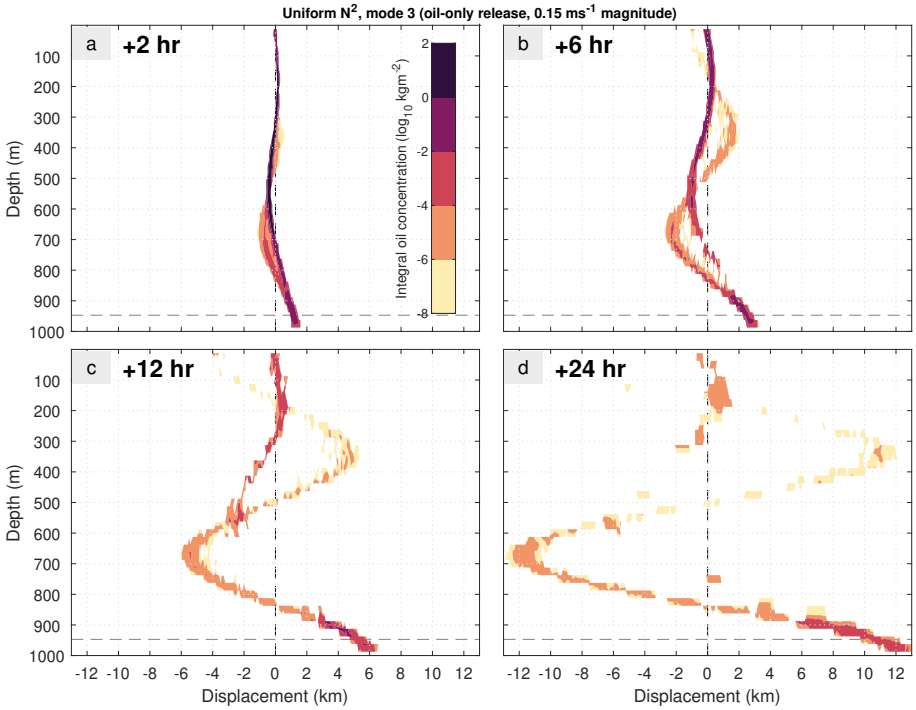

Figure C.6: Oil-only plume development for a plume in uniform N^2 and dynamic mode 3 with a maximum amplitude of $0.15\,\mathrm{m\,s^{-1}}$. (**a**) Cross-section of oil distribution 2 h after the beginning of the release. Coloured contours show the log zonal integral of oil concentration. Also shown are the release location (black dashed line) and plume termination depth (grey dashed line). (**b**) As (a) but 6 h after the beginning of the release. (**c**) As (a) but 12 h after the beginning of the release. (**d**) As (a) but 24 h after the beginning of the release.

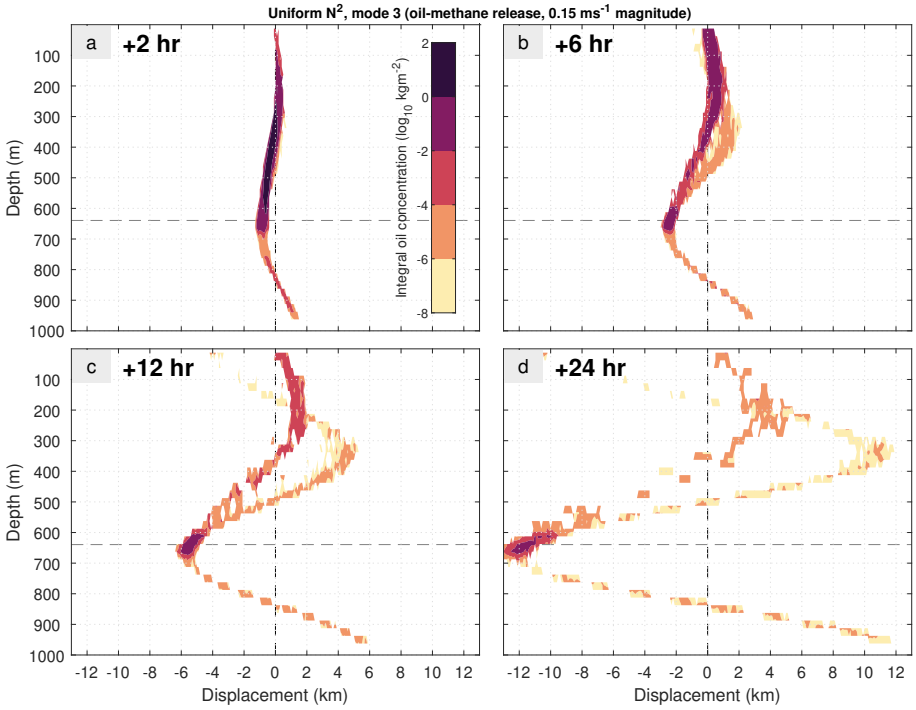

Figure C.7: As Fig. C.6 but for an oil-methane release.

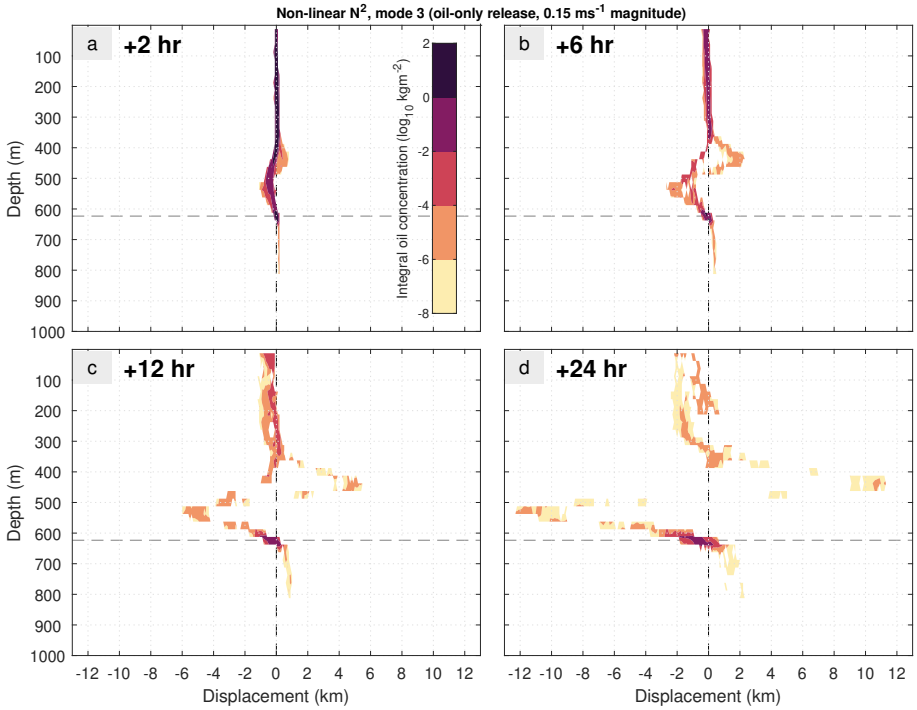

Figure C.8: Oil-only plume development for a plume in non-linear N^2 and dynamic mode 3 with a maximum amplitude of $0.15\,\mathrm{m\,s^{-1}}$. (**a**) Cross-section of oil distribution 2 h after the beginning of the release. Coloured contours show the log zonal integral of oil concentration. Also shown are the release location (black dashed line) and plume termination depth (grey dashed line). (**b**) As (a) but 6 h after the beginning of the release. (**c**) As (a) but 12 h after the beginning of the release. (**d**) As (a) but 24 h after the beginning of the release.

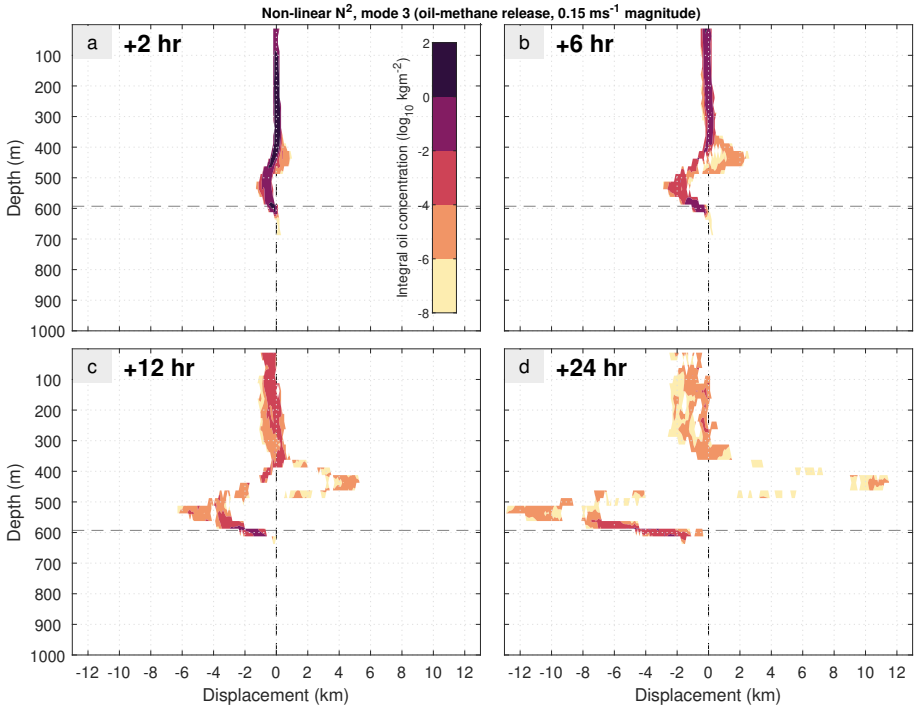

Figure C.9: As Fig. C.8 but for an oil-methane release.

D

THE CHALLENGES OF PREDICTING THE FATE OF OIL FROM A SPILL IN THE FAROE-SHETLAND CHANNEL[1]

The Deepwater Horizon deep-sea oil spill in the Gulf of Mexico was one of the worst marine environmental disasters in US history. The amount of oil released from the well-head at approximately 1500 m depth was so vast that if you had the same volume in petrol, you could drive an average UK car the equivalent distance of to the sun and back (forty-seven times). The spill caused extensive damage to the marine environment, with a million individual birds affected and over 2000 km of Gulf-state coastlines contaminated. A 'dirty blizzard' also formed in the Gulf of Mexico, which is a mixture of oil, microbes and algae that stick together in a highly viscous, difficult-to-clean-up mess. In total, Deepwater Horizon cost BP $145 Billion in fines and market loss.

Aside from in the Gulf of Mexico, the Faroe Shetland Channel (FSC) is another area of active oil and gas development, slightly north of the United Kingdom. There are 162 active well heads in the FSC, and more than three-quarters of these are situated off-shelf (deeper than 200 m). Some of these well-heads are over 1000 m below the sea surface. Assuming each site is equally likely to fail, there is a substantial chance

[1] This work was submitted as an article for *Ocean Challenge* (Gilchrist, 2020). This is the latest draft as of September 11th, 2019.

that oil will be released in the 'deep sea', at depths similar to Deepwater Horizon. Furthermore, recent oil release rate estimates suggest that the total volume of oil could be similar, too.

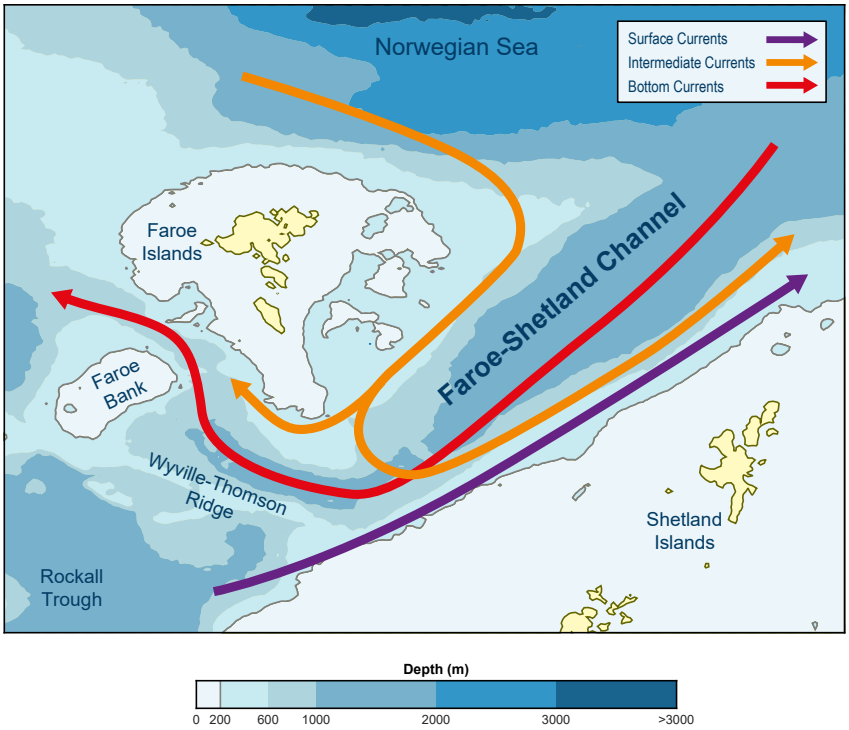

Figure D.1: Schematic of the water mass transport through the FSC. The surface current transports NAW. The intermediate current transports MNAW and AI/NIW. The bottom current transports NSAIW and FSCBW. Water mass acronyms are defined in the caption of Figure D.2.

It can take weeks to get the infrastructure that is required to clean up the spill on-site. It's therefore crucial to numerically model how the oil could disperse in the ocean, so that we can maximise the efficiency of the response and direct resources to the right place, at the right time. This is generally quite difficult to do in the FSC, because it's a very complicated and energetic dynamical system. Strong currents along the shelf and slope and deeper within the channel act to transport water from the North Atlantic near the surface, and the Norwegian Sea at depth (Figure D.1). Because of the resultant cross-flow (particularly near the Shetland shelf edge), a density interface exists at approximately 500 m depth between warm/saline water in the upper water-column and cool/fresh water in the lower water-column (Figure D.2). On a smaller scale, mesoscale eddies and meanders can enhance horizontal dispersion. Frequent stormy weather in and around this region compounds the issue, by providing more energy to disperse pollutant whilst at the same time stopping us

working to clean anything up.

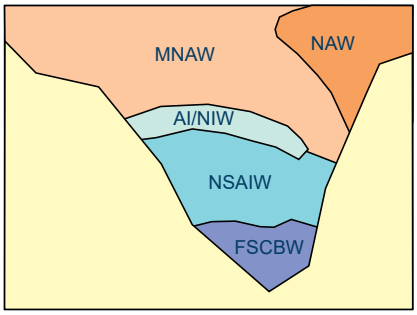

Figure D.2: Schematic of the stratification structure across the channel. NAW – North Atlantic Water; MNAW – Modified North Atlantic Water; AI/NIW – Arctic Intermediate/North Atlantic Water; NSAIW – Norwegian Sea Arctic Intermediate Water; FSCBW – Faroe-Shetland Channel Bottom Water.

Our research aims to improve spill prediction in the FSC, by furthering our knowledge of what happens in the channel in the event of a large, subsurface oil release. We use a state-of-the-art hydrodynamic model from the Met Office, in conjunction with an oil spill model used by institutions such as the Centre for Environment, Fisheries and Aquaculture Science (Cefas) and Oil Spill Response (OSRL). The ocean model is of the north-west European shelf, with a horizontal resolution of 1.5 km (FOAM AMM15 NWS). This is high enough to resolve processes such as eddies and meanders; processes that are not currently represented by the 7 km horizontal resolution ocean model Cefas and OSRL currently use. The spill model is Oil Spill Contingency and Response (OSCAR), which is maintained and developed by SINTEF.

We used these models to investigate how oil would be transported when released in a variety of locations. These scenarios include on the shelf slope, on the continental shelf, within the central FSC (the location shown as a cross in Figure D.3), and directly south of the Faroe Islands. Oil and gas were released from the seabed at between 150 m and 1200 m depth, depending on the location. For the central FSC release, the release depth was 1122 m. Each release lasted for nine days, and oil transport was simulated for a further three weeks.

Our results reveal that oil can be transported in a variety of directions. First and foremost, this depends on the depth the oil resides at. Oil in deeper water (comprising of approximately one-eighth of the total mass) travels westwards into the North Atlantic, whereas shallower and surfaced oil is transported north-eastwards towards

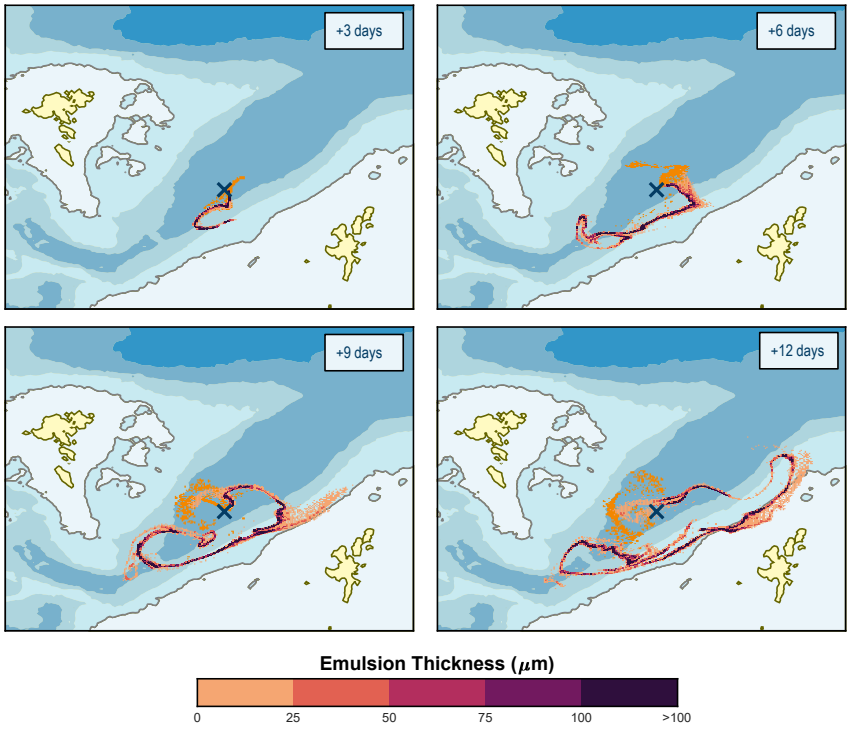

Figure D.3: Development of oil emulsion at the sea surface 3, 6, 9 and 12 days after the beginning of the release.

the Nordic Seas. Perhaps more alarmingly, oil that travels onto the continental shelf proceeds to head directly towards the Shetland Islands and Norway. This will likely lead to the beaching of oil, and considerable damage to our coastlines. Mesoscale eddies and meanders also act to break up the surfaced oil into smaller patches of emulsion (Figure D.3).

This research points towards the importance of international co-operation when dealing with an incident in the marine environment. By modelling the potential fate and trajectory of oil spills as robustly as possible, we can prepare for a range of conceivable scenarios in advance and make more informed emergency response decisions. Oil spills are sometimes disastrous, and they may be inevitable in a world dependant on fossil fuels, but prediction and forecasting can go a long way to minimising and mitigating their impact.